

THE OUTBURSTS AND ENVIRONMENTS OF NOVAE

Rebekah Hounsell
Astrophysics Research Institute

A thesis submitted in partial fulfilment of the requirements of
Liverpool John Moores University
for the degree of
Doctor of Philosophy.
May 4, 2012



IMAGING SERVICES NORTH

Boston Spa, Wetherby

West Yorkshire, LS23 7BQ

www.bl.uk

ANY MAPS, PAGES,
TABLES, FIGURES, GRAPHS
OR PHOTOGRAPHS,
MISSING FROM THIS
DIGITAL COPY, HAVE BEEN
EXCLUDED AT THE
REQUEST OF THE
UNIVERSITY

Declaration

The work presented in this thesis was carried out at the Astrophysics Research Institute, Liverpool John Moores University. Within Chapter 5 some work was conducted at the University of California San Diego and San Diego State University, USA, in collaboration with Liverpool John Moores University. Unless otherwise stated, it is the original work of the author.

While registered as a candidate for the degree of Doctor of Philosophy, for which submission is now made, the author has not been registered as a candidate for any other award. This thesis has not been submitted in whole, or in part, for any other degree.

Rebekah Hounsell
Astrophysics Research Institute
Liverpool John Moores University
Twelve Quays House
Egerton Wharf
Birkenhead
CH41 1LD
UK

MAY 4, 2012

Abstract

Classical and Recurrent novae (CNe/RNe) are interacting close binary systems in which mass is transferred from a donor star to the surface of an accreting compact companion resulting in an outburst. Their study is important for our understanding of several branches of modern day astrophysics.

The work presented in this thesis has focused on three particular topics: (i) Nova V458 Vulpeculae and its surrounding planetary nebula; (ii) Detailed nova light curves from the Solar Mass Ejection Imager (SMEI); and (iii) V1721 Aquilae, an usually fast, luminous, and highly extinguished nova. A brief account is also given of more generalised work on novae in M31, and areas for future investigation are discussed.

Nova V458 Vulpeculae is one of only two novae observed to lie within a planetary nebula (PN). Due to the outburst a light echo effect within the PN is experienced. Using H α data taken over four years the illumination of the PN with time has been examined and a 3D visualisation obtained. Comparison of light echo data from PN models generated with the morphokinematical modelling tool XS5 to observed PN light echo data indicate the presence of a PN with a bipolar external shell and an elliptical internal shell. Results have also confirmed that the PN is at a distance of 13 kpc.

SMEI is a space-borne instrument based on-board the Coriolis satellite. It provides precision visible-light photometry of point sources down to 8th magnitude and near complete sky-map coverage at 102-minute cadence. Using SMEI data detailed light curves of novae have been obtained which offer unprecedented temporal resolution

around, and especially before, maximum light, a phase of the nova eruption normally not covered by ground-based observations. They have allowed the exploration of fundamental parameters for individual objects including the epoch of the initial explosion, the reality and duration of any pre-maximum halt, the presence of secondary maxima, speed of decline of the initial light curve, plus precise timing of the onset of dust formation. The SMEI data archive undoubtedly holds a plethora of transient events and variable stars. A code designed to search for such events has been created and implemented on four years of SMEI data from one of its three cameras generating over 1500 variable objects, some of which were un-catalogued and are potentially very interesting.

Finally data on the unusually fast and luminous Nova V1721 Aquilae has been examined. Pre-outburst NIR images from the 2MASS catalogue revealed the presence of a progenitor system, the absolute magnitudes and colours of which suggested the object to have a sub-giant secondary, and so belong to the U Sco class of RNe. Post-outburst spectra of the object revealed the presence of triple-peaked $H\alpha$ and OI profiles. Spectral fitting of these profiles indicated a high ejection velocity of 3350 km s^{-1} . The triple-peaked nature of the $H\alpha$ profile suggested that the accretion disc of the system is viewed face-on. This is supported by models created in XS5, which also indicated an axis ratio of ~ 1.4 for the ejecta.

Publications

In the course of completing the work presented in this thesis, part of the contents of Chapters 3, 5, and 6 have been published in peer-reviewed journals:

1. **Hounsell, R.**, Bode, M.F., Hick, P.P., Buffington, A., Jackson, B.V., Clover, J.M., Shafter, A.W., Darnley, M.J., Mawson, N.R., Steele, I.A., Evans, A., Eyres, S.P.S., and O'Brien, T.J.: 2010, *Astrophys. J.* **724**, 480. *Exquisite Nova Light Curves from the Solar Mass Ejection Imager (SMEI)*
2. **Hounsell, R.**, Darnley, M.J., Bode, M.F., Harman, D.J., Helton, L.A., and Schwarz, G.J.: 2011, *Astron. Astroph.* **530**, A81. *A very luminous, highly extinguished, very fast nova - V1721 Aquilae*
3. Shafter, A.W., Darnley, M.J., Hornoch, K., Filippenko, A.V., Bode, M.F., Ciardullo, R., Misselt, K.A., **Hounsell, R.A.**, Chornock, R., and Matheson, T.: 2011, *Astrophys. J.* **734**, 12. *A Spectroscopic and Photometric Survey of Novae in M31*
4. McQuillin, R., Evans, A., Wilson, D., Maxted, P.F.L., Pollacco, D., West, R. G., **Hounsell, R.A.**, Bode, M. F.: 2012, *Monthly Notices of the Royal Astronomical Society* **419**, 330. *Novae in the SuperWASP data base*
5. Darnley, M.J., Ribeiro, V. A. R. M. Bode, M.F., **Hounsell, R.A.**, Williams, R. P.: 2012, *Astrophys. J.* **746**, 61. *On the Progenitors of Galactic Novae*

Acknowledgements



for Dad

REBEKAH HOUNSELL

MAY 4, 2012

I would like to take this opportunity to thank both my PhD supervisors Prof. Michael Bode and Dr Matthew Darnley for their advice and support over the last few years, as well as Dr Daniel Harman for all his hard work. I would also like to thank various staff members at the ARI especially Dr Phil James, Dr Susan Percival, Prof. Carole Mundell, and Dr Andrew Newsam.

A special thank you should be given to Dr Bernie Jackson, John Clover, Dr Paul Hick, and Dr Andrew Buffington for their support and help in the use of SMEI data, which has made this thesis what it is. I would also like to thank Dr Allen Shafter for his advice during my stay in America whilst working on SMEI data.

To Rob Barnsley (the king of code), Dr Zach Cano (wise words), Alyssa Drake (partner in crime), Clare Ivory (for making me smile), Dr Arna Karick (my inspiration), Dr Danae Polychroni (my sanity), Dr Vicky Scowcroft (queen of IRAF), and Dr Paul Westoby (IDL coach), thank you all so much. You have each played a huge part in my life during these many years and put up with my many rants.

To my grandmother, mother, brothers, sisters, Stacey Pilsworth, and Tanya Clark, thank you. Without your support and guidance I would not be where I am today.

And finally to my father, thank you for showing me the stars.

Contents

Declaration	ii
Abstract	iii
Publications	v
Acknowledgements	vi
Contents	viii
List of Tables	xiv
List of Figures	xvi
1 Introduction to Novae	1
1.1 Historical Overview	1
1.2 Classical Novae	3
1.3 Thermonuclear Runaway	5
1.4 Photometric Evolution	8
1.4.1 Nova Speed Class	8
1.4.2 Light Curves	9

1.4.3	Maximum Magnitude Rate of Decline Relationship	11
1.5	Recurrent Novae	13
1.6	Magnetic Novae	14
1.7	Dwarf Novae	15
1.7.1	Dwarf Nova light curves	16
1.7.2	Dwarf Nova Subclasses	16
1.8	Spectroscopic Observations	17
1.9	Observations of Novae in Quiescence	22
1.9.1	Accretion Discs and Inclination	23
1.9.2	Secondary stars and mass transfer rates	26
1.10	Populations and Frequency of Outbursts	28
1.11	Extragalactic novae	29
1.12	Progenitors of Type Ia Supernova	31
1.13	Outstanding Problems	33
2	Evolution of Nova Systems and Planetary Nebulae	37
2.1	Formation of a Planetary Nebula	38
2.2	Morphological Classifications	39
2.2.1	Haloes	42
2.2.2	Microstructure	42
2.3	Novae and Planetary Nebulae	43
2.3.1	Light Echoes	44

3	Observations of Novae with the Liverpool Telescope	46
3.1	The Liverpool Telescope	47
3.1.1	RATCam	47
3.1.2	SKYCam's	49
3.2	Observations of Galactic Novae	50
3.3	Observations of Extragalactic Novae	50
4	Nova V458 Vulpeculae	55
4.1	Introduction	55
4.2	Observations	56
4.3	Image Pre-processing	57
4.3.1	The Liverpool Telescope (LT)	57
4.3.2	Isaac Newton Telescope (INT)	58
4.3.3	William Herschel Telescope (WHT)	60
4.3.4	Nordic Optical Telescope (NOT)	60
4.4	Data Reduction	61
4.4.1	Image Examination and Alignment	61
4.4.2	PSF Modelling and Stellar Subtraction	63
4.4.3	Alignment of Star-Subtracted Images and Trimming	64
4.4.4	Seeing and Flux Normalization	65
4.5	Examination of the Two Dimensional system	67
4.6	Three Dimensional Visualisation of the System	74
4.7	Modelling of the Planetary Nebula using XS5	78

4.7.1	Modelling Trials: A Single Shell Structure	80
4.7.2	Modelling Trials: Internal and External Shell Structure	92
4.8	Discussion and Conclusion	98
5	Investigation of Novae with the Solar Mass Ejection Imager (SMEI)	101
5.1	Introduction	102
5.2	The Coriolis Satellite and SMEI	102
5.2.1	SMEI Design Requirements	107
5.2.2	SMEI Data Accumulation	109
5.2.3	SMEI Data Processing	109
5.3	Fitting Point Sources in SMEI maps	112
5.3.1	Least-Squares Fit of a Point Source	114
5.3.2	Star crowding	115
5.4	Finding Novae with SMEI	116
5.4.1	Data Processing	117
5.5	Nova Light Curves	121
5.5.1	Light Curves: First Class Data	121
5.5.2	Light Curves: Second Class Data	138
5.6	Solar TERrestrial RELations Observatory (STEREO) Heliospheric Imager	154
5.6.1	STEREO Data Processing	157
5.6.2	STEREO Observations of V5583 Sagittarii	157
5.7	Detection of Transients and Variable objects	160

5.7.1	Previous Detection of Transients and Variables in SMEI by Other Groups	160
5.7.2	Current Search for Transients and Variables	161
5.8	Discussion and Conclusion	168
6	A very luminous, highly extinguished, very fast nova - V1721 Aquilae (2008)	174
6.1	Introduction	175
6.2	Distance Determination	175
6.3	Post-Outburst Spectra	176
6.4	Pre-Outburst Identification	185
6.5	The Nature of the Secondary	187
6.6	Discussion and Conclusion	190
7	Summary and Future Work	196
7.1	Summary of Thesis Research	196
7.1.1	Examination of Extragalactic Novae	196
7.1.2	The Planetary Nebula Surrounding Nova V458 Vulpeculae	196
7.1.3	Nova Aquilae (2008)	198
7.1.4	Examination of Novae using data from the Solar Mass Ejection Imager (SMEI)	199
7.2	Future Work to be Conducted	201
7.2.1	Modelling of the PN Surrounding V458 Vulpeculae	201
7.2.2	The SMEI Data Archive	202

Bibliography	208
A Nova V458 Vul Images	224
B Known novae within the SMEI database	232
C Point Source Code: smei_findpnt	237
D Published Papers	256

List of Tables

1.1	Speed classes of nova light curves as given by Gaposchkin (1957), where t_2 is the number of days the nova takes to decline two magnitudes from maximum, and \dot{m}_V the rate of magnitude decline.	9
1.2	MMRD constants taken from Warner (2008) and references therein. .	12
1.3	Novae that are intermediate polars. Table reproduced from Warner (2008) and references therein.	16
1.4	Average rate of nova discovery. From work presented in Duerbeck (1990)	28
3.1	List of extragalactic novae observed as part of the work conducted within this thesis with the LT and FTN. Novae marked with a \star are used within Shafter et al. (2011).	52
3.2	Continuation of Table 3.1.	53
4.1	H α observations of Nova V458 Vul and its surrounding PN.	57
4.2	Estimated distance of each knot on the sky from the nova location. . .	70
4.3	Parameters used within χ^2 tests.	90
4.4	Parameters used within brute force χ^2 test.	93
5.1	Derived light curve parameters.	137
5.2	Derived light curve parameters of second class data.	154

5.3	Performance specifications of the HI instrument taken from Eyles et al. (2009).	156
6.1	Wavelength, FWHM, and relative velocity of fitted components of the triple-peaked H α structure presented in Figure 6.5.	183
6.2	Wavelength, FWHM, and relative velocity of primary fitted components of the triple peaked OI 8446 Å structure presented in Figure 6.6.	184
6.3	2MASS apparent and absolute magnitudes of the V1721 Aql progenitor (candidate), colours, and de-reddened colours of the NIR source located at the position of the nova. The extinction towards the nova has been taken as $A_V = 11.6$, and its distance as 2.2 kpc.	186
7.1	Refined parameters used within χ^2 test.	202
B.1	Classical and Recurrent Novae listed within the UCSD SMEI data base - continued in the next three tables.	233

List of Figures

1.1	Schematic view in the equatorial plane of a semi-detached binary system with equipotential lines and Lagrange points indicated. Adapted from Carrier et al. (2003).	4
1.2	Schematic illustration of the formation of a ring and its evolution into a disc. Image from Verbunt (1982).	6
1.3	Morphology of a nova light curve, from McLaughlin (1960)	8
1.4	Novae with typical Fe II spectra (Williams, 1992)	19
1.5	Novae with typical He/N spectra (Williams, 1992)	20
1.6	Evolution of the two spectral classes of novae from the permitted spectrum to the nebular spectrum (Williams, 1992)	21
1.7	Correlation between emission-line equivalent width $\langle W \rangle$ and inclination for $H\alpha$, $H\beta$ and He II 4686 Å. Image taken from Warner (1986).	24
1.8	Correlation between absolute magnitude M_V and inclination. Curve shown here is simply a fit to the data. Image taken from Warner (1986).	25
1.9	$(J-H)$ vs. $(H-K)$ diagram for novae in quiescence. Image taken from Weight et al. (1994).	27
1.10	Distribution of CNe in Galactic coordinates. Image taken from Warner (2008)	29

2.1	Morphologies of PN - images have been taken by the Hubble Space Telescope.	40
2.2	Anatomy of a light echo caused by dust scattering, (from Bode, 1979).	44
3.1	Founder of the Liverpool Telescope Prof. Mike Bode, stands in front of the telescope on La Palma in its fully-opening enclosure	48
3.2	Image of RATCam on the Liverpool Telescope.	48
4.1	Image of the PN surrounding Nova V458 Vul and the stars within its field. The image indicates the various regions used in analysis.	62
4.2	Plot illustrating calibration of stellar flux from one epoch's SANSIM image to a reference SANSIM image.	66
4.3	Summed image of aligned normalised star-subtracted PN data. The image shows the location of each knot and filamentary structure referred to in the text.	68
4.4	Summed image of aligned normalised star-subtracted PN data showing the location of each knot region sampled in <i>Gaia</i>	69
4.5	Plot showing the counts of equatorial regions 9, 5 and 4 (see Figure 4.4) in LT normalised star-subtracted median images for each epoch.	71
4.6	Plot showing the counts of polar regions 1, 2, 3, 6, 7, and 8 (see Figure 4.4) in LT normalised star-subtracted median images for each epoch.	72
4.7	Summed image of aligned normalised star-subtracted PN data indicating the position angle of the system in the plane of the sky. Angles written are given in degrees.	73

4.8	Left: The XY axis of the PN data representing what the observer would see on the plane of the sky. Here North is left and East is down. Right: The ZY axis of the PN data representing the distance along the line-of-sight to each point on the paraboloids. It should be noted that for the purposes of this image the nova centred mask has not been applied.	75
4.9	Radial displacement versus count plot for the all epochs within the 3D FITS cube. Plot indicates the progression of the light echo through the PN.	76
4.10	X and Y components of the radial displacement for dominant peaks found within 30 degree slices of Figure 4.9.	77
4.11	Models generated using XS5 - (a) Circle, (b) Ellipse, (c) Bipolar structure.	79
4.12	(a) Bipolar PN model created using XS5 with “uniform” illumination and set at a distance of 13 kpc with the following additional parameters: $A1A = 9''$, $B1A = 4''$, $PA1 = 30^\circ$, and $IN1 = 90^\circ$, $RISE = 1$ day, $FALL = 60$ days, and a seeing of $2.9''$ applied. (b) Light-echo observed from specified model 286 days after nova peak. (c) Light-echo observed from specified model 419 days after nova peak. (d) Light-echo observed from specified model 777 days after nova peak. Note that in each image North is left and East is down.	82
4.13	(a) XY axis projection of the observed PN light echo data. (b) XY axis projection of the light echo data created from the modelled PN via XS5. In these images and all following model images generated North is left and East is down in the XY plane.	84
4.14	(a) XZ axis projection of the observed PN light echo data. (b) XZ axis projection of the light echo data created from the modelled PN via XS5.	85

4.15	Top row: XY axis (North is left and East is down) projection of light echo data for (a) Observed PN at 13 kpc. (b) XS5 modelled PN at 15 kpc. (c) XS5 modelled PN at 17 kpc. (d) XS5 modelled PN at 19 kpc. Bottom row: XZ axis projection of light echo data for (e) Observed PN at 13 kpc. (f) XS5 modelled PN at 15 kpc. (g) XS5 modelled PN at 17 kpc. (h) XS5 modelled PN at 19 kpc.	86
4.16	(a) XY axis projection of the observed PN light echo data. (b) XY axis projection of the light echo data created from the modelled PN via XS5 with A1A = 18" and B1A = 8". North is left and East is down.	87
4.17	(a) XZ axis projection of the observed PN light echo data. (b) XZ axis projection of the light echo data created from the modelled PN via XS5 with A1A = 18" and B1A = 8".	88
4.18	Same as Figures 4.15 but using a semi-major axis of 18" and semi-minor axis of 8".	89
4.19	Top row: XY axis (North is left East is down) projection of light echo data for (a) Observed PN at 19 kpc. (b) XS5 modelled PN at 19 kpc. Bottom row: XZ axis projection of light echo data for (e) Observed PN at 19 kpc. (f) XS5 modelled PN at 19 kpc.	91
4.20	Histogram of χ^2 modelling results.	94
4.21	(a) Lowest χ^2 XS5 generated PN model. Seeing has not been applied. (b) Same as previous but with a 2.9" seeing applied. Within these images North is left and East is down.	95
4.22	Top row: XY axis (North left East down) projection of light echo data for (a) Observed PN data at 13 kpc. (b) XS5 modelled PN. (c) Same as b but using display parameters identical to those used within Figures 4.19. Bottom row: XZ axis projection of light echo data for (d) Observed PN data at 13 kpc. (e) XS5 modelled PN. (f) Same set up as c.	96

4.23	Histogram of DIST values for the first 1% of lowest χ^2 PN configurations. A Gaussian (in green) has been fit to the data with mean distance and one sigma error displayed.	97
5.1	(a) Coriolis spacecraft with SMEI instrument on-board prior to launch. (b) Titan II launch of the Coriolis spacecraft on 2003 January 6 th . . .	103
5.2	SMEI $3^\circ \times 60^\circ$ image frames from each of the three camera arranged in order furthest from the Sun. Image adapted from Jackson et al. (2004).	105
5.3	Hammer-Aitoff projection sky-map created from a full orbit's worth of frames. Image taken from Jackson et al. (2004)	106
5.4	Surface brightness versus solar elongation for zodiacal and star light, and of expected CME brightness extrapolated from <i>Helios</i> measurements. Image taken from Jackson et al. (2004).	108
5.5	Schematic of SMEI baffle with scale in centimetres. Image adapted from Jackson et al. (2004).	108
5.6	“Standard stars” (PSFs) for cameras 1, 2, and 3. Image taken from Hick et al. (2007)	113
5.7	Image taken from Hick et al. (2007) indicating the rotation of the SMEI PSF due to rotation of the spacecraft orbit relative to the sidereal background.	114
5.8	SMEI light curve of RS Oph (black squares) in terms of “SMEI magnitude” versus time (left-hand y-axis). Over-plotted (grey) are the <i>Swift</i> BAT 14-25 keV data.	123
5.9	Ground-based early V-band light curve of V1280 Sco. Data taken from the Das et al. (2008) light curve which was in turn created using data from the AFEOV.	125

5.10	SMEI light curve of V1280 Sco (black squares), superimposed (gray stars) are data from the “ π of the Sky” project.	126
5.11	Ground-based <i>V</i> -band light curve of V598 Pup reproduced from data in Pojmanski et al. (2007).	129
5.12	SMEI light curve of V598 Pup.	130
5.13	Light curve of KT Eri using <i>V</i> -band data taken from the AAVSO. . . .	131
5.14	SMEI (black squares) light curve of KT Eri with Liverpool Telescope SkyCamT data superimposed (grey stars).	133
5.15	SMEI light curve of T Pyx. The light curve clearly shows oscillations and light curve ends as the nova approaches the Sun-wards exclusion zone (see Section 5.2 for further details.	135
5.16	Period determination of T Pyx using Fourier analysis.	136
5.17	SMEI light curve of V1187 Sco indicating the peak of the nova and its initial decline. <i>Visual</i> and <i>V</i> -band data from AAVSO are over-plotted.	140
5.18	SMEI light curve of V2467 Cyg indicating the peak of the nova and its initial decline. <i>Visual</i> , <i>V</i> , and <i>R</i> -band data from AAVSO are over-plotted.	142
5.19	SMEI light curve of V2467 Cyg indicating the peak of the nova and its initial decline. <i>R</i> -band data from AAVSO are over-plotted.	143
5.20	SMEI light curve of V458 Vul indicating the multiple peaks of the nova. <i>Visual</i> , <i>V</i> , and <i>R</i> -band data from AAVSO are over-plotted. . . .	145
5.21	SMEI light curve of V597 Pup. <i>Visual</i> and <i>V</i> -band data from AAVSO are over-plotted.	146
5.22	SMEI light curve of V459 Vul. <i>Visual</i> , <i>V</i> , and \hat{R} -band data from AAVSO are over-plotted.	148
5.23	SMEI light curve of V2491 Cyg. <i>Visual</i> , <i>V</i> , and <i>R</i> -band data from AAVSO are over-plotted.	150

5.24	SMEI light curve of QY Mus. <i>Visual</i> and <i>V</i> -band data from AAVSO are over-plotted.	151
5.25	SMEI light curve of V5583 Sgr. <i>Visual</i> , <i>V</i> , and <i>R</i> -band data from AAVSO are over-plotted.	153
5.26	A cross sectional view through the HI instrument showing the fields-of-view of the two telescopes. Image taken from Eyles et al. (2009). .	155
5.27	SMEI and STEREO light curve of V5583 Sgr. <i>Visual</i> , <i>V</i> , and <i>R</i> -band data from AAVSO are over-plotted.	158
5.28	SMEI and STEREO light curves of V5583 Sgr covering the epoch of the detection within the SMEI data only.	159
5.29	A SMEI equatorial map from which zodiacal light, sidereal background, and the 5600 stars brighter than 6 th magnitude have been subtracted. With in this map the effects of poor stellar subtraction may be observed along with tails created by bright stars when near a cameras edge. . .	162
5.30	A SMEI equatorial map from which zodiacal light, sidereal background, and the 5600 stars brighter than 6 th magnitude have been subtracted, and which has undergone smoothing.	164
5.31	(a) Object detected at $\alpha = 02^h 33^m 52^s$ $\delta = +55^\circ 29' 27''$; J2000.	169
5.32	(a) Object detected at $\alpha = 06^h 15^m 0^s$ $\delta = +56^\circ 36' 13''$; J2000. (b) Object detected at $\alpha = 08^h 02^m 03^s$ $\delta = +63^\circ 04' 21''$; J2000	170
5.33	(a) Object detected at $\alpha = 19^h 12^m 40^s$ $\delta = -60^\circ 14' 43''$; J2000.	171
5.34	SMEI light curve of nova V1280 Sco. The black squares indicate data generated using then new <i>smei_findpnt</i> code; the red triangles are data using the old <i>smei_findpnt</i> code - both of these were conducted with <i>fix_centroid</i> switched on. The blue triangles indicate data using the new <i>smei_findpnt</i> code, but with <i>fix_centroid</i> switched off.	172

6.1	Apparent magnitudes of Nova V1721 Aql as observed by K. Itagaki. Additional tick marks on the X-axis represent the dates on which the Blue (see Figure 6.2) and Red (see Figure 6.3) spectra were taken. . .	177
6.2	Heliocentric velocity and extinction-corrected ($A_V = 11.6$, see Section 6.2) blue wavelengths optical spectrum of V1721 Aql, taken on 2008 September 25.19 (2.69 days after discovery) with the Steward Observatory Bok 2.29 m telescope. Continua have been subtracted using a cubic polynomial. Shorter wavelengths ($3550 \leq \text{\AA} \leq 5000$) have been excluded due to problems with noise.	179
6.3	As Figure 6.2, but Red spectrum, taken on 2008 September 25.25 (2.75 days after discovery). Continua have been subtracted using a cubic polynomial.	180
6.4	Relative velocity diagram of the $H\alpha$, OI 7773 \AA and OI 8446 \AA structures.	182
6.5	Observed $H\alpha$ structure (black line) with the sum of <i>Specfit</i> Gaussian components (red line). The blue lines represent separate Gaussian components. See Section 6.6 for further discussion. The lower plot shows the residual to the fit.	183
6.6	Observed OI 8446 \AA structure (black line) with the sum of <i>Specfit</i> Gaussian components (red line). The blue lines represent separate Gaussian components. Gaussian 4 represents a spectral artifact. Gaussians 2 and 5 represent components within the profile that are partially caused by fringing. Grey Gaussians represent fine structure caused by fringing effects. All fringing effects required fitting in order to produce the best overall match with observations. The lower plot shows the residual to the fit.	184

6.7	(a) 2MASS K_s band pre-outburst image. The nova is found within the centre of the black markers. (b) Unfiltered discovery image taken by K. Itagaki on 2008 September 22nd at the Itagaki Astronomical Observatory. The nova is found within the centre of the black markers.	186
6.8	NIR colour-colour diagram of quiescent classical nova systems reproduced from Hoard et al. (2002) using Table 1 of their data. The figure is adjusted to include the quiescent 2MASS colours of the nova V1721 Aql system.	188
6.9	(a) Plan view of modelled nova ejecta with an axis ratio of 1. The shell is smooth with uniform emission. (b) Plan view of modelled nova ejecta with an axis ratio of 1.4. Inclination of the system is such that the accretion disc is face-on to the observer, the shell is smooth with uniform emission. (c) Relative velocity diagram of the observed $H\alpha$ (black) structure and the two modelled systems created in XS5. The red line represents the system with an axis ratio of 1, the blue line represents the system with an axis ratio of 1.4. The difference between the modelled and observed line profiles is given in the lower part of the diagram.	191
6.10	(a) Plan view of modelled nova ejecta with an axis ratio of 1. Inclination of the system is such that the accretion disc is face-on to the observer and the shell is smooth with a slight emission enhancement within the equatorial region. (b) Plan view of modelled nova ejecta with an axis ratio of 1.4. Inclination of the system is such that the accretion disc is face-on to the observer, the shell is smooth with a slight emission enhancement within the equatorial region. (c) Relative velocity diagram of the observed $H\alpha$ (black) structure and the two modelled systems created in XS5. The red line represents the system with an axis ratio of 1, the blue line represents the system with an axis ratio of 1.4. The difference between the modelled and observed line profiles is given in the lower part of the diagram.	192

7.1	R-band peak magnitude as a function of characteristic decay time-scale for luminous optical transients and variables.	204
A.1	2008-05-21 data taken by the INT (a) Non-processed 99×99 pixel region centred on Nova V458 Vul. (b) Star subtracted normalised image of the same region.	225
A.2	Same as Figure A.1 except 2008-07-28 data taken by the LT.	225
A.3	Same as Figure A.1 except 2008-08-26 data taken by the LT.	225
A.4	Same as Figure A.1 except 2008-09-19 data taken by the NOT.	226
A.5	Same as Figure A.1 except 2008-09-21 data taken by the LT.	226
A.6	Same as Figure A.1 except 2008-09-30 data taken by the NOT.	226
A.7	Same as Figure A.1 except 2008-10-06 data taken by the LT.	227
A.8	Same as Figure A.1 except 2008-11-24 data taken by the LT.	227
A.9	Same as Figure A.1 except 2009-06-15 data taken by the WHT.	227
A.10	Same as Figure A.1 except 2009-06-30 data taken by the LT.	228
A.11	Same as Figure A.1 except 2009-08-18 data taken by the LT.	228
A.12	Same as Figure A.1 except 2009-09-23 data taken by the LT.	228
A.13	Same as Figure A.1 except 2009-10-20 data taken by the LT.	229
A.14	Same as Figure A.1 except 2009-11-14 data taken by the LT.	229
A.15	Same as Figure A.1 except 2010-07-23 data taken by the WHT.	229
A.16	Same as Figure A.1 except 2010-08-18 data taken by the LT.	230
A.17	Same as Figure A.1 except 2011-06-11 data taken by the LT.	230
A.18	Same as Figure A.1 except 2011-07-01 data taken by the LT.	230
A.19	Same as Figure A.1 except 2011-07-01 data taken by the LT.	231

A.20 Same as Figure A.1 except 2011-10-27 data taken by the LT. 231

Chapter 1

Introduction to Novae

1.1 Historical Overview

Nova from the Latin word novus meaning "new"

Novae were once thought to be new stars as they suddenly brightened in the night sky and then gradually faded away. The first records indicating the observation of novae were produced by Chinese astronomers as early as 200 BC. The observation of these unusual events then spread to other countries in the Far East where they were interpreted to be of astrological importance (Duerbeck, 2008). A detailed overview of Chinese, Korean, Japanese, European, and Arab celestial listings may be found in Stephenson & Green (2002)

With time interest in these mysterious objects increased and in 1786 the earliest known catalogue of objects which were seen to have "either disappeared, changed in brightness, or were new ones" was created (Pigott & Englefield, 1786). Within this list of 51 objects 12 were confirmed variables, four of which were novae, and the remaining 39 were yet to be authenticated.

During the early part of the 19th century increasing numbers of novae were found as a result of a large influx of amateur astronomer observations. However, in 1892

systematic photographic monitoring of the sky began and the detection of novae started to boom. This was then accelerated with the introduction of the 1P21 photomultiplier in the mid-1940s, increasing the sensitivity of photoelectric photometry and allowing for the detection of objects much fainter than those previously observed.

Although novae were known of and detected by astronomers for many centuries it was only in the 20th century that the physical interpretation of these objects developed. The understanding of nova theory was sparked by three major findings: (1) Schatzman (1951) discovered that ^3He could trigger thermonuclear runaways (TNRs); (2) Walker (1954) discovered the binarity of DQ Herculis; (3) Kraft (1964) confirmed that all novae occur in binary star systems. The evidence for this revelation came both from spectroscopic studies (using the *Hale* reflector), which indicated periodically varying radial velocities, and from intensive photometric examination. Additional optical studies of novae then led to an increased understanding of the white dwarf (WD) primary and accretion disc components of a nova system, with observations in the NIR between the 1970s and 1980s revealing the secondary donor star. More information about the WD component was then obtained via UV satellite observations (e.g. *IUE* and *Hubble*), with X-ray satellites revealing a new population of X-ray binaries in the 1970s. Finally the strong magnetic fields present in some nova systems were then revealed via polarisation studies.

Today the detection of novae is still carried out largely by the amateur astronomer community, and communication between these groups and professional astronomers is vital and aided via various web-based resources. The increased sensitivity of CCDs along with the quick response of telescopes especially robotic facilities (e.g. Liverpool Telescope, Faulkes Telescope North/South) means that the best information possible about a nova outburst may be obtained over multiple wavebands. The use of satellites and all-sky data surveys also provides a method in which to search for pre- and early outburst information along with the detection of otherwise undiscovered novae. However, even with all the advances made a full understanding these fascinating objects is still far from reach.

Scientific knowledge is in perpetual evolution; it finds itself changed from one day to the next - Jean Piaget.

1.2 Classical Novae

Classical Novae (CNe) belong to the Cataclysmic Variable (CV) class of objects. These are interacting close binary systems in which mass is transferred from a donor star to the surface of an accreting compact companion leading to a variety of behaviours, the most noticeable of which is outbursts (see Bode, 2010; Bode & Evans, 2008, for review). A typical CN system consists of a white dwarf (WD) primary and a cooler lower mass main sequence star known as the secondary (spectral type ranging from F to M). The dimensions of a binary system are determined via its orbital period (P_{orb}) and the mass of its components. Binary separation is usually less than a few solar radii with P_{orb} less than half a day (typically hours). P_{orb} can be used to determine the nature of the secondary star for example systems with a $P_{\text{orb}} \geq 8$ hours will have more evolved secondaries, rather than main sequence stars (Nelson et al., 2004). The P_{orb} of a Roche lobe-filling (see the end of this Section) main sequence star is given in Equation 1.1 (Warner, 1995) where M_2 is the mass of the secondary,

$$M_2/M_{\odot} = 0.0065 \cdot P_{\text{orb}}^{5/4} \text{ [hours]}. \quad (1.1)$$

The observed masses of WDs within CNe systems range between $0.5 M_{\odot}$ and $1.4 M_{\odot}$, the latter being the Chandrasekhar (1931) limit however, the lower limit is thought to be due to a selection effect as novae with higher mass WDs have a greater number of outbursts with higher peak luminosities.

The close proximity of the WD to its companion leads to significant interaction. The secondary becomes tidally distorted by the gravitational field of the WD causing the secondary to rotate synchronously with the orbital revolution and eliminating any eccentricity of its orbit. The total potential at any point in the system can be expressed as

the sum of the total gravitational potential and the effective potential of the centrifugal force, this is known as the Roche potential. Each star is said to be situated within a Roche lobe, this is the largest closed equipotential which can contain the mass of the star. Particles within the lobe experience the Roche potential, outside they do not and are lost from the system. Between the primary and secondary there is a point at which the forces acting on a particle exactly balance, known as the inner Lagrangian point (L_1). There are four other Lagrangian points which satisfy the same condition (see Figure 1.1). As the secondary expands it fills its Roche lobe and reaches L_1 . Here gas can escape from its atmosphere and onto the Roche lobe of the primary (see Figure 1.1). Only the secondary fills its Roche lobe making the system a semi-detached binary.



Figure 1.1: Schematic view in the equatorial plane of a semi-detached binary system with equipotential lines and Lagrange points indicated. The secondary star fills its Roche lobe. Adapted from Carrier et al. (2003).

The rate at which mass is lost from the secondary is given in Equation 1.2 (Warner, 1995)

$$\dot{M}_2 = Q\rho_{L_1}c_s, \quad (1.2)$$

where Q is the effective cross section of the stream leaving L_1 , ρ_{L_1} is the density at L_1 averaged over the cross section and c_s is the isothermal sound speed.

Material leaves the secondary as a stream and passes by the WD (unless the WD has a strong magnetic field, see Section 1.6). The trajectory of the stream lies in the orbital plane of the binary and eventually it collides with itself within the Roche lobe of the primary, close to the WD. The supersonic speeds of the material shocks the gas to a high temperature, radiating away a large amount of kinetic energy. Angular momentum is conserved however, and the lowest energy orbit is formed i.e. a circle. Successive collisions of particles in the gas lead to radiative dissipation of energy and cause the gas to spiral inwards. However, in order to conserve angular momentum particles must also move outward spreading the ring into a disc (see Figure 1.2). The disc size is limited by the tidal forces of the secondary and the maximum disc radius allowed is about 90% of the WD's Roche lobe radius (Pringle & Wade, 1985).

1.3 Thermonuclear Runaway

The nova outburst is caused by a thermonuclear runaway. Previous evolutionary processes have stripped the primary star of its original hydrogen envelope leaving an exposed WD. If the mass of the WD is less than $0.5 M_\odot$ the core consists of mainly helium, masses between $0.5 M_\odot$ and $1.2 M_\odot$ have carbon and oxygen cores, whilst masses $> 1 M_\odot$ contain oxygen and neon (Smith, 2007). Accreted material (mainly H) from the secondary star builds up in a layer on the surface of the WD. The bottom of this layer is hot and dense allowing electron degeneracy pressure to dominate. As the temperature in this layer increases H-burning can occur via two processes, the proton-proton chain (p-p chain; $p + p \rightarrow d + e^+ + \nu_e$; Schatzman, 1958) and CNO cycles. The p-p chain is important during the accretion phase of the outburst where the amount of accreted material is determined, but it is the CNO cycle that powers the final stages of

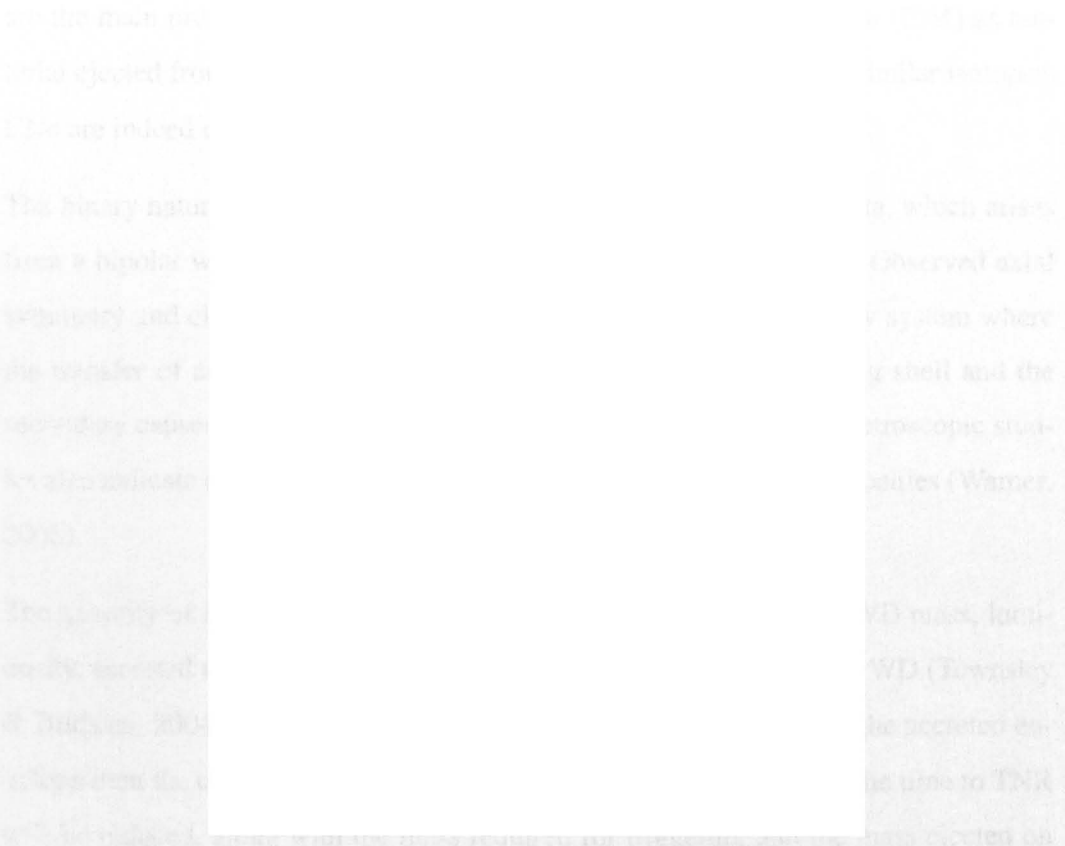


Figure 1.2: Schematic illustration of the formation of a ring and its evolution into a disc. Image from Verbunt (1982).

the thermonuclear runaway (TNR).

The pressure of a degenerate gas is largely independent of the temperature (T), thus the energy released in H-burning leads to a dramatic increase in T ($\epsilon_{CNO} \propto T^{18}$) with no expansion of the hot material, this leads to a TNR. Eventually the Fermi temperature is reached at the base of the envelope and the degeneracy is lifted causing the H-rich envelope to expand explosively forming a shock wave. The energy of the explosion ejects the H-rich envelope as a wind with outer layers being blown away by radiation pressure, once again leaving an exposed WD. This shock wave along with radiative-driven mass loss creates an expanding atmosphere of high absolute magnitude at maximum light. The mass loss decreases as the energy continues to be released causing a decline in the visual output. The average ejection velocity for CNe is $\approx 10^3 \text{ km s}^{-1}$ (Starrfield et al., 2008) with a mean ejected mass of $\approx 2 \times 10^{-4} M_{\odot}$ (Gehrz et al., 1998). Novae

are the main producers of ^{13}C , ^{15}N , and ^{17}O in the interstellar medium (ISM) as material ejected from the WD contains significant amounts of these and similar isotopes. CNe are indeed one source of metallicity enrichment in the ISM.

The binary nature of a nova system is reflected in the form of its ejecta, which arises from a bipolar wind and/or anisotropic irradiation of the ejecta shell. Observed axial symmetry and clumpiness of ejecta can only be explained via a binary system where the transfer of angular momentum and energy between the expanding shell and the secondary causes the aforementioned effects (Lloyd et al., 1997). Spectroscopic studies also indicate a binary nature through periodically varying radial velocities (Warner, 2008).

The quantity of accreted mass required for TNR is a function of the WD mass, luminosity, accreted mass composition, and the evolutionary history of the WD (Townsend & Bildsten, 2004). If mixing has occurred between the WD core and the accreted envelope then the opacity of the nuclear burning layer will increase and the time to TNR will be reduced, along with the mass required for triggering and the mass ejected on outburst. If the WD has a higher surface temperature and so more luminous (younger or not at quiescence after a previous outburst) then TNR can occur earlier and less mass is accreted. The critical mass for ignition as a function of WD mass is given in Equation 1.3 assuming all other parameters are constant (Starrfield et al., 2008)

$$P_{\text{crit}} = \frac{GM_{\text{WD}}M_{\text{crit}}}{4\pi R_{\text{WD}}^4}, \quad (1.3)$$

where M_{crit} is the ignition mass and P_{crit} is the critical pressure assumed as $\approx 10^{20}$ dyne cm^{-2} . A critical pressure must be reached within at the base of the accreted layer before TNR can occur. For a WD near the Chandrasekhar limit $M_{\text{crit}} < 10^{-5} M_{\odot}$, for a lower mass WD, e.g. $0.5 M_{\odot}$ $M_{\text{crit}} > 10^{-2} M_{\odot}$ (Starrfield et al., 2008). WDs spend most of their lives accreting material from the secondary at time-averaged rates of $\langle \dot{M} \rangle \approx 10^{-11} - 10^{-9} M_{\odot} \text{yr}^{-1}$ (Howell et al., 2001).

CNe are predicted to undergo outbursts once every 10^4 - 10^5 years (Hernanz, 2005).

The total radiant output of a single nova outburst is in the range of 10^{45} - 10^{46} erg with outburst amplitudes of approximately 10-20 magnitudes, absolute blue magnitudes of $M_B = -8$ at maximum, and a limit of around $-9.5M_B$ for the very fastest and most luminous CNe (Shafter et al., 2009, and references therein).

1.4 Photometric Evolution

The most common way to classify and examine novae is through their light curves. This is the plotting of an object's luminosity with time. An idealized light curve is shown in Figure 1.3.



Figure 1.3: Morphology of a nova light curve, from McLaughlin (1960)

1.4.1 Nova Speed Class

As indicated in Figure 1.3 most novae tend to rise rapidly (within one to three) days. This initial rise however, is not observed well enough to classify the nova, but its decline from maximum is. Novae are classified according to the number of days (t) that they take to decline n magnitudes from maximum, thus they are split into “speed

classes". These classes were first introduced by Gaposchkin (1957) and are given in Table 1.1. The table gives t_2 , but t_3 may also be used.

Table 1.1: Speed classes of nova light curves as given by Gaposchkin (1957), where t_2 is the number of days the nova takes to decline two magnitudes from maximum, and \dot{m}_V the rate of magnitude decline.

Speed Class	t_2 (days)	\dot{m}_V (mag d ⁻¹)
Very fast	<10	> 0.20
Fast	11-25	0.18-0.08
Moderately fast	26-80	0.07-0.025
Slow	81-150	0.024-0.013
Very Slow	151-250	0.013-0.008

As the nova declines it gets bluer, decaying slower in B than in V. This was interpreted by van den Bergh & Younger (1987) who formulated Equation 1.4,

$$\log t_2(V) = 0.953(\pm 0.013) \cdot \log t_2(B). \quad (1.4)$$

Novae have bolometric luminosities which are all at or above the Eddington Luminosity (Equation 1.5 - defined as the point where the gravitational force inwards equals the continuum radiation force outwards);

$$L_{\text{Edd}} = \frac{4\pi GMm_p c}{\sigma_T} = 1.3 \times 10^{38} \cdot \left(\frac{M}{M_\odot}\right) \text{ [ergs}^{-1}\text{]}. \quad (1.5)$$

The speed class can therefore be related to the initial generation of energy which is a function of the WD mass.

1.4.2 Light Curves

Each nova has its own unique optical light curve. However, they do share some common features and these are listed below (see Section 1.13 for problems regarding the standard nova light curve morphology).

- **Pre-maximum halt:** This occurs one to two magnitudes below maximum on the initial rise. The duration of the halt is related to the speed class of the nova (see

Section 1.4.1) lasting a few hours for fast novae (KT Eri, V598 Pup) and up to months for slow (HR Del, V1548 Aql, V723 Cas, and DO Aql). However, there is some controversy on the relation between speed class and pre-maximum halt duration as work by Kato et al. (2002) found that the rapidly evolving nova V463 Scti possessed a 24 day halt in its 2000 outburst. Based on this it was suggested that long pre-maximum halts may be more widely distributed amongst the speed classes than previously thought.

The physical reason behind the pre-maximum halt is not yet understood although several theories exist. Orio & Shaviv (1993) proposed that the pre-maximum halt is caused by a local or partial thermonuclear runaway on the surface of the WD. Hachisu & Kato (2004) were able to reproduce the long pre-maximum halt observed in V723 Cas and V463 Sct through the use of a steady-state optically thick wind model. Within this model they found that with WDs which have large enough H-rich envelopes the star expands to $R \geq 100 R_{\odot}$, decreasing the surface temperature to $T_{\text{eff}} \leq 7000$ K. The WD atmosphere is then said to mimic a supergiant. With changes in photospheric radius and temperature being insignificant compared to the increase in envelope mass the visual magnitude is saturated leading to the pre-maximum halt. This explanation however can only be applied to very specific nova systems and so a more general explanation to the pre-maximum halt still remains elusive.

- **Rise to peak magnitude:** This typically takes 1-2 days for fast novae from the pre-maximum halt and weeks for slow. The point of maximum is short-lived, lasting hours for fast novae and a couple of days for slow. Schmidt (1957) finds that the rate of the rise to maximum is correlated with the rate of decline after maximum. The time taken to rise the last two magnitudes is given in Equation 1.6

$$\log t_{r,2} = -0.3 + 0.7 \cdot \log t_2 = -0.5 \cdot \log t_3. \quad (1.6)$$

- **Decline from maximum:** As indicated in Figure 1.3, initial decline from maximum tends to be quite smooth for fast novae. Slow novae however may experience brightness variations of up to two magnitudes over time-scales of 1-20

days. When the nova is ≈ 3 -4 magnitudes below maximum 3 different types of behaviour can occur. This is called the “transition phase”, usually lasting until $\Delta m \approx 6$ mags below peak. The changes in magnitude occurring within the light curve are correlated with the system line intensities and velocities (Payne-Gaposchkin, 1964), and overall the spectrum changes from stellar to nebular. The different types of light curve behaviour that can occur within transition are listed below.

1. A deep minimum of 7-10 magnitudes lasting for months or years which is then followed by a decline extrapolated from the pre-transition phase (e.g. DQ Her, T Aur, LW Ser).
2. Large quasi-periodic oscillations with amplitudes of 1-2 mags (e.g. V603 Aql-12 days, GK Per-5 days, DK Lac-25 days; Pejcha, 2009).
3. No variation; this occurs for many novae especially the very fast or fast speed classes (e.g. CP Pup, V1500 Cyg, V1668 Cyg).

The observation of a deep minimum in the optical light curve is due to the formation of dust (grains $\sim 1\mu\text{m}$) within the ejected gas. This effect was initially understood through the infrared study of FH Ser by Hyland & Neugebauer (1970). With non-dust forming novae, the transition phase is regarded as the point in the eruption at which the stellar system components are revealed due to the ejecta becoming optically thin (Bath, 1978). Transition phenomena at visual wavelengths in these systems may therefore be understood in terms of changes in the physical properties of the underlying system.

1.4.3 Maximum Magnitude Rate of Decline Relationship

There is a relation between the maximum absolute magnitude (M) of a nova outburst and its rate of decline (t_n). This is called the Maximum Magnitude Rate of Decline (MMRD) relationship and can be used to ascertain the distance to the nova. It was first noted by Hubble (1929), and calibrated by Mclaughlin (1945). The linear form of the

MMRD is given in Equation 1.7 (Mclaughlin, 1945).

$$M = b_n \cdot \log t_n + a_n, \quad (1.7)$$

where M is the absolute magnitude at maximum, $n = 2$ or 3 , and a_n and b_n are MMRD constants given in Table 1.2.

Table 1.2: MMRD constants taken from Warner (2008) and references therein.

M	n	a_n	b_n	Reference
pg	3	-11.3	2.4	de Vaucouleurs (1978)
B	3	-10.67(\pm 0.30)	1.80(\pm 0.20)	Pfau (1976)
V	2	-10.70(\pm 0.30)	2.41(\pm 0.23)	Cohen (1985)
V	2	-11.32(\pm 0.44)	2.55(\pm 0.32)	Downes & Duerbeck (2000)
V	3	-11.99(\pm 0.56)	2.54(\pm 0.35)	Downes & Duerbeck (2000)

Buscombe & de Vaucouleurs (1955) also noted that novae of all speed classes have the same absolute magnitude 15 days after maximum. This is represented in Equation 1.8. However, it is not thought as reliable as the MMRD relation (see Darnley et al., 2006).

$$\langle M_V \rangle = -5.2 \pm 0.1. \quad (1.8)$$

One of the most important potential applications for novae is their use as distance indicators (Galactic and extragalactic). This is due to their high peak luminosities ($M_B > -9.5$ Shafter et al., 2009) and frequency (see Section 1.10). The absolute magnitude (M) can then be used within Equation 1.9 (distance modulus) below, in order to calculate the distance (d) to the object in parsecs, with m being the apparent or observed magnitude and A_V the extinction.

$$m - M = 5 \log d - 5 + A_V. \quad (1.9)$$

The relations in Equations 1.7 and 1.8 however, have various issues of uncertainty which are discussed in Section 1.13.

1.5 Recurrent Novae

Recurrent novae (RNe) are a subset of CVs similar to CNe, but have more than one observed outburst with recurrence time-scales of 10-100 years. There are currently 10 confirmed Galactic RNe (Schaefer, 2010). The RN system consists of a WD and an evolved main sequence, sub-giant or giant secondary star. The basic triggering and explosion mechanism of RNe is the same as for CNe, but there are some distinct differences in the properties of this subgroup. In order to reconcile the short quiescence period of a RN with TNR the WDs within the system are believed to be hotter, more massive (close to the Chandrasekhar limit), and have larger mass accretion rates ($\approx 10^{-8}$ - $10^{-7} M_{\odot} \text{ yr}^{-1}$) than CNe (Gännsicke et al., 2002; Kato, 1991; Starrfield et al., 1985). RNe are a very heterogeneous group however, they can be grouped into three distinct subtypes (Bode, 2010; Evans et al., 2008).

- **RS Oph:** These contain red giant secondaries and have a high rate of mass transfer, which causes a high outburst frequency. They are fast novae with a decline rate of $\approx 0.3 \text{ mag day}^{-1}$ (Anupama & Mikołajewska, 1999) and possess a long P_{orb} (\approx few hundred days). Their outburst spectrum contains broad emission lines which decrease over time. Initial ejection velocities are given as $V_{\text{exp}} \geq 4000 \text{ km s}^{-1}$, the deceleration of the expansion velocity is due to interaction of the ejecta with the red giant wind material. Typical mass ejected by these RNe is $\approx 3 - 4 \times 10^{-6} M_{\odot}$ (Bohigas et al., 1989). Models created for these long period RNe indicate that a high mass WD is required in order to achieve the observational effects indicated in their light curves. The models also find that after outburst not all accreted material has been ejected (e.g. Hernanz & José, 2008). Evidence of the accretion disc can be found in the optical light curve of these objects through a secondary maxima (as in the case of T CrB) or a plateau in the decline phase (RS Oph; Hachisu et al., 2006). During quiescence optical emission in these systems are dominated by the secondary component. *Group members:* RS Oph, T CrB, V3890 Sgr, and V745 Sco.

- **U Sco:** These have evolved secondaries and are some of the fastest novae observed. The quiescent spectra of this group is dominated by He-lines unlike CNe. *Group members:* U Sco, V394 CrA, V2487 Oph.
- **T Pyx:** These are RNe which show a slow decay with a short P_{orb} . *Group members:* T Pyx, CI Aql, and IM Nor.

The latter two subtypes of RNe given are short P_{orb} systems which have more evolved main-sequence or sub-giant secondaries. They are heterogeneous in nature when compared to the long P_{orb} RS Oph type RNe. The short P_{orb} systems can be split into two further groups based on similarities during outburst and quiescence. The first consists of the very fast novae with exceptionally high ejection velocities (initial FWHM $\sim 10000 \text{ km s}^{-1}$ for U Sco - Sekiguchi et al., 1988), ejecta masses of $10^{-7} M_{\odot}$ (as noted by Williams, 1992, for U Sco), and very fast spectral evolution (see Section 1.8). The second group consists of the slow novae with $V_{\text{exp}} \approx 800\text{-}2500 \text{ km s}^{-1}$, spectral evolution similar to CNe (see Section 1.8), and ejecta masses of $10^{-5} M_{\odot}$.

Models based on observations of RNe predict that they retain some of their accreted mass after outburst (e.g. Hernanz & José, 2008; Starrfield et al., 1985). Due to this it has been suggested that RNe may be the progenitors of Type Ia Supernovae (SNe Ia) as repeated cycle of accretion and ejection may one day lead to a WD with a mass reaching the Chandrasekhar limit i.e. $M_{\text{WD}} \geq M_{\text{Ch}}$. This is discussed further in Section 1.12.

1.6 Magnetic Novae

So far systems where the strength of the magnetic field on the WD is negligible have been considered. However, at least 25% of all known CVs have WDs with moderate to strong magnetic fields (Wickramasinghe & Ferrario, 2000). Magnetic WDs in CVs were first detected via polarization measurements. The field strength can be measured via Zeeman splitting of absorption lines from the WD or via humps in the spectrum at

optical or infrared wavelengths. These humps are due to the harmonics of cyclotron emission as electrons spiral down the magnetic field lines on to the WD. Two types of magnetic systems are considered.

- **Polars:** The magnetic field of the WD strong ($B \gtrsim 10^7$ G). Members of the polar group include V1500 Cyg, V1432 Aql, BY Cam and CD Ind. The strong magnetic field of the WD interacts with the weaker field of the secondary, forcing synchronization of the WD with P_{orb} through magnetic linkage. In these systems no accretion disc forms. Instead, ionized material is accreted from the secondary and on encountering the magnetosphere it becomes “tied” to the field lines and directed along them, creating an accretion stream. The material accelerates as it falls eventually creating a shock at the top of the accretion column, near a magnetic pole. The energy released from the system is enough to make it an X-ray source (see Cropper, 1990, for more details on Polars).
- **Intermediate Polars (IPs):** The magnetic field of the WD ranges between $10^6 \leq B \leq 10^7$ G. In this case the magnetic field is not strong enough to force the WD to spin with P_{orb} . The WD also has a smaller magnetosphere and so an accretion disc may form outside of it. Material accreted meets the magnetosphere at all points on the inner edge of the disc and so produces an accretion curtain rather than a stream (Cropper, 1990). Due to the presence of a disc some IPs show dwarf nova type outbursts. The mass of the disc is less than that of non-magnetic novae. A list of known polars and their eruptions is given in Table 1.3.

1.7 Dwarf Novae

The standard Dwarf Novae (DNe) are U Geminorum (U Gem) stars, named after the prototype observed in 1855 (Warner, 1995). DNe have semi-regular outbursts with amplitudes ranging from 2-6 magnitudes, outburst durations of a few days to 20 days, and recurrence time-scales which can be as short as weeks or as long as years (Osaki,

Table 1.3: Novae that are intermediate polars. Table reproduced from Warner (2008) and references therein.

Nova	Eruption	P_{orb} (h)	P_{rot} (s)
V533 Her	1963	5.04	64
DQ Her	1934	4.65	71
V375 Sct	1975	-	258
GK Per	1901	47.92	351
DD Cir	1999	2.34	670
HZ Pup	1963	5.11	1212
AP Cru	1936	5.12	1837
RR Cha	1953	3.37	1950
GI Mon	1918	4.32	2916
V1425 Aql	1995	5.42	5188
V697 Sco	1941	4.49	11916

1996; Sterken & Jaschek, 1996). With DNe the energy source of the outburst is the gravitational field of the WD. Mass from the secondary is stored in the disc and when dense enough it is transferred rapidly onto the WD. This process releases a vast amount of energy as material falls down the deep gravitational potential well. The actual processes that occur however are a lot more complicated than this brief explanation, but it is fair to say that the mechanism for the outburst is disc instability (Osaki, 1974).

1.7.1 Dwarf Nova light curves

The light curves of DNe contain a number of small amplitude variations which can occur on time-scales of seconds to minutes. These variations are due to changes in the amount of surface area visible on the tidally distorted secondary, eclipses, and pre-eclipse humps, which are due to the bright spot where the accretion stream runs into the disc.

1.7.2 Dwarf Nova Subclasses

DNe have three main recognised subclasses.

1. SS Cygni (SS Cyg) stars: These systems have $P_{\text{orb}} > 3$ hours and exhibit regular

quasi-periodic outbursts with typical intervals of 30-100 days with each lasting about 3-10 days.

2. Z Camelopardalis (Z Cam) stars: These systems have outbursts every 10-30 days and $P_{\text{orb}} > 3$ hours (Sterken & Jaschek, 1996). They alternate between periods of normal outburst and non-outburst/“standstills”. At a standstill the star remains at a point about 0.7 mag below maximum; this can last for months.
3. SU Ursae Major (SU UMa) stars: These have mainly normal outbursts (lasting a few days) but do experience occasional super-outbursts. These super-outbursts last longer (5 times normal outburst duration) and are of greater amplitude (at least a magnitude greater). During a super-outburst the light-curve has super-humps which drift in orbital phase. This is characteristic of an elliptical disc with the long axis precessing around the orbit.

1.8 Spectroscopic Observations

Spectral analysis of novae (CNe, RNe, magnetic, or DNe) is extremely important as it provides a method by which to better understand the geometry/structure of the system, the evolution of the nova ejecta, surface nuclear reactions, gas ejection mechanisms, and the formation of dust. Spectra of CNe and RNe can be interpreted as arising from a two-component gas, one which is a discrete shell associated with the outburst and the other a continuous wind that follows the outburst. Both of these components are sites of emission line formation.

A large amount of material is ejected from the surface of the WD at outburst. However, the material remaining on the WD has a high enough temperature to allow further surface nuclear reactions to occur in equilibrium. These can last for months maintaining L_{Edd} . The energy generation causes the expansion of the surface and the formation of an extended atmosphere which can engulf the secondary, this is called a common envelope (CE). Mechanisms that drive the wind from the extended atmosphere are the frictional dissipation of energy from the secondary star (MacDonald, 1980) and the

radiation pressure from the luminous WD remnant (Bath & Shaviv, 1976). It is the surface nuclear reactions and the wind which then determine the spectrum emitted after outburst. At maximum the extended atmosphere has a T_{rad} of less than 10,000 K, and so the excitation level is low. As the wind mass loss rate decreases the photospheric radius shrinks and T_{rad} increases, and so the excitation level goes up and eventually coronal lines can be emitted. With time the surface nuclear reactions stop and T_{rad} decreases along with the excitation level (Williams, 1992).

All novae show the progressive development of four systems of absorption lines and five of emission. These phases of spectral evolution are called the *Pre-Maximum*, *Principal*, *Diffuse Enhanced*, *Orion*, *Nebular*, and *Post-Nova*. Within the *Principal Spectrum* the average velocities of the absorption lines correlate with the speed class. McLaughlin (1960) found that the velocities can be represented by,

$$\log V_{\text{ej}} [\text{kms}^{-1}] = 3.70 - 0.5 \cdot \log t_3 [\text{days}] = 3.57 - 0.5 \cdot \log t_2 [\text{days}]. \quad (1.10)$$

From the *Diffuse Enhanced spectrum* average velocities maybe found from,

$$\log V_{\text{ej}} [\text{kms}^{-1}] = 3.81 - 0.41 \cdot \log t_3 [\text{days}] = 3.71 - 0.4 \cdot \log t_2 [\text{days}]. \quad (1.11)$$

Novae can be classified by their spectra. This depends upon which non-Balmer emission lines are strongest within 3500 Å -7500 Å during the first few days after outburst. There are two main spectral classes of novae: those which have prominent Fe II lines, and those which have prominent He/N lines. The spectral properties of the two classes and how they evolve are discussed below and presented in Figure 1.6, as defined by Williams (1992).

1. Fe II Novae

- Spectra arise predominantly from a wind.
- P Cygni type absorption profiles are present in Balmer and Fe II lines.
- Spectral development is slower than He/N novae ~ few weeks.

Figure 1.4: Novae with typical Fe II spectra (Williams, 1992)

- Emission lines are narrower than He/N novae ($\text{HWZI} < 2,500 \text{ km s}^{-1}$).
- Low ionization fluorescence lines in the red e.g. Fe II lines at 1.69 and 1.741 μm .
- Forbidden lines are present - auroral [N II], [O II], [O III] and [O I].
- On evolution to the nebular phase forbidden lines may develop that are similar to those of a Galactic nebula, although some become neon novae producing strong lines of [Ne III] or [Ne V].

2. He/N Novae

- Spectra arise predominantly from a shell ejected at maximum light.
- Not as homogeneous as the Fe II group.

Figure 1.5: Novae with typical He/N spectra (Williams, 1992)

- Evolve faster than Fe II novae.
- Excitation levels of emission lines are higher than Fe II novae.
- Broader lines than the Fe II novae ($\text{HWZI} \approx 5000 \text{ km s}^{-1}$).
- Line peaks are flat-topped or saddle shaped, and jagged.
- Absorption components not usually present in optical spectra.
- Intensity of He II $\lambda 4686$ becomes greater than $\text{H}\beta$.
- Flat blueish continuum.
- On evolution to the nebular phase the line spectra either fade quickly into the continuum and show no forbidden lines, have strong coronal forbidden lines, or become neon novae.

There are some types of novae that can change spectral classes during the early permit-

Figure 1.6: Evolution of the two spectral classes of novae from the permitted spectrum to the nebular spectrum (Williams, 1992)

ted emission line phase. These are known as hybrid novae, some may evolve from an Fe II nova into a He/N nova, whereas others may have emission from both components at the same time.

Some years after outburst (maybe decades) the ejected shell may become spatially resolved allowing spectroscopy of the individual components of the ejecta and imaging of the expanding shell in the light of individual spectral lines, to be obtained. Examples are DQ Her, GK Per and CP Pup (see O'Brien & Bode, 2008, for a review).

The type of spectrum produced by a RN depends upon whether it is a short or long period system. With long period RNe the early phase spectra have permitted lines and coronal lines develop by the time it has faded 2-3 magnitudes from maximum. When entering the nebular phase these lines fade. At quiescence (see Section 1.9) the optical spectrum is dominated by that of the secondary with emission lines due to H I and He I. He II is not present but lines of Fe II, Ca II and O II 8446 Å are except in T CrB. Group 1 of the short period RNe have very fast spectral evolutions with high ionisation and no forbidden lines, thus their spectral evolution are like that of a He/N CNe. At quiescence the spectra is dominated by He II lines and weak H lines if any. He enrichment is thought to be due to material accreted from the evolved main sequence secondary. Group 2 early spectra contain H I, Fe II, N III and O I lines with P Cyg profiles. The spectra evolve from being Fe II dominant to He/N dominant and thus are

similar to a hybrid nova (Evans et al., 2008).

1.9 Observations of Novae in Quiescence

It is as important to observe nova systems at minimum (i.e quiescence) as it is to observe them at maximum. It is during this “quiet” phase that many properties about the nova system itself are revealed (e.g. that they are binary systems where material is transferred from a late-type star to a WD).

Within a nova binary system the mass transfer rate (\dot{M}) is high, and the surface temperature (T_{eff}) of the primary is $\approx 50,000$ K. After eruption the temperature of the primary has increased causing an escalation in the irradiation of the secondary leading to an expansion of its atmosphere and higher \dot{M} . T_{eff} and \dot{M} are dependent on each other and as the primary cools \dot{M} decreases as $t^{-\alpha}$ ($\alpha \simeq 0.43$, Kovetz et al., 1988) for about a century after outburst. The system is then thought to enter in to a very low \dot{M} state where in some cases \dot{M} effectively reaches zero, causing the system to pass into “hibernation”. Mass transfer is eventually restored after loss of angular momentum from the system, through magnetic braking or gravitational radiation. This is the expected evolutionary scenario for binary systems with $P_{\text{orb}} \geq 4$ hr. However the theory of hibernation is speculative and evidence by Somers et al. (1996) suggests that this does not happen for at least 200 yrs. One argument in support of this low \dot{M} phase is given by the fact that no novae noted in Oriental records over two thousand years ago are observable today (Shara, 1989).

If the binary separation of the system is small, i.e. $P_{\text{orb}} \leq 4$ hr, then the primary is prevented from cooling below T_{eff} due to enhanced irradiative heating of the secondary by the primary and the hot central region of the disc. This results in a greatly enhanced \dot{M} and a high \dot{M} equilibrium is re-established after eruption (Warner, 2002). It is this effect which results in many novae having similar magnitudes before and after an outburst (Robinson, 1975). This self-sustained high \dot{M} may be maintained for centuries slowing the cooling of the WD, delaying DN outbursts, and preventing descent into

hibernation (Warner, 2002).

During quiescence a nova system may experience several optical effects such as reflection, quasi-periodic oscillations, and super-humps. Reflection effects are where large amplitude (1.1-1.2 mag) variations are observed and are thought to occur in systems where there has been a recent eruption and the accretion disc does not dominate the luminosity of the system. Quasi-periodic oscillations are thought to be caused by vertical thickening of the accretion disc which is moving near the inner edge of the disc as a wave. This reflects and obscures radiation from the central source. Super-humps are thought to be caused by an eccentric shaped accretion disc (Warner & Woudt, 2003).

Robinson (1975) also found that many nova light curves demonstrated a rise of 0.25-1.5 magnitudes 1 to 15 years before an eruption event thus enabling anticipation of an outburst. This work however has been cast in to doubt by Collazzi et al. (2009) who after re-examination of old literature found that four of the five novae which were claimed to have pre-eruption rises were due to mistakes. Examination of 22 nova eruptions within Collazzi et al. (2009) using original archival photographic plates did however reveal two novae (V533 Her and V1500 Cyg) with significant pre-eruption rises. Unfortunately it is evident that this signal is not found with all novae. This is due to the fact that pre-outburst light does not consist of one source but three: the WD primary, late-type secondary, and the accretion disc. It is not clear which of these three is the producer of the pre-eruption rise, however it must be the dominant source if it is to be detected. Work by Adamakis et al. (2011) using wavelet analysis however, has indicated that it is possible to find a signal which may be used to predict a nova outburst and these authors have presented such a study using RS Ophiuchi.

1.9.1 Accretion Discs and Inclination

At quiescence the luminosity of the accretion disc tends to dominate the system in the optical. Thus when obtaining the absolute magnitude (M_V) of a nova remnant it is important to take the disc and its inclination into account. To obtain a fuller picture, the contribution of the secondary at minimum must also be considered.

The accretion disc inclination can be obtained directly if an eclipse is observed. This is found however in very few nova systems. The equivalent widths $\langle W \rangle$ of emission lines produced from these systems are correlated with the disc inclination. It has been shown by Warner (1986) that systems viewed edge-on have much larger relative line strengths than those seen face-on. This correlation is shown in Figure 1.7 and thought to be due to reduction in continuum brightness as the disc is seen at larger inclinations. It should be noted that the secondary's contribution to $\langle W \rangle$ should be taken into account to obtain accurate inclination angles. When considering the effect that inclination has on the M_V of the system Warner (1986) finds a strong correlation (see Figure 1.8).

Figure 1.7: Correlation between emission-line equivalent width $\langle W \rangle$ and inclination for $H\alpha$, $H\beta$ and He II 4686 Å. Image taken from Warner (1986).

This correlation shows that the absolute magnitude of a nova system in quiescence is actually accretion disc inclination dependent. At maximum the relation does not hold as the accretion disc is no longer the dominant source of luminosity. Using the

Figure 1.8: Correlation between absolute magnitude M_V and inclination. Curve shown here is simply a fit to the data. Image taken from Warner (1986).

DN U Geminorum Paczynski & Schwarzenberg-Czerny (1980) established a relation between the inclination of the accretion disc and M_V , this is given in Equations 1.12 and 1.13.

$$\Delta M_V(i) = -2.5 \cdot \log \frac{L(i)_{\text{disc}}}{\langle L_{\text{disc}} \rangle}, \quad (1.12)$$

$$= -2.5 \log \left[\cos(i) + \frac{3}{2} \cos^2(i) \right], \quad (1.13)$$

where a limb-darkening coefficient of 0.6 has been used.

For face-on systems no contribution from the secondary is expected for $P_{\text{orb}} \leq 12$ hr. However systems at a higher inclination and with shorter orbital periods the secondary may be detectable. Only GK Per ($P_{\text{orb}} = 48$ hrs) is known to require a correction for secondary contamination at minimum as the system contains a sub-giant, this is also the case for some types of RNe.

1.9.2 Secondary stars and mass transfer rates

The mass-transfer rate (\dot{M}) of a CN system along with the nature of the secondary star may be estimated through the use of infrared (IR) colours. The position of a nova system on a $(J-H)$ vs. $(H-K)$ colour-colour diagram is determined in part by the nature of the secondary star. Systems with main-sequence stars will occupy a different region to those with a giant counterpart. In a system containing a main-sequence star the accretion disc dominates the luminosity adding a significant overall blue contribution. With systems containing a giant, the red contribution of the secondary and blue contribution of the disc are comparable, thus causing a different occupation region of the colour-colour diagram. Using this method it is also possible to determine the presence of suspected RNe.

As stated previously the optical luminosity of a system containing a main-sequence secondary star is dominated primarily by the flux of the accretion disc. If \dot{M} is high then the effect is to make the system appear blue. If the \dot{M} were to fall the disc would cool making the system redder and the flux from the secondary would start to make a significant contribution to the IR colours, also reddening the system. There are therefore several factors which effect the position of a nova system on a IR colour-colour diagram;

1. The mass of the secondary (M_2)/its spectral type.
2. The mass-transfer rate \dot{M} .
3. The reddening towards the system, E_{B-V} .

4. The inclination of the disc i .
5. The mass of the primary.

The effect of the primary is found to be negligible and the inclination of the disc is only seen to play a part if it is approaching face-on (i.e. $i \leq 30^\circ$). Taking the reddening of the system into account it is therefore possible to obtain the nature of the secondary and the \dot{M} of the system. Such work has been conducted by Weight et al. (1994). Spectral types between K5-M5 and \dot{M} values from 10^{-11} - $10^{-6} M_\odot \text{ yr}^{-1}$ are presented in Figure 1.9 from which one can in principle read off both the spectral type and the expected \dot{M} . Their work indicated that a change in \dot{M} from 10^{-8} to $10^{-9} M_\odot \text{ yr}^{-1}$ results in an increase in $(J-K)$ of ≈ 0.2 magnitudes.

1
;

Figure 1.9: $(J-H)$ vs. $(H-K)$ diagram for novae in quiescence. Filled circles-CNe; filled squares-known RNe and symbiotic novae; open circles-data for old novae examined within Harrison (1992). Grid represents combinations of dwarf secondaries and accretion discs having spectral types and $\log \dot{M}$ as indicated. The regions occupied by giants, sub-giants (data from Lee, 1970) and Miras are also given. Data is de-reddened for interstellar extinction; arrow represents dereddening vector of $A_V = 1$. Image taken from Weight et al. (1994).

They also found that \dot{M} decreased by no more than 70% in the first century after outburst, thus finding no evidence for the onset of hibernation.

1.10 Populations and Frequency of Outbursts

Various surveys have attempted to measure the outburst rate of Galactic CNe over the past century. Such work was done by Duerbeck (1990) who accounted for non-uniform time coverage of the novae and his results are presented in Table 1.4.

Table 1.4: Average rate of nova discovery. From work presented in Duerbeck (1990)

m_V (max mag)	Discovery rate (yr^{-1})	m_V (max mag)	Discovery rate (yr^{-1})
< 1	0.004	4-5	0.05
1-2	0.002	5-6	0.14
2-3	0.004	6-7	0.47
3-4	0.003	7-8	0.58

The results above however are greatly affected by lack of detection, selection effects, and interstellar extinction. This point is made clear when the mean detected Galactic Nova rate calculated from Table 1.4 is 3 yr^{-1} , whereas investigations such as Shafter (2002) derive a total Galactic rate of $30 \pm 10 \text{ yr}^{-1}$, once all aforementioned effects have been taken into account.

Galactic novae tend to populate the Galactic bulge and plane as indicated in Figure 1.10. However, studies by della Valle et al. (1992) have indicated that fast novae are found at $z < 100 \text{ pc}$ and associated with the disc (Population I environment) whereas slow novae are found up to $z \leq 1000 \text{ pc}$ and associated with the Galactic Bulge (Population II environment). This finding is consistent with novae observed in extragalactic systems such as M31 (Capaccioli et al., 1989). The occurrence of dual populations of novae may be caused by differences in the progenitor. High and low z novae differ in their speed class and maximum magnitude at outburst. The important parameters which govern the speed class of a nova are its WD mass and magnetic field strength. If the WD is more massive the nova outburst is faster and brighter therefore nova systems containing higher mass WDs could be concentrated closer to the disc. Evidence for this has been produced by de Kool (1992). If the WD is not very massive ($\simeq 0.9 M_{\odot}$; Orio et al., 1992) but has a high magnetic field (10^6 Gauss) the mass loss may be accelerated and thus it appear as a fast novae, without the higher luminosity at maximum. These systems may also belong to the disc and thus further study is required in

Figure 1.10: Distribution of CNe in Galactic coordinates, with the Galactic core at the centre of the diagram and increasing longitude towards the left. Filled circles give the location of 132 fast novae, open circles are 40 slow novae, crosses are 58 unclassified novae and small dots are 58 uncertain novae. Data are from Downes et al. (2005); image taken from Warner (2008).

order to fully understand the bimodal distribution of novae with stellar population.

1.11 Extragalactic novae

Much has been learnt from the study of novae with the Galaxy. However, Galactic data are not ideal for establishing population characteristics of novae. This is due to the influence of various selection effects. The study of extragalactic novae is important in order to understand nova populations including the dual nova progenitor hypothesis (see Section 1.10).

The discovery of novae outside of the Milky Way began in the early 20th century with work by Ritchey (1917) leading the way. The first systematic survey of extragalactic novae was conducted by Hubble (1929) using the Andromeda galaxy (M31) where he made 63 nova discoveries. From his work he derived an overall galactic nova rate of $\sim 30 \text{ yr}^{-1}$. In comparison with modern day studies, M31 is seen to have a high global nova rate of $65^{+16}_{-15} \text{ yr}^{-1}$ (Darnley et al., 2004, 2006). Examination of the nova distribution by authors such as Capaccioli et al. (1989) and more recently Darnley et al. (2006) reveal that the nova rate of the bulge of M31 is greater than that of the

disc. This pattern has also been confirmed for M81 in which the spatial distribution of novae follows the bulge light much better than the disc or total light (Neill et al., 2004).

An explanation for the distribution of novae within M31 was proposed by Ciardullo et al. (1987). They suggested that many nova binary systems were created in the globular clusters of M31 and were later injected into the bulge via three body interactions in clusters and/or the tidal disruptions of clusters. This has led to the search for novae within globular clusters, with limited success (see Shafter & Quimby, 2007; Shara & Zurek, 2002).

In order to compare nova rates of different galaxies the rate for each galaxy must be normalised by the stellar mass contained in the galaxy. This can be done via the use of the galaxy's K band magnitude, as novae are found within an evolved stellar population. The normalised nova rates are called Luminosity Specific Nova Rates (LSNR - Ciardullo et al., 1990b). The LSNR has allowed astrophysicists to conclude that nova rates should increase in galaxies with active star formation, providing support for the results found by della Valle et al. (1992).

Due to the high outburst luminosities of novae ($-7 < M_V < -10$) and their frequency, novae are of great interest as distance indicators. They are on average two magnitudes brighter than Cepheids, and are found in both Population I and II environments. The scatter on the Galactic MMRD relation, due to difficulty in measuring accurate distances to novae, can be improved via the observation of novae within external galaxies such as M31. Although a linear relation given in Equation 1.7 above worked for Galactic novae, more complicated relations are proposed from extragalactic data (della Valle & Livio, 1995).

$$M_V = -7.92 - 0.81 \cdot \arctan\left(\frac{1.32 - \log t_2}{0.23}\right), \quad (1.14)$$

The use of novae as distance indicators however, is not wide spread. This is due to lack of adequate observations in which the peak and decline of the nova is well observed

and so inadequate t_2 and t_3 times are obtained. The effect of stellar population on nova properties also complicates the MMRD relation and questions its universality.

1.12 Progenitors of Type Ia Supernova

Type Ia supernovae are one of the most energetic transient events in the Universe, releasing $\sim 10^{51}$ erg of energy at outburst. They are characterized by a lack of H and He in their spectra during outburst, a clear Si II absorption line at 6150 Å, and Fe emission in their late-time spectra.

SN Ia are of major astrophysical importance. Understanding of these objects will aid in determining metallicity evolution and the star-formation history of galaxies. The objects also act as standard candles allowing distance determination on cosmological scales (red-shift $z > 1$; Filippenko, 1997). For this reason they are significant in cosmology as they are used to measure the expansion history of the Universe. The evolution of their peak luminosity as one looks back to the early Universe may however depend upon the nature of the progenitor, which is still poorly understood.

Evidence (listed below) suggests that SNe Ia are due to the explosion of CO WDs which have exceeded M_{Ch} (see Nugent et al., 2011).

- The total energy released is consistent with that released in the C+O to Fe conversion.
- The maximum light spectra of SNe Ia contain no H lines, which is characteristic of a WD that has had its envelope stripped away.
- The light curve of a SN Ia is in agreement with energy deposition from radioactive decay of Fe-peak elements as expected for the product of CO WD deflagration (Pritchett et al., 2008).

There are two standard models for progenitors of SNe Ia. These are the double degenerate (Iben & Tutukov, 1984; Webbink, 1984) and single degenerate (Whelan & Iben,

1973) models (DD & SD).

The double degenerate model: This consists of a close binary system made up of two CO WDs (hence no H), which then merge via angular momentum loss due to the radiation of gravitational waves. The objects coalesce bringing the overall mass above M_{Ch} . This final object cannot sustain hydrostatic equilibrium and thus a SN Ia occurs. Possible evidence of the DD scenario is presented by Napiwotzki et al. (2004) who detected three short period WD binaries with masses close to M_{Ch} . These systems have been estimated to merge within 4 Gyrs to two Hubble times.

The single degenerate model: This represents a WD accreting matter from an efficient mass-transferring companion star. Eventually enough material is accreted on to the WD to bring it to or above M_{Ch} , leading to a SN Ia. Theory finds that the maximum initial mass a CO WD can have before accretion is $\approx 1.1 M_{\odot}$. If greater than this C-ignition can occur and almost the entire star is converted to O and Ne before a CO core WD configuration is attained (Dominguez et al., 1993). Therefore the minimum mass a WD may need to obtain and retain is an extra $0.3 M_{\odot}$ of material for SN Ia. It is often thought that RNe systems are the progenitors for the SD model as the WD can be pushed over its M_{Ch} through the gain of material over repeated cycles of the RN lifetime. However, with this model there are problems which need to be considered. The RN system (particularly those of RS Oph type) contains a lot of H. In order for these to be the progenitors of SN Ia somehow this H must not be seen at the time of eruption. Another issue is that the average mass accretion rate multiplied by quiescent time must be greater than the mass ejected at each eruption in order to obtain a mass $\geq M_{\text{Ch}}$.

Both the DD and SD models have their flaws and although the SD model is currently favoured there is no firm conclusion as to the exact progenitor of SNe Ia. Recent work by Li et al. (2011) when making use of historical imaging obtained at the location of SN 2011fe/PTF11kly has found that observations favour either the DD scenario or Roche lobe overflow from a sub-giant or main-sequence star rather than a giant. This has thrown speculation on to whether systems such as RS Oph and T CrB can lead to SN Ia.

1.13 Outstanding Problems

CNe and RNe are second only to gamma ray bursts and supernovae in their energetics however, novae are far more frequent in a given galaxy than both. The high outburst luminosities of CNe and RNe make them potentially powerful probes of the evolution of binary systems in different (extragalactic) stellar populations, and the rapid formation of large amounts of dust in many novae post-outburst makes them unique laboratories in which to explore cosmic dust grain formation. Novae also provide an insight into the nuclear physics of explosions on degenerate objects; the shaping of nebular remnants, with implications for planetary nebulae; ejecta and accretion physics, and elemental abundances.

There are however, many outstanding problems in the nova field, with a selection of these listed here. It is the aim of this project to try to address some of these issues in the Chapters mentioned below.

- **Supernova Type Ia Progenitors:** As discussed in Section 1.12, the exact nature of the progenitors of SNe Ia still remain elusive. Through examination of the SN Ia rate and the stellar death rate Pritchett et al. (2008) find that the SD route to SN Ia can only be made to match the SN Ia rate if WDs are converted to SN Ia with a uniform efficiency of $\sim 1\%$, independent of mass. As low mass progenitors are thought to have lower conversion efficiencies they determine that the SD model cannot be the only progenitor scenario and that some new theory is required to explain observed results. The lack of H or He in the spectra of SN Ia is also very unusual as these are the most abundant elements in the secondary stars. If either were discovered, the DD scenario would be ruled out. A more detailed understanding of individual RNe, and the RN population as a whole, will help in determining if the SD model is tenable.
- **Pre-Nova Binary Evolution:** During binary evolution, multiple CE stages may be entered which can lead to spiral-in phases creating a close binary system. However, these CE stages are very complex and not well understood. The under-

standing of the evolution of binary systems to CN/RN systems maybe increased through the study of novae such as GK Persei (Bode et al., 1987) and V458 Vulpeculae (Wesson et al., 2008) both of which occurred inside a planetary nebula (PN). Observation and modelling of the morphology of such systems could provide a vital insight into pre-outburst evolution. See Chapter 4 for work on nova V458 Vul.

- **Details of the TNR:** Many important details of the TNR and the explosion mechanism are poorly understood. For example the exact mass required for TNR is uncertain as it is dependent upon core material mixing with the accreted material. Thus further study of this area is needed.
- **Nova Binary Components:** It is important to ascertain the mass and composition of stars in a nova binary system in order to assess its evolution, likelihood of being a SN Ia progenitor, and to refine TNR models. Spectroscopy can determine the mass and composition of a WD via radial velocity and chemical abundance measurements respectively. Multi-frequency photometry is required to obtain the nature of the secondary and constrain mass accretion rates. The measurement of secondary mass however, is greatly influenced by the inclination of the system. Inclination and other system parameters may be obtained through the examination of spatially resolved remnants. These provide clues to the progress of the TNR on the WD surface, and remnant shaping mechanisms. Accurate distances to systems can also be determined via expansion parallaxes which are vital in calculating the energetics of the outbursts. Only a few resolved remnants have been studied in significant detail and more effort should be put into finding such resolved ejecta, taking multi-frequency observations, and the creation of 3D simulations. See Chapter 6 for work conducted in this area.
- **Differences between Observations and Theory:** There are several current theoretical and observational disagreements. One significant difference is the ejected mass on outburst. Theoretically determined ejecta masses (e.g. Starrfield et al., 2008) can be up to a factor of 10 times smaller than the observationally determined masses (see Warner, 1995, Chapter 5). It is important to solve this

discrepancy by further observational and theoretical work which will improve understanding of the nova outburst and the contribution of novae to the chemical evolution of the Galaxy.

- **Distance Indicators:** Unfortunately novae are not used widely as extragalactic distance indicators. This is due in part to technical factors such as appropriate and significant use of telescope time, which is required to obtain nova speed class and calibrate their peak luminosity. There is also the nagging question about the universality of the MMRD relation, and evidence suggesting that the t_{15} relation does not even exist (Darnley et al., 2006). These factors have dampened interest in using novae as distance indicators while more systematic studies are required (see Section 1.4.3).
- **Relation to Stellar Population:** The understanding of nova speed classes in different stellar populations comes largely from the light curves of novae in the LMC and the bulge of M31, which were contaminated by disc novae. A greater number of light curves from both Population I and Population II environments are required in order to obtain a more accurate view of speed class distribution of novae and give greater statistical significance to measurements made. Only when variations in speed class distributions between galaxies are better understood will more accurate absolute nova rates be obtained, the abundance of nova systems with different stellar populations be explored, and the usefulness of the MMRD relationship enhanced (see Sections 1.4.3, 1.10). Work conducted to address this issue is given in Chapter 3.
- **General Observational Issues:** Photometric and spectroscopic monitoring of novae tends to be very sporadic with only slower novae having any reasonable coverage. Many phases of evolution (especially the early stages) are missed and spectra may not be taken at all. It is not yet clear if there are “advanced symptoms” which signal an oncoming outburst. However, there has been investigation into such signatures with the RN RS Oph which suggest some initial effect (Adamakis et al., 2011). The light curve presented in Section 1.4.2 is unrealistic for most novae whose light curves are a lot more variable at all wavelengths and

on all time-scales. Work by Duerbeck (1990) also suggests that due to various effects (see Section 1.10) many bright novae are being missed each year. This claim is further supported by Shafter (2002) where it was found that as many as ~ 6 CNe per year should have peak magnitudes of 8^{th} mag or brighter. On average however only one or two of these bright novae are actually observed. Greatly increased numbers of spectral and photometric observations, especially in earlier phases of the nova outburst when combined with detailed modelling would help to provide an overall better understanding of the outburst. Finally sub-millimetre and far infrared observations of novae are very rare and would also provide valuable information, particularly on the parameters of the ejecta. These issues have been addressed in Chapters 3 and 5.

In the next Chapter planetary nebulae (PNe) and the role of binary systems in shaping them are discussed. The importance of PNe which have had nova eruptions occur within them is also examined.

Chapter 2

Evolution of Nova Systems and Planetary Nebulae

The first planetary nebula (PN) was observed by Charles Messier in 1764, but it was Herschel (1784, 1785) who named them PNe as he found their appearance resembled the greenish disc of a planet. As telescopic instrumentation improved nebulae made of stars (i.e. galaxies) were separated from those made up of mainly gaseous material. PNe were further distinguished from other galactic diffuse nebulae by their definite structures and often associated with a central star. In 1864 William Huggins increased understanding of these objects through spectroscopy revealing that the spectra of PNe are found to be dominated by emission lines, and not the continuum spectrum expected for a star or the reflected emission of starlight (Kwok, 2000).

It was Herschel (1791) who proposed the idea that PNe might be deriving their energy from a nearby star. Hubble (1922) expanded on this idea when he found a correlation between the magnitude of the central star and the size of the nebula. He stated that the emission-line spectrum seen in a PN was due to the absorption of radiation from the central star. Improved spectral capabilities led to the discovery that emission lines in PNe are broad, or even split and thus indicate the expansion of the nebula.

At the beginning of the 20th century, PNe were thought of as young stars due to their

high temperatures. Curtis (1918) disputed this, finding that PNe were more akin to late-type stars. Later Shklovskii (1956) suggested that PNe were the progenitors of WDs and the descendants of red giants, understanding that both these stars evolve rapidly. However, it was not until Abell & Goldreich (1966) realised that PNe were the ejected atmospheres of red giants that the understanding of PNe grew and that their role in stellar evolution was better understood (Kwok, 2000).

2.1 Formation of a Planetary Nebula

PNe represent a short (10^4 years) phase of stellar evolution between the asymptotic giant branch (AGB) and WD. When stars with initial main sequence masses between $1.5M_{\odot}$ and $8M_{\odot}$ (Kwok et al., 2003) reach the end of the AGB phase they undergo mass loss at a rate of $\approx 10^{-7} M_{\odot} \text{ yr}^{-1}$ with stellar wind velocities of $10\text{-}15 \text{ km s}^{-1}$. This rate of mass loss then suddenly increases in intensity to $\approx 10^{-4} M_{\odot} \text{ yr}^{-1}$ (Delfosse et al., 1997). This “super-wind” phase quickly depletes the H-envelope. When the envelope mass has fallen below $10^{-3} - 10^{-4} M_{\odot}$ the photospheric radius shrinks and the effective temperature rises. Mass loss gradually decreases to $\approx 10^{-8} M_{\odot} \text{ yr}^{-1}$ and the wind speed increases to $200\text{-}2000 \text{ km s}^{-1}$ (Perinotto, 1989). This wind ploughs into the previously ejected material creating a high-density shell which is ionised by the core star. The shell is compressed on both sides by dynamical pressure, developing a definite shell structure. This method of PN formation was proposed by Kwok et al. (1978) and is called the interacting stellar wind (ISW) model with more recent modifications made by various authors (e.g. Frank, 1994) re-naming it as the Generalised ISW (GISW). The super-wind is thought to depart from spherical symmetry and so the resulting nebula is not spherical. This model can explain the PN gas density structure, kinematics and morphology (for the main body of the PN) but not the trigger to the super-wind or PN geometry.

2.2 Morphological Classifications

PNe are traditionally identified according to their apparent morphology. Curtis (1918) attempted morphological classification of PNe based on observational surveys of the objects. Clarification of this work has been attempted by Stanghellini & Pasquali (1995) and Manchado et al. (1996). Classification is important as it reveals the outcomes of processes shaping the PNe. There are four basic nebular types: round (R), elliptical (E), bipolar (Bp; pair of lobes), and irregular (these tend to be rarer). These types may also be split into subgroups. For instance BPs may be split into “butterfly” nebulae where the waist is pinched in the centre, or “bi-lobed” in which a pair of outer lobes connects to a central smaller R or E nebula.

Mechanisms that have been proposed for the formation of density contrasts and so the various PN morphologies include the following (see Livio, 1993, for review).

- Protostellar disc left over from the star formation process.
- Equatorially compressed outflow.
- Stellar rotation.
- Effects of stellar magnetic fields.
- Action of a binary companion.

There is currently much debate over whether non-spherical PN morphologies can be formed via a single AGB star or if their shaping requires interaction with a companion star. Work by Nordhaus et al. (2007) argues that with a single AGB star the magnetic field can not be sustained long enough to have any significant effect on the shaping of the PN. This is because the field drains the star of angular momentum on short time-scales and quenches itself. A source of angular momentum is required and could effectively be produced by a stellar or sub-stellar companion. Binary interaction is therefore necessary to produce the variety of PN morphologies seen; this is known as the “binary hypothesis” (de Marco, 2009). The PN forms during the AGB common

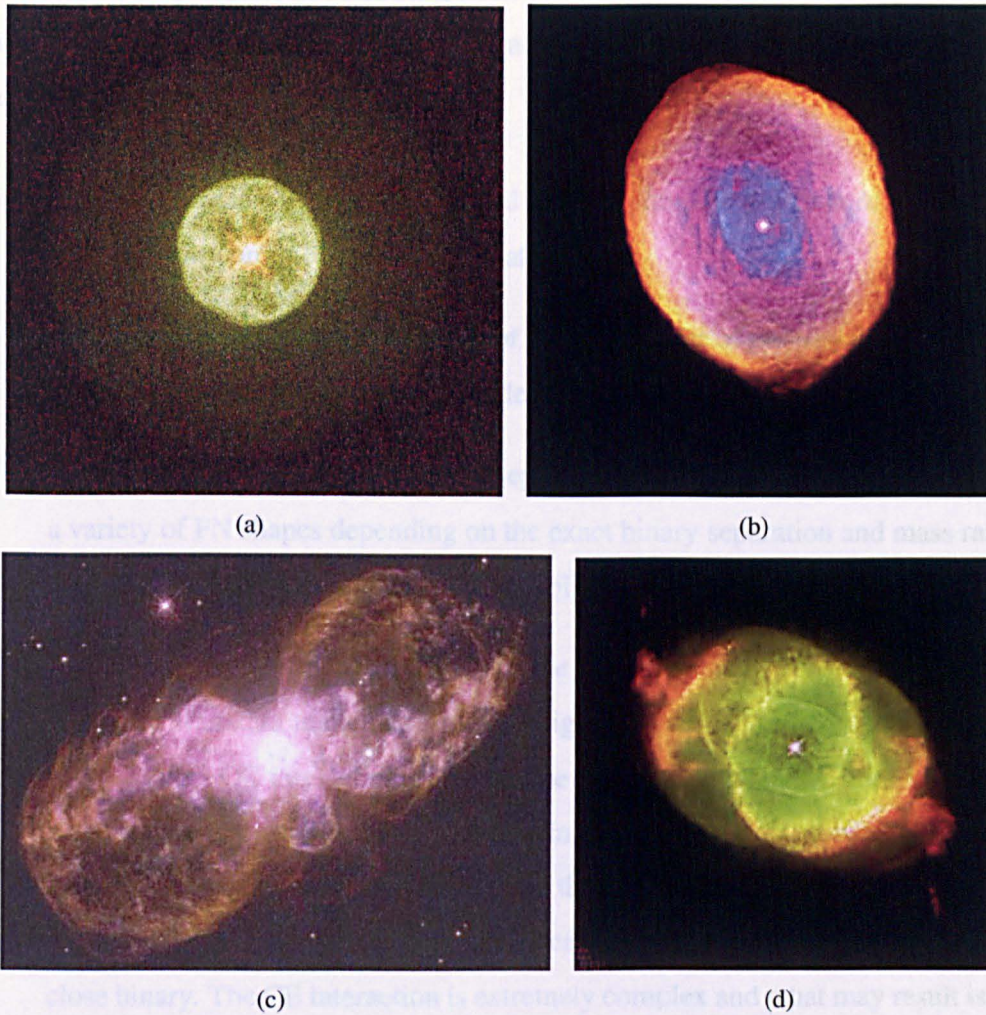


Figure 2.1: Morphologies of PN - (a) Round PN: IC 3568. (b) Elliptical PN: Spirograph nebula. (c) Bilobed PN: Hubble 5. (d) Irregular PN: Cat's Eye nebula. All images have been taken by the Hubble Space Telescope and are credited to the Hubble Space Telescope (<http://hubblesite.org>) and STScI (<http://www.stsci.edu/portal/>).

envelope (CE) phase of the binary system. Binaries which are close enough to interact during the AGB phase have a variety of ways in which they can shape the AGB and/or post AGB mass loss. They can do this either directly or indirectly. PNe take on different morphologies depending on the binary separation, mass ratio, and several other additional parameters. Following work by Soker (1997), de Marco (2009) distinguish five types of PN-shaping binary interactions which can be matched to different morphologies.

1. *Very wide binaries*: The orbital period is larger than the life-time of the PN and thus may only produce small-scale features.
2. *Wide binaries*: The orbital period is of the same order of the life-time of the PN ($\sim 100 - 1000$ AU) and can produce deviations from axi-symmetry, like jets.
3. *Closer binaries which avoid a CE*: Separations in the ~ 100 AU range lead to a variety of PN shapes depending on the exact binary separation and mass ratio. Such variations include spiral, elliptical, bipolar, and quadrupolar structures.
4. *Common envelope interactions where the binary survives*: When an RGB or AGB star transfers matter at a rate so high that it can not be accreted by the companion a CE interaction occurs. The companion expands, fills its Roche lobe and the two stars become engulfed in the primary's envelope. Energy and angular momentum are transferred from the secondary to the primary and can unbind the envelope. If the companion can eject the envelope then it forms a close binary. The CE interaction is extremely complex and what may result is an elliptical or bipolar PN.
5. *Common envelope interactions that result in a merger*: If the envelope is not ejected then the two stars merge. The companion can become tidally shredded as it approaches the primary which results in the formation of a disc which can cause the ejection of jets. Due to spinning up of the envelope the resulting PN could be elliptical.

2.2.1 Haloes

Surrounding the core PN structure is a faint halo. These haloes were originally discovered by Duncan (1937) and interpreted as the result of multiple PN ejections. We now know that the majority (70%) of PNe have these external structures. The structure is believed to reflect a previous history of heavy mass loss during the final stages of evolution on the AGB. The halo material is usually contiguous with the main PN shell and a tenth of its density. Stanghellini & Pasquali (1995) find that there are three basic types of halo morphology.

1. Detached halo: There is a minimum in the surface brightness between the inner PN shell and the outer rim of the halo.
2. Attached halo: Halo brightness fades gradually from the inner PN shell to the the outer edge.
3. Irregular attached halo: Halo shows irregularities and high ellipticity.

2.2.2 Microstructure

Approximately 50% of all PNe also contain “microstructure/fine structure”, such as knots or jets (see Gonçalves et al., 2001). Below is a description of a few of these structures.

- FLIER: Pair of small (0.01 pc) bright knots of low ionisation gas along the major axis. Found mainly in elliptical PNe. They are of low ionisation states and high supersonic Doppler shifted velocities (50 km s^{-1}). FLIER stands for fast low-ionisation emission regions (Balick et al., 1994). They are enriched with N/O and may have been ejected from the central star after the slow wind ejection ended.
- Cometary knots: Dark objects with a luminous cusp representing a high concentration of matter and which appear as a silhouette against the background

emission. Cusps have tails trailing away from them lying on radial lines passing between them and the central star, giving them their comet-like appearance. Cusps are likely photo-ionised.

- Jets: Thin usually radial features with no sign of widening. Corkscrew shaped jets are often called bipolar rotating episodic jets (BRETS).

2.3 Novae and Planetary Nebulae

It is thought that $\approx 10\%$ – 15% of all PNe contain close binary systems (Bond, 1994). As such it is possible a classical nova eruption may be observed within a PN.

The predicted long recurrence time-scales of CNe ($10^4 - 10^5$ years, Hernanz, 2005) means that we would observe and record only a single outburst from each system. An indication of how many outbursts a CN system may have undergone is given by the presence, or not, of a PN. If a nova is surrounded by a PN this indicates that the binary system is experiencing its first outburst as previous eruptions would have swept the PN away, or the PN would have simply dissipated during the system's quiescent phase.

There are however, only two observed novae to occur within a PN. The first of these is GK Persei (Bode et al., 1987) which erupted in 1901, and is not considered a typical CN due to the presence of a strong magnetic field making it an IP (see Section 1.6). The GK Per nova system is thought to be surrounded by a 10^5 year old, large (> 40 arcmin), Bp PN that was formed from a massive secondary star during a CE phase in which the WD became a “born again” AGB (Dougherty et al., 1996). The ionisation of this PN is thought to be maintained by accretion. The other nova observed to have occurred within a PN is V458 Vulpeculae (Wesson et al., 2008) which is the subject of Chapter 3. The outbursts of both GK Per and V458 Vul were accompanied by the observation of a light echo in the surrounding material (Couderc, 1939; Kapteyn, 1901; Wesson et al., 2008).

2.3.1 Light Echoes

The light echo phenomenon occurs when light from an eruptive variable is scattered by dust or re-emitted by gas in its vicinity, reaching the observer at progressively later times as the wave of illumination is seen to propagate outwards. For an instantaneous light flash, the echo surface at any given time is well approximated by the paraboloid given by:

$$z = x^2/2ct - ct/2. \quad (2.1)$$

where x is the projected distance from the star in the plane of the sky, z is the distance along the line of sight, c is the speed of light, and t is the time since outburst.



Figure 2.2: Anatomy of a light echo caused by dust scattering, (from Bode, 1979).

The nova's outburst light is reflected from the material at M , P and Q at time t days after outburst as illustrated in Figure 2.2. If $NM = ct$ then $NQ = ct/2$ in order for both reflections to be seen at the same time by the distant observer. Therefore Equation 2.1 can be re-arranged to give Equation 2.2.

$$NM + z = a = \sqrt{(x^2 + z^2)}. \quad (2.2)$$

If the plane including UV is perpendicular to that of z then the reflection will appear to originate in a circle of radius d given in Equation 2.3 (Couderc, 1939).

$$d = (2ctb + c^2t^2)^{1/2}. \quad (2.3)$$

The expansion velocity of this circle (V_d) can then be taken from Equation 2.4 where $V_d \geq c$ for all $b, t \geq 0$ (Couderc, 1939).

$$V_d = (cb + c^2t)(2bct + c^2t^2)^{-1/2}. \quad (2.4)$$

The appearance of a light echo is governed by the time-dependent brightness of the illuminating source, the density and scattering properties of the reflective/re-emitting medium, and the distance to the star.

A light echo effect has also been found with other eruptive objects such as V838 Monocerotis, a nova-like variable which erupted in February 2002 (Crause et al., 2005), and V605 Aquilae which underwent a thermal pulse in 1919 (Pollacco et al., 1992). The observed expansion rate of a light echo eventually yields the nature of the scattering material, the distance between the star and the material, and a direct geometric distance determination to the system; they have therefore provided valuable information on the aforementioned objects.

In the next Chapter the observation of Galactic and extragalactic novae with the Liverpool telescope is discussed.

Chapter 3

Observations of Novae with the Liverpool Telescope

Photometric data for selected novae in Section 3.3 have been published within Shafter et al. (2011). The data for these novae were obtained by myself via the LT, and quality checked each night. Calibration of the data and subsequent generation of light curves was carried out by Dr Matthew Darnley (LJMU). Data were then passed onto Prof. Allen Shafter (San Diego State University) for further analysis.

3.1 The Liverpool Telescope

The Liverpool Telescope¹ (LT) is a fully automated robotic telescope located at the Roque de Los Muchachos Observatory, La Palma, Spain and operated by the LJMU Astrophysics Research Institute (Steele et al., 2004). The primary science objective of the telescope is to enable monitoring observations of variable sources on time-scales of minutes to years. The telescope is of an altitude-azimuth design with Ritchey-Chrétien hyperbolic optics ($f/10$ focus) achieving a pointing specification of 10 arcsec rms. It consists of a 2 m Cassegrain reflector (focal ratio $f/3$, 0.45 m central bore) and a 0.62 m diameter secondary mirror which moves axially for focus. The LT currently has eight different instruments in operation and up to five of these instruments may be mounted at any one time. Of these one may be mounted at the “straight through” position with the others at side ports which are accessible through a rotating “science fold” tertiary mirror. The change time between instruments is ~ 40 seconds.

Current instrumentation includes an optical imaging CCD camera (RATCam), a fast readout imaging polarimeter (RINGO2), a dual-beam integral-field input spectrograph (FRODOspec), a fast-readout camera (RISE), an Infrared-Optical wide field camera (IO), and three wide field cameras (SKYCamA, SKYCamT, SKYCamZ). All data obtained with the LT are processed via instrument specific pipelines which conduct basic instrumental reductions. Calibration frames are updated daily and so the latest available data are used as standard. Of these instruments, RATCam, FRODOspec, and the SKYCamS are predominantly used in the investigation of novae. Technical details of instruments used within work conducted as part of this thesis are given below.

3.1.1 RATCam

RATCam is the LT’s optical camera (see Figure 3.2). The detector is a 2048×2048 pixel CCD camera, with eight core filters (Sloan u' , g' , r' , i' , z' , Bessell B , V , $H\alpha$). The field of view of the camera is 4.6 arcmin, where each pixel is $13.5 \mu\text{m}$ and there are

¹<http://telescope.livjm.ac.uk/>



Figure 3.1: Founder of the Liverpool Telescope Prof. Mike Bode, stands in front of the telescope on La Palma in its fully-opening enclosure

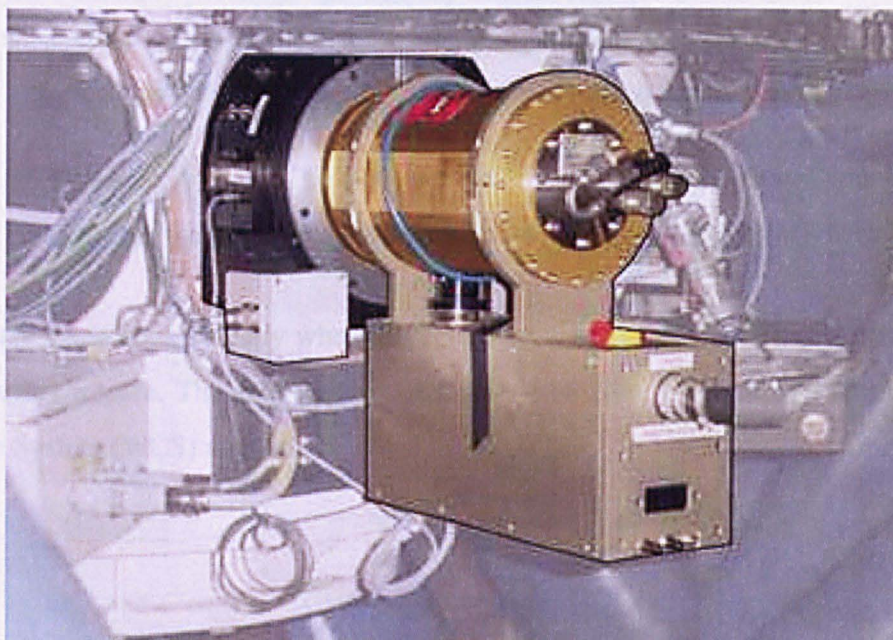


Figure 3.2: Image of RATCam on the Liverpool Telescope.

0.135 arcseconds per pixel. The readout noise is < 5 electrons and data can be binned in either a 1×1 (gain 2.34 electrons/count), 2×2 (2.13 electrons/count), 3×3 , or 4×4 mode. Peak quantum efficiency of the instrument is at 500 nm. As stated above basic instrumental reductions are applied to all RATCam data before data is passed to the user. For RATCam this includes bias subtraction, trimming of the overscan regions and flat fielding (a more detailed description of this is given in Section 4.3.1).

It should be noted that the $H\alpha$ filter generates weak ghost images from any bright sources within a field with the flux of the secondary image being 1% of the primary.

3.1.2 SKYCam's

The “SKYCam” project aims to obtain wide field observations in addition to normal LT data. The project consists of three cameras.

1. **SKYCamA:** A near all-sky camera on a fixed mount inside the LT enclosure able to detect objects down to about 6^{th} magnitude using a 4.5 mm fisheye lens.
2. **SKYCamT:** A medium field camera with a field of view (FOV) $\sim 21^\circ$. It is located on the LT mount which parallel points with the telescope. Able to detect objects down to 12^{th} magnitude using a 35 mm focal length lens.
3. **SKYCamZ:** A zoomed field camera (FOV $\sim 1^\circ$) on the LT mount which points parallel with the telescope. Able to detect point sources down to 18^{th} magnitude.

Data are taken automatically when the enclosure is open, with a 10 second exposure once every minute. The data are then dark-subtracted, flat-fielded, and a World Coordinate System (WCS) applied.

3.2 Observations of Galactic Novae

The LT's rapid robotic reaction is very well suited to photometric and spectroscopic coverage of novae in outburst and their systematic follow-up². The observations of Galactic novae by the LT can be used to improve various relations and obtain system parameters. The MMRD relation and t_2/t_3 times can be improved via the use of uncontaminated multi-band photometry, and more accurate distances to the objects determined through the use of spectroscopy and radio imaging, which can for example be obtained via eMERLIN³. The causes of nova variability, such as sporadic mass ejection, may be explored through the investigation of brightness increases which should be related to changes in broad-band colour indices, excitation of spectra, and line profiles. Flux calibration of spectra via photometry allows a greater understanding of line flux evolution, physical conditions, ejected element abundances, and the TNR and its relation to the composition and mass of the WD. Within this thesis two Galactic novae have been observed using the LT, the first being nova V458 Vulpeculae (RATCam - H α) which is the subject of Chapter 4, the second is KT Eridani (SKYCamT) the results of which are presented in Section 5.5.1.

3.3 Observations of Extragalactic Novae

A greater number of extragalactic light curves from both Population I and Population II environments are required in order to explore the dual nova progenitor hypothesis and to obtain a more accurate view of the speed class distribution of novae, giving greater statistical significance to measurements made. Only when variations in speed class distributions between galaxies are better understood will more precise absolute nova rates be obtained and the usefulness of the MMRD relationship be enhanced (see Section 1.11).

From October 2008 to January 2010 work conducted as part of this thesis exploited

²A list of all Galactic novae observed by the LT from 2004 to 2008 can be found at <http://www.astro.ljmu.ac.uk/~rah/Table/bigtablef.pdf>

³For information on eMERLIN and its facilities please see <http://www.e-merlin.ac.uk/>

the evolving photometric capabilities of the LT (via proposals JL09B03, RF08B3, and JL08A01) to obtain better coverage of extragalactic novae through outburst and decline. Additional facilities such as the Faulkes Telescope North (FTN, with similar specifications to the LT, sited on Maui) were also used on specific objects of interest. A list of the novae observed within this project is given in Tables 3.1 and 3.2.

Each object was entered into the relevant telescope scheduler on notification of outburst. The decline of the object was then monitored carefully to ensure the correct location and that it was visible. If three consecutive non-detections were found for any one object in any one filter then that filter was dropped from the observation list until the object completely faded. Calibration of the data and the generation of nova light curves was carried out by Dr Matthew Darnley.

Novae marked with a \star have been used to provide complementary photometric data for acquired spectra on the objects in Shafter et al. (2011). Within this paper a multi-year (1990 to the end of 2009) spectroscopic and photometric survey of novae in M31 was conducted. This consisted of 53 spectra of 48 nova candidates. It was found that 75 (82%) of the novae examined were members of the Fe II spectroscopic class, with the remaining 16 (18%) belonging to the He/N (and related) class. These values are consistent with those found for Galactic novae. No significant evidence was found within the investigation to suggest that the spectroscopic class of a nova depends on its spatial position or population within M31, but the distribution of He/N systems was slightly more extended than that of the Fe II class. However, evidence of a correlation between speed class and ejection velocity (based on line width) was found, this is also true for Galactic novae. Photometry of nova events allowed the determination of light curve parameters for 47 of the 91 novae with known spectroscopic class in M31 (before 2010). It was confirmed that the more luminous novae faded the fastest, and that He/N novae were typically faster and brighter than their Fe II counterparts. A weak dependence of nova speed class on position in M31 was also found. In this case the spatial distribution of the fastest novae was slightly more extended than that of slower novae.

Table 3.1: List of extragalactic novae observed as part of the work conducted within this thesis with the LT and FTN. Novae marked with a \star are used within Shafter et al. (2011).

Nova	R.A. (J2000.0)	Dec (J2000)	Discovery Date UT	Discover(s)	Telescopes	Filters
M31N 2008-10a \star	00:42:44.35	41:54:44.2	2008/10/07.71	Koichi Nishiyama	LT + FTN	$r', i', z', B, V, H\alpha$
M31N 2008-10b \star	00:43:02.42	41:14:09.9	2008/10/18.91	Henze et al. (2008)	LT + FTN	$r', i', z', B, H\alpha$
M81N 2008-03	09:55:36.11	69:03:22.0	2008/10/21.50	Kasliwal et al. (2008)	LT	$r', i', z', B, V, H\alpha$
M31N 2008-11a \star	00:41:32.26	41:06:01.2	2008/11/04.72	Koichi Nishiyama and Fujio Kabashima; K. Hornoc; Shafter et al. (2008)	LT + FTN	$r', i', z', B, H\alpha$
M33N 2009-01a	01:33:40.42	30:25:42.1	2009/01/07.54	Koichi Nishiyama and Fujio Kabashima; Nakano (2009)	LT + FTN	$r', i', z', B, V, H\alpha$
M31N 2009-02a	00:43:43.85	41:36:39.9	2009/02/06.43	Koichi Nishiyama and Fujio Kabashima; E. Ovcharov et al. Ovcharov et al. (2009b)	LT + FTN	$r', i', z', B, V, H\alpha$
M81N 2009-02a	09:55:35.96	69:01:51.0	2009/02/13.40	P60-Fast Transients In Nearby Galaxies (PDF); Kasliwal et al. (2009)	LT + FTN	$r', i', z', B, V, H\alpha$
M31N 2009-02b	00:42:27.77	41:13:42.4	2009/02/20.13	Pietsch et al. (2009a)	LT + FTN	$r', i', z', B, V, H\alpha$
M31N 2009-08a \star	00:42:58.06	41:17:29.8	2009/08/04.43	Pietsch et al. (2009b)	LT + FTN	$r', i', B, V, H\alpha$

Table 3.2: Continuation of Table 3.1.

Nova	R.A. (J2000.0)	Dec (J2000)	Discovery Date UT	Discover(s)	Telescopes	Filters
M31N 2009-08b*	00:44:09.91	41:48:51.0	2009/08/09.78	Koichi Nishiyama et al.; Koichi Itagaki; Rodríguez-Gil et al. (2009)	LT + FTN	$r', i', B, V, H\alpha$
M31N 2009-08c	00:42:41.20	41:17:01.7	2009/08/12.42	Kamil Hornoch and P. Zasche; Henze et al. (2009)	LT + FTN	$r', i', B, V, H\alpha$
M31N 2009-08d*	00:42:46.78	41:15:36.9	2009/08/12.42	Kamil Hornoch and P. Zasche; Henze et al. (2009)	LT + FTN	$r', i', B, V, H\alpha$
M31N 2009-08e*	00:42:36.23	41:18:01.6	2009/08/25.90	University of Sofia; Ovcharov et al. (2009a)	LT	$r', i', B, V, H\alpha$
M31N 2009-10a*	00:45:14.01	42:04:39.1	2009/10/03.62	Koichi Itagaki; Fabrika et al. (2009b)	LT	B, V
M31N 2009-10b	00:42:20.77	41:16:44.5	2009/10/11.41	Koichi Itagaki; Koichi Nishiyama and Fujio Kabashima; Nakano & Yusa (2009)	LT	B, V
M31N 2009-10c	00:42:45.76	41:15:57.1	2009/10/09.12	Fabrika et al. (2009a)	LT	B, V
M31N 2009-11a*	00:43:04.76	41:41:08.2	2009/11/03.56	Koichi Nishiyama and Fujio Kabashima; Nishiyama & Kabashima (2009)	LT	B, V
M31N 2009-12a	00:40:19.40	41:15:47.6	2009/12/22.49	Koichi Nishiyama and Fujio Kabashima; Nishiyama et al. (2009a)	LT	B, V
M31N 2010-01a	00:42:56.74	41:17:21.0	2010/01/11.13	Burwitz et al. (2010)	LT	B, V

Although the work of Shafter et al. (2011) has allowed the exploration the spatial distribution of novae in M31 to a greater extent than previously possible, a full understanding of nova populations requires additional spectra and light curve data for novae erupting in galaxies spanning a range of morphological types.

In the next Chapter the examination of Nova V458 Vulpeculae is discussed. This nova occurred within a Planetary Nebula (PN) and has been observed using the LT (and various other telescopes) over many epochs revealing the progression of its light echo through the surrounding structure.

Chapter 4

Nova V458 Vulpeculae

4.1 Introduction

V458 Vulpeculae ($\alpha = 19^h54^m24^s.61$, $\delta = +20^\circ52'52''.6$; J2000) was discovered in outburst by Nakano et al. (2007a) on 2007 August 8th at a magnitude of 9.5, reaching its peak visual magnitude a few days later at $V = 8.1 \pm 0.1$ (Wesson et al., 2008). The object is considered a fast nova with $t_3 = 21$ days. It has an ejection velocity of $\sim 1500\text{-}2000$ km s⁻¹, an outburst amplitude of ≈ 10 mags (Wesson et al., 2008), and examination of spectra indicates that it is a hybrid nova (see Section 1.8). A light curve of Nova V458 Vul has been generated using data from the Solar Mass Ejection Imager (SMEI) and can be found in Section 5.5.2.

By chance, approximately six weeks before the outburst the nova region was observed by the IPHAS survey (Drew et al., 2005) which revealed the presence of a PN surrounding the central system with an H α magnitude of 18.04 ± 0.02 . Due to flash ionisation by the nova event, light is being re-emitted by the PN gas creating a light echo effect (Couderc, 1939; Kapteyn, 1901, see Section 2.3.1). Based on light travel time arguments and the MMRD relation the object has an estimated distance of ≈ 13 kpc (Wesson et al., 2008). The Galactic coordinates of V458 Vul are $l^{II} = 58.63^\circ$, $b^{II} = -3.61^\circ$. Using Equation 4.1 and taking R as 13 kpc a value of $z = -0.8$ kpc is obtained.

Given the nova's fast classification its situation with the Galaxy is therefore unusual (see Section 1.10). Based on a distance of 13 kpc the WD mass is also expected to be high.

$$z = R \cdot \sin(b) \text{ [pc]} \quad (4.1)$$

Measurements of the PN made by Wesson et al. (2008) give an ionized mass of $0.2M_{\odot}$ and a low expansion velocity of $\approx 14 \text{ km s}^{-1}$, consistent with a 14,000 year old PN.

Nova V458 Vul is a very rare event as it is one of only two novae known to have occurred inside a PN, the other being GK Per (Bode et al., 1987) which erupted in 1901, and is not considered a typical CN due to the presence of a strong magnetic field making it an IP (see Section 1.6). V458 Vul may therefore be the first CN system observed within a PN providing a unique opportunity in which to examine the PN morphology, geometry, and overall evolution of the binary system. This object is therefore worthy of the detailed further study, as described here.

4.2 Observations

Since 2007, V458 Vul has been imaged several times by various telescopes producing 19 epochs of data between 2008 and 2011⁴ (see Table 4.1 and images in Appendix A). In each case the observation was conducted in $H\alpha$, optimizing conditions for systematic examination of the extended PN line emission.

Observations of the PN using the LT made between October 2008 and October 2011 were conducted as part the work of this thesis. The observing sequence of each epoch implemented the use of a 3×3 mosaic, consisting of $30''$ offsets around the central nova position. Such a configuration was used in order avoid the effect of ghosts in the $H\alpha$ images (see Section 3.1.1).

⁴For a movie showing the progression of the light echo for several of the epochs and star subtracted data visit <http://www.astro.ljmu.ac.uk/rah/NovaVul/movie.html> and <http://www.astro.ljmu.ac.uk/rah/NovaVul/NovaVul.html>

Table 4.1: H α observations of Nova V458 Vul and its surrounding PN.

Date (yyyy-mm-dd)	Telescope	Instrument	N $^{\circ}$ of images	Effective exp time (sec)
2008-05-21	INT	WFC	27	4859
2008-07-28	LT	RATCam	60	1800
2008-08-26	LT	RATCam	112	3360
2008-09-19	NOT	ALFOSC_FASU	29	3480
2008-09-21	LT	RATCam	20	3000
2008-09-30	NOT	ALFOSC_FASU	37	1110
2008-10-06	LT	RATCam	27	4050
2008-11-24	LT	RATCam	27	4050
2009-06-15	WHT	ACAM	5	1500
2009-06-30	LT	RATCam	49	3675
2009-08-18	LT	RATCam	18	5400
2009-09-23	LT	RATCam	18	5400
2009-10-20	LT	RATCam	18	5400
2009-11-14	LT	RATCam	18	5400
2010-07-23	WHT	ACAM	15	4500
2010-08-18	LT	RATCam	27	8100
2011-06-11	LT	RATCam	27	8100
2011-07-01	LT	RATCam	27	8100
2011-10-27	LT	RATCam	27	8100

4.3 Image Pre-processing

In many cases data received from the LT, INT, NOT and WHT were already pre-processed by the facilities' own processing pipelines. The relevant pre-processing steps implemented by each facility are given below.

4.3.1 The Liverpool Telescope (LT)

Details about the LT and its set-up may be found in Section 3.1. As mentioned in Section 3.1.1 all RATCam images undergo basic instrumental reduction before they are passed onto the user, details of this reduction are given here⁵.

⁵See <http://telescope.livjm.ac.uk/Info/TelInst/Inst/RATCam/> for additional details on the pipeline.

1. **Bias Subtraction:** The structure of the bias is very minimal and as such bias subtraction is based on analysis of the under-scan region. RATCam does have a small ramp in the bias down each column and so a first order linear regression is applied. This is used to determine a fit to the bias counts as a function of pixel row number and values are deducted across the image according to this smooth function.
2. **Over-scan Trimming:** The over-scan regions are trimmed off the frames leaving a 2048×2048 image assuming binning is not used.
3. **Dark Subtraction:** Dark current is deemed insignificant when the camera is at a normal operational temperature. Dark subtraction is not therefore performed.
4. **Flat Fielding:** A master flat field of appropriate filter and binning is selected from the LT library for the current exposure. This library holds reciprocal flat-fields normalized to unity because of the computational efficiency of multiplying rather than dividing. The image data are therefore multiplied by the library flat. Master flats are updated every 2-3 nights at twilight by taking the median of 3-5 normalized raw sky-flats for each filter/binning combination.
5. **Vignetting:** Each filter is affected differently by vignetting. The worst effect is in the extreme corners of the *i'* and *g'* bands where the flux is reduced by up to 15%. In other bands this effect is only about 5% and falling from the edge. Flat fielding generally removes this problem.

4.3.2 Isaac Newton Telescope (INT)

The INT is one of a group of telescopes (Isaac Newton Group of Telescopes - ING⁶) operating at the Roque de Los Muchachos Observatory on the island of La Palma. Other telescopes within the group include the William Herschel Telescope (WHT - see Section 4.3.3) and the Jacobus Kapteyn Telescope (JKT).

⁶See <http://www.ing.iac.es/> for more details on the ING.

The optical system of the INT consists of a conventional Cassegrain with a parabolic primary mirror of 2.54 m in diameter and a hyperbolic secondary mirror. The focal length of the primary is 7.5 m, giving a focal ratio of $f/2.94$ at the uncorrected primary focus. When corrected the focal ratio is $f/3.29$. The telescope currently has two instruments in operation: a Wide Field Camera (WFC) and an Intermediate Dispersion Spectrograph (IDS). The WFC is an optical mosaic camera for use at the primary focus. It consists of four thinned EEV $2k \times 4k$ CCDs with a pixel size of 13.5 microns corresponding to a 0.33 arcseconds/pixel. The coverage of each CCD chip is 22.8×11.4 arcmin, giving a total field size of 0.29 square degrees. Data obtained using the INT's WFC was reduced using *WFCRED*⁷ (see Irwin & Lewis, 2001), a package written specifically for IRAF⁸. The processing of frames with *WFCRED* can be broken down into the following steps.

1. **Linearity Correction:** Data from the WFC is non-linear at some level for each chip and comes from the analogue-to-digital converter (ADC). This non-linearity varies with time and a correction is therefore required. Values which require correction are those which are above a mean bias level which is calculated from the over-scan region.
2. **CCD Processing:** This is the debiasing and flat fielding. Debiasing is done either via subtraction of a mean bias frame (determination of the value in the over-scan region and then combining the input frames into a mean frame) or via the subtraction of a constant bias value as found from an over-scan region for an individual target frame. Flat fielding is applied using a previously defined mean flat field frame.
3. **Defringing:** The $H\alpha$ pass-band is not greatly affected by fringing effects.
4. **Squishing:** Initial mosaic camera images are large (72 MB each) and processing essentially doubles the file size in size. Squishing refers to the clipping of data to

⁷<http://www.ing.iac.es/astrow/InstSoft/wfcred/manual.html>

⁸IRAF is distributed by the National Optical Astronomy Observatory, which is operated by the Association of Universities for Research in Astronomy (AURA) under cooperative agreement with the National Science Foundation.

its useful ranges (say -1000 and 80000 counts) and then compression to scaled 16-bit integers.

4.3.3 William Herschel Telescope (WHT)

The WHT is an optical telescope with a parabolic primary mirror 4.2 m in diameter and a focal length of 10.5 m ($f/2.5$). The Auxiliary-port CAMera (ACAM) is mounted permanently at a folded cassegrain focus. It has a field of view in imaging mode of 8.3 arcminutes (0.25 arcseconds/pixel). Most ING filters can be mounted on ACAM⁹. The reduction procedure of the WHT is the same as that discussed in Section 4.3.2. The instrumental reduction of the 2009 WHT data was conducted by Professor Boris Gaensicke (Department of Physics, University of Warwick). The reduction of the 2010 data was conducted as part of the work of this thesis using routines in IRAF and the procedures documented at the CASU INT Wide Field Survey pipeline processing website¹⁰.

4.3.4 Nordic Optical Telescope (NOT)

The NOT is a 2.56 m (focal ratio of $f/2.0$) telescope with Ritchey-Chrétien type primary mirror and altazimuth mounting. The secondary mirror has a diameter of 0.51 m. As with the ING telescopes the NOT is located at the Observatorio del Roque de los Muchachos, La Palma. The Andalucía Faint Object Spectrograph and Camera¹¹ (ALFOSC) has a field of view of 6.4×6.4 arcminutes consisting of 2048×2048 pixels with 0.19 arcseconds/pixel.

All NOT data given in Table 4.1 were provided pre-processed. The instrumental reduction of the 2008 September 19th data was conducted by Dr Cristiana Zurita (Observatorio Astronómico Nacional, Instituto de Astronomía, Universidad Nacional Autónoma de México) with reduction of the 2008 September 30th data conducted by Dr Helena

⁹See <http://catsserver.ing.iac.es/filter/> for a list of compatible filters.

¹⁰<http://www.ast.cam.ac.uk/wfcsur/technical/pipeline/>

¹¹<http://www.not.iac.es/instruments/alfosc/>

Uthas (Department of Astronomy, Columbia University). ALFOSC data is bias and flat corrected both of which are conducted in a similar manner to that described above.

4.4 Data Reduction

The region surrounding Nova V458 Vul's PN is fairly crowded and contains many bright stars, as indicated in Figure 4.1. Some of the stars within the field are also seen to "contaminate" the PN. The subtraction of all stars for every exposure within an epoch was required in order to obtain the PN structure only, and allow its detailed examination. In order to achieve this, several procedures were implemented. A description of each of these procedures is given below. Each step was carried out using packages from within the NOAO IRAF environment.

4.4.1 Image Examination and Alignment

Upon receiving data for each epoch individual exposures were examined by eye in detail to ascertain the quality of the set. Each exposure was judged on factors such as seeing and performance of the auto-guider system. Exposures were also checked for any major sources of error such as excessive bad pixel columns interfering with the region around the PN. On completion of this quality check the exposures were further examined using IRAF's *daoedit*; from this an average FWHM of the stars within an exposure was obtained.

Using IRAF's *starfind* task and the HWHM calculated from the previously obtained FWHM a list of stars was created for every exposure within the epoch's data set. The set was then aligned to a chosen reference exposure (the best quality exposure - often the central exposure of the mosaic). This alignment was conducted using three IRAF packages: *xyxymatch* to produce lists of matched reference coordinates; *geomap* to calculate second-order geometric transformations between images; and *geotran* to apply the geometric transforms to the images. These transformed images were then used to

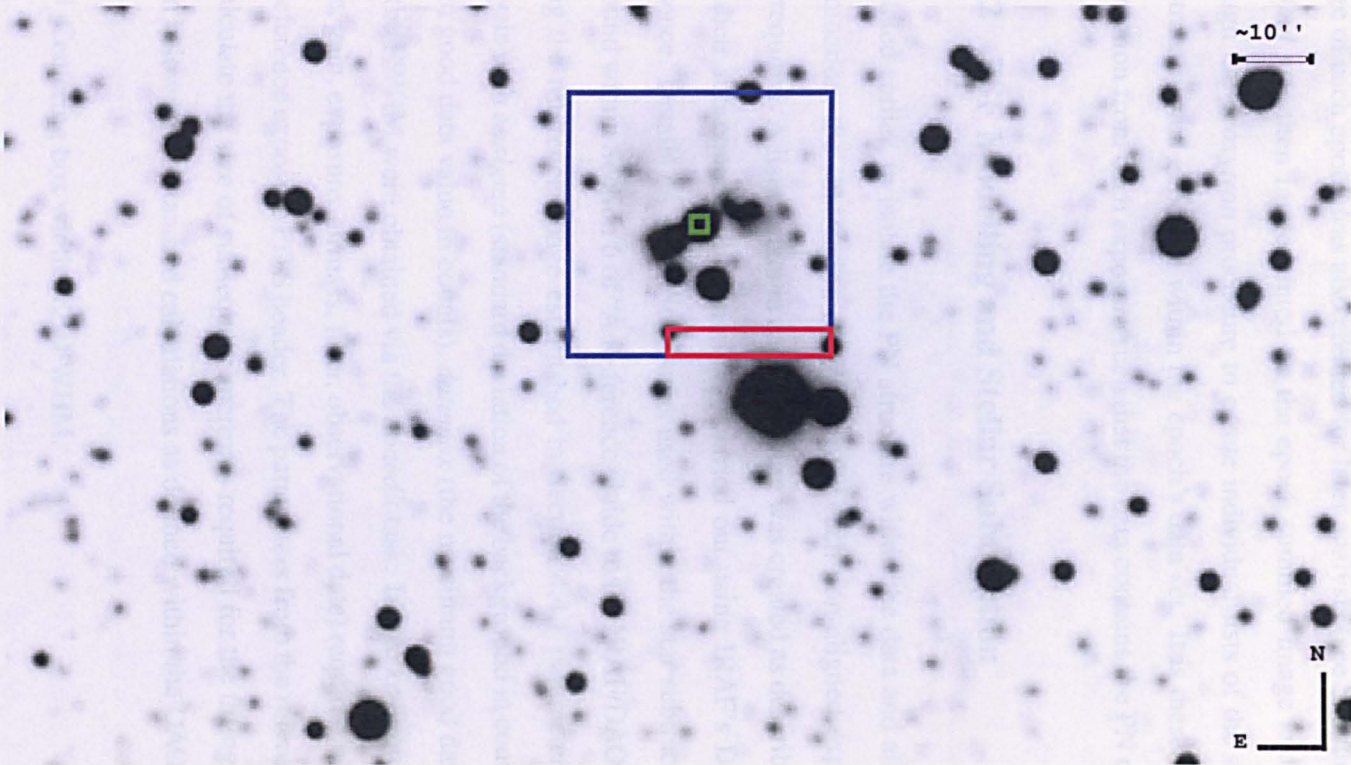


Figure 4.1: Image of the PN surrounding Nova V458 Vul and the stars within its field, image size is 282×503 pixels. The region bound by the blue box is 99×99 pixels and represents the size of the images used in the final evaluation of the PN. The regions bound by the red and green boxes are the size of the masks applied in later processing (see Section 4.4.4). Image is the sum of each epoch's aligned normalised median combined image (see end of Section 4.4.4).

produce a summed stacked image and a median stacked image for each epoch via IRAF's *imcombine* task. Summing of exposures was applied such that each star (including fainter ones) could be clearly identified within an epoch. A median combined image of each epoch was also created for later analysis (see Sections 4.4.3 and 4.4.4). *Starfind* was then implemented on the epoch summed image and the output passed through the *geoxytran* procedure to create individual lists of the same stars for each non-transformed exposure within the epoch's data set. It is these stars which require subtraction from each exposure such that the data contains the PN only.

4.4.2 PSF Modelling and Stellar Subtraction

As stated earlier, to isolate the PN structure within the data and allow for its detailed examination, the subtraction of all stars for each non-aligned exposure in an epoch was required. A list of stars in each exposure was created as described in Section 4.4.1 and their subsequent subtraction was carried out using IRAF's DAOPHOT analysis sequence. Details on the various steps used within the star subtraction procedure can be found within Section 6 of "A Reference Guide to the IRAF/DAOPHOT Package¹²". Using the reference image established in Section 4.4.1 parameters required for this analysis such as *sigma* (standard deviation of the background in counts), *datamin* (minimum good data value in counts), *datamax* (the maximum good data value in counts), and the FWHM were obtained via the *doaedit* task. Image keyword parameters (read-noise, gain, exposure, airmass, filter, observational date) required were also taken from the reference exposure FITS header. The parameters from the reference were then used to calculate the size of subsequent apertures required for the fitting routines, these are given below as are standard calculations as defined within the DAOPHOT guide:

- Centering box width = $2 \times \text{FWHM}$.
- Inner radius of the sky annulus = $4 \times \text{FWHM}$.
- Width of the sky annulus = $2.5 \times \text{FWHM}$.

¹²See <http://iraf.net/irafdocs/daorefman.pdf>

- Radius of the photometry aperture = FWHM.
- Maximum radius of the PSF model = $4 \times \text{FWHM} + 1$.
- PSF model fitting radius = FWHM.

Within the star subtraction sequence the analytic component of the PSF was set as *auto* allowing computation of the best PSF model. The order of PSF variation was also adjusted at this stage to compute the cleanest subtraction, along with the *fitsky* parameter which was set to *yes* in order to recompute the group sky value during the fit.

Once stars were removed from each exposure within an epoch they were then aligned using the previous transformations calculated in Section 4.4.1 and a summed image created, again via *imcombine*. On this summed image *starfind* was implemented using a lower threshold to detect any fainter stars which had previously been missed. The output of this procedure was then manipulated via *geoxytran* to create individual faint star lists for each non-aligned initial star-subtracted exposure. Using the previously computed PSF model these stars were then removed from the initial star-subtracted exposures and the procedure repeated (using a lower threshold value in *starfind* each time) until all detected stars were removed. Once satisfactory subtraction had been conducted on each exposure the final star-subtracted exposures were aligned and a median combined image created (with a sigclip rejection) for the epoch.

4.4.3 Alignment of Star-Subtracted Images and Trimming

For the comparison of each epoch's star-subtracted median image, each image needed to be aligned to a reference. To do this transformations based on the non star-subtracted median image of each epoch produced in Section 4.4.1 were required. Using these images and a similar procedure to that documented in Section 4.4.1 transformations were computed, taking the reference epoch to be that containing the largest sized pixels (i.e. the INT 2008 May 21st epoch at 0.33 arcseconds/pixel). These transformation parameters were then applied to both the non star-subtracted median image (to be

used in Section 4.4.4, see Appendix A) and the star-subtracted median image of each epoch. On alignment images were trimmed to a 282×503 pixel region ($\sim 2' \times 3'$) which corresponded to the image overlap, this enabled a reduction in computational time.

4.4.4 Seeing and Flux Normalization

The next step required for comparison was the normalization of each epoch's aligned star-subtracted median image with regards to both seeing and flux. The processes used to do this are described below. For ease aligned non star-subtracted median images will now be referred to as ANSM images and aligned star-subtracted median images as ASSM.

- **Seeing:** For each epoch's ANSM image *starfind* was conducted to produce a list of 20 bright stars and their HWHM. Taking the image with the worst seeing to be that with the highest HWHM (the LT July 2008 image with a value of 2.9 pixels) a scaling factor was calculated for every other epoch. This was calculated using Equation 4.2 below

$$C = (B^2 - A^2)^{1/2}, \quad (4.2)$$

where A is highest HWHM, B is the HWHM of the image being examined, and C the scaling factor. Using IRAF's *gauss* task and taking C as the sigma of the Gaussian function in pixels each epoch's ANSM and ASSM image were then adjusted for seeing. The resultant seeing-corrected images are now referred to as SANSM and SASSM images.

- **Flux normalization:** This was implemented in two stages and used aperture photometry within Starlink's *Gaia*¹³.

1. For every epoch SANSM image a set of 30 specific stars (the same ones for each image) were examined using aperture photometry where the same

¹³GAIA is a derivative of the Skycat catalogue and image display tool, developed as part of the VLT project at ESO. Skycat and GAIA are free software under the terms of the GNU copyright.

aperture parameters were applied each time. The number of counts for each of the 30 stars in an image were obtained and plotted against the counts of the same set of stars for a chosen reference SANSM image, allowing a gradient and intercept to be obtained with respect to the reference. Using these values and IRAF's *imarith* task both the SANSM and SASSM images were then normalized with respect to the reference based on stellar flux (see Figure 4.2). The resultant stellar flux-corrected images are referred to as SfSANSM and SfSASSM respectively.

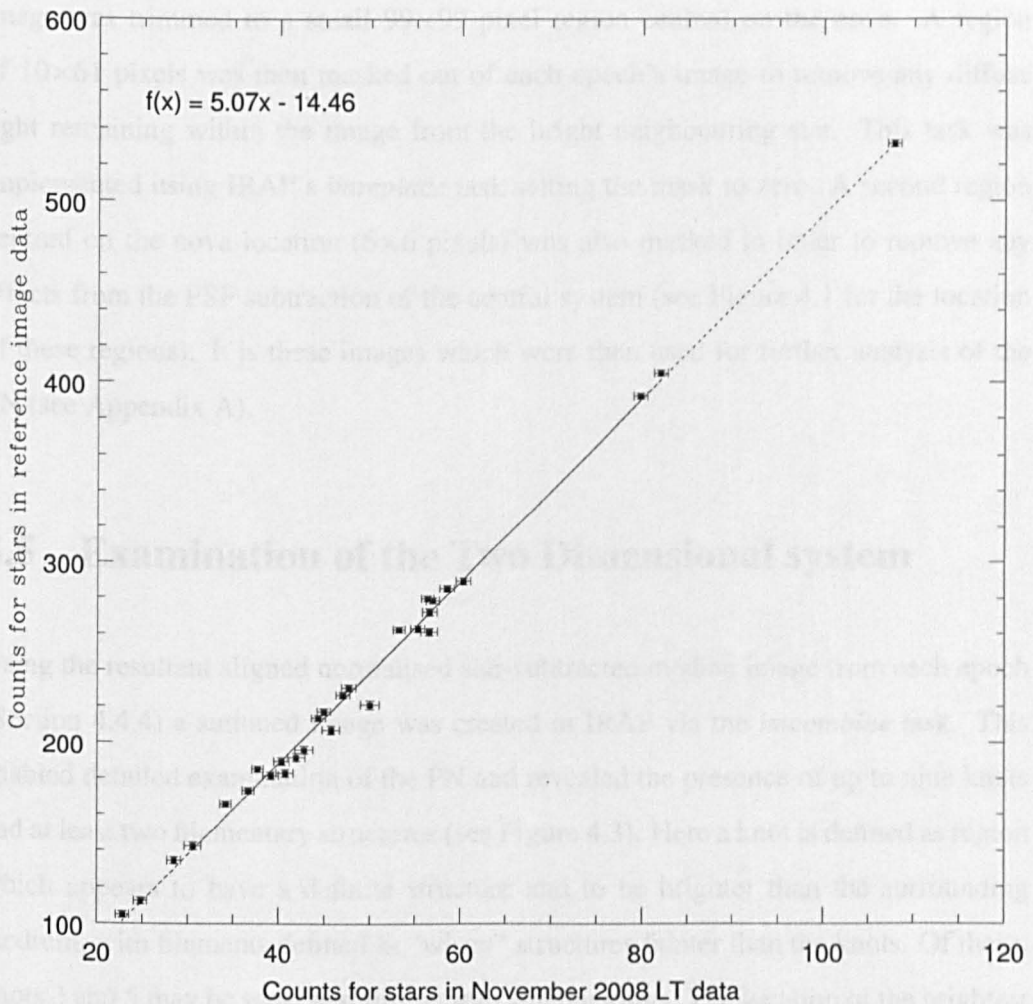


Figure 4.2: Plot illustrating calibration of stellar flux from one epoch's SANSM image to a reference SANSM image.

2. The background flux of each epoch's SfsASSM image also needed to be taken into account. To do this *Gaia's image region* technique was used to obtain the statistics of 10 specific background regions within each epoch's SfsANSM image. Taking the mean value of these regions the background was subtracted away from each SfsASSM image including the reference (via *imarith*) in order to obtain an almost zero background flux, resulting in an aligned normalised star-subtracted median image for each epoch.

On completion of this task each epoch's aligned normalised star-subtracted median image was trimmed to a small 99×99 pixel region centred on the nova. A region of 10×61 pixels was then masked out of each epoch's image to remove any diffuse light remaining within the image from the bright neighbouring star. This task was implemented using IRAF's *imreplace* task setting the mask to zero. A second region centred on the nova location (6×6 pixels) was also masked in order to remove any affects from the PSF subtraction of the central system (see Figure 4.1 for the location of these regions). It is these images which were then used for further analysis of the PN (see Appendix A).

4.5 Examination of the Two Dimensional system

Using the resultant aligned normalised star-subtracted median image from each epoch (Section 4.4.4) a summed image was created in IRAF via the *imcombine* task. This enabled detailed examination of the PN and revealed the presence of up to nine knots and at least two filamentary structures (see Figure 4.3). Here a knot is defined as region which appears to have a definite structure and to be brighter than the surrounding medium, with filaments defined as "wispy" structures fainter than the knots. Of these, knots 3 and 5 may be separated further into smaller knots. The location of the brightest point in a given knot was obtained via the *imcentroid* task in IRAF. Each of these knots and their positions with respect to the nova position are given in Table 4.2.

Individual examination of each knot region (see Figure 4.4) using the *image regions*

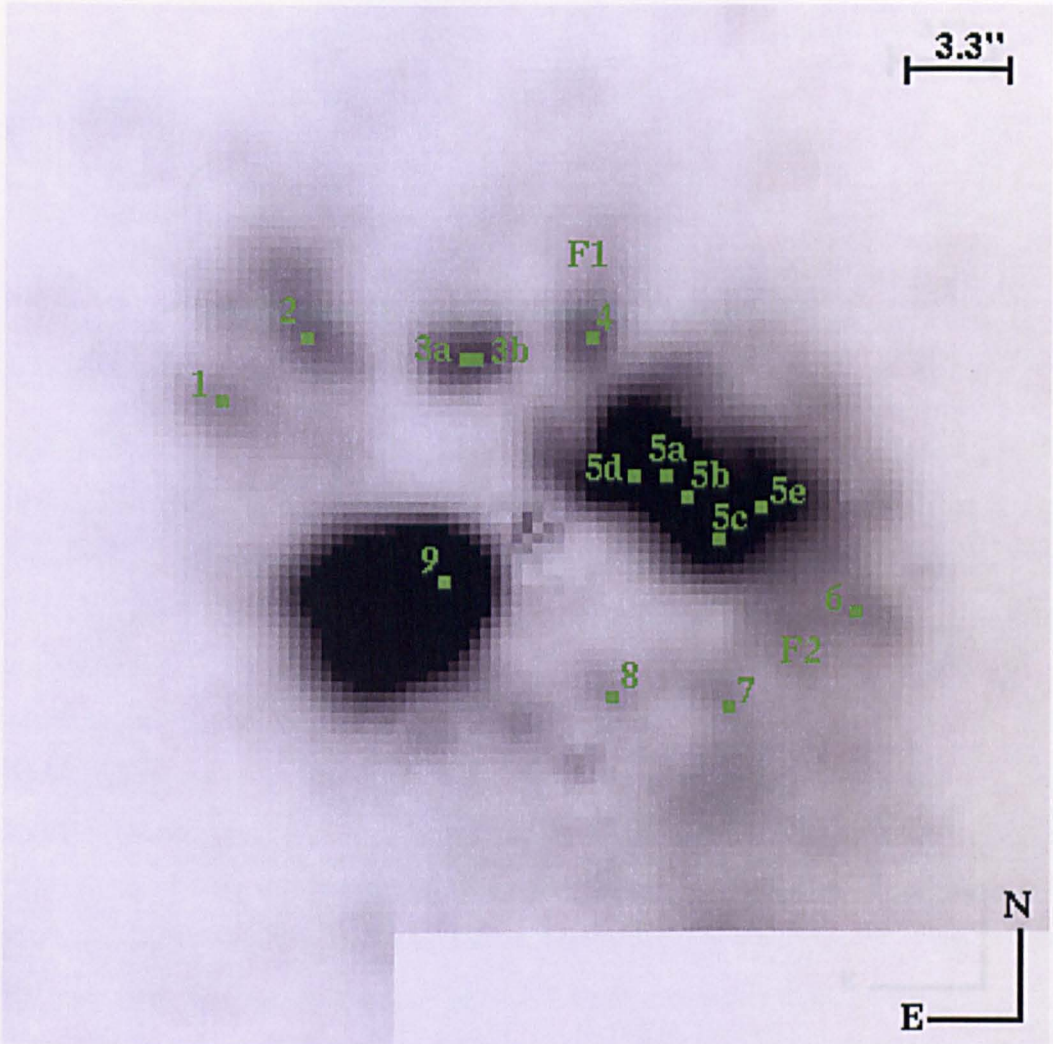


Figure 4.3: Summed image of aligned normalised star-subtracted PN data. The image shows the location of each knot and filamentary structure referred to in the text.

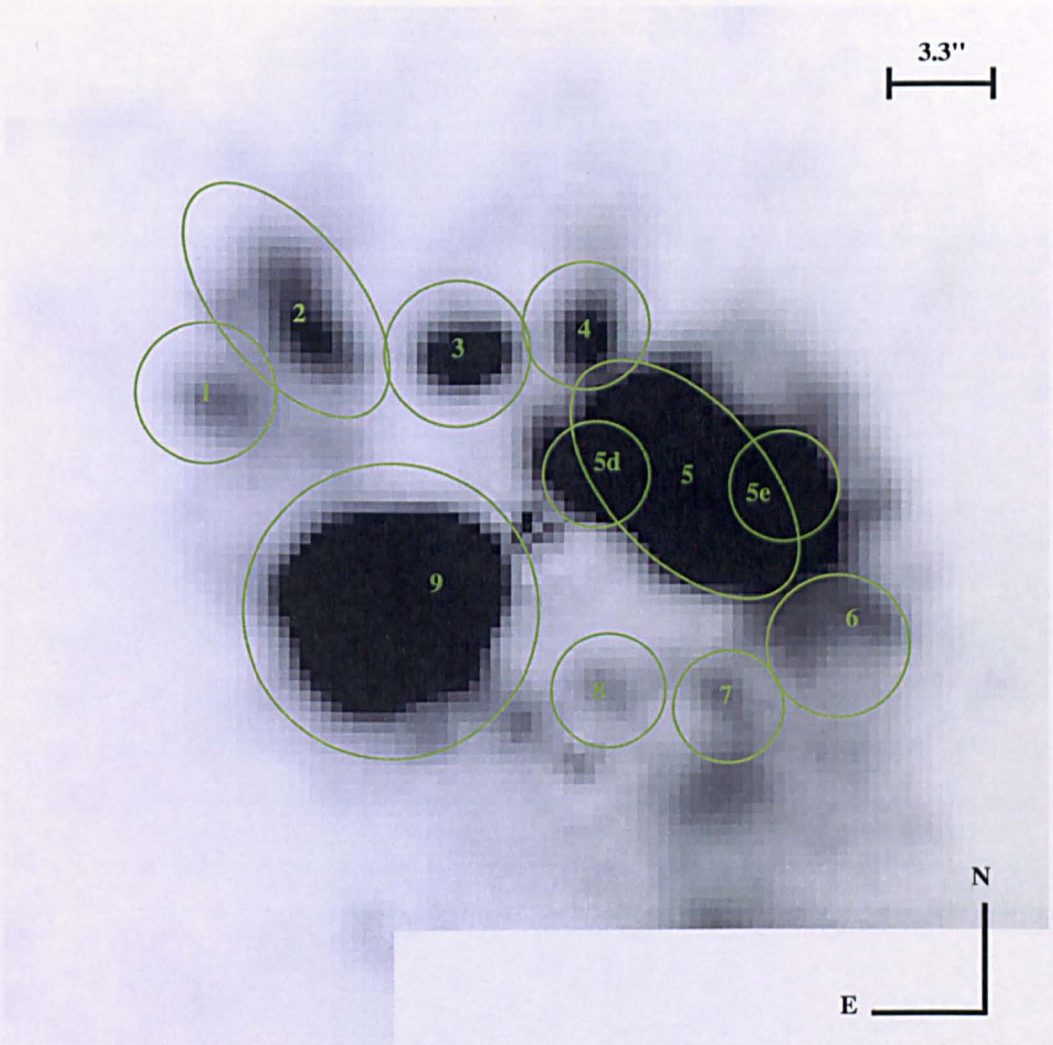


Figure 4.4: Summed image of aligned normalised star-subtracted PN data. The image shows the location of each knot region sampled in *Gaia*. This sampling was conducted on individual epochs not the summed image presented here.

Table 4.2: Estimated distance of each knot on the sky from the nova location.

Knot	Distance from star (")	Error on Distance (")	Peak brightness
1	10.17	0.03	September 2008
2	9.14	0.02	October 2008
3a	5.65	0.01	November 2008
3b	5.58	0.01	-
4	6.15	0.02	Mid 2009
5a	4.60	0.01	Late 2009
5b	5.20	0.01	-
5c	5.95	0.01	-
5d	3.62	0.01	-
5e	7.37	0.01	November 2008
6	10.47	0.03	October 2008
7	8.41	0.03	September 2008
8	5.76	0.02	August 2008
9	3.15	0.01	Mid 2009

task in *Gaia* on each epoch's aligned normalised star-subtracted median image has revealed several things about the illumination of the PN by the light echo. The SE equatorial structure (knot 9) reaches its brightest around mid-2009 after which it starts to decline; this pattern seems to be matched by knot 4. The NW equatorial structure appears much more "bulgy" (5a, b, c and e) and seems to brighten a little later towards the end of 2009 (see Figure 4.5). Whilst the propagation of light through the SE equatorial knot is most evident, the NW equatorial structures do brighten significantly. Using the location of knot 9 and knot 5a (see Table 4.2) a distance between the knots of $\sim 7.7''$ is derived, this may act as an estimate for the minor axis of a possible bilobal structure. Knots found in the extreme north and south (1, 2, 3, 6, 7, and 8) of the PN all become more dominant between August 2008 and November 2008 (see Figure 4.6), with a separation of $17.55''$ between knots 2 and 9. It should be noted that within this analysis only LT data were used as these were the most consistent on comparison of background flux.

The almost mirror symmetrical illumination of the PN would suggest that the axis of symmetry (polar) is in the plane of the sky and that the PN is not face-on (where face-on $i = 0^\circ$) but rather side-on ($i = 90^\circ$) to the observer in the sky. However, a face-on PN

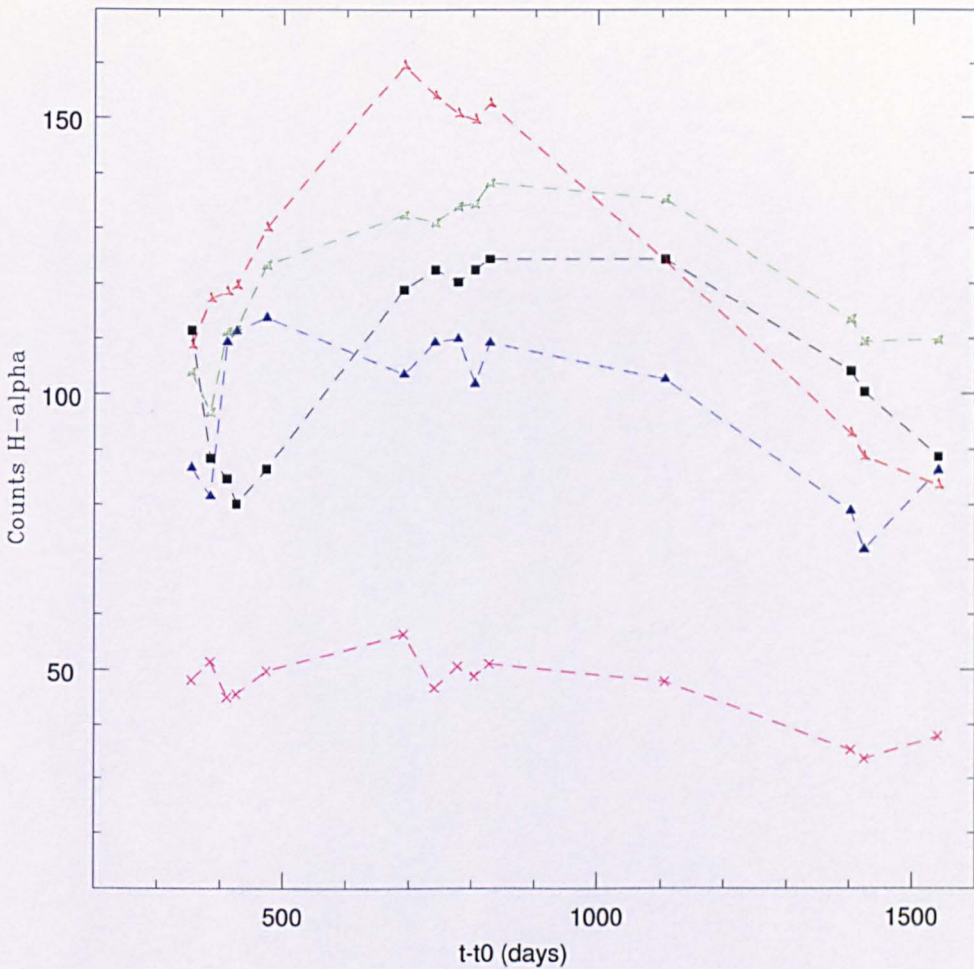


Figure 4.5: Plot showing the counts of equatorial regions 9, 5 and 4 in LT normalised star-subtracted median images for each epoch. Black squares: knot 5d; blue triangles: knot 5e; green open squares: knots 5a/5b/5c; red open triangles: knot 9; pink crosses: knot 4. It should be noted that this is a preliminary reduction and as such does not include error analysis.

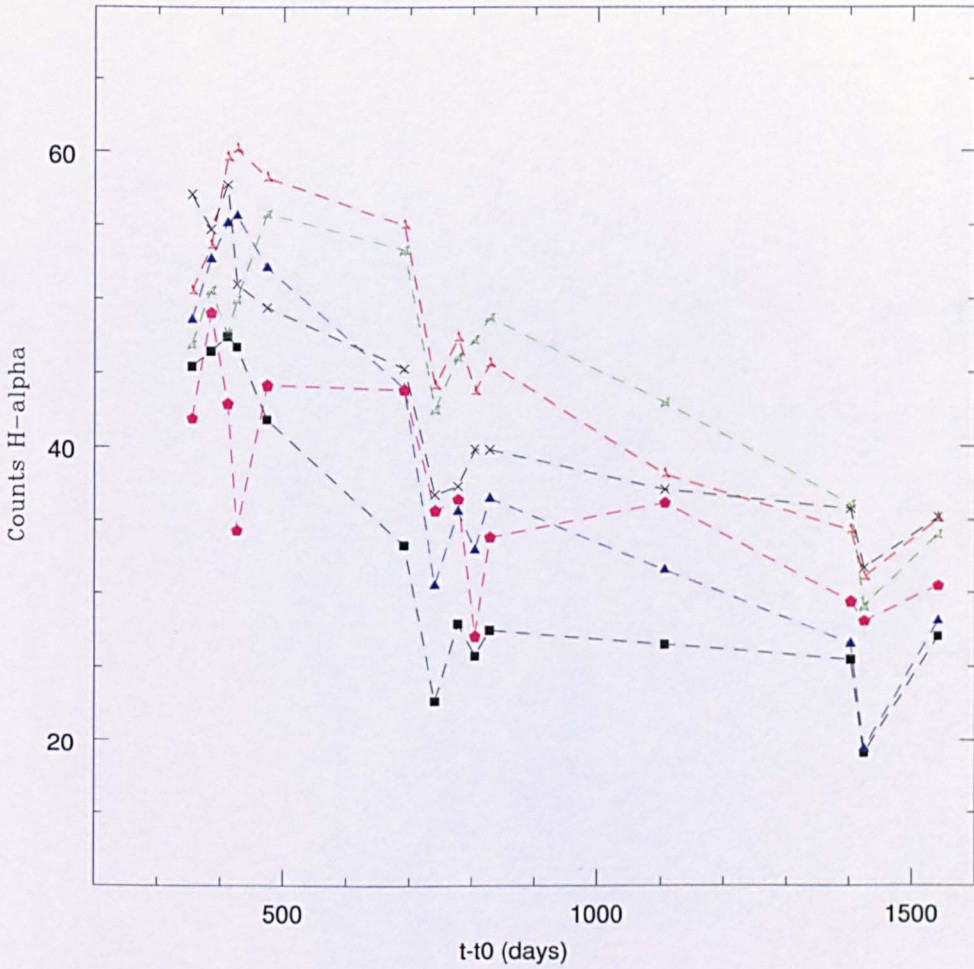


Figure 4.6: Plot showing the counts of polar regions 1, 2, 3, 6, 7, and 8 (see Figure 4.4) in LT normalised star-subtracted median images for each epoch. Black squares: knot 1; blue triangles: knot 2; green open squares: knots 3a/3b; red open triangles: knot 6; black crosses: knot 7; pink stars: knot 8. It should be noted that this is a preliminary reduction and as such does not include error analysis.

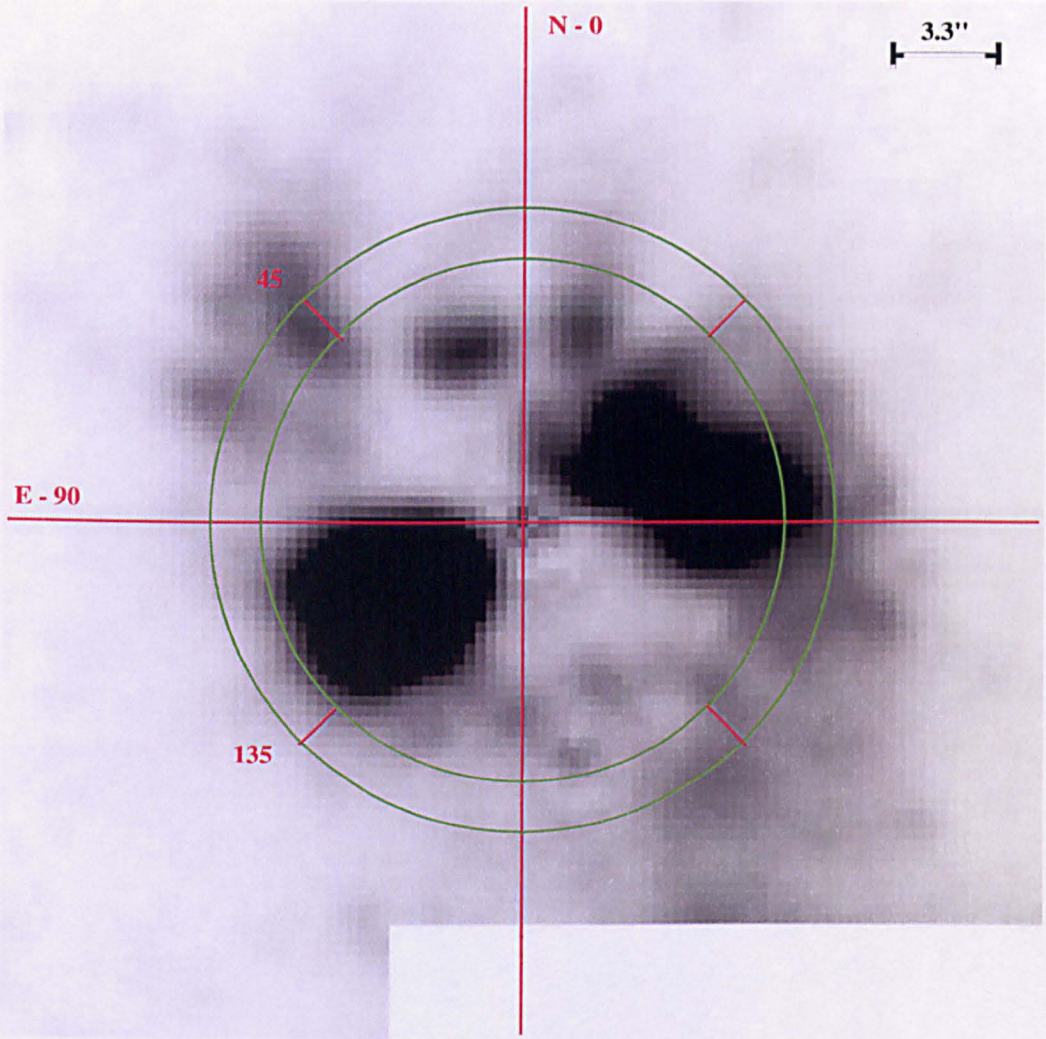


Figure 4.7: Summed image of aligned normalised star-subtracted PN data indicating the position angle of the system in the plane of the sky. Angles written are given in degrees.

with a clumpy structure can not be ruled out, although a PN with symmetrical clumps is unlikely. An almost side-on PN may be the cause of the time delay between the brightening of the equatorial knots 9 and 5. This delay could however be caused by the proper motion of the binary system itself if the system moves in the SE direction; further investigation would be required to confirm this. Using knots 5 and 9 a position angle (taken from North to East) of $25\text{-}35^\circ$ on the sky may be inferred for the PN (see Figure 4.7). As the knots north and south of the nova location appear to brighten at the same time and before the equatorial knots reach their peak this would suggest that these are associated with the poles of an internal structure rather than that of the structure which includes the equatorial knots 5 and 9.

4.6 Three Dimensional Visualisation of the System

By studying the illumination of the PN with time it is possible to obtain a 3D reconstruction of its morphology as each image provides a one-off map of the PN material for a given light echo paraboloid.

Assuming that the PN luminosity is dominated by the light echo, the line-of-sight displacement (z) for each aligned normalised star-subtracted median epoch image has been calculated based on the light echo model presented in Section 4.1 using Equation 2.1. These data have been used to construct a 3D visualisation of the illuminated PN in the C programming language using the *cfitsio* package. This 3D visualisation can be displayed via Starlink's *Gaia* package allowing the user to obtain a "God's eye view" of the PN.

Due to the time intervals between each epoch, a linear and cubic b-spline interpolation were conducted across the data to aid in the examination of the PN. The non-interpolated 3D visualisation is presented in Figure 4.8. Within the 3D FITS cube the focus of each parabola (and the location of the nova) is taken as the centre of the cube.

Examination of the counts at each radial point from the nova centre within the created 3D FITS cube reveals several things. This examination was conducted using a distance

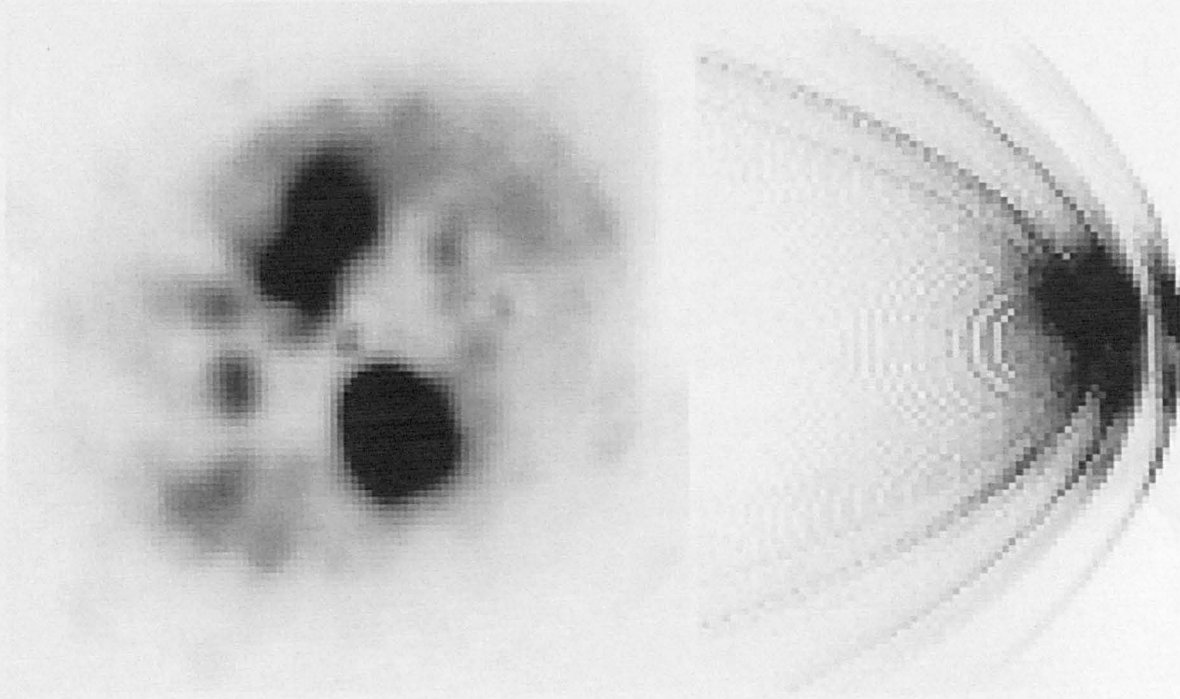


Figure 4.8: **Left:** The XY axis of the PN data representing what the observer would see on the plane of the sky. Here North is left and East is down. **Right:** The ZY axis of the PN data representing the distance along the line-of-sight to each point on the paraboloids. It should be noted that for the purposes of this image the nova centred mask has not been applied.

of 13 kpc (Wesson et al., 2008) to calculate the physical size of the PN in pc.

1. The radial displacement vs counts plot in Figure 4.9 indicates four dominant peaks representing the four clusters of epoch data (08, 09,10,11) and provides evidence of the propagation of the light echo through the PN. Each peak on its own has a complex structure with the brightest knots contributing the most.

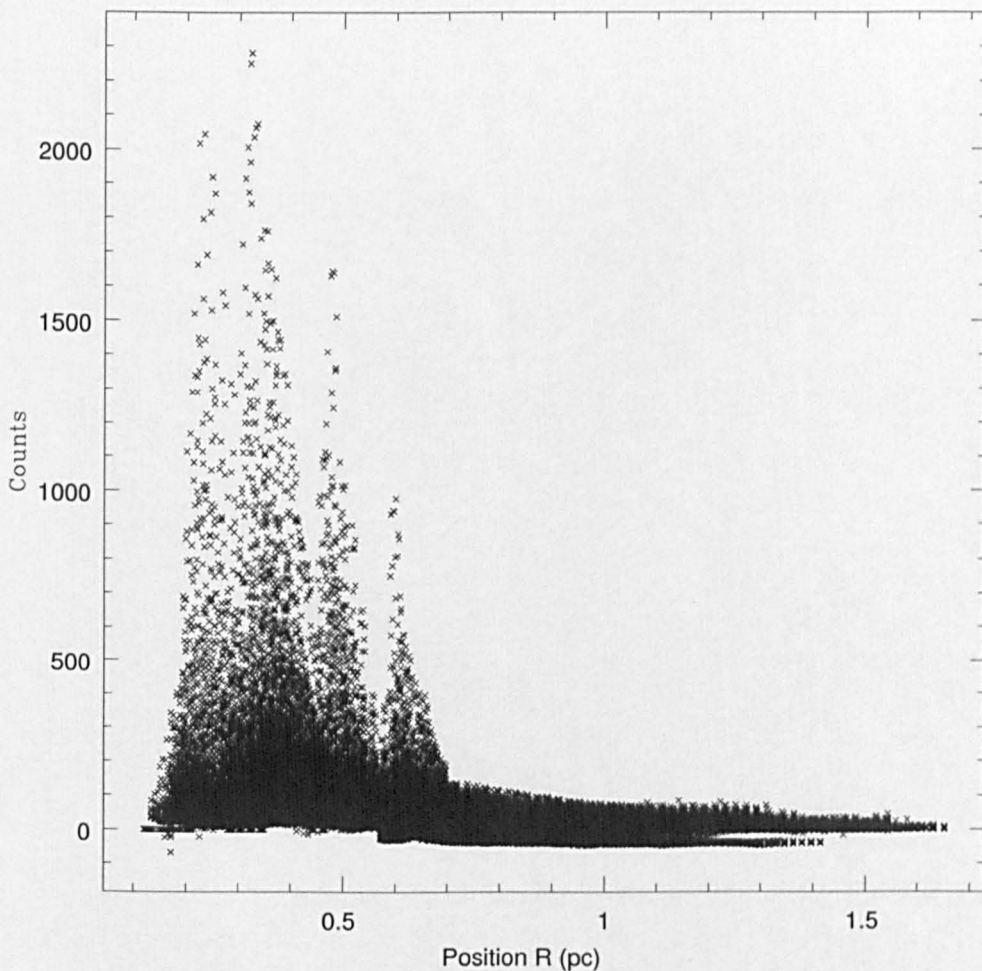


Figure 4.9: Radial displacement versus count plot for the all epochs within the 3D FITS cube. Plot indicates the progression of the light echo through the PN.

2. Examination of the radial displacement of the bright peaks in 30 degree slices of the x-y plane (see Figure 4.10) indicates that the system is not face-on as if it was the plot produced would present a circular shape. This plot also enabled the

determination of a probable axis ratio of 1.3 (major/minor). However, this will be heavily affected by the inclination of the system and should not therefore be relied upon at this stage. It is noted that the inner most data of this plot should be ignored as this will be most affected by any residual of the nova subtraction not covered by the nova centred mask and affected by the mask itself.

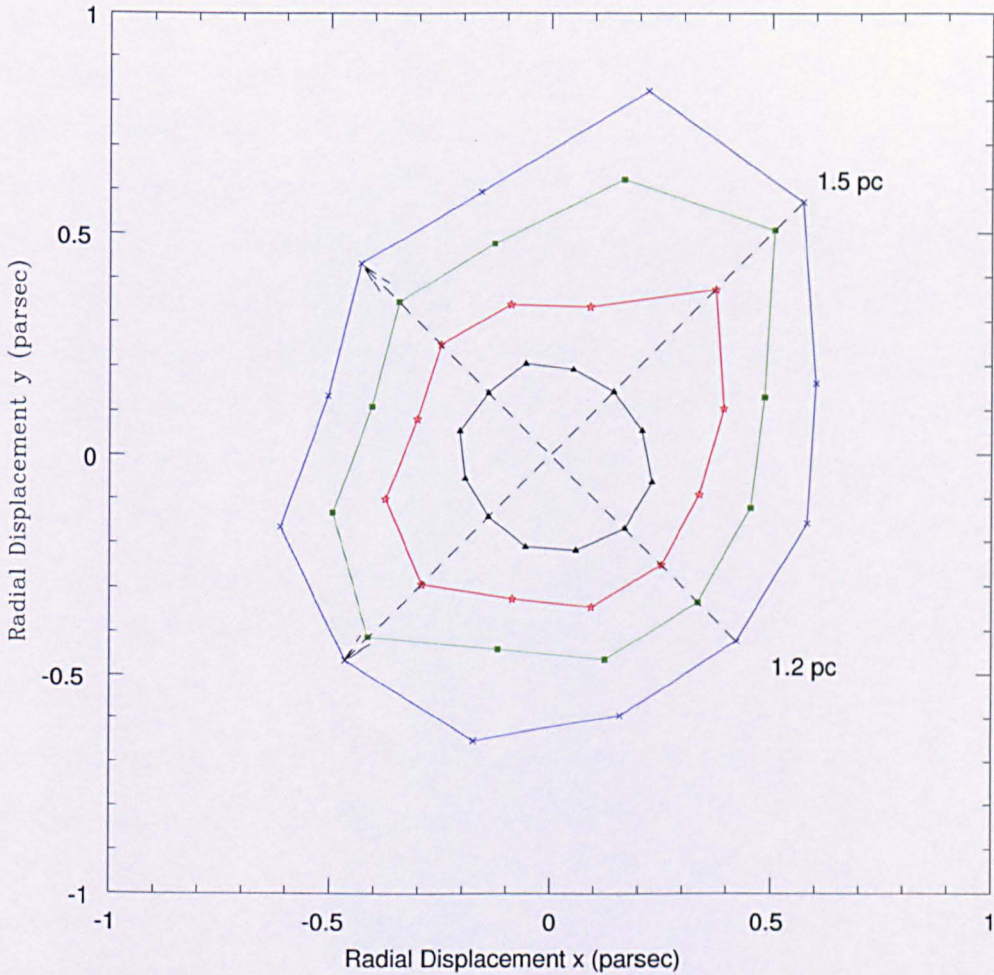


Figure 4.10: X and Y components of the radial displacement for dominant peaks found within 30 degree slices of Figure 4.9. Black triangles represent 2008 data, red stars 2009, green squares 2010, and blue crosses 2011.

The observed expansion rate of the light echo will eventually yield the nature of the scattering material, the distance between the star and the material, and a direct geometric distance determination to the system itself from the Earth.

4.7 Modelling of the Planetary Nebula using XS5

In order to ascertain the geometry of the PN and confirm parameters suggested by Section 4.5 a morphokinematical modelling tool called XS5 has been utilised. XS5 was written and developed by Harman et al. (2003) with the original goal of creating and combining 3D geometrical shapes (spheres, ellipsoids, hour-glass/bipolar structures, see Figures 4.11a, 4.11b, and 4.11c for examples) for comparison to observed PN structures. Within the software, the designed shapes can be rotated to match the position angle (PA1) and inclination (IN1) of the observed nebula. Fundamental parameters of the model may also be adjusted such as the semi-major (A1A - for a bipolar structure this is defined as the distance between waist and the pole) and semi-minor axis (B1A - for a bipolar structure this is defined as half the size of the waist) values, equatorial and polar ring width, polar ring angle, flux of the equatorial ring, polar ring, and background. Additional features may also be included such as seeing conditions, field size, filter bandpass, heliocentric radial velocity, and random clumpiness. A simulation of a spectrometer slit may also be placed across the generated model at any position angle and position velocity arrays created which can be compared to observed spectra. As well as being used to model PNe it may also be used to model novae ejecta (see Section 6.5).

The XS5 tool is written in the C programming language and uses the QT¹⁴ graphical interface. In order to translate a model into an image, the code utilizes the NASA/JPL library tool called Hierarchical Equal Area isoLatitude Pixelization (HEALPix)¹⁵. This tool allows the pixelization of a sphere and the calculation of θ and ϕ (equivalent to longitude and latitude). The resolution of the sphere can be adjusted to generate either a coarse or fine grid allowing fast or slow computation. HEALPix sets each pixel of the sphere such that it has an equal area which is equivalent to an equal solid angle. Emission (via a flux) is assigned to each pixel dependent on its value of ϕ . This method of assigning flux takes into account equatorial and polar emission enhancements later on. Each point of the generated sphere is then extruded into a chosen model shape

¹⁴<http://qt-project.org/>

¹⁵<http://healpix.jpl.nasa.gov/index.shtml>

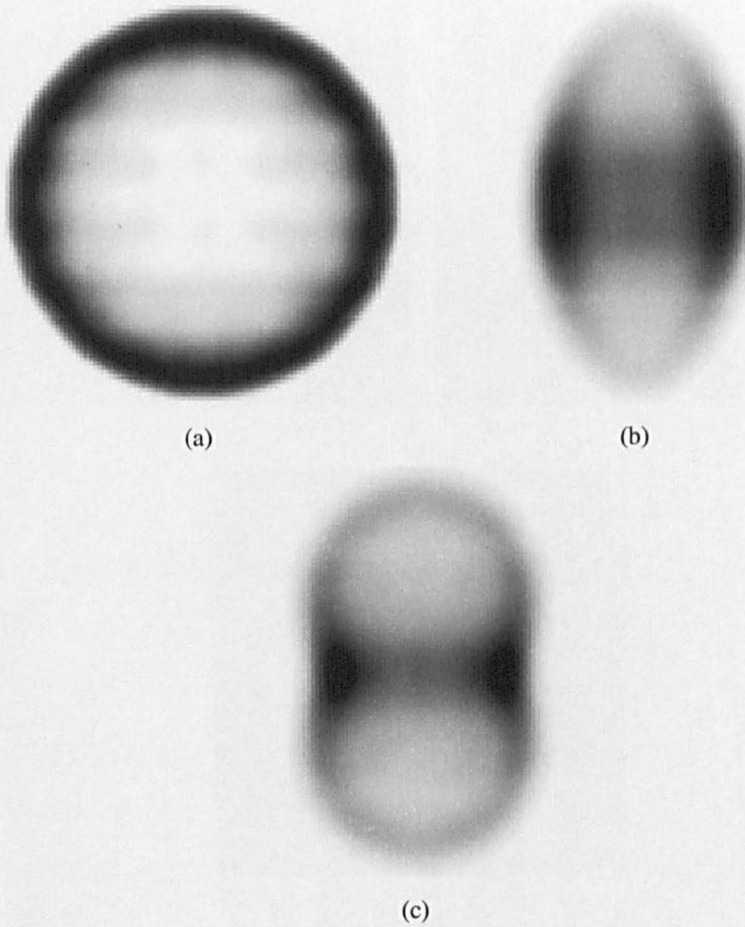


Figure 4.11: Models generated using XS5 with a box size of 99 pixels (0.33 arcseconds/pixel) and a seeing of $2.9''$ applied. Here North is up and East is left. Position angle and inclination of each model were chosen as 0° (North to East) and 90° respectively; “uniform” illumination was applied for each. (a) Circle - $A1A = 15''$, $B1A = 15''$. (b) Ellipse - $A1A = 15''$, $B1A = 7.5''$. (c) Bipolar structure - $A1A = 15''$, $B1A = 7.5''$

(sphere, ellipse, bipolar/hour-glass) by giving each point a shape dependent radius and ϕ coordinate, resulting in a three dimensional Cartesian coordinate for any point of the chosen model shape. Although the flux through each pixel remains the same (the same solid angle is still drawn out with respect to the origin), the number of counts per unit area for that pixel will drop when the radius increases and *visa versa*.

For rotation to occur a solid body matrix transformation is applied to rotate the model to the correct orientation (this is given by a used specified position angle - PA1 and inclination - IN1) on the sky.

To create a light echo the radial distance (r) of each point (with a line-of-sight distance z) from the origin is calculated. The Equation 4.3 is then used to determine the epoch of the image,

$$r/c - z/c = \text{epoch.} \quad (4.3)$$

This epoch is equivalent to the time it takes the light to travel to a point on the created model and then to the observer minus the time it takes for the light to travel from origin to the observer only.

Within XS5 a nova light-curve is modelled via the use of two half Gaussians for which the user is able to define the HWHM. The rising Gaussian HWHM is defined by a parameter called RISE and falling Gaussian by FALL, each are defined with respect to the nova peak.

4.7.1 Modelling Trials: A Single Shell Structure

Using the XS5 gui, PN models were generated. For the purposes of this work, the field of view for all models was set as 99×99 pixels corresponding to approximately $33'' \times 33''$ on the sky and a seeing of $2.9''$ applied. These parameters were chosen such that they matched¹⁶ those of the aligned normalised star-subtracted images produced

¹⁶It should be noted that the $2.9''$ used was based on HWHM of the seeing corrected observed data in pixels (see Section 4.4.4). The seeing that should have been applied to the modelled data is $1.9''$

in Section 4.4.4 (these will now be referred to as the observed PN light echo data). A “uniform” illumination for the entire model was assumed for each generated PN (note that the distribution of flux is not uniform but dependent on the distance of each point from the nova centre, see Section 4.7 for further explanation) and a distance of 13 kpc (taken from Wesson et al., 2008). The parameters which govern the creation of the light echo were adjusted such that the rise was set to one day with the fall initially set as 60 days. A 60 day fall was chosen as work by Ciardullo et al. (1990a) finds that the median time for a nova to decline three magnitudes in $H\alpha$ is ~ 240 days with a decrease of 0.0125 mag/day. Using a linear decline as assumed in Ciardullo et al. (1990a) the HWHM of the fall-off of the light curve ($t_{0.75}$) is equal to 60 days. The passage of the light echo through the model was then calculated within XS5 for each epoch given in Section 4.2 and light echo images generated. These images were then placed within the 3D visualisation code and comparison of modelled and observed 3D data conducted by eye.

With the above configuration of XS5 an initial series of spherical structures were created with diameters ranging from 2'' to 18'' (two arcsecond increments), based on initial measurements made in Section 4.5. It soon became evident however, that a spherical structure was unable to produce key observed features in the PN such as the equatorial and polar knots. Ellipsoidal structures were then examined using semi-major axes (A1A) between 6''-20'' (two arcsecond increments) and semi-minor axes (B1A) of 2''-12'' (two arcsecond increments for each). Again key features of the PN morphology were not reproduced in these models.

Based on these trials it was deemed that a bipolar structure would be more appropriate. Using parameters obtained via visual inspection in Section 4.5 a bipolar PN was constructed with $A1A = 9''$, $B1A = 4''$ (axis ratio = 2.25), $PA1 = 30^\circ$, and $IN1 = 90^\circ$. This PN model is displayed in Figure 4.12(a) with Figures 4.12(b), 4.12(c), & 4.12(d)

($2.9 \times 2 \times 0.33$). This over estimate in seeing which has been applied to all modelled data, however is thought not to significantly influence the outcome of any results obtained for the following reasons: 1. What is being modelled is extended emission and what is being reproduced is the very brightest parts, which will be minimally affected by the seeing, 2. Within the brute force test conducted in Section 4.7.2 the difference in size between geometric parameters i.e (A1A, B1A, A2A, and B2A) is 2 arcseconds so the test itself was not sensitive to the additional one arcsecond spread.

representing the passage of the light echo through the PN at day 286, 419, and 777 after nova peak.

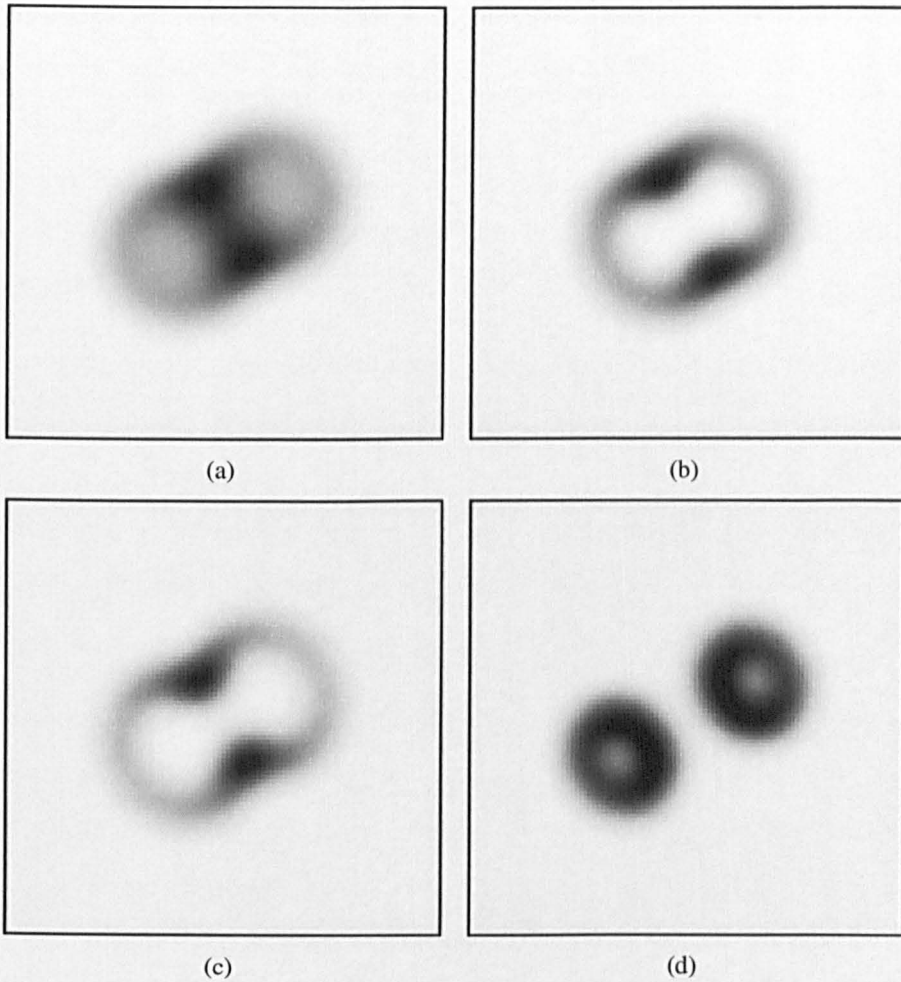


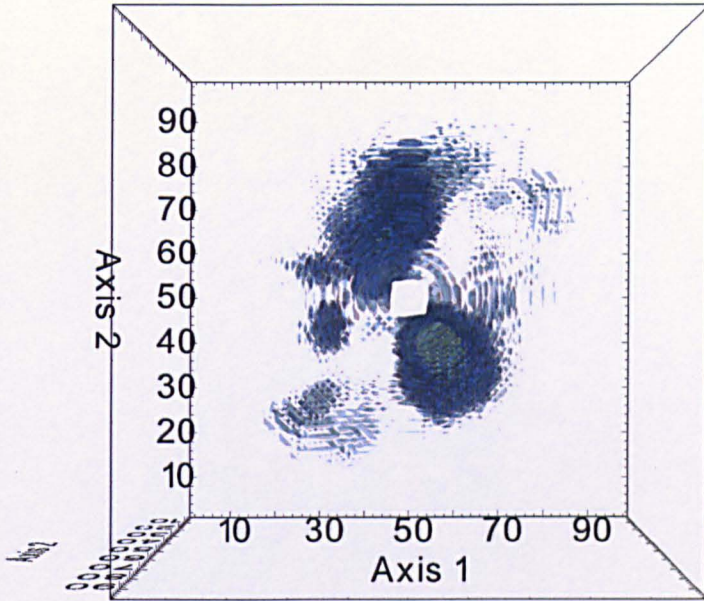
Figure 4.12: (a) Bipolar PN model created using XS5 with “uniform” illumination and set at a distance of 13 kpc with the following additional parameters: $A1A = 9''$, $B1A = 4''$, $PA1 = 30^\circ$, and $IN1 = 90^\circ$, $RISE = 1$ day, $FALL = 60$ days, and a seeing of $2.9''$ applied. (b) Light-echo observed from specified model 286 days after nova peak. (c) Light-echo observed from specified model 419 days after nova peak. (d) Light-echo observed from specified model 777 days after nova peak. Note that in each image North is left and East is down.

As previously, the light echoes generated for each epoch were then placed into the 3D visualisation code described in Section 4.6 and a 3D fits cube created. Visual examination of the 3D composite images was then conducted. Figure 4.13(a) and Figure 4.14(a) show the XY and XZ projection of the observed PN light echo data respectively at a distance 13 kpc, with Figure 4.13(b) and Figure 4.14(b) representing the model light echo data created in XS5 using the parameters stated above. Examination

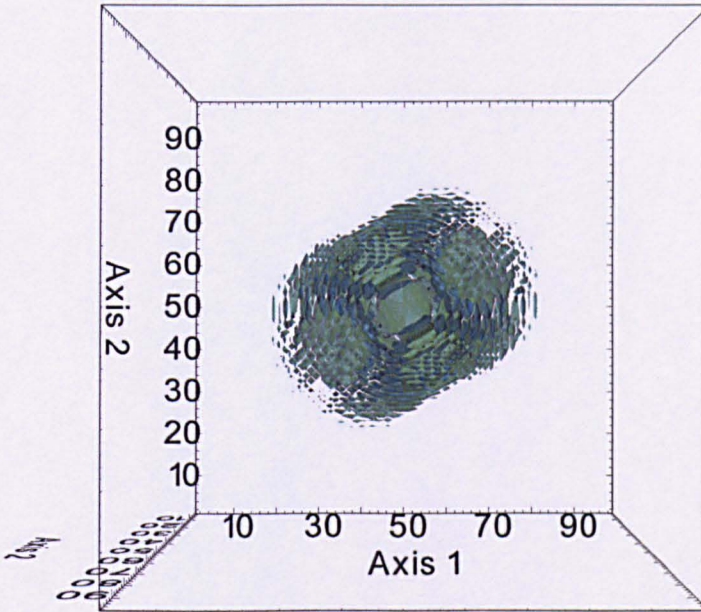
of Figures 4.13(a) and 4.13(b) indicates that although the model may reproduce the equatorial regions relatively well, filamentary structures and the knots furthest from the nova centre are not reproduced. Comparison of Figures 4.14(a) and 4.14(b) also indicates that the observed propagation of the light echo through the modelled PN is too fast with the light echo breaking out of the structure very early on. The images indicate that the chosen semi-major and semi-minor axis values are too small and/or that the PN may be situated at a distance further than that calculated within Wesson et al. (2008).

To investigate the effect of increasing the distance to the PN a series of models were created in XS5 using the same parameters stated previously but with distances of 15 kpc (Figures 4.15b and 4.15f), 17 kpc (Figures 4.15c and 4.15g), and 19 kpc (Figures 4.15d and 4.15h). These figures reveal that by increasing the distance the light echo breaks out of the back of the structure at a later time. However even at 19 kpc a reasonable model of the PN is still not reproduced.

Alternatively, to investigate the effect of increasing the size of the semi-major and semi-minor axes these parameters were doubled giving $A1A = 18''$ and $B1A = 8''$. PN models were then generated, keeping all previously defined parameters the same. The results of light echo data for these models are presented in Figure 4.16(b) and Figure 4.17(b). Examination of Figures 4.16(a) and 4.16(b) suggests that a larger major and minor axis is better at reproducing the equatorial and filamentary structures, but not as effective in reproducing knots closer to the nova centre. Comparison of Figures 4.17(a) and 4.17(b) indicates that although the light echo does not break out of the structure, its propagation is still too fast with it reaching the polar caps of the model earlier than that potentially observed. By increasing the distance to the modelled PN (see Figures 4.18) a more accurate propagation is obtained. These investigations suggest that a small structure (with $A1A$ and $B1A$ values obtained in Section 4.5) encompassed by a larger structure may be required to reproduce all features observed in the PN data and place it at a reasonable distance (see end of this section for explanation of this).

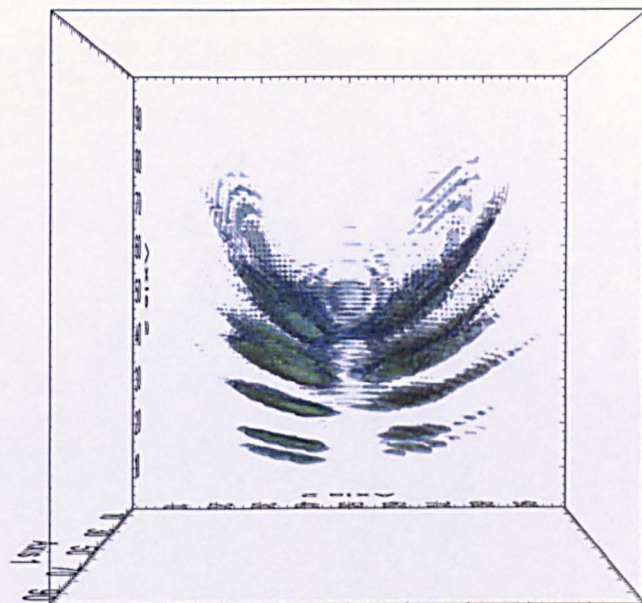


(a)

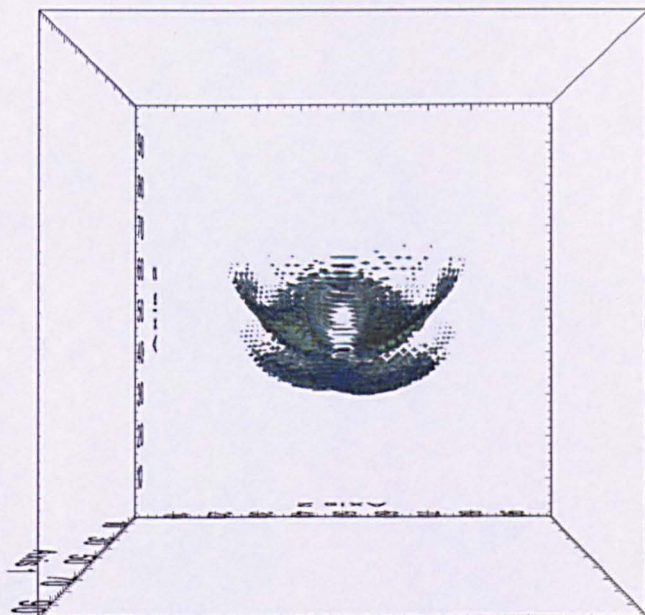


(b)

Figure 4.13: (a) XY axis projection of the observed PN light echo data. (b) XY axis projection of the light echo data created from the modelled PN via XS5. In these images and all following model images generated North is left and East is down in the XY plane.



(a)



(b)

Figure 4.14: (a) XZ axis projection of the observed PN light echo data. (b) XZ axis projection of the light echo data created from the modelled PN via XS5.

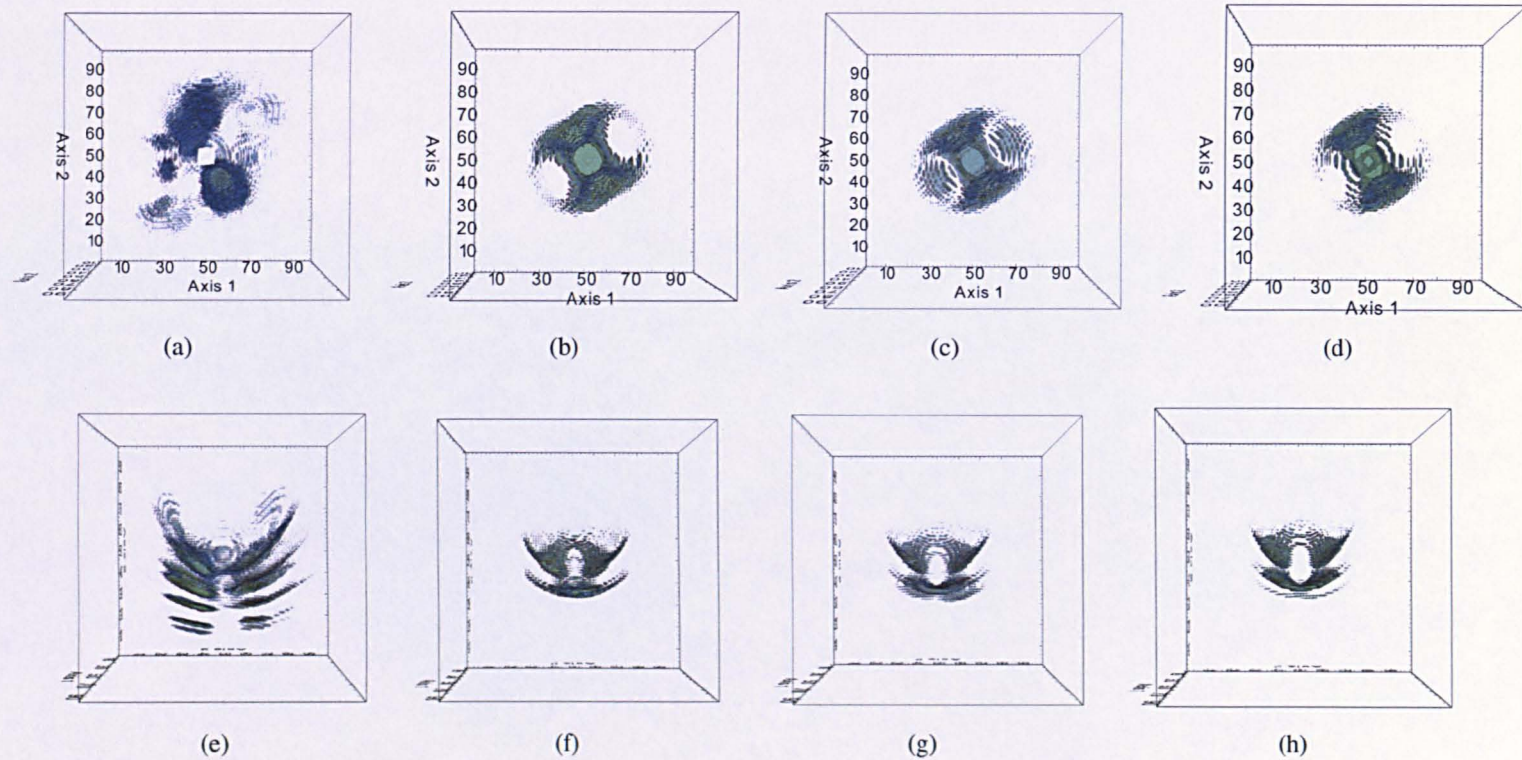
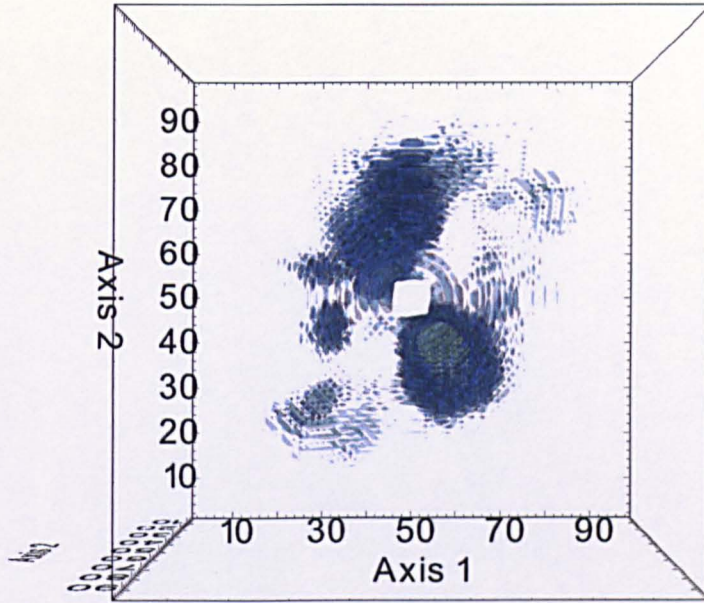
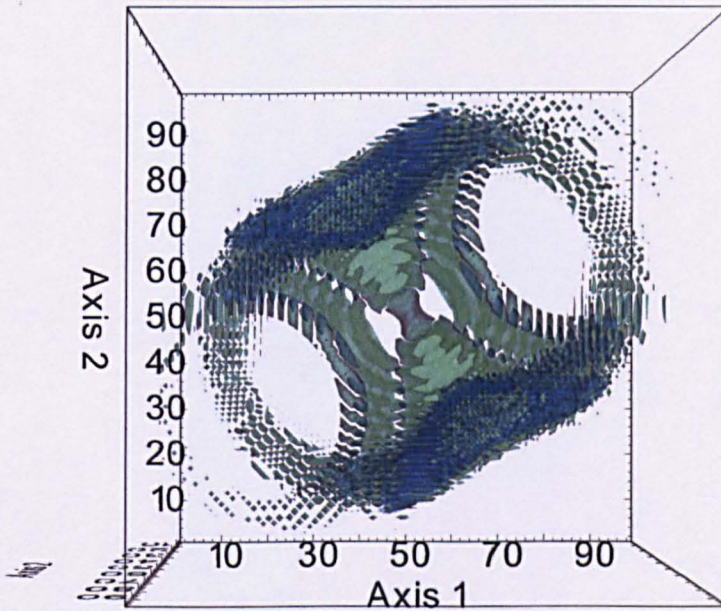


Figure 4.15: **Top row:** XY axis (North is left and East is down) projection of light echo data for (a) Observed PN at 13 kpc. (b) XS5 modelled PN at 15 kpc. (c) XS5 modelled PN at 17 kpc. (d) XS5 modelled PN at 19 kpc. **Bottom row:** XZ axis projection of light echo data for (e) Observed PN at 13 kpc. (f) XS5 modelled PN at 15 kpc. (g) XS5 modelled PN at 17 kpc. (h) XS5 modelled PN at 19 kpc.

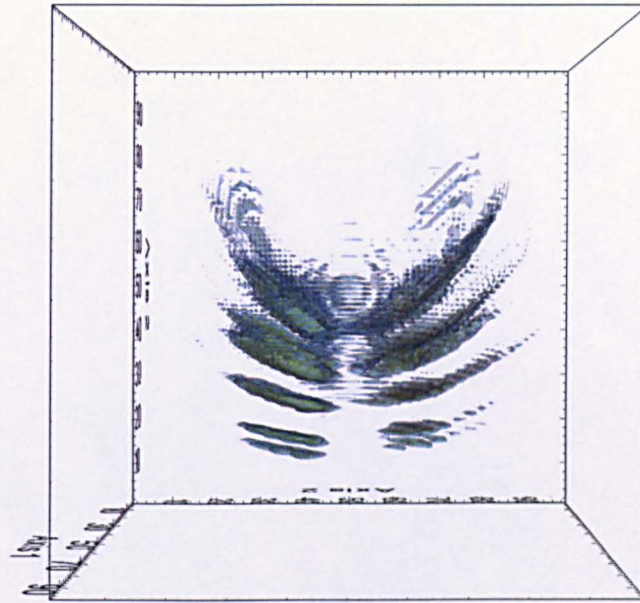


(a)

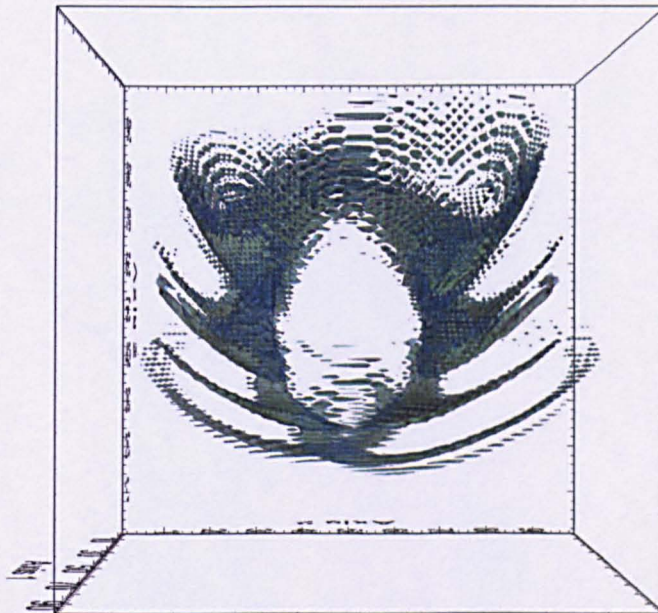


(b)

Figure 4.16: (a) XY axis projection of the observed PN light echo data. (b) XY axis projection of the light echo data created from the modelled PN via XS5 with $A1A = 18''$ and $B1A = 8''$. North is left and East is down.



(a)



(b)

Figure 4.17: (a) XZ axis projection of the observed PN light echo data. (b) XZ axis projection of the light echo data created from the modelled PN via XS5 with $A1A = 18''$ and $B1A = 8''$.

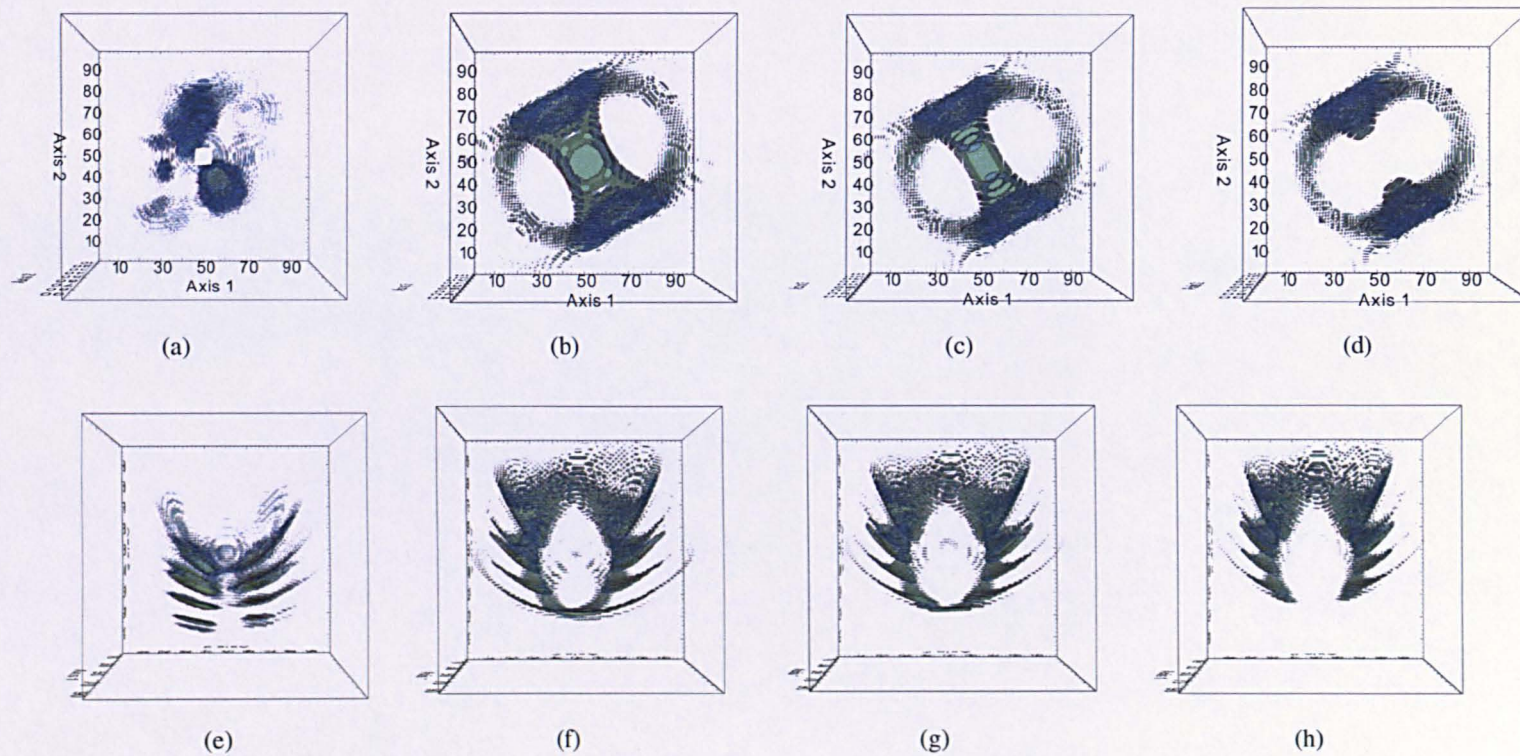


Figure 4.18: Same as Figures 4.15 but using a semi-major axis of $18''$ and semi-minor axis of $8''$.

Table 4.3: Parameters used within χ^2 tests.

Test 1: PA1=30°, IN1=90°, DIST=13 kpc, FALL=60 days, RISE=1 day	
A1A''	5, 10, 15, 20, 25, 30, 35, 40
B1A''	2, 4, 6, 8, 10, 12, 14, 16, 18, 20, 25, 30, 35
Test 2: A1A & B1A first 50 combinations from Test 1 DIST=13 kpc, FALL=60 days, RISE=1 day	
PA1°	24, 26, 28, 30, 32, 34, 36, 38, 40
IN1°	70, 75, 80, 85, 90
Test 3: P1A, IN1, A1A & B1A first 50 combinations from Test 2 FALL=60 days, RISE=1 day	
DIST (pc)	2000, 4000, 6000, 8000, 10000, 12000 13000, 15000, 17000, 18000, 19000

In order to explore a range of bipolar morphologies at a range of distances, a series of tests were conducted in which various geometric parameters were adjusted (see Table 4.3). Quantitative comparison of the observed PN light echo data to XS5 light echo data generated from models was achieved through the calculation of a χ^2 (where each point was uniformly weighted) for the composite 3D modelled and observed data images. Test 1 fixed PA1, IN1, DIST, FALL, and RISE, but adjusted A1A and B1A parameters as stated in Table 4.3. The results of this test were then sorted in ascending order of the χ^2 and the top 50 configurations passed onto Test 2. Within Test 2 the PA1 and IN1 were then adjusted (parameters given again in Table 4.3) and again the top 50 configurations passed on to Test 3 which assessed the distance to the PN.

From these tests the lowest χ^2 was achieved with the following PN configuration: PA1 = 30°, IN1 = 90°, A1A = 20'', B1A = 4'', DIST = 19 kpc, RISE = 1 day, and FALL = 60 days. This would suggest that the PN has a very tight-waist and an axis ratio of 5. Comparison of the modelled PN light echo data (Figure 4.19d) to the observed PN light echo data (Figure 4.19c) finds that even at this distance the light echo is propagating through the PN model too fast leaving the equatorial structure too soon. The correct light echo observation would only occur if the structure were at distances greater than 25 kpc which is improbable as at this distance the nova would be placed 1.6 kpc below the Galactic plane making its situation even more unusual (see Section 4.1). At 25 kpc the nova would also have to be at least four times more luminous. An alternative to this is if it possessed a distance of 19 kpc and the structure has an axis ratio of 2.5.

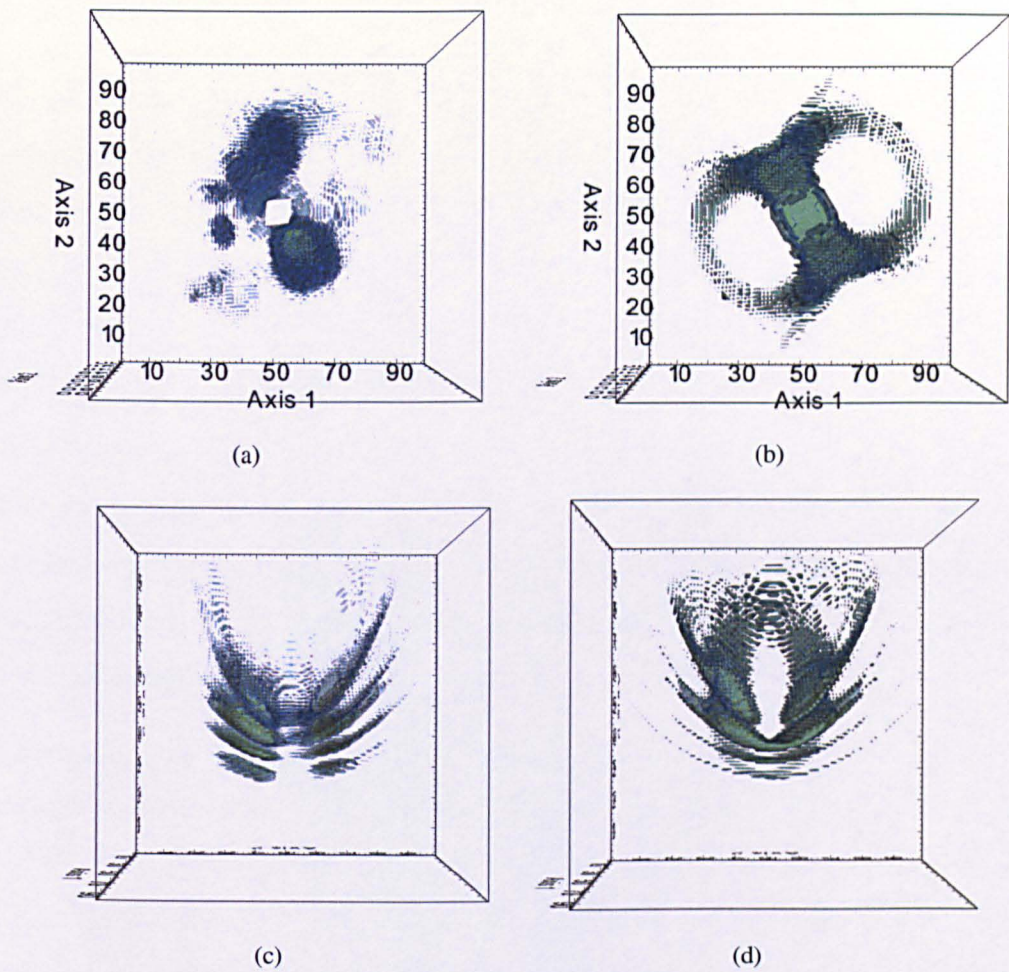


Figure 4.19: **Top row:** XY axis (North is left East is down) projection of light echo data for (a) Observed PN at 19 kpc. (b) XS5 modelled PN at 19 kpc. **Bottom row:** XZ axis projection of light echo data for (c) Observed PN at 19 kpc. (d) XS5 modelled PN at 19 kpc.

This suggests that the PN parameters obtained from the initial run are incorrect. As in previous models, polar knots are still not reproduced (see Figures 4.19a and 4.19b for comparison) and as stated earlier the PN may therefore require an internal as well as an external shell to produced all observed features and situate the structure at a more probable distance.

4.7.2 Modelling Trials: Internal and External Shell Structure

It is evident that both internal and external structures/shells are required to successfully model the observed PN. As mentioned in Section 2.2 the morphologies of PNe are far from simple. Many PNe exhibit multiple shells (Chu, 1989; Chu et al., 1987), multipolar structures, highly collimated outflows, micro-structures, and peculiar geometries which may not be easily explained with simplistic models and multiple physical processes occurring at the same time may be required.

When combining internal and external shells however, the flux ratio of the internal to the external needs to be taken into account. A lower flux for the internal structure would suggest that the material is of a lower density and as such less light is emitted back to the observer. If the flux is higher than that of the external shell the material would be considered relatively more dense.

Separate internal (semi-major axis defined as A2A, semi-minor as B2A) and external structures were created in XS5 with the internal shape set as an ellipse for simplicity and the external remaining as a bipolar structure. The internal structure was set such that its inclination and position angle would always match that of the external as this seems the most likely scenario. The flux of the internal structure was also adjusted such that it was a multiple factor of that chosen for the external (see Table 4.4). The light echo data for both the internal and external structures was passed through to the 3D visualisation code where they were co-added and a combined flux file created. The outputted file was then compared to observed PN light echo data (set at the same distance), which was also passed through the 3D visualisation code, and a χ^2 (again each point was uniformly weighted) calculated. Just under 5 million PN models were created using a series of *for* loops and the parameters given in Table 4.4. It should be noted that the FALL time of the second Gaussian was allowed to vary to compensate for the linear decline assumption made previously. This is a brute force approach to obtaining the best fit PN morphology and as such computational time was large. In order to reduce computational time a slightly coarser grid was applied to construct the model in XS5 (see Section 4.7). Comparison of trial results using the fine and

Table 4.4: Parameters used within brute force χ^2 test.

Test All: RISE=1 day	
FALL (days)	40, 60, 80, 100
DIST (pc)	1000, 2000, 3000, 5000, 10000, 11000, 12000 13000, 14000, 15000, 16000, 17000, 18000, 19000
PA1°	26, 28, 30, 32, 34
IN1°	70, 75, 80, 85, 90
A1A''	14, 16, 18, 20, 22, 24, 26
B1A''	2, 4, 6, 8, 10, 12, 14, 16, 18, 20
FLUX factor	0.05, 0.1, 0.2, 0.25, 0.33, 0.5, 1, 2, 3, 4, 5
A2A''	8, 10, 12, 14, 16, 18, 20
B2A''	2, 4, 6, 8, 10, 12, 14, 16, 18

coarse grid indicated a scatter in the χ^2 of only 0.001 and a decrease in computational time by a factor of four. This method of creating PN models was independent of other parameters, unlike that presented in Section 4.7.1. However the work conducted within Section 4.7.1 refined the choice of PA1, IN1, A1A, and B1A values used.

A histogram of the χ^2 modelling results obtained via the brute force test is presented in Figure 4.20. This test has found only a relatively small number of low χ^2 models, with the best PN defined by the following parameters: PA1 = 28°, IN1 = 90°, A1A = 20'', B1A = 6'', A2A = 16'', B2A = 4'', FLUX ratio = 0.20, FALL = 80 days, DIST = 13 kpc¹⁷. The PN model is displayed in Figure 4.21(a) where seeing has not been applied and Figure 4.21(b) where the 2.9'' seeing has been applied. Light echo data for this modelled PN is also given in Figures 4.22(b), 4.22(c), 4.22(e), and 4.22(f) along with the observed PN light echo data at 13 kpc (Figures 4.22a and 4.22d).

It should be noted that parameters obtained via modelling in XS5 define the limits of the geometry and not the geometry of the PN itself. In order to obtain major and minor axis values measurements of the structure were made on Figure 4.21(b) i.e. the PN the observer would see. This has resulted in a minor axis of $\sim 16''$ and approximate major axis of $\sim 41''$ giving an axis ratio of ~ 3 . Measurements of the internal structure are difficult to obtain and without the light echo this structure will have gone unnoticed.

¹⁷These results are preliminary and will suffer from the same error as mentioned in footnote 16 (page 80). However, for the reasons mentioned within the previous footnote the conclusions are believed to be valid within the uncertainties of the analysis.

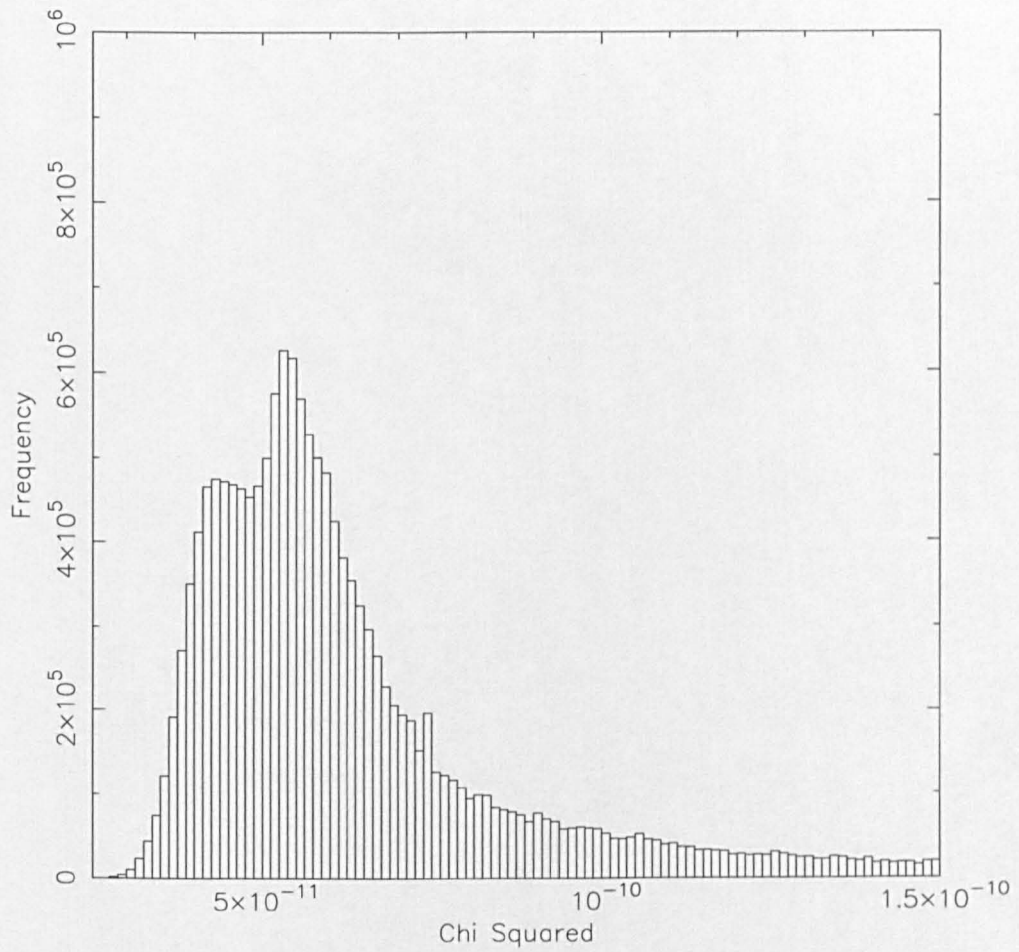
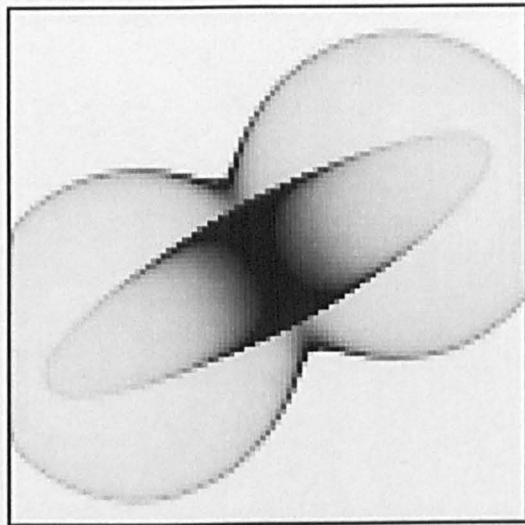
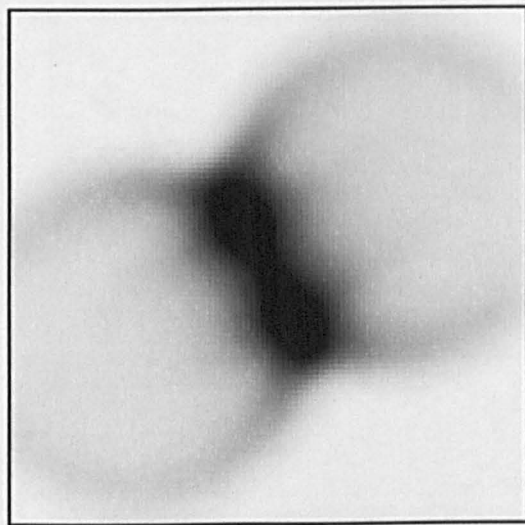


Figure 4.20: Histogram of χ^2 modelling results.



(a)



(b)

Figure 4.21: (a) Lowest χ^2 XS5 generated PN model. Seeing has not been applied. (b) Same as previous but with a $2.9''$ seeing applied. Within these images North is left and East is down.

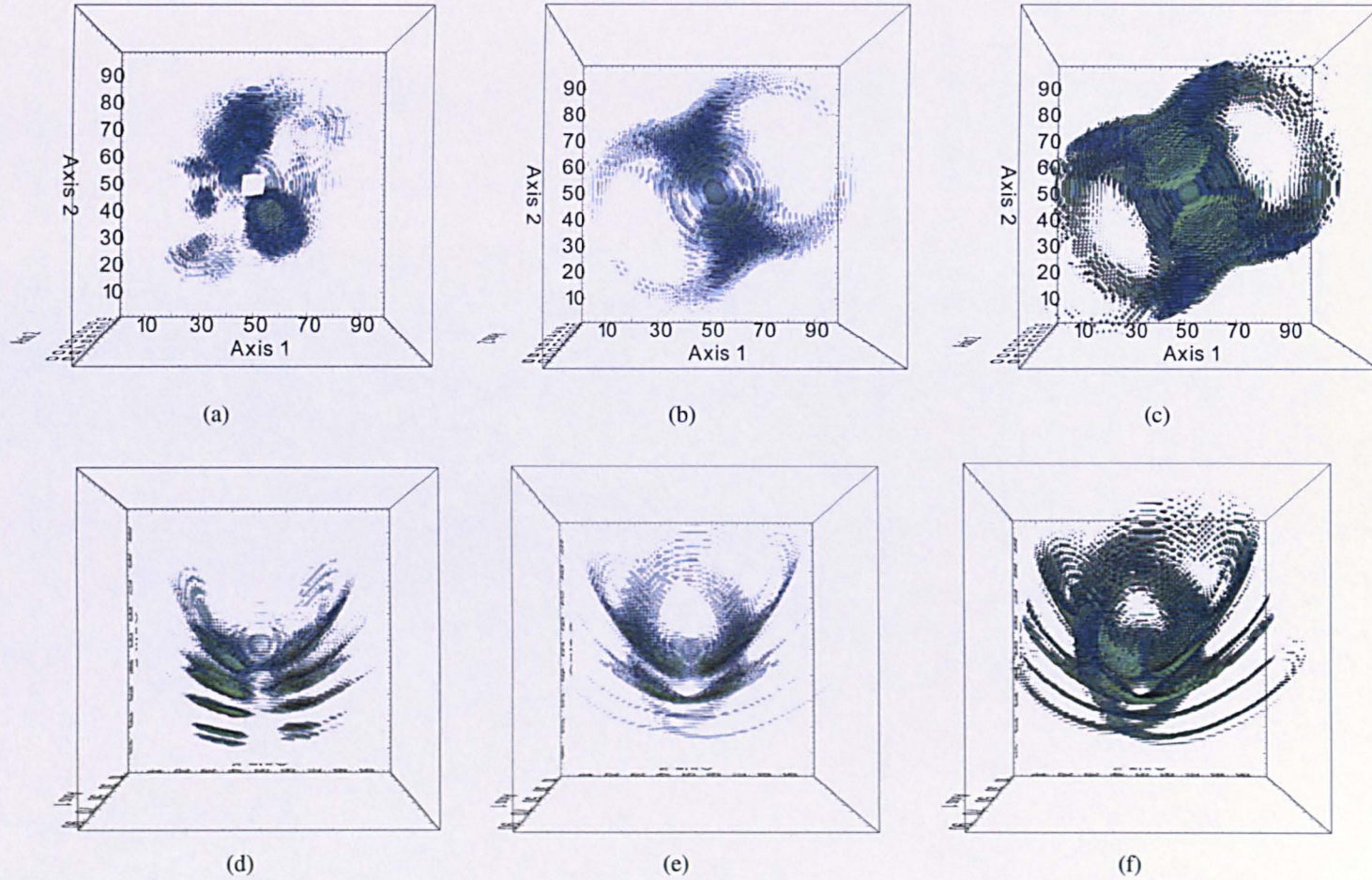


Figure 4.22: **Top row:** XY axis (North left East down) projection of light echo data for (a) Observed PN data at 13 kpc. (b) XS5 modelled PN. (c) Same as b but using display parameters identical to those used within Figures 4.19. **Bottom row:** XZ axis projection of light echo data for (d) Observed PN data at 13 kpc. (e) XS5 modelled PN. (f) Same set up as c.

The data presented in Figures 4.22(b/e) and 4.22(c/f) indicate that although some polar features are observed, dominant knots 2 and 3 are not and the propagation of the light echo still seems inaccurate. The PN model generated is therefore imperfect. In order to refine the parameters of the PN model and allow further testing, the first 1% of the lowest χ^2 configurations generated from the brute force test were analysed. This revealed the following dominant parameters: DIST = 14 kpc, FALL = 100 days, PA1 = 28° , IN1 = 90° , A1A = $22''$, B1A = $6''$, A2A = $14''$, B2A = $4''$, Flux = 0.20. The major results of the DIST analysis are presented in Figure 4.23. On the assumption of a normalised distribution (which may not be the case) a Gaussian has been fit to the data and a distance of 13.6 ± 0.9 kpc derived. It is noted that this may not be an accurate distance determination.

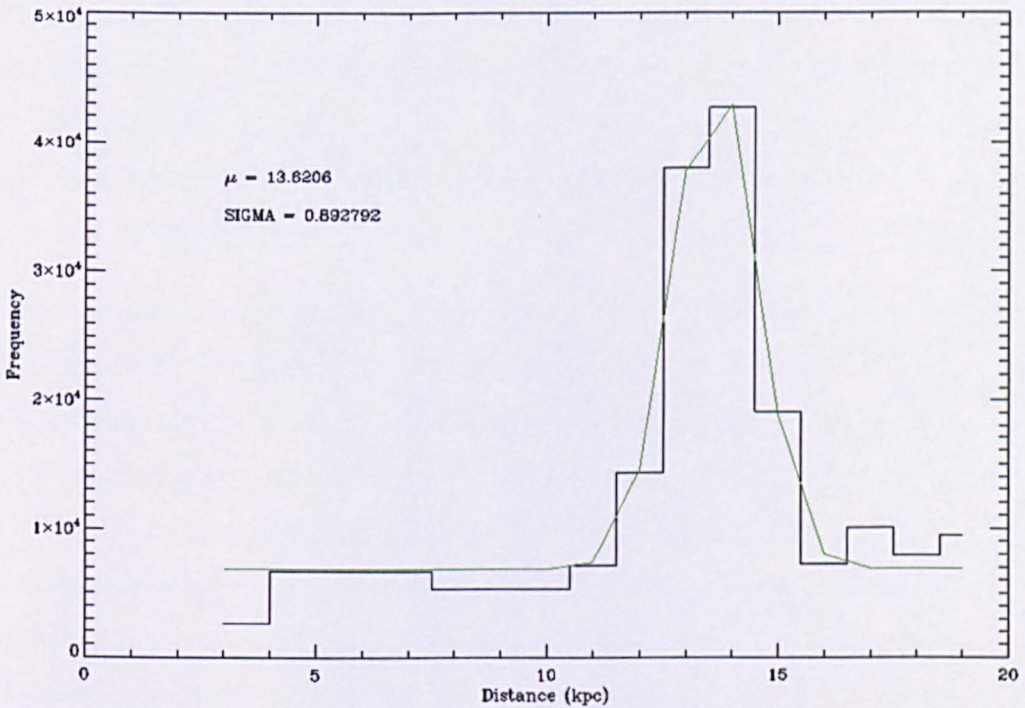


Figure 4.23: Histogram of DIST values for the first 1% of lowest χ^2 PN configurations. A Gaussian (in green) has been fit to the data with mean distance and one sigma error displayed.

An additional brute force test is currently being conducted with refined parameters based upon the results presented above (see Section 7.2.1).

4.8 Discussion and Conclusion

The PN surrounding Nova V458 Vul has been observed in $H\alpha$ over the past four years by the INT, LT (most prominently), NOT, and WHT. Examination of star-subtracted images has revealed the progression of the light echo through the PN illuminating several features such as knots and filamentary structures. Inspection of these knots, their location from the nova (at the centre of each image), and peak time of illumination, has suggested the presence of both internal and external shells. This hypothesis has been supported through the creation of several single shell structures of various morphologies in XS5 which failed to reproduce observed features on the passing of a light echo through the model.

A novel way of displaying the light echo data was created in the C programming language, in which each data frame is projected onto its equivalent paraboloid in time. Examination of the compiled 3D data cube clearly illustrated the progression of the light echo through the PN and has provided a unique way of comparison between observed and modelled data.

Given the failure of a single shell to reproduce the PN a brute force test using a range of fundamental parameters was implemented using a bipolar external structure and an ellipsoidal internal structure in XS5. This test compared the light echoes generated for just under five million PN configurations to the observed light echo data, conducting a χ^2 test in order to obtain the best structure. The results of this test suggest a tight-waisted external shell (axis ratio 3.3) $A1A = 20''$, $B1A = 6''$, with a more diffuse and so fainter (Flux ratio = 0.20) internal shell (axis ratio of 4) $A2A = 16''$, $B2A = 4''$. Generation of this PN model with the applied seeing however, gives an axis ratio for the bipolar external shell as ~ 3 with the internal structure not observed. The position angle of the system was found to be 28° (measured North to East) and inclination of 90° obtained. The fall-off time for the light echo was also found to be 80 days, slightly longer than that given in Ciardullo et al. (1990a) which is also not unexpected as this assumed a linear decline. The distance to the PN using this configuration was found to be 13 kpc which is in agreement with Wesson et al. (2008). On application of a

Gaussian to the distances obtained for the top 1% of PN configurations a value of 13.6 ± 0.9 kpc was derived. This however assumes a normalised distribution which may not be the case and can not be taken as a true value.

As stated in Section 2.2 bipolar PNe may be split into “butterfly” nebulae where the waist is pinched in the centre, or “bi-lobed” structures in which a pair of outer lobes connects to a central smaller spherical or equatorial nebula. In the case of the PN surrounding Nova V458 Vul a relatively tight-waisted bi-lobed classification seems appropriate. The PN model generated however is not perfect and further work to obtain a more accurate structure is required. The results presented here were created using very coarse parameters and refinement of the brute force test is being conducted using the most dominant parameters found within the first 1% of the initial results. This will enable a more accurate PN structure to be obtained. On creation of the PN several assumptions were also made which include “uniform” illumination of each structure, an elliptical internal shell, and that the internal shell has the same position angle as the external. All assumptions made require investigation (see Section 7.2.1). The effect of the masked region applied to the nova location within each observed PN image along with the effect of any residual caused by PSF subtraction of the nova itself must also be taken into consideration and may account for observed differences within the central region of the PN model.

Corradi & Schwarz (1995) estimate that only $\approx 11\%$ of all PNe are bipolars and that this class of PN is produced by more massive progenitors ($M \leq 1.5M_{\odot}$) than other classes. Bipolar structures are said to be formed by a generalized wind-blown bubble (Frank, 1999, GWBB,) where a spherical, fast, weak wind is blown into a previously ejected axi-symmetrical slow wind, which is assumed to have a higher density near the equatorial plane. This higher density wind forces the fast wind to “blow” a prolate nebula, with the major axis along the symmetry axis. If the equatorial to polar density ratio is very high, a bipolar nebula is formed. This sort of formation model however only produces elliptical PNe or bipolar PNe with wide waists and not the tighter-waisted PNe. To form such a bipolar system a collimated fast wind (CFW, see Soker & Rappaport, 2000) is needed and caused by dense gas in the equatorial plane surrounding the

wind blowing star e.g. an accretion disc (see Soker, 2002). Tight-waisted bipolar PNe are therefore thought to require both fast and slow winds blowing together at some stage. These two winds may also interact creating various features (see Soker, 2002; Soker & Rappaport, 2000).

Two pre-nova evolutionary scenarios for Nova V458 Vul have been suggested by Wesson et al. (2008). The first considers a GK Per like system where the PN originated from a massive secondary star during a CE phase, and the ionization of the nebula is maintained by the accretion disc. The second scenario considers a more canonical model where the ionization is due to the central PN star. However, there are various issues with both cases (see Wesson et al., 2008) and further work on evolutionary scenarios needs to be conducted.

In the next Chapter, light curves of novae generated using data from the Solar Mass Ejection Imager (SMEI), a space-based differential photometer, are presented along with their subsequent analysis.

Chapter 5

Investigation of Novae with the Solar Mass Ejection Imager (SMEI)

The contents of this Chapter up to Section 5.5.2 are published within Hounsell et al. (2010a) in collaboration with Prof. Michael Bode (LJMU), Dr Paul Hick (University of California San Diego - UCSD), Dr Andrew Buffington (UCSD), Dr Bernie Jackson (UCSD), John Clover (UCSD), Prof. Allen Shafter (San Diego State University - SDSU), Dr Matthew Darnley (LJMU), Neil Mawson (LJMU), Prof. Iain Steele (LJMU), Prof. Aneurin Evans (Keele University), Dr Stuart Eyres (University of Central Lancashire), and Dr Tim O'Brien (University of Manchester). The paper was written by myself with the supervision and input on specific novae by Prof. Michael Bode and Dr Matthew Darnley. I obtained, reduced, and analysed all nova data from the SMEI archive using pipelines which were written by Dr Paul Hick and John Clover. SkyCamT data were obtained and reduced by Neil Mawson and Prof. Iain Steele. Work on T Pyxidis has been published on-line within Hounsell et al. (2011b).

5.1 Introduction

Based on an extrapolation of the observed nova density in the solar neighbourhood, Shafter (1997) has estimated a Galactic nova rate of approximately 35 yr^{-1} . Of these an average of roughly one CN per year has been *observed* to reach $m_V = 8$ or brighter (see Figure 2 of Shafter, 2002). Since these historical observations are clearly incomplete at $m_V = 8$, the actual number of novae reaching this brightness is expected to be significantly higher (see also Warner, 2008). It is therefore suggested that many bright novae are being missed each year.

With the advent of all-sky missions, ground and space-based, there is new hope for detecting a more complete sample of novae. Although the detection of transient events may not be the original science objective of these missions, their archives could hold a wealth of data on many events. These observations may contain great detail and provide data on many previously poorly examined, and so understood, phases of evolution. Examination of these archives is therefore exceptionally important. One such space-based all-sky mission is SMEI.

5.2 The Coriolis Satellite and SMEI

The Coriolis spacecraft (Figure 5.1a) is home to two instruments: a rotating radiometer called Windsat (intended to measure ocean winds), and an all-sky Solar Mass Ejection Imager (SMEI). Launched by the United States Department of Defence on 2003 January 6th from Vandenberg AFB on a Titan II booster (Figure 5.1b), the spacecraft operates within a Sun-synchronous polar terminator orbit. This orbit is nearly circular, 840 km above the surface of the Earth, and has an inclination of 98° relative to the equatorial plane (Eyles et al., 2003).

The SMEI instrument is a joint effort between the University of Birmingham (UK), the University of California San Diego (UCSD, USA), Rutherford Laboratory (UK), the Air Force Research Laboratory Space Vehicles Directorate (USA), Boston Univer-

sity (USA), and Boston College (USA). It consists of three baffled CCD cameras (see Figure 5.5) each with a $60^\circ \times 3^\circ$ field of view, combining to sweep out a 160° arc of sky (Hick et al., 2007). The SMEI cameras and their fields of view are directed approximately 30° above the local horizon, avoiding light from the Earth, and sunlight reflecting from the rotating Windsat antenna. Each camera has an aperture area of 1.76 cm^2 and alignment of the cameras is such that Camera 1 points away from the Sun, Camera 3 towards the Sun, and Camera 2 covering the section in-between. With this configuration SMEI maps out nearly the entire sky with each 102-minute orbit of the spacecraft.

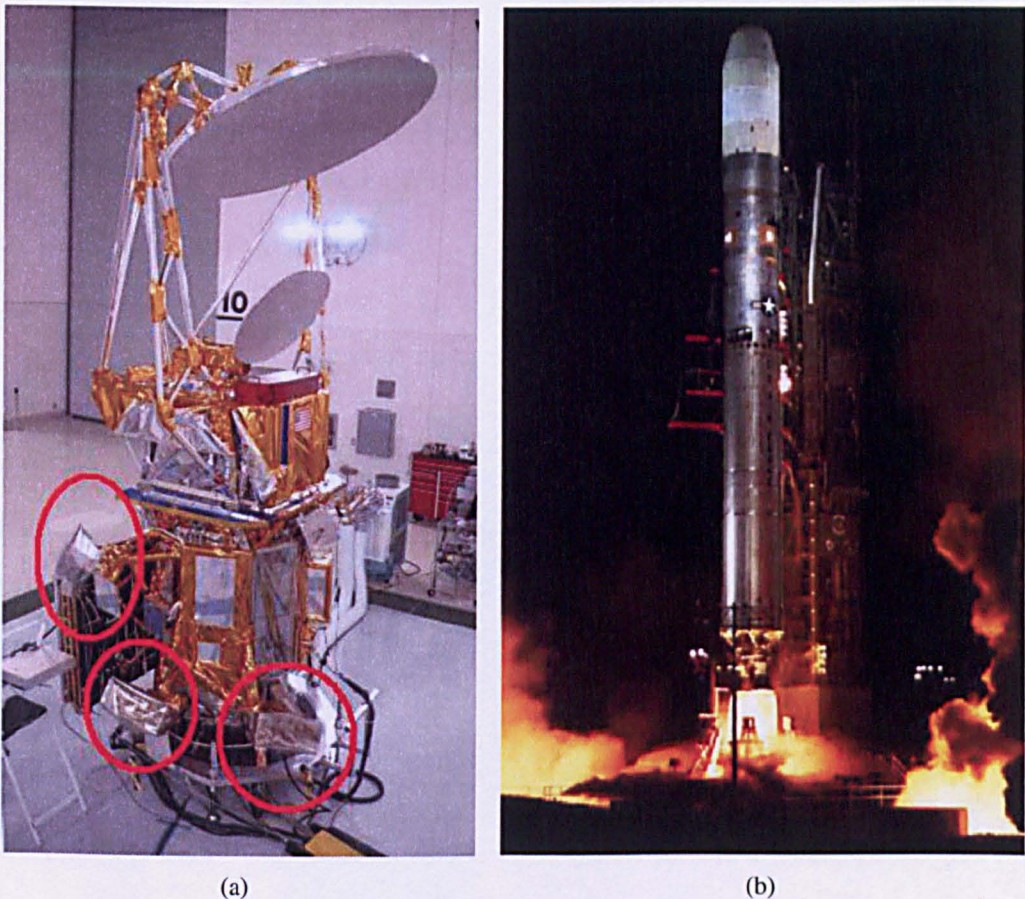


Figure 5.1: (a) Coriolis spacecraft with SMEI instrument on-board prior to launch. The three camera baffles (red circles) are seen in the lower portion of the spacecraft. (b) Titan II launch of the Coriolis spacecraft on 2003 January 6th.

SMEI is specifically designed to map large-scale variations in heliospheric electron densities from Earth orbit by observing the Thomson-scattered sunlight from solar

wind electrons in the heliosphere. The instrument is intended to view and forecast the arrival of solar coronal mass ejections (CMEs), co-rotating structures, and solar wind density variations (Jackson et al., 2004). To do this SMEI is operated as a high precision differential photometer (Buffington et al., 2006, 2007; Jackson et al., 2004) with a peak quantum efficiency at approximately 700 nm (corresponding roughly to an “R” photometric band) and a FWHM of ~ 300 nm. The SMEI CCD readout noise is given as $\sim 14 e^-$ rms, which is deemed insignificant when the SMEI cameras are operated at their design temperature of -30°C . Cameras 1 and 2 reached this temperature successfully. However, Camera 3, the Sun-wards facing camera, did not and currently operates at a temperature between -10°C and 3°C . The SMEI instrument was designed such that stray light background is carefully controlled providing a photometric sky signal which does not vary significantly over the time interval of the heliospheric structures being measured.

As the instrument orbits the Earth, the 3° narrow dimension of the cameras sweeps across the sky (see Figure 5.2) taking continuous 4 second exposures, mapping nearly the entire sky within each orbit. A specific sky location is inside the field of view for typically a minute or more (depending on camera and sky location). With a 4 second exposure this implies that about a dozen or more separate measurements from sequential CCD frames are available for each sidereal skybin. These are combined to provide one measurement per orbit, approximately 1500 frames per camera per orbit are available to compose a full-sky-map. Point sources can be and are fit from these sidereal maps (see Section 5.3). An example of a sky-map produced by SMEI is given in Figure 5.3. The orbit geometry and the requirement to prevent the cameras from receiving direct sunlight account for the 20° diameter Sunward and smaller anti-Sunward exclusion zones.

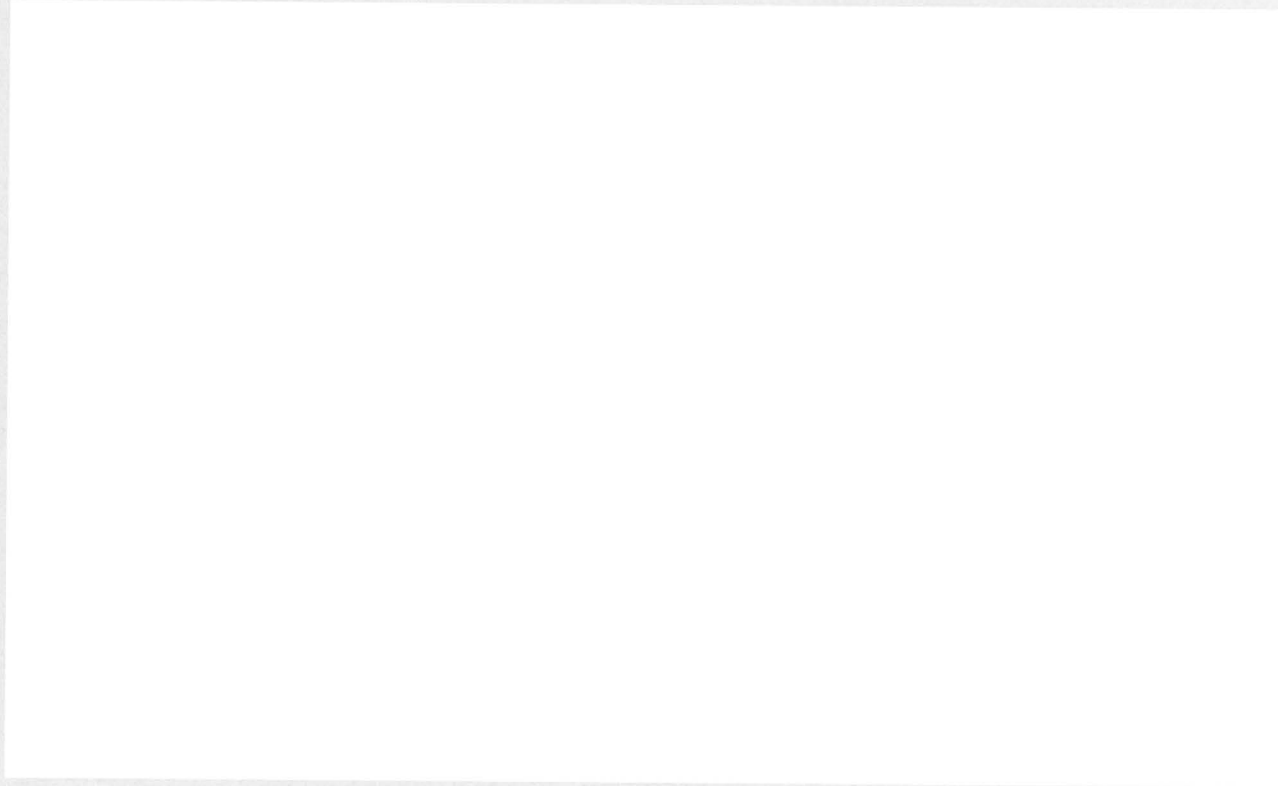


Figure 5.2: SMEI $3^\circ \times 60^\circ$ image frames from each of the three camera arranged in order furthest from the Sun. In each frame the Sun is located towards the left. Image adapted from Jackson et al. (2004).

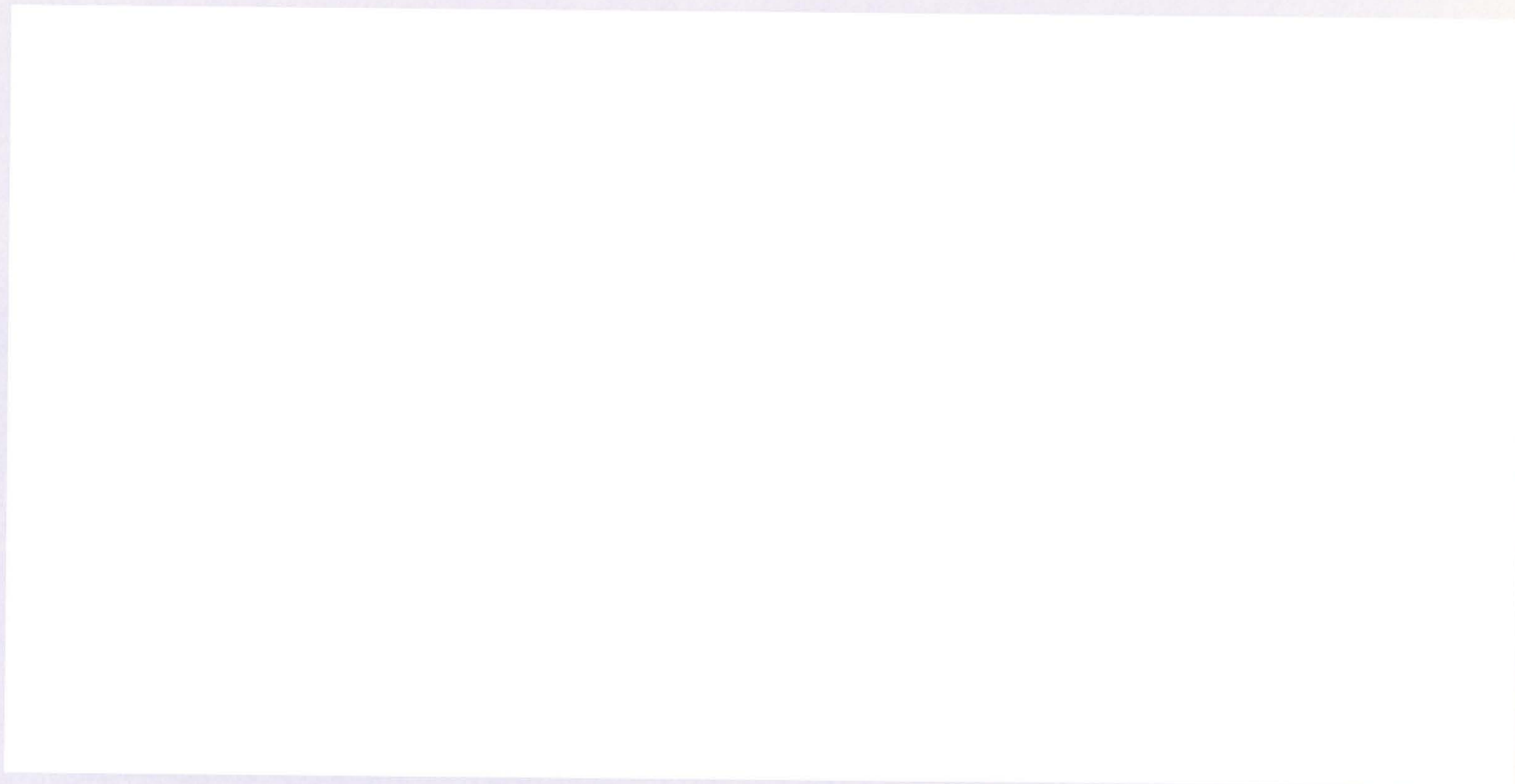


Figure 5.3: Hammer-Aitoff projection sky-map created from a full orbit's worth of frames. A typical composite map consists of ~ 4500 individual frames (1500 from each camera). The Sun is at the centre of the map with the ecliptic plane along the horizontal axis. Bright features are labelled on the map. Blank areas are regions excluded from the composite map either because they were not accessible to the cameras during the orbit, were too close to the Sun and so too bright (shutter of Camera 3 closed), or contaminated by high energy particle enhancements (slash in upper left of image). This image has been taken from Jackson et al. (2004).

5.2.1 SMEI Design Requirements

In order to isolate the faint Thomson-scattered sunlight, much larger white-light contributions must be taken into account. Such contributions include: background light from the Sun, Moon and Earth scattered into the SMEI field of view; light from the zodiacal dust cloud; and starlight (individual point sources such as bright stars and planets, and a mottled contribution to the diffuse sky brightness referred to as the sidereal background). Each of these must be determined and removed. The estimated contribution of these signals as a function of elongation from the Sun is given in Figure 5.4 (taken from Jackson et al., 2004), with the Sun having an equivalent brightness of 4×10^{14} S10 units.

The optics of SMEI are fast ($\sim f/1$). In order to provide a reproducible photometric response, an unresolved point image occupies approximately 200 CCD pixels ($\sim 1/2$ a square degree). The response in this square degree from other sources must be constant or slowly-varying (to a fraction of an S10 unit) such that heliospheric structures can be separated. During the time of observation of a sidereal location an accurate measurement of the stars must be obtained along with the background sky brightness. To prevent the sidereal and zodiacal light from overwhelming the fainter heliospheric signal the differential photometer specification must be better than that required to remove stellar signals alone. Therefore the differential photometric specification for all signals incident on the SMEI focal plane at 90° elongation in one square degree of sky in a single camera passage has been set at 0.1% (Jackson et al., 2004).

To ensure that this specification is met the SMEI baffle was created as indicated in Figure 5.5. The baffle was designed to reduce unwanted sources of noise, including scattered light from the space instrumentation and Earth shine. However, the baffles prove unsuccessful if a camera is pointing towards the Sun and the solar limb approaches within 18° - 27° of the camera's narrow and wide field of view respectively. It should also be noted that certain regions in the sky near the Moon, bright stars, variables, and planets, may also exceed the 0.1% specification.

SMEI pixels are prevented from saturation by two factors. The first is that the exposure



Figure 5.4: Surface brightness versus solar elongation for zodiacal and star light (Cox, A. N., 2000), and of expected CME brightness extrapolated from *Helios* measurements. A calculation of an ambient medium having a density of $10 \text{ e}^- \text{ cm}^{-3}$ at 1 AU and an inverse-square density drop-off within solar distance is also shown (image taken from Jackson et al., 2004).



Figure 5.5: Schematic of SMEI baffle with scale in centimetres. Apertures are numbered Z0 to Z8 in advancing distance towards incident light along the baffle centreline. Top image is the narrow dimension, bottom image is the wide dimension (Image adapted from Jackson et al., 2004).

time of a single CCD frame is limited to 4 sec and the second is the fact that images from the camera are intentionally defocused. The point sources are extended into a fish like shape spreading the light over 200 CCD pixels ($\sim 1/2$ a square degree). The electron full-well capacity of SMEI is 350,000.

5.2.2 SMEI Data Accumulation

SMEI data is stored on the Coriolis satellite in a solid-state recorder (SSR) until X-band downlink to the ground. It is then processed and sent to various institutions for analysis. The SSR can hold 12 hrs of data until it is overwritten. On-board a single CCD frame are 1272×256 pixels (mode 0) with a pixel size of about 0.05° . Due to telemetry considerations the CCD frames are re-binned on-board to 4×4 pixels (318×64 - mode 2). Unfortunately due to the higher operating temperature of Camera 3 (which points at the Sun) the camera has been forced to operate in a 2×2 binning mode (636×128 - mode 1) rather than the 4×4 mode of Cameras 1 and 2, resulting in “science mode” resolutions of 0.2° and 0.1° respectively. Mode 0 frames are used for calibration purposes only.

5.2.3 SMEI Data Processing

The processing steps used at UCSD to convert the raw CCD images into photometrically accurate white-light sky-maps consist of procedures that perform quality checks, correct the data for instrumental and non-heliospheric effects, and create all-sky images for each orbit. The end result is a set of sky-map images that can be presented in any convenient sky coordinate system such as Sun-Centred Hammer-Aitoff or “fish-eye”. The UCSD processing uses 32-bit computing, Fortran, C++, and interactive data language (IDL) programming. The basic steps required for conditioning are given below with the first seven items applied to individual CCD frames and the last three applied to single orbit maps. More detail on each of these steps can be found within Jackson et al. (2004) and Hick et al. (2005).

1. **Integration of new data into the SMEI database:** Data is downloaded at a rate of 4 GB a day.
2. **Identification and removal of corrupted data frames:** Frames may retain telemetry and other errors and are therefore checked. Frames are determined bad and removed if they have anomalous values of electronic offset and dark current. Frames are also removed if a large amount of the image is saturated by the Sun, Moon, or other bright sources (see below).
3. **Pixel Pattern Removal:** A pixel pattern, including hot pixels, is created using weekly on-orbit calibrations and subtracted from the SMEI data frames.
4. **Removal of electronic offset (pedestal) and temperature dependent dark current pattern:** The pedestal is determined from two 4-pixel wide columns found to the right and left edge of mode 0 frames (2 or 1 columns in mode 1 and 2 respectively). The dark current is determined from a set of neighbouring 4-pixel wide columns which are covered. These columns may be affected by cosmic rays and so a cut-off threshold is determined empirically based on the median value. This value varies with camera and mode, but remains constant throughout the mission.
5. **Particle Detection and Saturation:** If a pixel value is significantly higher than its surrounding eight pixels then these pixels are removed (constructed in such a way as to not act on stars). If the pixel-to-pixel response variation is excessive then many particles may have hit and the frame itself removed.
6. **Flat field, optical, and geometric corrections:** Flat fields were determined for each camera prior to flight to a $\sim 1\%$ accuracy using an exposure of a uniformly-illuminated white cloth. These flat fields have been improved to the 0.1% differential photometric specification through on-board analysis, and the analysis of long term trends in the stellar background. The viewing perspective and pixel-per-pixel observed surface brightness increases towards the inside of the CCD frame arcs (see Figure 5.2) are also included here, separately

and analytically. These are geometric effects and not caused by CCD response variations.

7. **Indexing and removal of cosmic rays, space debris, and bad pixels:** This is the registration and averaging of frames for placement onto a high-resolution sidereal grid using spacecraft pointing information. The pointing of the spacecraft is determined to within $\sim 0.01^\circ$ using the spacecraft quaternions which average 20 measurements throughout the 4 second exposure. Further accuracy is obtained using stars, bringing the pointing to $\sim 0.004^\circ$ for 4×4 binned pixels. The sky-maps are achieved using an Hierarchical Triangular Mesh (HTM) grid (Kunszt et al., 2001) with an angular resolution of 0.1° . The pixels of the frames are “indexed” by placing them into the appropriate triangles in the HTM grid. Every 0.05° pixel in mode 0 (0.1° in mode 1, and 0.2° in mode 2) makes up several triangles. Each HTM triangle is a sidereal location on the sky and made up of a dozen or so frame contributions. These multiple contributions of the same location can be used to flag up cosmic rays, space debris, hot pixels, and “flipper pixels” (most evident in Camera 3).
8. **Formation of a set of sidereal maps of sky brightness:** On completion of indexing a full-sky HTM grid is assembled, and a planar representation of the sky is made using an equatorial grid (RA and Dec; J2000). The angular resolution of these maps is 0.1° and consists of a rectangular map of the equatorial region from -60° to $+60^\circ$ Dec (3600×1200 bins), and two polar maps for regions above and below $\pm 50^\circ$ Dec (800×800 bins). These maps retain the original SMEI data frame resolution as well as the PSF orientation which is stored for later use. Other sky-maps (e.g. Sun-centred Hammer-Aitoff and fisheye) with different coordinate systems are obtained from these maps.
9. **Removal of zodiacal light and sidereal sky brightness:** Removal of the zodiacal light is done through the subtraction of a Sun-centred model which approximates its angular shape and brightness. Bright point sources are removed via PSF subtraction (see Section 5.3). Signals from the sidereal sky (fainter stars, Milky Way, nebulae, and galaxies) must be subtracted from each orbit’s sky-map. The

sidereal background is removed via the subtraction of an average sidereal orbit map. This map consists of 34 median combined day orbit maps (from which zodiacal light and bright stars have already been removed) taken bi-monthly over a six year period. Only Cameras 1 and 2 were used in the construction of the sidereal orbit map as Camera 3 suffers from greater noise.

10. **Provision of derivative data products for use in further analysis:** As well as providing data on original items of interest, SMEI is capable of providing stellar time series of point sources with a 102-minute time resolution, reliably detecting brightness changes down to $m_{\text{SMEI}} \sim 8$ (see Section 5.3.1).

5.3 Fitting Point Sources in SMEI maps

To achieve the photometric precision of SMEI (0.1% differential photometry per square degree), point sources brighter than 6th magnitude must be fit and subtracted from the all-sky maps. Subtraction is conducted on the composite images and not individual CCD frames. The UCSD SMEI database contains a list (J2000 position and apparent magnitude) of 5600 sources expected to be brighter than 6th magnitude in the SMEI sky-maps, taking into account the SMEI band pass (i.e. $m_{\text{SMEI}} < 6$, see end of this Section). The brightest planets have also been added to this list (Venus, Mars, Jupiter, and Saturn).

As stated in Section 5.2.3 the final output of the SMEI procedure is three maps, the largest containing the equatorial region (3600×1200 bins), and two smaller maps containing the poles (800×800 bins). Each map has an angular resolution of 0.1°. Within each map the shape and size of a bright star is influenced by three factors:

1. A given star is made up of the average of a dozen sequential frames, where the star crosses the field of view at an angle of $|\theta| < 30^\circ$ from the optical axis of the camera, therefore the PSF width varies as $\cos\theta$.
2. The orbital plane of the Sun-synchronous orbit rotates 360° over a year and so

Figure 5.6: “Standard stars” (PSFs) for cameras 1, 2, and 3 (left to right). For each camera a $2^\circ \times 2^\circ$ square is shown. The cross indicates the location of the centroid for the brightness distribution. The standard star is constructed with an angular resolution of 0.025° . The effective non-zero area of the PSF is 1.18 square degrees for Camera 1, 1.32 for Camera 2, and 1.03 for Camera 3. In these images North is up. Image taken from Hick et al. (2007).

the PSF rotates around its centroid in the sky-map as well.

3. The map projection distorts the PSF depending on its location in the sky-map.

The standard PSF used for fitting was created via the observation of many bright isolated stars over a year (see Hick et al., 2007). For the selected sky-maps the stars were superimposed and averaged after background subtraction and correction for the above three effects. The resulting PSF shape has a full width of approximately 1° , is highly asymmetric, and “fish-like” in appearance; this is caused by comatic and spherical aberrations of the optics (Hick et al., 2007). The PSF for each camera is given in Figure 5.6.

As stated above the orientation of the PSF on the sidereal sky rotates over 360° during the course of a year. Near the poles this change is near uniform rotation, but away from the poles it becomes increasingly non uniform. An example of this rotation is shown in Figures 5.7(a) and (b). The orientation of the PSF for every star can be calculated knowing the spacecraft pointing information and the star location.

The width of the PSF is inversely proportional to $\cos\theta$ as the position increases from the optical axis of the camera in the long dimension of the field of view. Only the width perpendicular to the PSF symmetry axis is affected, i.e. along the θ direction. Therefore the PSF of a star becomes narrower the further from the optical axis it gets.



Figure 5.7: The Orion constellation from SMEI all-sky-maps as viewed by Camera 1. Left: (a) Orbit from 2005 November 10 at 03:24:54 UT. Right: (b) Orbit from 2006 January 19 at 176:37:21 UT. Rotation of the PSFs is due to rotation of the spacecraft orbit relative to the sidereal background. The grey-scale is set to saturate at 1000 ADU. Only HD 33111 and δ Ori are not saturated. The map covers the area $75^\circ < \alpha < 95^\circ$, $-13^\circ < \delta < 11^\circ$. Image taken from Hick et al. (2007).

5.3.1 Least-Squares Fit of a Point Source

Point sources (stars and the brightest planets) are fitted to the standard PSF using a least-squares fitting procedure implemented in IDL Hick et al. (see 2007, routine named *smei_star_fit*). In its simplest form the fit provides an analytic solution for a planar background and the brightness of the point source under examination (with respect to the “standard star”). Within this fit, PSF centroid, width (scaling factor of $\cos^{-1}\theta$), and orientation must be taken into account. An area around each star is used within the least-squares fit and includes all sky-bins that map to equivalent locations inside the effective area of the PSF. An additional area is also used, which extends out a certain radius from the centroid (wing radius). This is to ensure that enough sky-bins are used to fit the background, and that these are safely away from the PSF itself. At the expense of a substantial increase in computational resources the quality of the fit can be improved by iteratively fitting the PSF centroid, width, and orientation (see Hick et al., 2005, 2007, for further details).

As described in Buffington et al. (2007) a bright-star calibration of the SMEI data was conducted. This calibration was made via the comparison of the surface brightness response of SMEI to the SOHO-LASCO C3 coronagraph using measurements of 17 bright (< 4.5 magnitude) stars observed by both instruments. These stars were not known variables and had no neighbouring stars brighter than 6th magnitude within 1° on the sky. The SMEI and LASCO C3 coronagraph data are per-pixel electron counts gathered from the CCD within a certain integration time, with SMEI these counts are referred to as analogue-to-digital units (ADUs). A common surface brightness unit to use is an S10 unit, this is defined here as the equivalent number of 10th visual-magnitude G-type stars per square degree. The 17 stars used with the Buffington et al. (2007) analysis were not solar-type G stars, but their spectral types were known and spectra available (Neckel & Labs, 1984; Pickles, 1998). The visual magnitude of each star was corrected by the ratio of the star’s spectrum to that of the Sun, integrated over λ and multiplied by the appropriate CCD response and mirror reflectivity versus λ . The resulting “ m_{SMEI} ” then connects SMEI’s observed number of ADUs to the S10 brightness scale. It was found that one S10 unit = 0.46 ± 0.02 ADUs. The conversion of a star’s brightness to m_{SMEI} is given in Equation 5.1¹⁸,

$$m_{\text{SMEI}} = \frac{-2.5 \cdot \log(F/G) - a}{b} \quad (5.1)$$

where F is equal to the brightness of the examined star (with respect to the “standard”: I/I_{std}), G the gain of the camera, and calibration constants with values of 1.65 and 0.99 represent a and b respectively.

5.3.2 Star crowding

A star of interest is considered crowded when it lies less than one PSF width from another bright star (typically 6th magnitude or brighter). In order to fit and remove such stars a simultaneous fit must be done (i.e. multiple stars in a single fit). Currently the

¹⁸See http://supercat.ucsd.edu/~poncho/help/smei/SMEI_frames.html for all SMEI IDL documentation and calculations.

simultaneous fitting of stars is conducted when stellar separation is within $0.25^\circ - 1.0^\circ$ (originally the maximum was set as 0.75° and this value was used in Section 5.5.1). In this instance the brightness contributions of the two stars can be separated and contamination of the sources is considered minimal. However, if stellar separation is less than 0.25° the stars can not be separated. The brighter star is fit first and is assumed to include the brightness of the fainter star (which is not fit at all), the source is then considered to be contaminated. The SMEI pipeline is currently able to fit four bright stars simultaneously using the least-squares fit, therefore many crowded regions of the sky such as close to the Galactic plane, are off-limits¹⁹. The surrounding region of each point of interest must therefore be assessed on an object-by-object basis for levels of potential contamination.

If a star of interest has a bright neighbour which is at a distance greater than 1.0° this may also be included in the fitting procedure but subtraction will occur as normal i.e the brightest star fit first and then the fainter. This may be important in removing any stray light from the bright star in the fit of the fainter star, and so contamination.

5.4 Finding Novae with SMEI

As noted above, SMEI can reliably detect brightness changes in point sources down to $m_{\text{SMEI}} \sim 8$ (see Section 5.3.1 for details on m_{SMEI}). Therefore one class of optical variables that are potentially within the detection limit of SMEI is novae. The results of Shafter (2002) indicate that as many as ~ 6 CNe per year are then potentially detectable by SMEI. The high cadence of SMEI along with its ability to monitor objects appearing closer to the Sun than is possible from ground-based observations, makes it feasible not only to constrain the observed nova rate, but also to measure nova light curves near and especially before maximum light with unprecedented temporal resolution.

For the purpose of this work a supplementary star catalogue was added to the UCSD SMEI data base. This catalogue contains the names, co-ordinates, and discovery mag-

¹⁹For example, the lowest Galactic latitude where a nova has been detected without contamination is 1.5°

nitudes of 62 CNe and 3 RNe (RS Oph, U Scorpii, T Pyxidis) with eruptions dating between 2003 and 2011 (see Appendix B). As an initial trial, 22 of the brightest novae were examined. The choice of these 22 novae was based on whether they were visible above the background noise within the SMEI sky-maps around peak.

5.4.1 Data Processing

The processes required for the examination and subsequent creation of the nova light curves within the SMEI data archive are discussed below.

Visual Inspection

Individual novae and their surrounding region were visually inspected within the composite sky-maps produced by the SMEI data pipeline. This was achieved using a tool provided in the SMEI data analysis software called *qsmei_sky*. This tool enables the user to determine several important factors:

1. **Confirmation of the nova outburst:** The tool allows the user to examine the object from one orbit to the next. An animated gif may also be constructed at the location to further assess if there is a brightness increase of the object with respect to the surrounding environment. If the nova event was not seen within these images the object was dismissed, either because the event was too faint, or that the object was located within a region crowded by many bright stars and so its outburst is made indistinguishable.
2. **The camera the object is located within during the outburst:** The user may also determine if and when there is any overlap of this location between the cameras.
3. **The identification and location of any bright stars surrounding the nova:** If these bright stars are far enough away to be accounted for within a simultaneous fit or if they are too close and so become a source of contamination (see

Section 5.3.2).

4. **Identification of bad orbits during the nova outburst:** These orbits are removed from the time-series once a fit conducted. An orbit may be considered bad for several reasons. These include: close passage of a bright planet or space debris to the nova; high energy particle bombardment of the frame; an approaching Sunwards or anti-Sunwards mask that affects the area surrounding the nova which would be used for the fit; and engineering issues with the instrument itself.

Once points 1 to 3 were undertaken an initial fit for a nova could be constructed and this fit evaluated (see Section 5.4.1). The final point listed above was then implemented on the resulting time-series.

Parameter Adjustment

The photometry of each nova was obtained using the extended least-squares fit described in Section 5.3.1. This procedure implemented the iterative fitting of PSF centroid (*fix_centroid*), width (the direction cosine angles, *fix_fovangle*), and orientation (the PSF rotation angle, *fix_psfangle*). Zodiacal (*rmzld*) and sidereal background light (*rmbkgnd*) were also taken into account during the fitting stage. The fitted value for the flux of the nova (and neighbouring stars where applicable) was then converted into an unfiltered SMEI apparent magnitude (m_{SMEI}) using Equation 5.1, and its error calculated using photon counting statistics and error laws. Within the fitting procedure several parameters may be adjusted or defined in order to achieve the best fit and so produce the best nova light curve.

For any fit the area used to sample the surrounding stellar region (wing radius) from the PSF centroid (see Section 5.3.1) is often set as *auto_wing*. The value of this parameter is however is dependent upon the magnitude listed for the nova within the catalogue (see Equation 5.2). These values are often discovery magnitudes and as such not always appropriate. The size of the region may therefore be adjusted to a user specified radius using the *wing_radius* command. The size of the chosen wing radius may also

be dependant on what is within the surrounding stellar region.

$$auto_wing = 0.1^\circ \cdot (3 - m_{SMEI}) + 1.4 \text{ [degrees]}. \quad (5.2)$$

A smaller wing radius may be appropriate under the following circumstances:

1. If the object is close to several bright stars and a smaller surrounding stellar region would reduce their contamination in the fit.
2. If the object is close to a masked region and a smaller radius is required so as to not include this mask.

The choice of wing radius is assessed via visual inspection and examination of certain parameters produced on fitting of the nova when using varying radii. These parameters are as follows:

1. **Correlation Coefficient of the Fit (cvmin):** For every orbit within the specified time period the object is fit and a correlation coefficient is calculated (correlation to the SMEI PSF/“standard star”). For novae with peak magnitudes brighter than $m_{SMEI} = 7$ a threshold value of 0.6 is used, where data below this limit are removed. For novae with peak magnitudes at or below $m_{SMEI} = 7$ a lower limit of 0.4 is used, with the understanding that the errors on this data will be far greater. Each light curve produced with a certain wing radius is assessed on the basis of the number of points above and below the relevant cut-off value.
2. **Pixels inside the PSF (n_fitpsf):** The number of pixels inside the PSF can be a good indicator of whether the object in question is being affected by a masked region or transition into another camera. If the number of pixels varies significantly it may be wise to opt for a smaller wing radius in order to prevent overlap of the sampling region and the masked/transition region.
3. **Background Constant (back_const):** The background constant is a measure of fitted background. For bright novae the edges of PSF fitted do not spread far

enough, meaning that not all of the nova light is accounted for in the fit and may be included within the wing radius and so the fitted background. Examination of this background indicates this under- or over-subtraction (depending on the object). In some cases this affect may be reduced by applying a larger wing radius. However, the size of the radius applied is also dependent on the surrounding region as described above (i.e. bright stars or masks).

Consideration of the above properties as well as the surrounding nova region determined the wing radius used for the fit.

If a simultaneous fit was required, additional parameters could also be modified. These include *skip_dist* and *include_dist*, which specify the angular distance from the object of interests centriod in which additional objects can be fit or ignored. These are typically set at 0.25° and 1.0° respectively. Although both parameters can be increased only *include_dist* can be successfully reduced (see Section 5.3.2). On the simultaneous fitting of multiple objects *fix_centroid* will adjust the centroid of the group of objects whilst keeping the relative location of the objects fixed (as implied by the catalogue positions). Using this centroiding can be very important when correcting for pointing errors, which affect all objects in a group in the same way. An additional parameter may also be used called *fit_pattern*. In this case the centroids of all objects in the group are adjusted individually thus changing the relative locations of the objects.

If a nova were seen to pass from one camera to the next the effect of this transition is taken into account using an additional fit parameter called *clean_edge*.

Once an object was fit, bad data (corrupt orbits and low correlation values) were removed. The resulting nova light curves obtained through this process are presented in Section 5.5.

5.5 Nova Light Curves

In total 13 erupting novae were detected and investigated in further detail. The remaining 9 novae were not clearly detected due to several effects. Many of these novae have low ($\text{mag} \sim 7 - 9$) peak magnitudes making detection difficult, some were missed due to technical difficulties with the imager itself, or due to transient stray light from the Sun and/or planets (e.g. the U Sco 2010 outburst, Schaefer, 2010, was missed due to its location within the 20° mask of the Sun), finally a few novae were located in such densely populated regions that obtaining accurate photometry of the object was impossible.

Four of the 13 novae detected produced highly detailed nova light curves. These four uniquely detailed light curves are discussed in Section 5.5.1 and are the subject of Hounsell et al. (2010a,b). The additional 9 novae detected are discussed in Section 5.5.2. With the outburst of T Pyxidis in 2011 (see Hounsell et al., 2011b) this object was then added to the SMEI list of novae and investigated in detail, the results of which are presented in Section 5.5.1.

5.5.1 Light Curves: First Class Data

The light curves presented in this section are unprecedented in their detail and present data on phases that previously were both poorly covered observationally, and are poorly understood. Table 5.1 summarises the main findings.

RS Ophiuchi

RS Ophiuchi is a recurrent nova (see Section 1.5) whose latest outburst was first observed by Narumi et al. (2006) on 2006 February 12.83 UT (MJD 53778.83) at $m_V = 4.5$. The 2006 outburst was observed in great detail across the electromagnetic spectrum (see A. Evans, M. F. Bode, T. J. O'Brien, & M. J. Darnley, 2008, and references therein). Of particular note was the interaction of the high velocity ejecta with

the pre-existing wind of the red giant in the system, leading to the rapid establishment of strong shocks (e.g. Bode et al., 2006).

RS Oph showed a very rapid rise to maximum in the SMEI data (see Figure 5.8), increasing in brightness by 2.3 magnitudes in 0.9 days. This value is measured using the first reliable detection of the nova on its rise to maximum and the peak magnitude itself. The SMEI light curve shows clear evidence of a pre-maximum halt (see inset in Figure 5.8) starting 2006 February 12.31 UT (MJD 53778.31) and lasting just a few hours with a mean $m_{\text{SMEI}} = 4.50 \pm 0.05$ (defined as the mean magnitude over the duration of the halt, quoted error is the RMS scatter). The duration of the halt (for RS Oph, V598 Pup, and KT Eri, see below) is taken to be the time between the first and third change in the gradient of the rising light curve and is appropriate for the speed of the nova as proposed by e.g. Payne-Gaposchkin (1964). Note that this halt (and subsequent ones in other novae - see below) looks like a temporary reversal in the light curve and may be related to a change in mass loss rate this however, needs to be investigated in detail. Peak brightness of the nova was reached on 2006 February 12.94 (MJD 53778.94) ± 0.04 UT at $m_{\text{SMEI}} = 3.87 \pm 0.01$. It is noted that the peak magnitude derived from the SMEI data is over half a magnitude brighter than ground-based estimates. This discrepancy may be caused by a slight over-subtraction within the fit of the SMEI PSF or the fact that the ground-based observations are visual magnitude estimates, compared to the broader band of SMEI, or both. After peak, the nova declined very rapidly with $t_2 = 7.9$ days (see Section 1.4.1)

RS Oph remains the only nova to be detected at outburst with the *Swift* Burst Alert Telescope (BAT; Bode et al., 2006; Senziani et al., 2008). It was clearly detected in the 14-25 keV channel for ~ 5 days around discovery, with a marginal detection in the 25-50 keV band at this time. Figure 5.8 shows the BAT 14-25 keV results over-plotted on the SMEI data. It is apparent that the initial rise of the optical and hard X-ray is coincident within the temporal uncertainty. As the hard X-ray emission is thought to arise from the interaction of the fastest moving ejecta with the pre-outburst wind of the red giant (Bode et al., 2006), the coincidence of the onset of the outburst as seen in the optical with that found in the BAT data implies that significant high velocity mass

loss occurs very early in the outburst itself. As the optical peak may indicate the time of highest mass loss rate from the surface of the WD, one might reasonably expect $[t_{\max}]_{\text{BAT}} \gtrsim [t_{\max}]_{\text{SMEI}}$ as appears to be the case here.

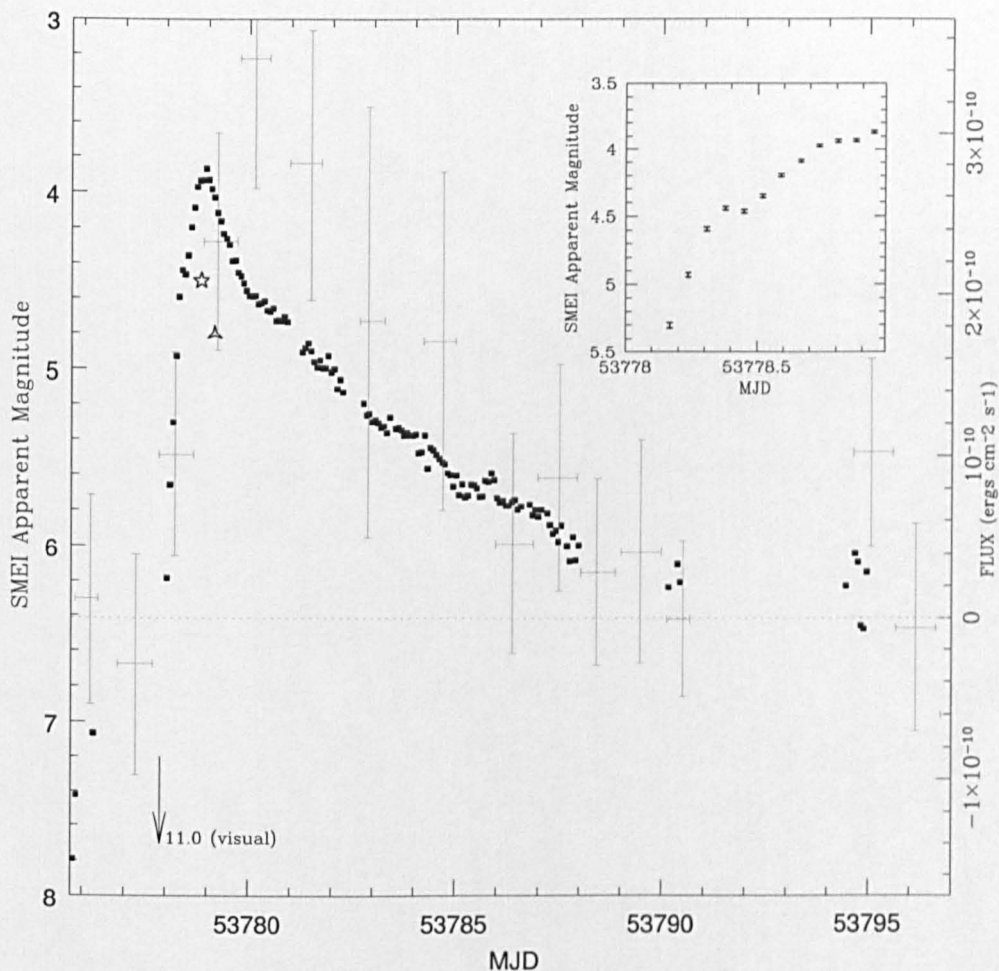


Figure 5.8: SMEI light curve of RS Oph (black squares) in terms of “SMEI magnitude” (see Buffington et al., 2007) versus time (left-hand y-axis). Over-plotted (grey) are the *Swift* BAT 14–25 keV data from Bode et al. (2006, right-hand y-axis), the grey dashed line indicates zero flux on the right-hand y-axis. The star represents the discovery magnitude of the nova taken from Narumi et al. (2006). The triangle is the peak magnitude listed by the AAVSO²⁰. The apparent discrepancy between ground-based and SMEI magnitudes is discussed in Section 5.5.1. An arrow is used to indicate the latest observed magnitude of the nova before rise, according to the AFOEV²¹ data set. The inset shows the rising portion of the light curve with an expanded time scale.

²⁰American Association of Variable Star Observers - <http://mira.aavso.org/tmp/data5167.txt>

²¹Association Francaise des Observateurs d’Etoiles Variables - <http://cdsarc.u-strasbg.fr/aftev/oph/rs>

V1280 Scorpii

V1280 Sco was discovered in outburst by Yamaoka et al. (2007b) on 2007 February 4.86 UT (MJD 54135.86) at an unfiltered magnitude of 9.9. Twelve days later it reached visual maximum quoted as $m_V = 3.79$ (Munari et al., 2007b). Although the initial rise of the nova is lost in the SMEI data, due to transient stray light from the Sun, and from Jupiter as it moves across the sky, Figure 5.10 shows that the climb to maximum on 2007 February 16th is very slow with the first recorded SMEI point occurring on 2007 February 13.61 UT (MJD 54144.61) at $m_{\text{SMEI}} = 6.19 \pm 0.03$. It takes 2.54 days for the light curve to rise by approximately two magnitudes to peak. The slow rise of the nova is consistent with the 12 day rise noted by various authors (e.g. Chesneau et al., 2008).

Canonically, the supposed pre-maximum halt is defined as occurring one to two magnitudes below peak optical brightness (see Warner, 2008, and references therein). With this in mind there appears to be a halt before the first maximum of V1280 Sco lasting 0.42 days (duration of halt is defined here as the time between the first and second change in gradient of the rising light curve) with a mean $m_{\text{SMEI}} = 5.231 \pm 0.003$. However, there is evidence of an earlier plateau in the nova light curve, but which is not within the magnitude range expected. Peak visual magnitude occurred on 2007 February 16.15 (MJD 54147.15) ± 0.04 UT with $m_{\text{SMEI}} = 4.00 \pm 0.01$ (see Figure 5.10). The nova then experienced two major episodes of re-brightening peaking at February 17.34 (MJD 54148.34) ± 0.04 UT and 19.18 (MJD 54150.18) ± 0.04 UT, with $m_{\text{SMEI}} = 4.23 \pm 0.01$ and 4.13 ± 0.01 respectively. The existing published visual light curves lack such fine detail (see Figure 5.9 taken from Das et al., 2008). Data from the “ π of the Sky”²² project are superimposed in Figure 5.10. These are white light unfiltered magnitudes, confirming the SMEI calibration and following the general trend of the light curve. Note that the discrepancy between the last “ π of the Sky” data point and the SMEI data is probably due to the fact that at this point the detection is being made well below SMEI’s limiting magnitude threshold. Overall, the SMEI data contain the best known pre-maximum values for the nova from a homogeneous

²²<http://grb.fuw.edu.pl/pi/index.html>

observational set and illustrate the current lack of coverage of this phase of evolution.

The subsequent decay of the SMEI light curve is marked by a distinct change in decline rate in visual light on 2007 February 26.4 (MJD 54157.37) ± 0.1 UT (see inset in Figure 5.10) at $m_{\text{SMEI}} = 5.14 \pm 0.02$. The overall decline that then ensues is thought to be the effect of rapid formation of dust in the nova ejecta (Das et al., 2008; Rudy et al., 2007).

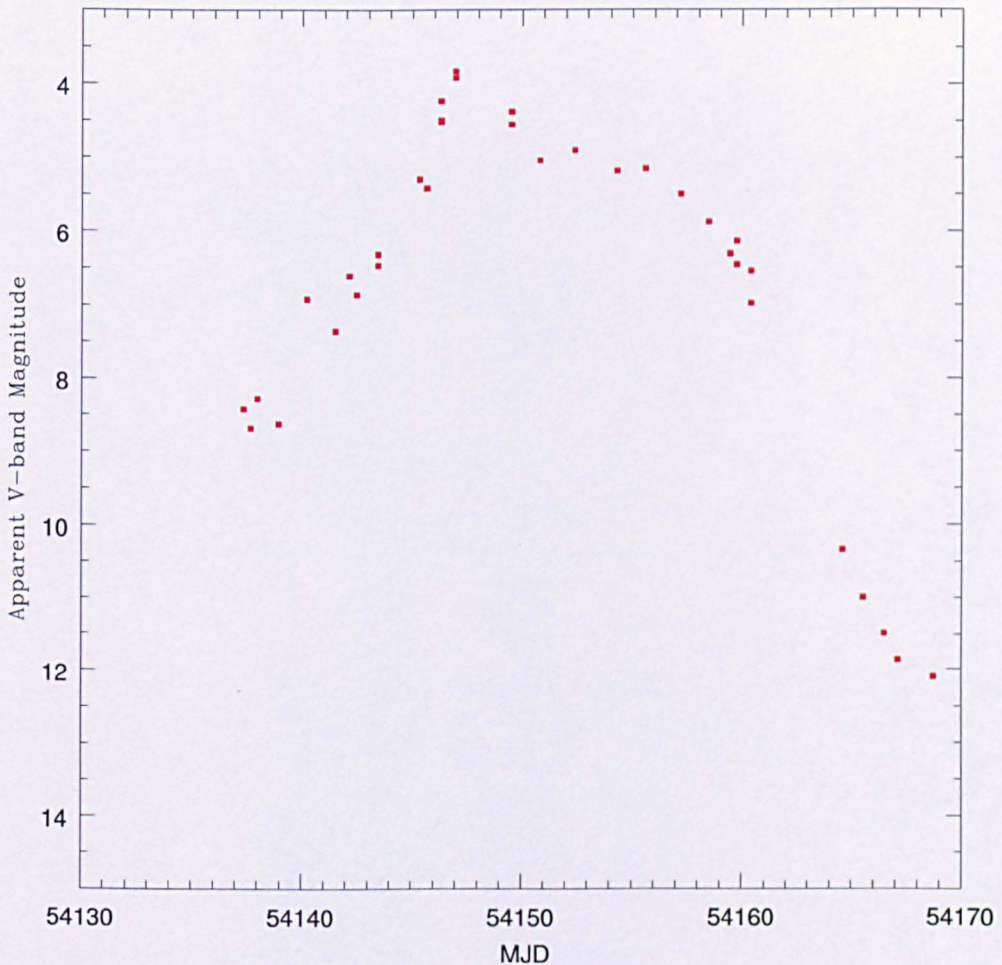


Figure 5.9: Ground-based early V-band light curve of V1280 Sco. Data taken from the Das et al. (2008) light curve which was in turn created using data from the AFEOV.

The change in slope on February 26.4 UT may be identified with the onset of large-scale dust formation. Chesneau et al. (2008) note that the first unambiguous evidence

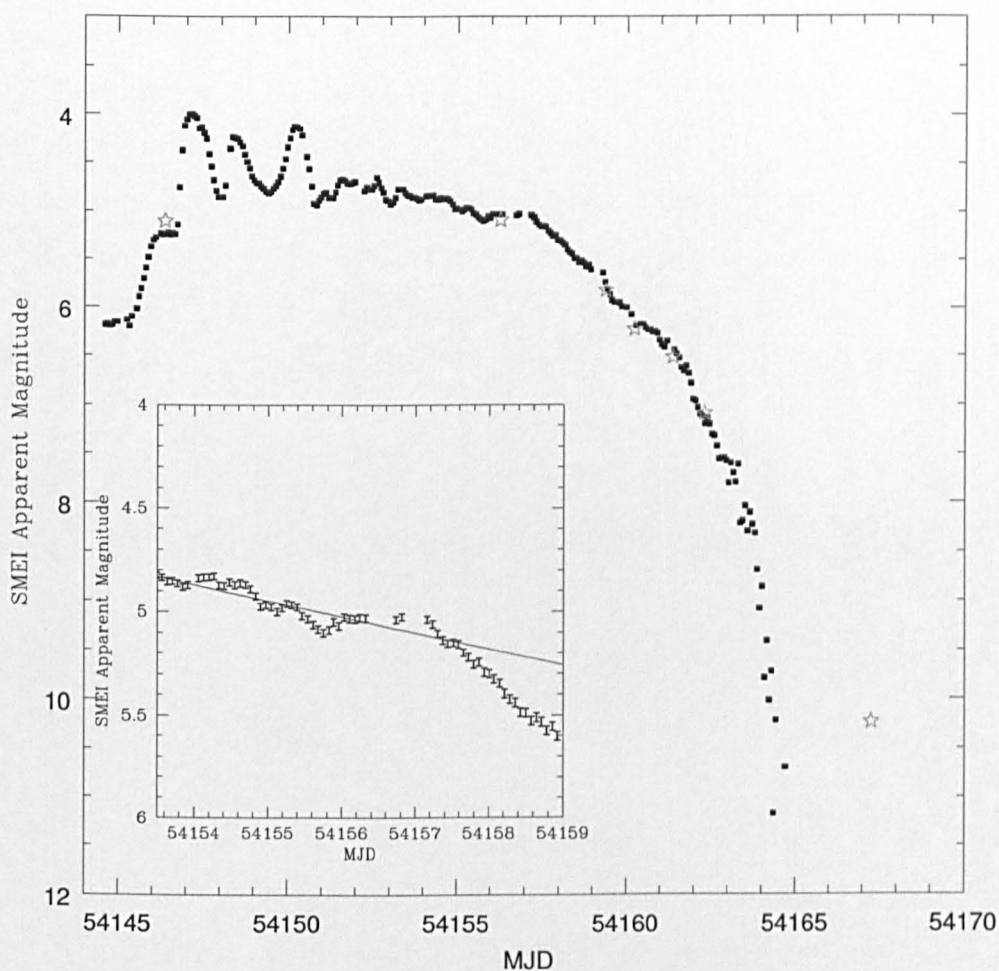


Figure 5.10: SMEI light curve of V1280 Sco (black squares), superimposed (gray stars) are data from the “ π of the Sky” project. The inset shows the region around the light curve break which is associated with the onset of dust formation. The solid line shows the fit to the pre-break SMEI light curve and its extrapolation. Note that the discrepancy between the last “ π of the Sky” data point and the SMEI data is probably due to the fact that at this point the detection is being made well below SMEI’s limiting magnitude threshold.

of dust emission dominating the near-infrared spectra is on March 7th, but they suggest that the absence of obvious emission in the spectrum of February 26.97 UT (MJD 54157.97) does not rule out the presence even at that stage of an extended optically thin dust shell. Certainly, the change in light curve slope on February 26.4 UT is a subtle effect that can only be derived from photometry with the temporal sampling and small intrinsic scatter of the SMEI data. As noted, the rise to maximum light was very

slow. From consideration of infrared photometry of the fireball expansion phase, Das et al. (2008) find that the outburst commenced ~ 2.35 days before discovery, on 2007 February 2.5 UT (MJD 54133.5). Assuming that extensive mass loss began at this time, from the SMEI results, this gives the condensation time of dust grains from the ejecta as $t_c \sim 24$ days. This time-scale, together with the observed ejection velocity ($\sim 600 \text{ km s}^{-1}$, Das et al., 2008) and an assumed condensation temperature of dust grains ($T_c = 1200\text{K}$, Evans & Rawlings, 2008; Gehrz, 2008) leads to an estimate of the nova's luminosity at this time, assuming the nucleation centres act as black bodies as

$$L_\star = 2.4 \times 10^4 \cdot (t_c/24 \text{ days})^2 \cdot (v_{\text{ej}}/600 \text{ km s}^{-1})^2 \cdot (T_c/1200\text{K})^4 L_\odot. \quad (5.3)$$

Taking this as the Eddington luminosity of the WD (e.g. Gehrz, 2008, Equation 5.4) in turn implies $M_{\text{WD}} = 0.6 M_\odot$.

$$\frac{L_{\text{Edd}}}{L_\odot} = 3.8 \times 10^4 \left(\frac{M_{\text{WD}}}{M_\odot} \right) \quad (5.4)$$

The equilibrium temperature of the nucleation centres may be higher than that of a black body for the same L_\star and distance from the nova, hence M_{WD} is likely to be an upper limit. This compares with the $M_{\text{WD}} = 1$ to $1.25 M_\odot$ estimated by Das et al. (2008) from consideration of the time-scale of mass loss, plus outburst amplitude A , and expansion velocity v_{exp} . These authors admit however that such a high mass estimate is incompatible with what appears spectroscopically to be an explosion on a carbon-oxygen WD, for which the estimate made here of M_{WD} would be compatible.

The derived L_\star and a spectrum near maximum light akin to that of an F star (Bolometric Correction ~ 0) gives $M_V = -6.2$. Taking the line-of-sight (interstellar) extinction to be $A_V = 1.2 \pm 0.3$ (Chesneau et al., 2008) and $m_V^{\text{max}} = 4$ yields a distance to the nova of $d = 630 \pm 100 \text{ pc}$, roughly half that derived by Chesneau et al. (2008). A linear extrapolation of the nova light curve is used between 2007 February 20.59 UT (MJD 54151.59) and 26.59 UT (MJD 54157.59) in order to determine t_3 . The data for

the extrapolation are taken after the last re-brightening event, but before the dust break (i.e. removing the influence of dust formation) shown in Figure 5.10. A t_3 value of ~ 34 days is determined, i.e. an estimated decline of 0.1 magnitude per day. From the MMRD relation given in Downes & Duerbeck (2000), $M_V \sim -8$. However, the applicability of the MMRD is questionable in the context of such gross variability around maximum light, followed by a slow and steady decline.

V598 Puppis

V598 Pup was discovered by Read et al. (2007) in the XMM-Newton slew survey on 2007 October 9.0 UT (MJD 54382) as a transient X-ray source, designated XMMSLI J070542.7-381442. It was later identified as a nova by Torres et al. (2007) whilst trying to identify the object's optical counterpart. The peak visual magnitude was noted by Pojmanski et al. (2007) as $m_V \leq 4$ on 2007 June 5.968 UT (MJD 54256.968) (see Figure 5.11).

From the SMEI data shown in Figure 5.12, the rise to maximum is found to be very steep with the nova increasing 4.1 magnitudes within 2.8 days. A pre-maximum halt is indicated on 2007 June 3.82 UT (MJD 54254.82) with a mean $m_{\text{SMEI}} = 5.2 \pm 0.1$ and duration a few hours (see inset in Figure 5.12). The nova then rose to its peak visual magnitude of $m_{\text{SMEI}} = 3.46 \pm 0.01$ on 2007 June 6.29 (MJD 54257.29) ± 0.04 UT. Decline from maximum also appears steep. However a section of this decline phase has been missed in the SMEI data due to a failure of the star tracker, causing the spacecraft to assume a Sun-pointing mode. This failure lasted ~ 21 days. An estimate of t_2 using an extrapolated linear fit to the initial decline of the nova (between 2007 June 6.29 [MJD 54257.29] and 8.33 [MJD 54259.33] UT) yields $t_2 = 4.3$ days.

It should be noted that V598 Pup is located close ($\sim 0.1^\circ$) to HD 54153, a 6th magnitude star. In order to reduce the star's effect on the nova, a forced simultaneous fit was conducted. This procedure is ideally suitable for larger stellar separations (between $0.25^\circ - 1.0^\circ$, see Section 5.3.2 for further details) and thus cannot consistently remove the contaminating star especially as the nova starts to fade. The variability seen in

the light curve of Figure 5.12 at later times ($\text{MJD} \gtrsim 54280$) is therefore most likely due to contamination from the nearby bright star and problems occurring in the fitting procedure.

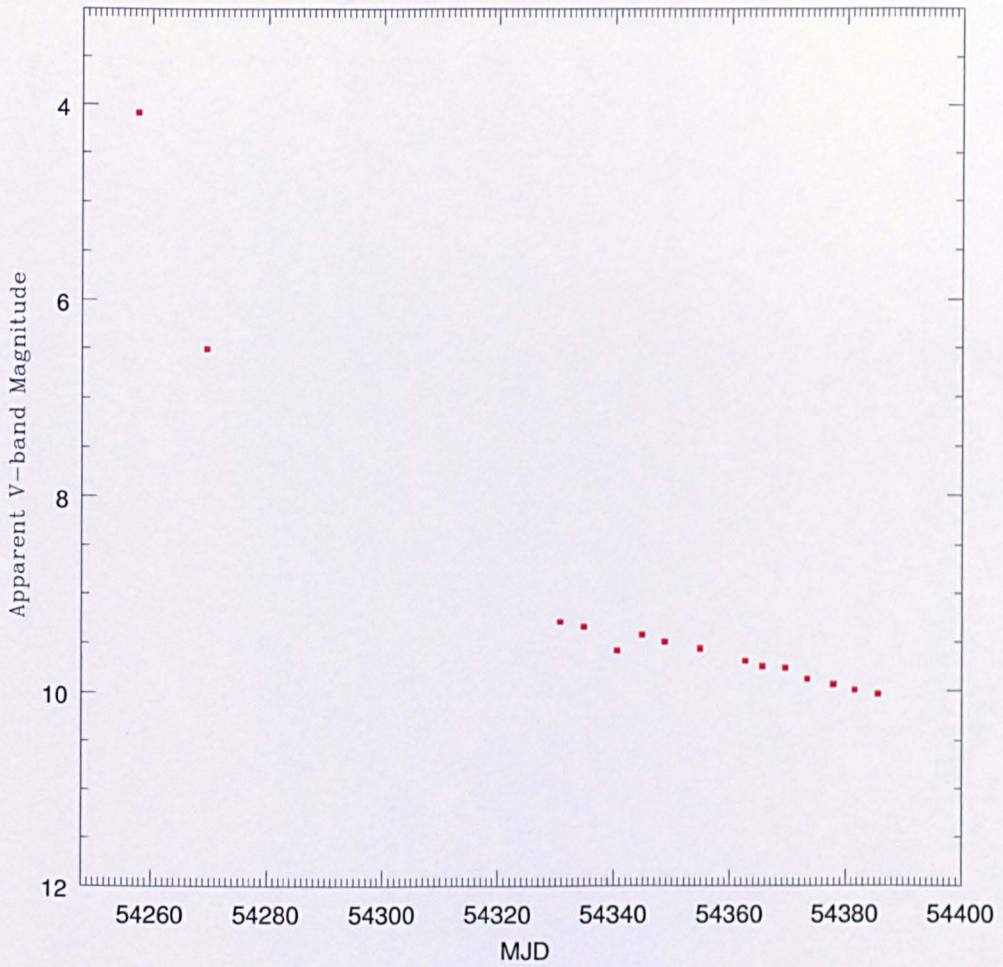


Figure 5.11: Ground-based V-band light curve of V598 Pup reproduced from data in Pojmanski et al. (2007).

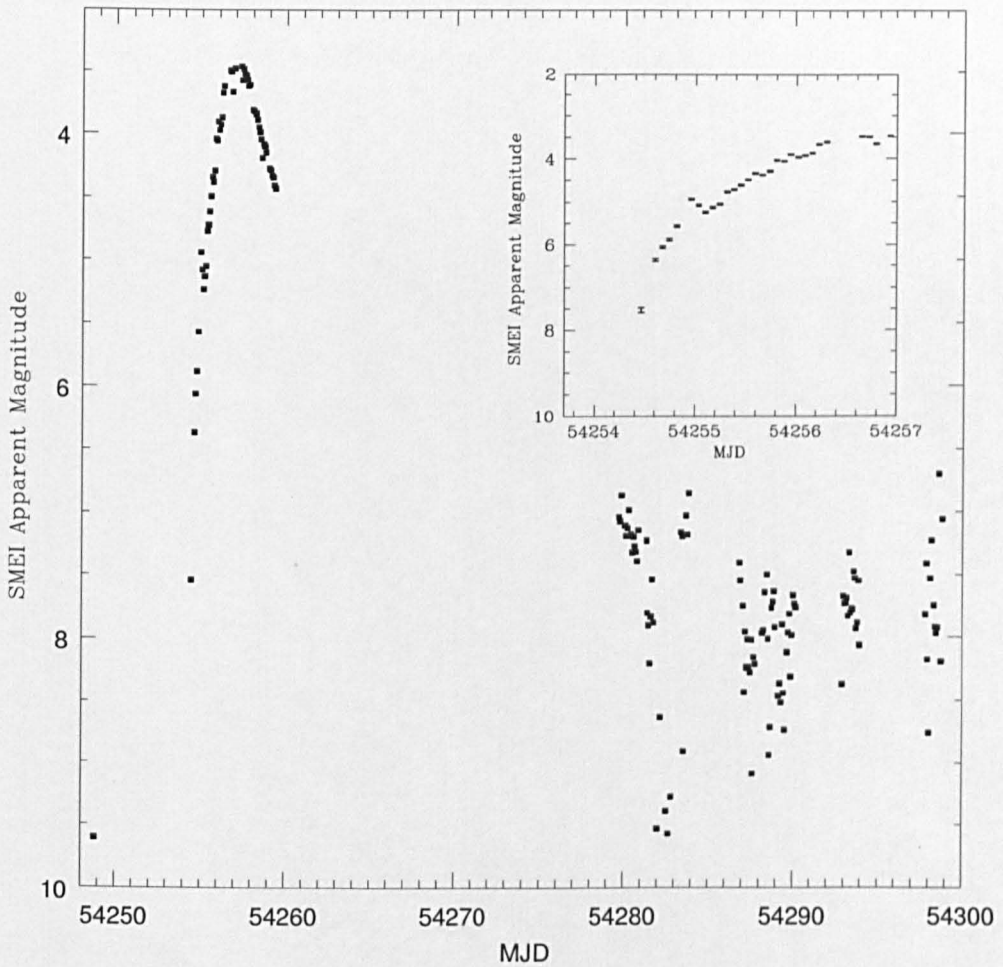


Figure 5.12: SMEI light curve of V598 Pup. The inset shows the rising portion of the light curve with an expanded time scale. Note that the variation of the light curve at $\text{MJD} \gtrsim 54280$ is most likely due to contamination from a bright neighbouring star and problems within the fitting procedure; see Section 5.5.1 for further details.

KT Eridani

KT Eri was discovered on 2009 November 25.536 UT (MJD 55160.536) by Itagaki (2009) with an unfiltered CCD magnitude of 8.1. Like V598 Pup, KT Eri was missed at peak brightness and only discovered a considerable time later. Its outburst was found in pre-discovery images with a peak visual magnitude given as 5.4 on 2009 November 14.63 UT (MJD 55149.63, Yamaoka et al., 2009, see Figure 5.13 for AAVSO light curve).

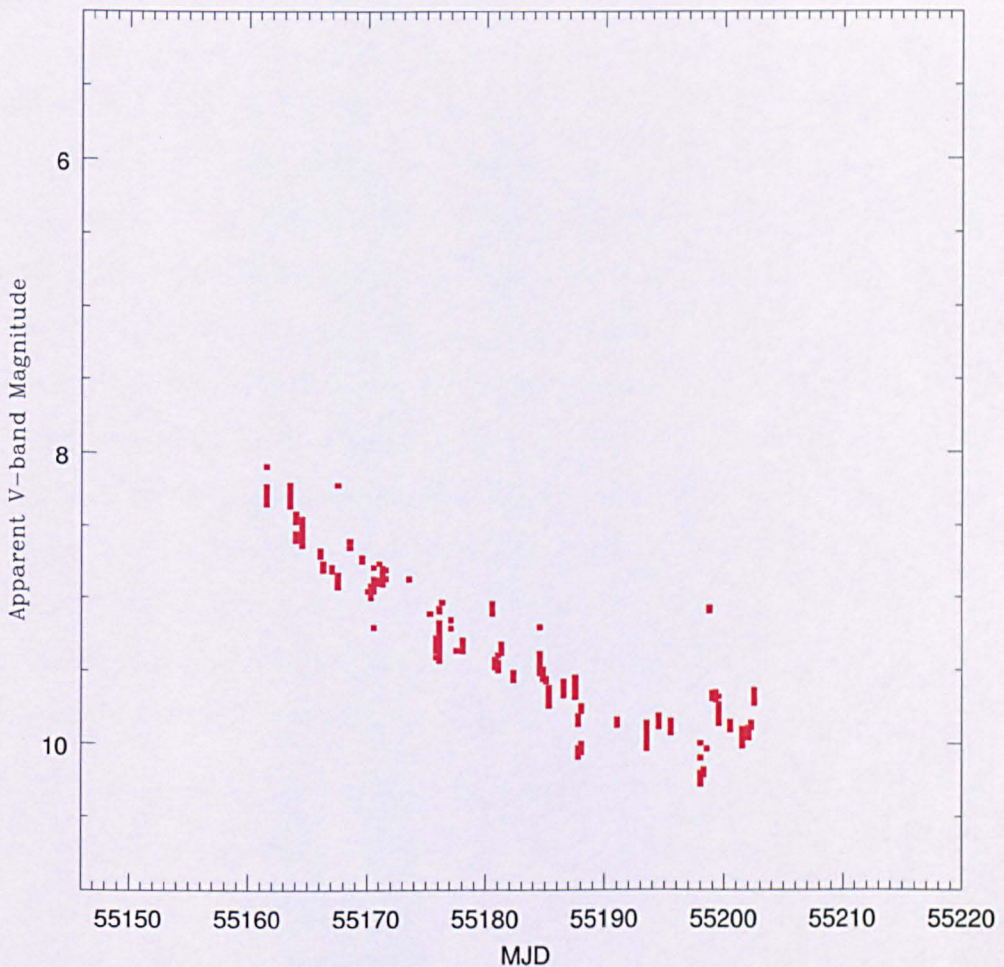


Figure 5.13: Light curve of KT Eri using V-band data taken from the AAVSO.

Pre- and post-outburst data for this object have been obtained by SMEI (Hounsell et al., 2010b) and the SkyCamT (SCT) instrument which is mounted to parallel-point with

the main beam of the LT (Steele et al., 2004, see also Section 3.1.2 for further details). The LTSCT camera operates continuously throughout the night, taking a 10 second exposure once per minute in the direction of the main telescope pointing, giving a limiting magnitude of ~ 12 . As with SMEI, the data are unfiltered (i.e. white light) and are calibrated with respect to four bright isolated USNO-B stars in the field of view.

The SMEI and LT light curves are shown in Figure 5.14. SMEI data indicate the initial rise of the nova is steep (rising 3.0 magnitudes over 1.6 days) first being clearly detected in outburst on 2009 November 13.12 UT (MJD 55148.12) with $m_{\text{SMEI}} = 8.44 \pm 0.09$. Evidence of a pre-maximum halt occurring on 2009 November 13.83 (MJD 55148.83) ± 0.04 UT with a mean $m_{\text{SMEI}} = 6.04 \pm 0.07$ is given by SMEI with LTSCT observations adding two important points to the coverage of the halt (see inset in Figure 5.14). The duration of this halt is again only a few hours. SMEI observations indicate that the nova reached maximum light on 2009 November 14.67 (MJD 55149.67) ± 0.04 UT with $m_{\text{SMEI}} = 5.42 \pm 0.02$. LTSCT observations bracket the peak seen with SMEI. The nova then subsequently declined rapidly with $t_2 = 6.6$ days confirming KT Eri as a very fast nova (Warner, 2008). The last reliable SMEI detection of the nova occurred on 2009 November 27.23 (MJD 55162.23) ± 0.04 UT at $m_{\text{SMEI}} = 8.3 \pm 0.1$. LTSCT observations extend the optical coverage of the light curve until 2010 January 19.85 UT (MJD 55215.85). The LTSCT data also confirm the calibration of the SMEI photometry and general trends in the resulting light curve. Similar results are also found within “ π of the Sky” data.

KT Eri has been detected as a radio source (O’Brien et al., 2010) and a luminous soft X-ray source (Bode et al., 2010). Attention has been drawn to the similarities of its optical spectral and X-ray evolution to that of the recurrent nova LMC 2009a (Bode et al., 2010). Its outburst has also been associated with a highly variable stellar progenitor at mag ~ 15 showing evidence for pre-outburst circumstellar material and with similarities to the soft X-ray transient CSS081007:030559+054715 (Drake et al., 2009). It is noted that the very fast decline and relatively low amplitude of the outburst ($A \sim 10$ mags) place KT Eri in an anomalous position on the A vs speed class diagram

for CNe (e.g. Warner, 2008), but much more in line with that for recurrent novae such as U Sco (Schaefer, 2010).

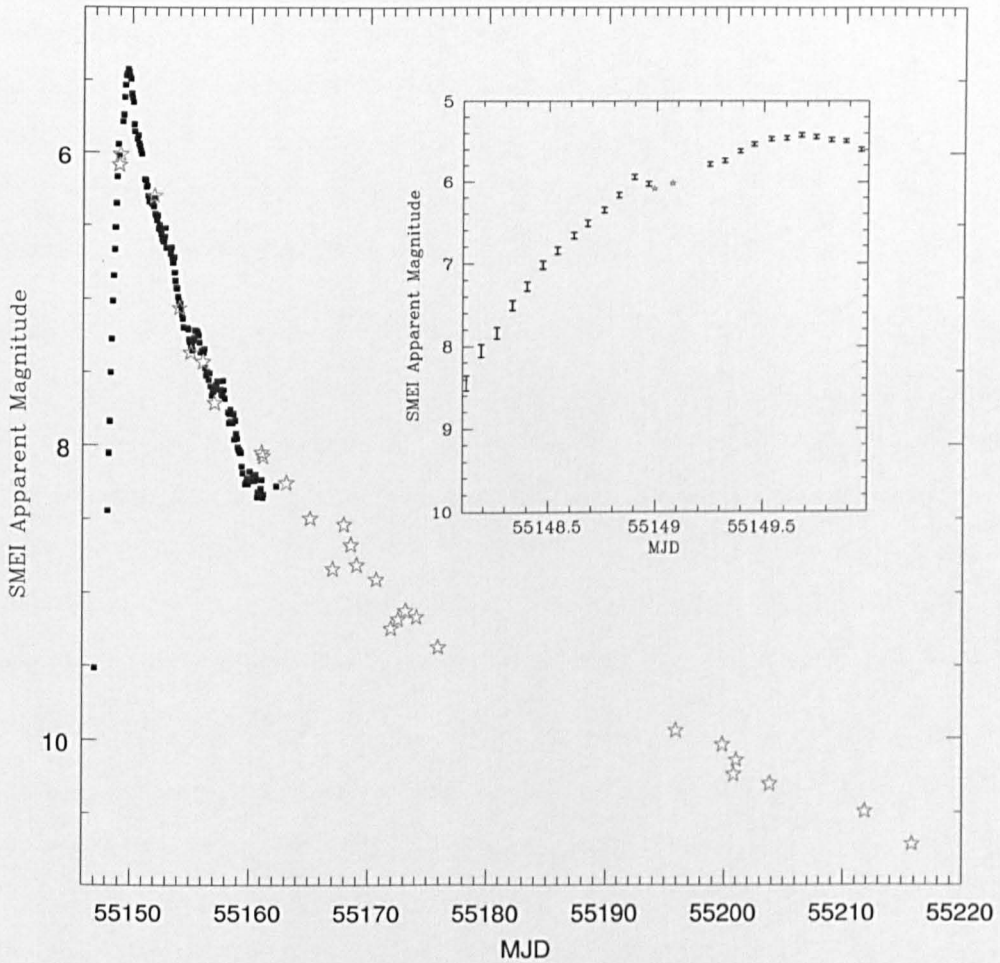


Figure 5.14: SMEI (black squares) light curve of KT Eri with Liverpool Telescope SkyCamT data superimposed (grey stars - see Section 5.5.1 for details). SMEI and LTSCCT data seem to be in good agreement with each other confirming statements made within Buffington et al. (2007). The inset shows the rising portion of the light curve with an expanded time scale

T Pyxidis

The 2011 outburst of T Pyx was discovered at a visual magnitude of 13.0 on 2011 April 14.29 UT (MJD 55665.29; taken as $t = 0$ days; Waagan et al., 2011). This is the first outburst of T Pyx since 1966 December 7th, with previous recorded outbursts in

1890, 1902, 1920, and 1944.

Swift XRT observations of the nova began on 2011 April 14.59 UT (MJD 55665.59; $t = 0.3$ days) with initial data indicating a soft spectrum (Kuulkers et al., 2011). Additional spectra of the nova were subsequently obtained by the Southern African Large Telescope (SALT) using the RSS spectrograph on April 15.89 UT (MJD 55666.89; $t = 1.6$ days; Nordsieck & Shara, 2011), and a detection made in the radio using the EVLA on May 1.10 UT (MJD 55682.10; $t = 16.8$ days; Chomiuk et al., 2011). The mean reddening of the object is given as $E_{B-V} = 0.44 \pm 0.18$ (Shore et al., 2011).

The first reliable detection of the nova outburst by SMEI occurred at the end of the rapid rise seen in AAVSO data, at $m_{\text{SMEI}} = 8.80 \pm 0.10$ on 2011 April 15.84 UT (MJD 55666.84; $t = 1.6$ days, see Figure 5.15). Following the initial SMEI detection, the light curve rose very slowly over the following 12 days, reaching an average magnitude of approximately 7.98 on 2011 April 27th (MJD 55678.34; $t = 13.1$ days). During this almost "plateau" phase, quasi-periodic variations were observed, with peak-to-peak times varying between one and two days. The amplitudes of these variations ranged between 0.35 and 0.50 mags.

Following this plateau phase there was a gap in the SMEI data (due to instrumental problems) lasting ~ 1.4 days, after which the light curve was seen to rise more steeply to $m_{\text{SMEI}} = 6.88 \pm 0.04$ on 2011 May 5.31 UT (MJD 55686.31; $t = 21.0$ days). It subsequently declined to $m_{\text{SMEI}} = 7.43 \pm 0.05$ on 2011 May 8.35 UT (MJD 55689.35; $t = 24.1$ days) and then rose again to $m_{\text{SMEI}} = 6.78 \pm 0.04$ on 2011 May 10.53 UT (MJD 55691.53; $t = 26.2$ days). The amplitude of these variations ranged between 0.55 and 0.65 magnitudes. A further rise occurred after the latter peak where the nova reached an optical peak of $m_{\text{SMEI}} = 6.33 \pm 0.03$ on 2011 May 12.23 (MJD 55693.23; $t = 27.9$ days). This peak occurred in conjunction with the predicted peak presented in the nova light curve template of Schaefer (2010), based on the 1966 observation.

The variations seen in the SMEI light curve during its rise are similar to those found by Schaefer (2010) who reported "rapid" oscillations in the 1966 outburst light curve (Landolt, 1970) with amplitudes of approximately 0.5 to 1.0 magnitudes, on a time-

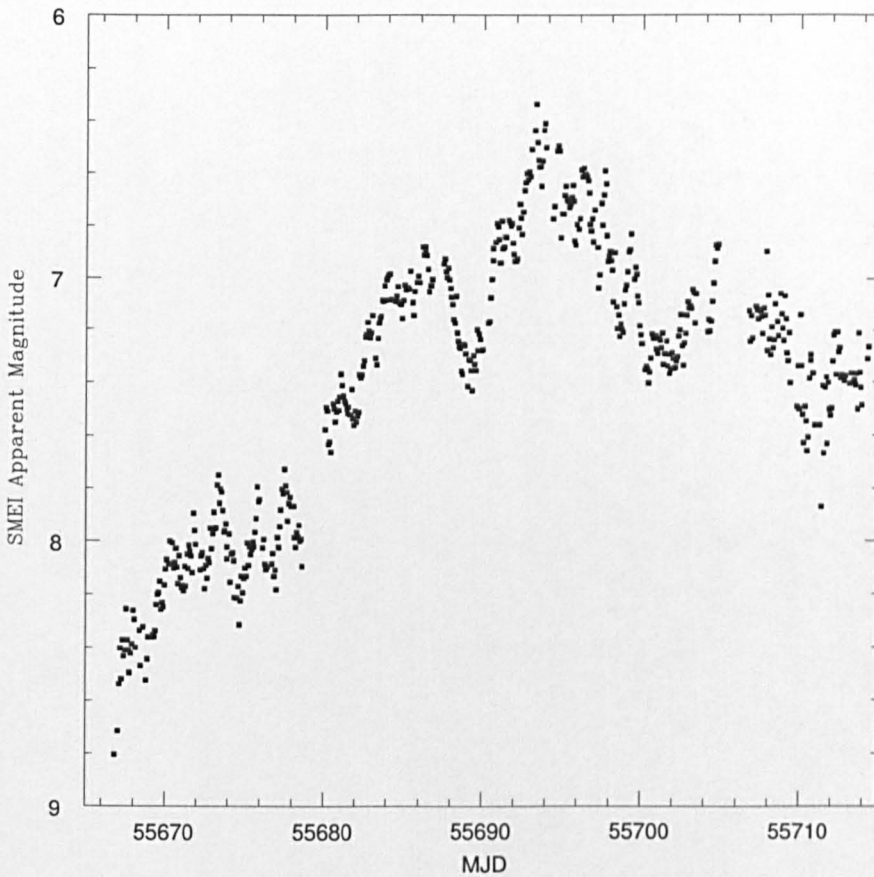


Figure 5.15: SMEI light curve of T Pyx. The light curve clearly shows oscillations and light curve ends as the nova approaches the Sun-wards exclusion zone (see Section 5.2 for further details).

scale of about a day. The oscillations within the SMEI data were studied in detail using Starlink's *PERIOD*²³ package. Periods were determined using a classical discrete Fourier Transform on the data which sums the mean-square amplitude of the results to form a power spectrum. A period range between 0.04 - 100 days was explored and instrumental aliases considered within the analysis using a data window technique. The data window depends on the manner in which the sampling of the signal was performed and does not depend on the signal itself. The lower plot of Figure 5.16 indicates several possible periods with the most dominant being just under two days. However, the presence of several other peaks around the 0.5 day region means that no

²³Information on PERIOD may be found at <http://www.starlink.rl.ac.uk/docs/sun167.htx/sun167.html>

clear period may be derived.

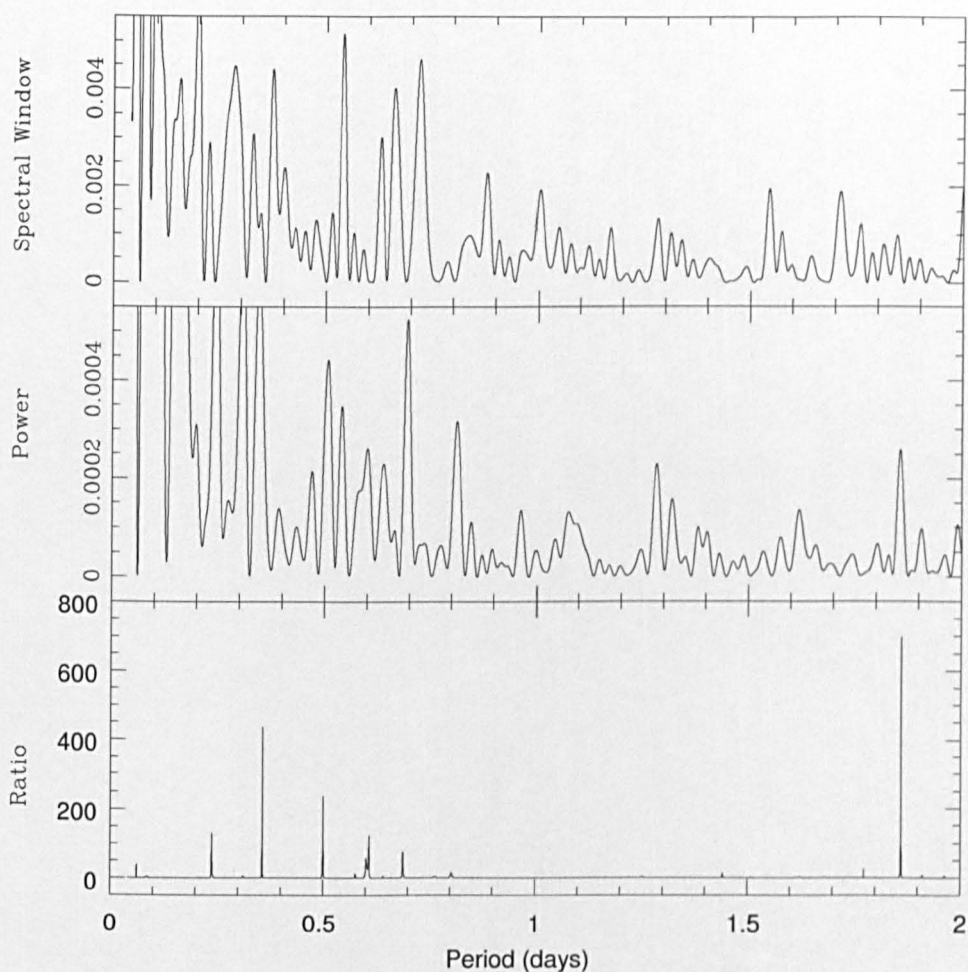


Figure 5.16: Period determination of T Pyx using Fourier analysis. Data windowing results (top), power spectrum result (middle), and ratio of power spectrum to data window (bottom). The bottom plot indicates that there is a period under half a day and another under two days.

The last reliable detection of the nova by SMEI was at $m_{\text{SMEI}} = 7.26 \pm 0.05$ on 2011 June 2.32 UT (MJD 55714.32; $t = 49.03$ days). After this point the nova approached the Sun-mask exclusion zone and further detection proved unreliable and then impossible as it entered the masked region. This has prevented the calculation of a t_2 time. Due to the nature of the light curve it is also difficult to determine the existence of a pre-maximum halt and thus such data are not provided within Table 5.1.

Table 5.1: Derived light curve parameters.

Name	Onset of Outburst yyyy/mm/dd ± 0.04 days	Time of Maximum yyyy/mm/dd ± 0.04 days	Peak SMEI magnitude	t_2 (days)	t_3 (days)	Pre-max halt du- ration (days) ^{Ψ}	Pre-max halt mean magni- tude	Δm_{SMEI} from halt to peak ^{ϕ}	Δt from halt to peak (days)	wing radius (deg)
RS Oph	2006/02/12.03	2006/02/12.94	3.87 ± 0.01	7.9	-	0.14	4.50 ± 0.05	0.63	0.49	1.25
V1280 Sco	-	2007/02/16.15	4.00 ± 0.01	21.3 [†]	34.3 [†]	0.42	5.231 ± 0.003	1.23	0.49	1.25
V598 Pup	2007/06/3.47	2007/06/06.29	3.46 ± 0.01	4.3 [°]	-	0.28	5.2 ± 0.1	1.74	2.19	1.4
KT Eri	2009/11/13.12	2009/11/14.67	5.42 ± 0.02	6.6	13.6*	0.14	6.04 ± 0.07	0.63	0.71	1.25
T Pyx	2011/04/15.84	2011/05/12.23	6.33 ± 0.03	-	-	-	-	-	-	1.4

^{Ψ} The duration of the halt is taken to be the time between the first and third change in the gradient of the rising light curve for RS Oph, V598 Pup and KT Eri. With V1280 Sco it is taken to be the time between the first and second change in gradient of the rising light curve.

^{ϕ} Δm from halt to peak is calculated using the mean magnitude of the pre-maximum halt

[†]Using an extrapolation ignoring dust extinction (see text for details)

[°]Using a linear extrapolation of the initial decline (see text for details)

*Using the extrapolation of SMEI and LT data.

5.5.2 Light Curves: Second Class Data

The light curves presented in this section are much fainter than those given in Section 5.5.1. Many of these objects have peak magnitudes at or around 8th magnitude, below which detection is unreliable. The light curves derived, although more noisy than those of the first class data above, have however provided precise dates for the peak, outburst magnitudes, and in many cases decay time.

All light curves were generated using the extended least-squares fitting routine described in Section 5.3.1 however, data produced for each object were processed in a slightly more automated manner than described in Section 5.4.1. For each nova, light curves were generated using wing radii set to *auto_wing* 1.2, 1.3 and 1.4 respectively. Due to the faintness of each nova and crowding in some areas, simultaneous fitting of the nova and any close bright stars was conducted, along with the fitting of other bright stars within $\sim 1^\circ$ - 2° where appropriate. Via a combination of *cshell* scripts each file was then assessed on several criteria, these are described below.

1. Points must have a correlation coefficient greater than 0.4, those that did were passed to a separate file for further evaluation.
2. Points from the output file of step 1 were then assessed on the combined RA and Dec difference from the nova catalogue position. Only those with a combined difference $\leq 0.1^\circ$ were kept and again written to a separate file. This step was conducted to prevent data points resulting from large jumps in position (caused by centroiding during the fit) being counted. This jump may be caused due to the fitting of a residual from a nearby bright star which may have been poorly subtracted during the multiple fitting routine. If the nova is very faint the residual may be fit rather than the nova, this becomes more of an issue as the nova fades.
3. The output file from step 2 was then assessed on the number of points used within the PSF fitting area. To do this the mean *npsf* value was calculated and an allowance of ± 20 was applied. These points were then written to a final file.

The wing radius for each nova was then chosen based on the final file which possessed

the highest number of “valid” points. Visual inspection of the SMEI images for data within the chosen nova file was then conducted and any bad orbit data removed. The resultant light curves and a general overview of each nova are given below with Table 5.2 summarising the main findings.

V1187 Scorpii

Nova V1187 Sco ($\alpha = 17^{\text{h}}29^{\text{m}}18.^{\text{s}}81$, $\delta = -31^{\circ}46'01''.5$; J2000) was discovered prior to peak at $m_V = 9.9$ on 2004 August 2.07 UT (MJD 53219.07) using data from the All Sky Automated Survey (ASAS)-3 patrol. It subsequently rose to a peak magnitude of $m_V = 7.42$ on 2004 August 3.58 UT (MJD 53220.58 Yamaoka, 2004). The initial decline gives $t_2 = 8.7$ and $t_3 = 15$ days (Lynch et al., 2006), making V1187 Sco a very fast nova. Near-IR spectroscopic observations of the object by (Lynch et al., 2006) indicated the development of a nova explosion on an ONeMg WD which did not form dust before entering its nebular phase. The emission lines found within the spectra were complex, double-peaked profiles. Using the double emission lines of HII, Lynch et al. (2006) modelled the nova ejecta finding a ring or partial sphere-like emitting region. An extinction of $A_V = 4.68 \pm 0.24$ was derived using OI lines in combination with the optical spectra, and with this a distance of at 4.9 ± 0.5 k pc via the MMRD relation.

Using data from the SMEI archive a light curve for Nova V1187 Sco was created (see Figure 5.17). The SMEI data give the peak of the nova as $m_{\text{SMEI}} = 6.87 \pm 0.04$ on 2004 August 3.77 ± 0.04 UT (MJD 53220.77). This is 0.55 magnitudes brighter and 0.19 days later than the peak given in the lower time resolution Yamaoka (2004). The difference in declining brightness between the SMEI light curve and that of the AAVSO data (see Figure 5.17) may be caused by several factors; the first may be due to a difference in band-pass as the SMEI instrument is more sensitive in the *R*-band than the *V*; the second and most likely cause is due to contamination of the data by several bright neighbouring stars, and although simultaneous fitting was conducted along with the fitting of additional bright stars in the larger surrounding region, some

contamination may have still remained. The approximated t_2 time of the SMEI data is ~ 9.4 days. This is similar to results presented in Lynch et al. (2006), and agrees with the very fast nova classification. The SMEI light curve also reveals several oscillations in the data as the nova declines. Due to the faintness of the object and the limitations of the SMEI detection at this range the reality of such oscillations may be questioned.

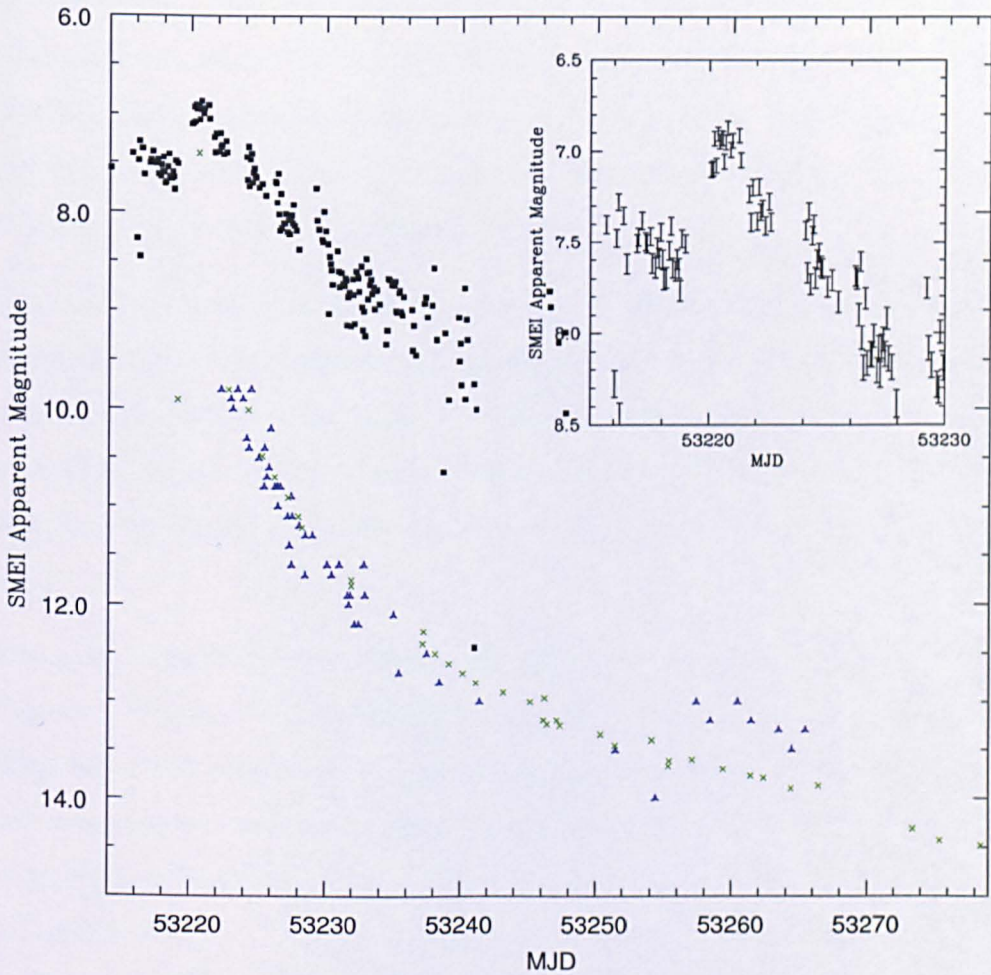


Figure 5.17: SMEI light curve (filled black squares) of V1187 Sco indicating the peak of the nova and its initial decline. The inset shows the SMEI data alone with error bars. The open blue triangles represent *Visual* data and the green crosses *V*-band data; these data are from the AAVSO.

V2467 Cygni

Nova V2467 Cyg ($\alpha = 20^h28^m12^s.47$, $\delta = +41^\circ48'36''.4$; J2000) was discovered by A. Tago at $m_V = 7.4$ (Nakano et al., 2007c) on 2007 March 15.8 UT (MJD 54174.8), it then proceeded to a peak magnitude of 6.7 on 2007 March 16.77 UT (MJD 54175.77). An early spectrum of the nova obtained on 2007 March 16.8 UT (MJD 54175.8) indicated an expansion velocity of $\sim 1200 \text{ km s}^{-1}$ and an Fe II-type nova classification (Munari et al., 2007a). A distance of 1.5 - 4 kpc was calculated for the nova (via MMRD), with an outburst amplitude of $\sim 12 \text{ mag}$ (Steeghs et al., 2007). This distance coincides with the $2.2 \pm 0.2 \text{ kpc}$ distance estimates made by Hachisu & Kato (2010) using a modified version of the MMRD relation.

The transition phase of the object was seen to start in 2007 April after fading approximately 4 magnitudes. Within this phase, six quasi-periodic oscillations were observed with periods from 19 to 25 days and amplitudes of ≈ 0.7 magnitudes. Swierczynski et al. (2010) proposed that the period found within the optical light curve and changes found in the subsequent X-ray detections, could only be explained if the system were an IP.

Using data from the SMEI archive a light curve for nova V2467 Cyg was created (see Figures 5.19 & 5.18). The SMEI data shows the initial rise of the nova which is very steep rising 2.81 magnitudes in approximately 2 days. Within this rise to peak no pre-maximum halt is found mainly due to a lack of data around 8.5 magnitudes. The peak magnitude of the nova is given as $m_{\text{SMEI}} = 6.24 \pm 0.03$ on 2007 March 16.56 ± 0.04 UT (MJD 54175.56), this is 0.46 magnitudes brighter and 0.21 days earlier than the peak given in Nakano et al. (2007c). As indicated in Figure 5.19 the decay of the SMEI light curve coincides best with that of the *R*-band AAVSO data. The approximated t_2 time of the SMEI data is ~ 8 days and classifies the nova as very fast.

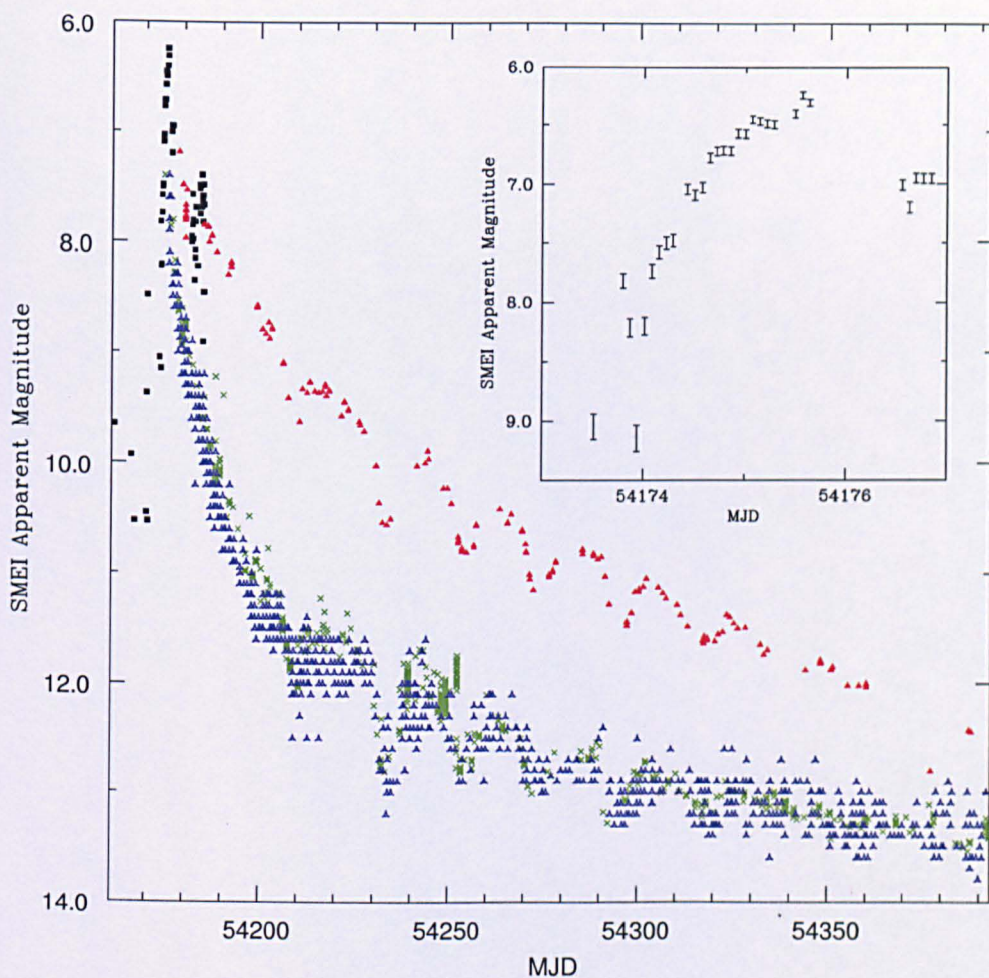


Figure 5.18: SMEI light curve (filled black squares) of V2467 Cyg indicating the peak of the nova and its initial decline. The inset shows the SMEI data alone with error bars. The blue open triangles represent *Visual* data, the green crosses *V*-band data, and the filled red triangles *R*-band data; these data are from the AAVSO.

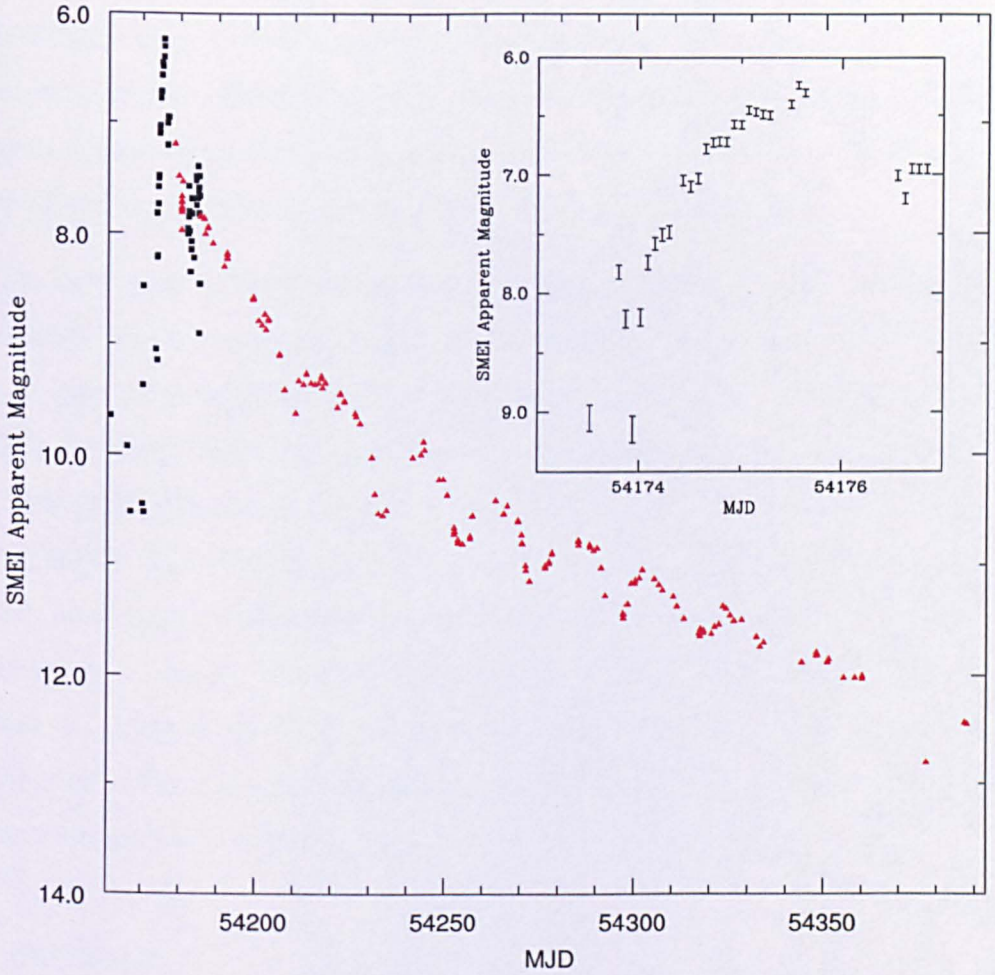


Figure 5.19: SMEI light curve (filled black squares) of V2467 Cyg indicating the peak of the nova and its initial decline. The inset shows the SMEI data alone with error bars. The filled red triangles represent R-band data; these data are from the AAVSO.

V458 Vulpeculae

Nova V458 Vul was discovered in outburst by Nakano et al. (2007a) at a magnitude of 9.5 on 2007 August 8th, reaching its peak visual magnitude a few days later at $V = 8.1 \pm 0.1$ (Wesson et al., 2008). The nova's t_3 time is given as 21 days and it is therefore classified as a fast nova. The decline of the object was disrupted by two re-brightenings, the first occurring 20 days after maximum. Spectra taken after the outburst revealed the nova to be of the hybrid spectral class (Poggiani, 2010), with early spectra being of the Fe II type and later spectra indicating a He/N nova. This nova was seen to occur within a PN and is the subject of Chapter 4.

The light curve of Nova V458 Vul produced by the SMEI data set (see Figure 5.20) indicates that there are two bright peaks separated by a fainter rise. The magnitude and times of each peak are given as $m_{\text{SMEI}} = 7.96 \pm 0.07$ on 007 August 9.79 \pm 0.04 UT (MJD 54321.79), $m_{\text{SMEI}} = 8.30 \pm 0.08$ on 2007 August 11.48 \pm 0.04 UT (MJD 54323.48), and $m_{\text{SMEI}} = 7.94 \pm 0.07$ on 2007 August 13.66 \pm 0.04 UT (MJD 54325.66). The SMEI data are again seen to match *R*-band data better than *V* or *Vis* data (see Figure 5.20). AAVSO data indicate that the peak *V*-band magnitude reached by the nova was $m_V = 8.13 \pm 0.003$ on 2007 August 9.42 UT (MJD 54321.43), the first peak detected by SMEI is therefore seen to coincide well with the *V*-band data. However, SMEI data indicate that this is not the brightest magnitude observed and that the maximum occurs later.

V597 Puppis

Nova V597 Pup was discovered in outburst by Pereira et al. (2007) at a visual magnitude of 7.5 on 2007 November 14th, reaching a peak visual magnitude of $m_V = 6.4$ on 2007 November 14.48 UT (MJD 554418.48). The nova then declined rapidly with a $t_2 = 2.5$ days (Naik et al., 2009), making it one of the fastest novae recorded, with only V838 Her and MU Ser being faster. Naik et al. (2009) classified the nova as a He/N-type with a WD close to the Chandrasekhar limit. A pre-eruption detection is found within the Digitized Sky

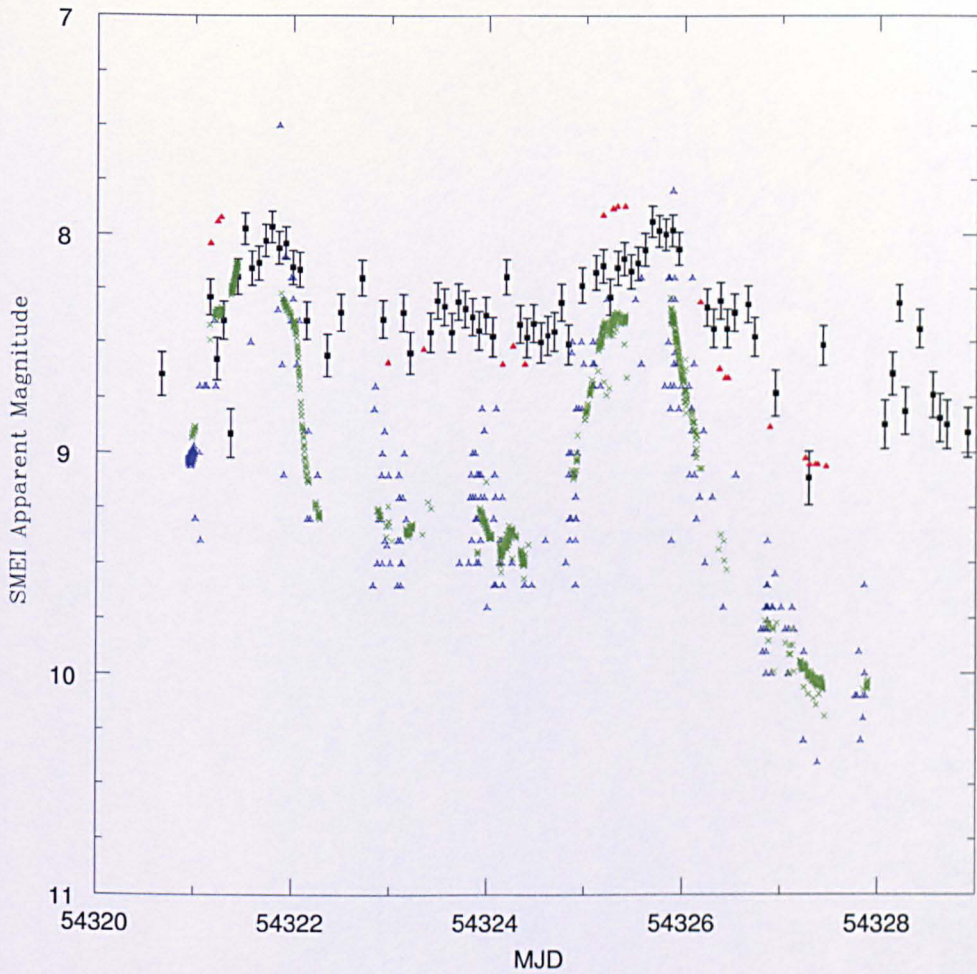


Figure 5.20: SMEI light curve (filled black squares) of V458 Vul indicating the multiple peaks of the nova. The open blue triangles represent *Visual* data, the green crosses *V*-band data, and the filled red triangles *R*-band data; these data are from the AAVSO.

Survey (Pereira et al., 2007) with a source at $V \sim 20$, that coincides with the nova position. Continued monitoring of the object by Warner & Woudt (2009) revealed the nova as an IP in the orbital period gap ($P_{\text{orb}} = 2.67$ hrs), with a rotational period of 8.7 minutes. Observation of the object a year after outburst also revealed the presence of a deep secondary eclipse caused by the passage of the optically thick disc in front of the irradiated side of the secondary star. The object is considered unique as it the first CV found to have this deep eclipse. Using a modified MMRD relation Hachisu & Kato (2010) derived a distance to the object of 16 ± 2 kpc.

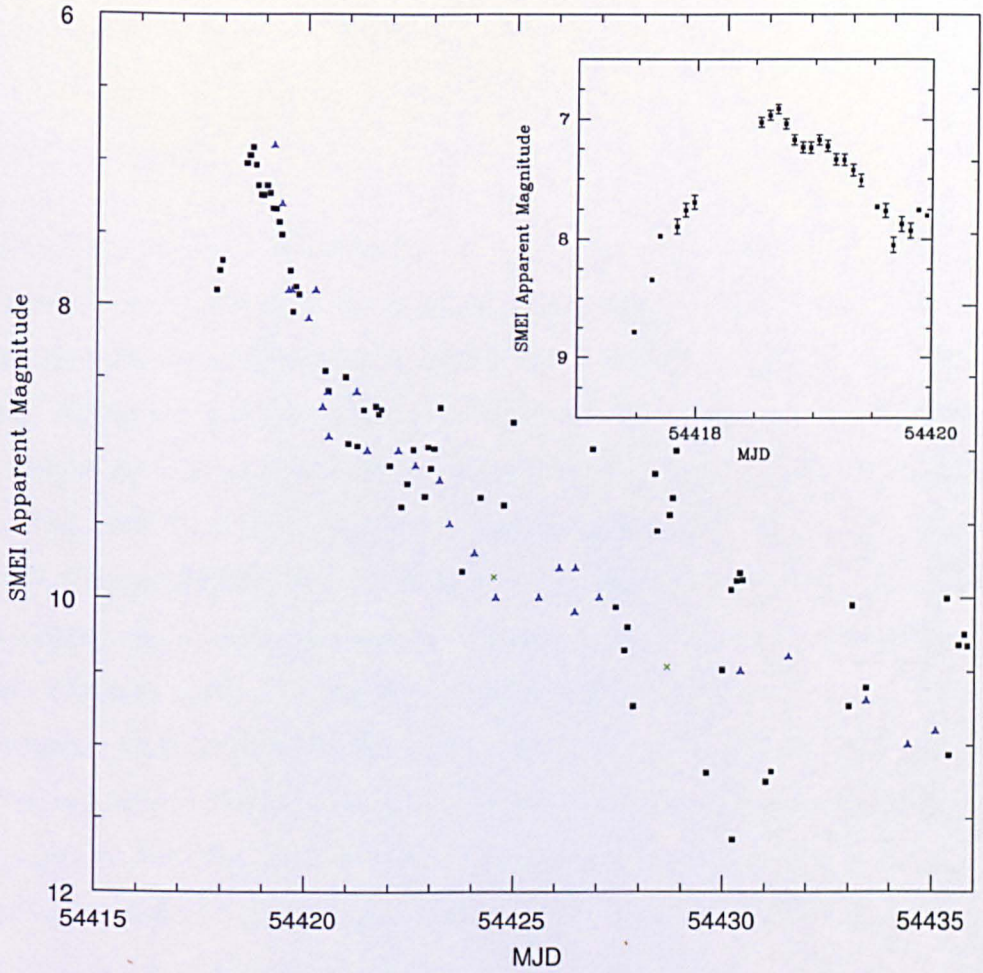


Figure 5.21: SMEI light curve (filled black squares) of V597 Pup. The open blue triangles represent *Visual* data, the green crosses *V*-band data; these data are from the AAVSO. The inset is of the SMEI data only with error bars. Within this inset SMEI data with a correlation coefficient between 0.3-0.4 have been allowed for completeness; these points are given without error bars. These data may show evidence for a pre-maximum halt.

The light curve created using the SMEI data set indicates the latter part of the initial rise, peak, and early decline (see Figure 5.21). Examination of the initial rise data hints at the possibility of a pre-maximum halt, but as some of these data are of a lower correlation coefficient (between 0.3 and 0.4 - due in part to the limiting magnitude of SMEI; slightly larger *npsf* and combined RA and Dec values were also used here) this can not be confirmed. The peak of the light curve is given as $m_{\text{SMEI}} = 6.91 \pm 0.04$ on 2007 November $14.68 \pm \text{UT}$ (MJD 554418.68). The decline of the nova is seen to

be exceptionally fast with a t_2 of 2.3 days; this is similar to that given in Naik et al. (2009), confirming the very fast classification.

V459 Vulpeculae

Nova V459 Vul ($\alpha = 19^h48^m08^s87$, $\delta = +21^\circ15'26''8$; J2000) was discovered independently by Hiroshi Kaneda and Akihiko Tago (Nakano et al., 2007b, 2008a) at an average unfiltered magnitude of 8.7 on 2007 December 25.35 UT (MJD 54459.35) and 2007 December 26.38 UT (MJD 54460.38) respectively. Spectroscopic observation of the object by Yamaoka et al. (2007a) revealed the presence of several Fe II multiplets making V459 Vul an Fe II-type nova. A candidate progenitor with $m_r \sim 20$ was identified in the red POSS-II plates, but no IR counterpart was found within 2MASS. The progenitor magnitude found suggests an outburst amplitude of 12.5 magnitudes (Henden & Munari, 2008). The maximum magnitude of V459 Vul was $m_V = 7.58$ on 2007 December 27.25 (MJD 54461.25) with t_2 and t_3 times given as 18 ± 2 days and 30 ± 2 days respectively (Poggiani, 2010). Using photometric data, Poggiani (2010) went on to obtain an extinction of $A_V = 2.75 \pm 0.38$, an absolute magnitude range between -8.7 and -7.7, and as such a distance range of 2.3 - 5 kpc (MMRD). The absolute magnitude at maximum is related to the mass of the WD (M_{WD} Livio, 1992; Warner, 1995) via Equation 5.5,

$$M_B \sim M_V = -8.3 - 10.0 \cdot \log \frac{M_{WD}}{M_\odot} \quad (5.5)$$

from which a WD mass in the range of 0.9 - 1.1 M_\odot was also derived (Poggiani, 2010).

The light curve obtained by SMEI is given in Figure 5.22. Although the initial rise of the nova appears to be caught by the instrument no pre-maximum halt can be clearly observed as the data are sparse during this time and of poor quality. The peak magnitude of the light curve is given as $m_{SMEI} = 6.51 \pm 0.03$ on 2007 December 27.96 \pm 0.04 UT (MJD 54461.96), and the nova is seen to decline with a $t_2 \sim 16.2$ days. The SMEI peak is 1.07 magnitudes brighter and 0.71 days later than that given in Poggiani (2010) and with the estimated t_2 value being slightly smaller. The difference in t_2

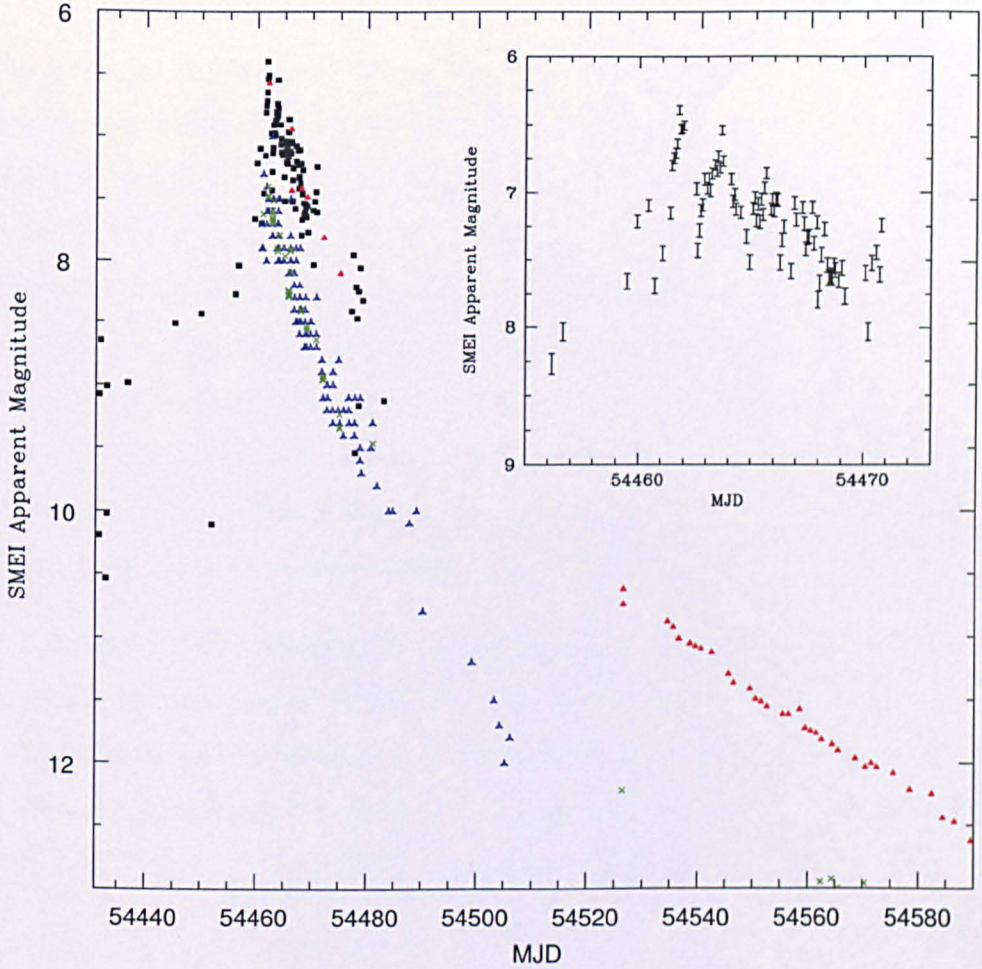


Figure 5.22: SMEI light curve (filled black squares) of V459 Vul. The open blue triangles represent *Visual* data, the green crosses *V*-band data, and the filled red triangles *R*-band data; these data are from the AAVSO. The inset is of the SMEI data only with error bars.

time may be due to the difference in the band-pass, indicated through the matching of SMEI and *R*-band AAVSO data. The SMEI light curve also indicates that there may be several osculations in the decline however, as the data is quite scattered at this point their reality is questionable although the *R*-band data does seem to follow the same oscillatory pattern.

V2491 Cygni

The discovery of Nova V2491 Cyg was presented in (Nakano et al., 2008b). The nova reached maximum at $m_V = 7.45 \pm 0.05$ on 2008 April 11.37 \pm 0.01 UT (MJD 54567.37 Munari et al., 2011b). Spectra indicated that it belongs to the He/N class of novae (Helton et al., 2008b). V2491 Cyg has a rapid optical decline with a $t_2 = 4.8$ days and as such is classified as a very fast nova (Darnley et al., 2011; Munari et al., 2011b). Approximately 15 days after outburst a secondary maxima was observed with an $m_V = 9.49 \pm 0.03$. Based on the spectra of the nova many authors (e.g. Tomov et al., 2008) believe that the object is in fact a RN. Using the interstellar Na I line a reddening of $E_{B-V} = 0.23 \pm 0.01$ was found which led to a distance determination of 14 kpc via the MMRD relation (Munari et al., 2011b).

Unfortunately SMEI was only able to detect a few points around the peak of the nova, these data are presented in Figure 5.23. The peak magnitude is given as $m_{\text{SMEI}} = 7.45 \pm 0.05$ on 2008 April 10.75 UT (MJD 54566.75), slightly earlier than that given in Munari et al. (2011b) but matching quite nicely the unfiltered magnitude of 7.7 on 2008 April 10.8 UT (MJD 54566.8) presented in Nakano et al. (2008b).

QY Muscae

QY Mus ($\alpha = 13^h 16^m 36^s 44$, $\delta = -67^\circ 36' 47'' 8$; J2000) was discovered by Liller et al. (2008), at a magnitude of 8.6 on 2008 September 28.998 UT (MJD 54737.998). The nova then reached a peak unfiltered magnitude of 8.1 on 2008 September 30.40 UT (MJD 54739.40). Nova classification was determined using low-resolution spectra which indicated the presence of a single broad $H\alpha$ emission line.

The SMEI light curve (see Figure 5.24) indicates that the nova reached a peak magnitude of $m_{\text{SMEI}} = 6.85 \pm 0.04$ on 2008 September 29.34 \pm 0.07 UT (MJD 54738.34). The peak magnitude given by SMEI is significantly brighter than the AAVSO data, which again may be due to differences in the V-band sensitivity of the instruments. However, on examination of the location of the nova within the SMEI sky-maps the

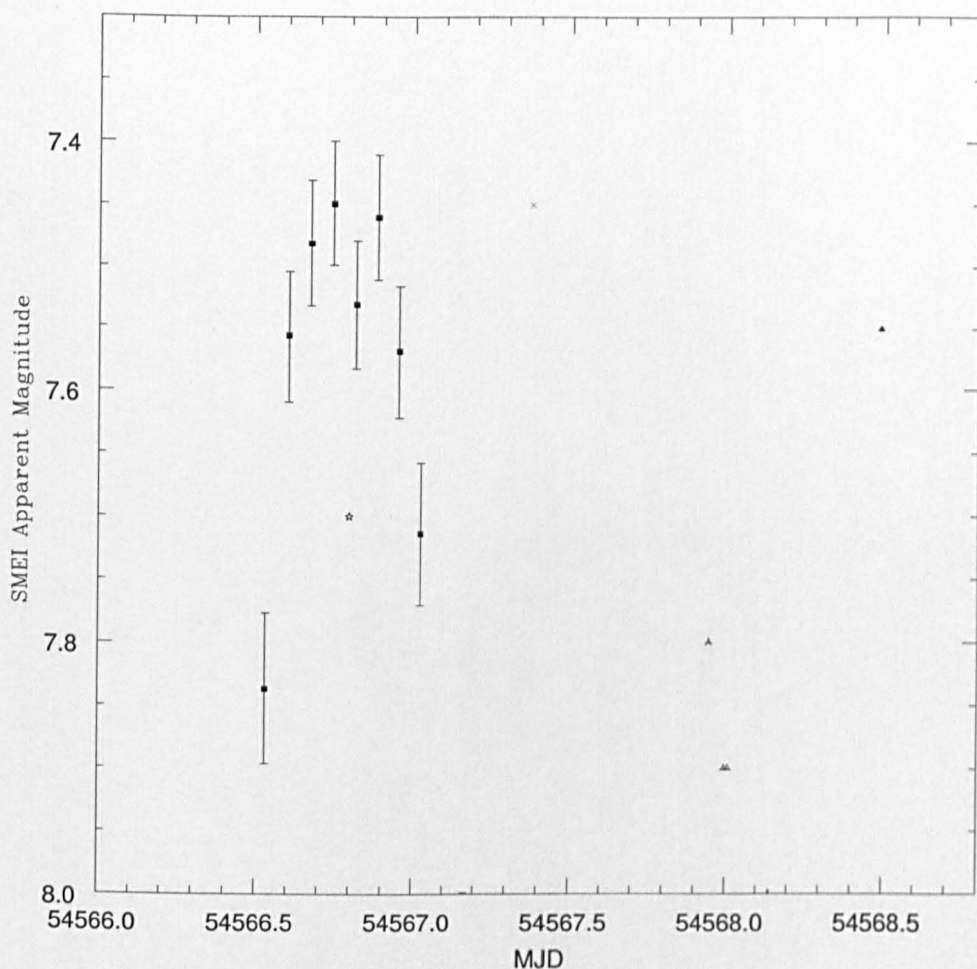


Figure 5.23: SMEI light curve (filled black squares) of V2491 Cyg. The open blue triangles represent *Visual* data, the green crosses *V*-band data, and the filled red triangles \widehat{R} -band data; these data are from the AAVSO. The black star represents the peak as obtained in Nakano et al. (2008b)

differences between the data sets is most likely caused by neighbouring bright stars (again simultaneous fitting of these objects was conducted along with the fitting of additional bright stars in the larger surrounding region). The decay of the SMEI light curve is quite consistent with the AAVSO data. However, the scatter in the SMEI light curve is evident and due both problems in fitting the source, as it goes below the limiting SMEI magnitude, and contamination from the surrounding bright stars. The t_2 time of the nova as given by SMEI is difficult to determine due to the scatter of the light curve however, it can be estimated as ~ 9 days, indicating the nova as very fast.

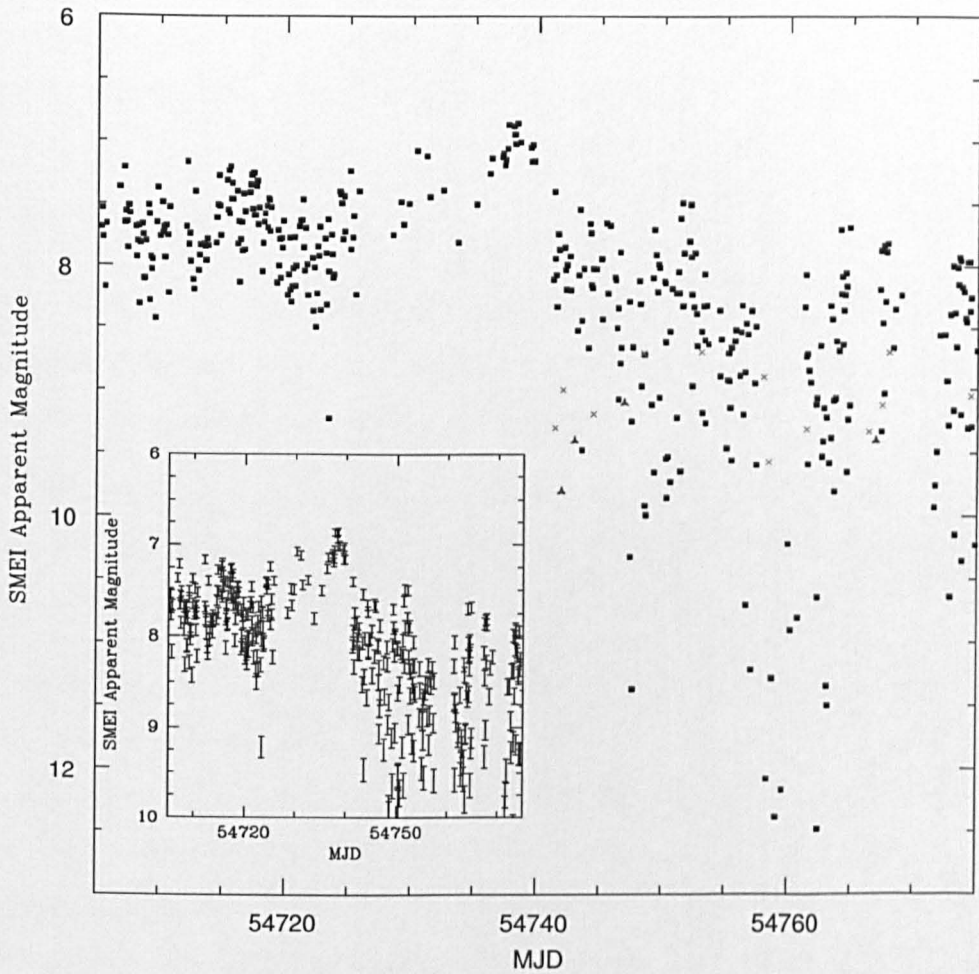


Figure 5.24: SMEI light curve (filled black squares) of QY Mus. The open blue triangles represent *Visual* data, and the green crosses *V*-band data; these data are from the AAVSO. The inset indicates the SMEI data only, with errors.

V5580 Sagittarii

Nova V5580 Sgr was discovered by Liller (2008) at a magnitude of approximately 8.0 on 2008 November 29.04 UT (MJD 54799.04). The variable was also present on November 23.037 UT (MJD 54793.037) at a magnitude of approximately 10.3, but was not visible ($\text{mag} > 11.0$) on November 20.035 (MJD 54793.035). The object is located at $\alpha = 18^{\text{h}}22^{\text{m}}01^{\text{s}}.39$, $\delta = -28^{\circ}02'39''.8$; J2000).

Although the nova may be detected within the SMEI data only a few reliable points

were obtained due to the passage of Venus and its poor subtraction. The peak magnitude found for the object is at $m_{\text{SMEI}} = 7.01 \pm 0.04$ on 2008 November 30.85 UT (MJD 54800.85). This coincides well with that mentioned in Liller (2008).

V5583 Sagittarii

This nova has been observed by both SMEI and the Solar TERrestrial RELations Observatory (STEREO) Heliospheric Imager. A review of STEREO and the light curve generated for this object is discussed in Section 5.6.

V5583 Sgr is a fast CN which was discovered by Nishiyama et al. (2009b) at a magnitude of 7.7 on 2009 August 6.5 UT (MJD 55049.5). Hachisu & Kato (2010) determine an absolute magnitude of $M_V = 0.5$ and a distance of 11 kpc.

The object is detected in SMEI on 2009 August 1.44 UT (MJD 55044.44) at $m_{\text{SMEI}} = 8.65 \pm 0.10$. It is then seen to rise (Figure 5.25) to a peak magnitude of $m_{\text{SMEI}} = 6.94 \pm 0.05$ on 2009 August 7.08 UT (MJD 55050.08). A peak of $m_{\text{SMEI}} = 6.82 \pm 0.04$ is noted on 2009 August 6.80 UT (MJD 55049.80), however due to its briefness and the subsequent light curve pattern it is not believed to be the optical peak and to be caused by some other, perhaps instrumental, effect. A pre-maximum halt may be present on 2009 August 6th at an average of $m_{\text{SMEI}} = 7.2$. However this does not seem to fit in with the 1-2 magnitudes below maximum range that has been generally proposed for the halt (see Section 1.4.2). Approximately one day after maximum the object seems to enter a “plateau” phase which lasts for 1.76 days with an average $m_{\text{SMEI}} = 7.55$, after which the light curve declines. It should be noted that data with a correlation coefficient ≤ 0.4 have been used in Figure 5.25 (and again slightly larger *npsf* and combined RA and Dec values). Within this figure data points with a correlation coefficient above 0.3 are represented by stars and data with a correlation coefficient value between 0.2 and 0.3 by squares. Although correlation coefficients much lower than standard have been used, the pattern of the light curve is evident and the scatter seems minimal, supporting their use.

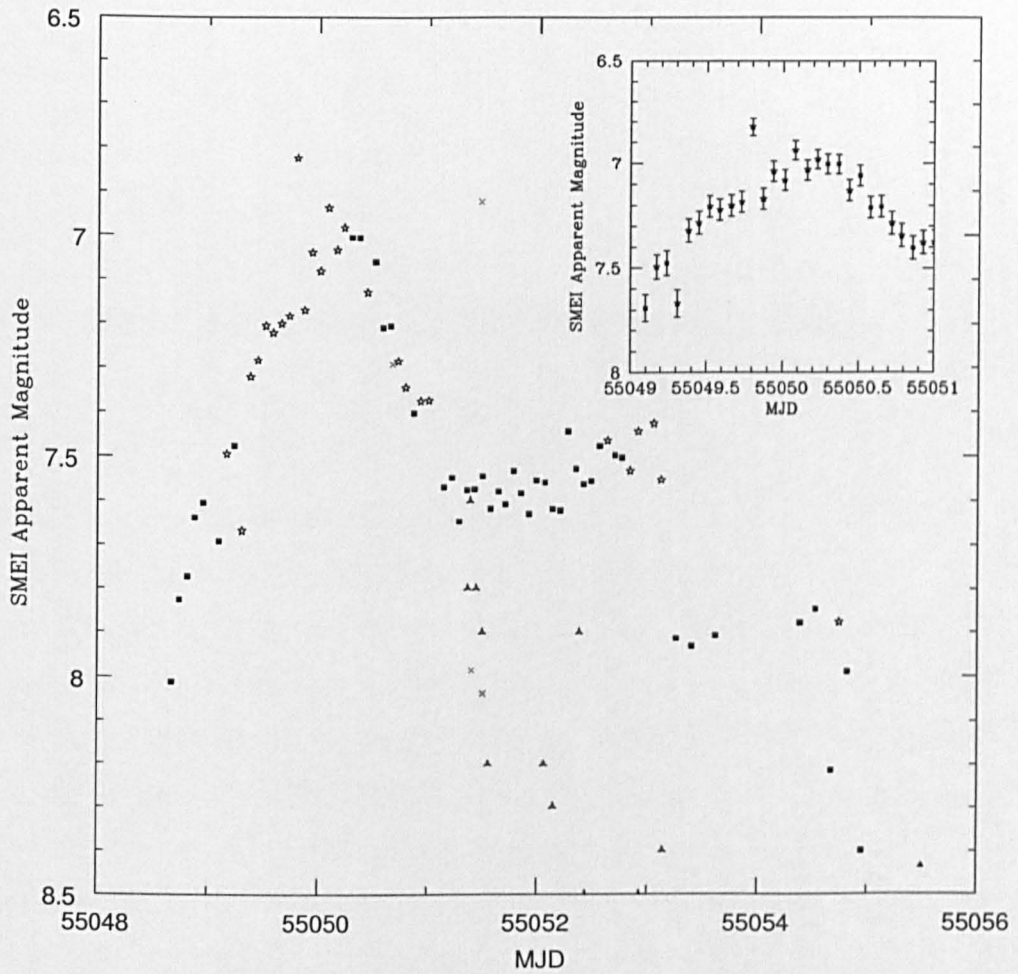


Figure 5.25: SMEI light curve of V5583 Sgr. SMEI data with a correlation coefficient ≥ 0.3 are given as stars, data with a correlation coefficient between 0.2 and 0.3 are represented by squares. The open blue triangles represent *Visual* data, the green crosses *V*-band data, and the filled red triangles *R*-band data; these data are from the AAVSO. The inset indicates the SMEI data only, with errors.

Table 5.2: Derived light curve parameters of second class data.

Name	Time of Maximum yyyy/mm/dd ± 0.04 days	Peak SMEI magnitude	t_2 (days)	wing radius (deg) ²⁴
V1187 Sco	2004/08/3.77	6.87 ± 0.04	9.4	<i>auto-wing</i>
V2467 Cyg	2007/03/16.56	6.24 ± 0.03	8.0	<i>auto-wing</i>
V458 Vul	2007/08/13.66	7.94 ± 0.07	-	<i>auto-wing</i>
V597 Pup	2007/11/14.68	6.91 ± 0.04	2.3	1.3
V459 Vul	2007/12/27.96	6.51 ± 0.03	16.2	<i>auto-wing</i>
V2491 Cyg	2008/04/10.75	7.45 ± 0.05	-	1.3
QY Mus	2008/09/29.34	6.85 ± 0.04	~ 9	<i>auto-wing</i>
V5580 Sgr	2008/11/30.85	7.01 ± 0.04	-	<i>auto-wing</i>
V5583 Sgr	2009/08/7.08	6.94 ± 0.05	-	1.4

5.6 Solar TERrestrial RELations Observatory (STEREO) Heliospheric Imager

STEREO is a NASA-funded mission intended to study the propagation of CMEs from the Sun into the heliosphere out to around 1 AU. It consists of two spacecrafts which were launched on 2006 October 26th from the Cape Canaveral Air Force Station in Florida. STEREO-A (the leading craft - ahead) is at a distance of 0.96 AU from the Sun, and STEREO-B (the lagging craft - behind) at 1.08 AU. During the course of the mission the orbit of STEREO-A varies over 0.95-0.97 AU with a period ≈ 1 yr, and STEREO-B over 1.00-1.09 AU. The orbital configuration of the crafts are such that each one recedes from the Earth by 22.5° a year as measured by the spacecraft-Sun-Earth angle. Mounted on the sides of each of these widely separated spacecraft are five remote-sensing instruments; an Extreme Ultra Violet Imager (EUVI), two coronagraphs (COR-1 & COR-2) with FOVs $\sim 4^\circ$ from the Sun, and two telescopes known as the Heliospheric Imagers (HI) which are wide-angle visible light imagers. The HI instruments like SMEI have an incorporated baffled design to eliminate scattered light so as to better observe CME's. Each HI instrument consists of two cameras HI-1 (FOV $\sim 20^\circ$) and HI-2 (FOV $\sim 70^\circ$) and are off-pointed from the Sun by 14.0° and 53.7° respectively, with optical axes aligned in the ecliptic plane. The configuration of the

²⁴See Section 5.4.1 for information on *auto-wing*.



Figure 5.26: A cross sectional view through the HI instrument showing the fields-of-view of the two telescopes. Image taken from Eyles et al. (2009).

cameras are such that there is coverage over solar elongation angles 4.0° to 88.7° . HI instruments have been performing scientific observations since early 2007. As well as observing CME's one of the original science objectives of the STEREO mission was also to conduct stellar variability studies. The HI cameras are able to continuously monitor sources down to 13^{th} magnitude for periods of 20 (HI-1) to 70 days (HI-2). The quantum efficiency reaches peak (93%) at around 550 nm but drops to 23% and 30% at 300 and 900 nm respectively (Eyles et al., 2009).

During operation it was noted that the PSF of HI-2B is broader and more asymmetric than that of HI-2A. This has caused a spreading of the stars in the images. The cause of this problem is thought to be due to manufacturing or assembly issues with the HI-B lens. The degraded PSF of the HI-2 instrument has implications on the detailed examination of point sources and models are being created to correct for the PSF. An additional complication to observing sources within the data is caused by occasional and random discontinuities in the pointing of HI-1B relative to the spacecraft attitude solutions by up to $0.1^\circ/0.2^\circ$. The discontinuities usually manifest themselves as steps in plots of pointing attitude against time. Sometimes however, the pointing disconti-

Table 5.3: Performance specifications of the HI instrument taken from Eyles et al. (2009).

Specification	HI-1	HI-2
Direction of centre of FOV from Sun centre	14.0°	53.7°
Angular FOV	20°	70°
Angular range	4-24°	18.7-88.7 °
CCD pixel size	35 arcsec	2 arcmin
Image array (2×2 binning)	1024×1024	1024×1024
Image bin size	70 arcsec	4 arcmin
Spectral band-pass	630-730 nm	400-1000 nm
Exposure time	40 s	50 s
Exposures per summed image sequence	30	99
Summed image cadence	40 min	2 hr
Brightness sensitivity (B_o = solar disc)	$3 \times 10^{-15} B_o$	$3 \times 10^{-16} B_o$
Stray-light rejection (outer edge of field)	$3 \times 10^{-13} B_o$	$10^{-14} B_o$

nities occur during the exposures. This causes stars in the image to be smeared, have trails, or even split. The reason for this issue is thought to be the fact that HI-B faces into the direction of motion of STEREO-B, leading to the impact of dust particles on the instrument. It is not yet clear if a similar issue is found with HI-2B due to the degradation of the PSF. Originally the pointing of the instruments was calculated using preflight instrumental offsets from the STEREO spacecraft along with spacecraft attitude data. Work conducted by Brown et al. (2009) has been used to improve the pointing of the HI instruments by matching known catalogue stars to those identified in the background of HI images and adjusting the pointing parameters to optimise the fit between the predicted and observed star positions. The method described in Brown et al. (2009) essentially avoids any problems in data analysis due to the pointing discontinuities as the HI cameras are used as star trackers and the images become self-calibrating. The issue of pointing now only becomes a problem in a few percent of images where stars are significantly smeared and improved attitude solutions can not be obtained, these images are flagged and not used in analysis.

5.6.1 STEREO Data Processing

Data from the STEREO imagers are made available via the UK Solar System Data Centre (UKSSDC). Each HI image is the sum of many shorter full-resolution (2048 × 2048 pixel) exposures that have each been “cleaned” to remove cosmic-rays which would otherwise dominate the final summed image. The resultant images are then binned to 1024 × 1024 pixels and transmitted to Earth. For calibration purposes a small number of full resolution single exposures (of a few seconds) are downloaded.

STEREO data analysis is conducted using IDL and the solarsoft libraries²⁵, with calibration of the HI data carried out using *secchi_prep.pro*. The steps involved in the calibration and processing of STEREO data are described within “Working with data from the NASA STEREO Heliospheric Imager an essential guide”²⁶.

To remove stars from the HI images a routine called *hi_remove_starfield.pro* is initiated (see above guide for further details). It processes the images with no prior knowledge of what stars are in the FOV. Stars in the data are simply identified by analysing the ∇^2 (divergence of the gradient) field of the image. A successive overrelaxation (SOR) method is then used to reconstruct only the pixels where the stars were identified. The user is able to determine what the minimum intensity star the program is able to detect via a threshold value which is set to 1.0 as a default. The lower the threshold, the fainter the stars removed, but the more pixels required for reconstruction and so longer the processing time.

5.6.2 STEREO Observations of V5583 Sagittarii

Using STEREO data, a light curve of V5583 Sgr has been generated by Daniel Holdsworth (UCLan). STEREO data have been scaled to SMEI by the subtraction of two magnitudes. This comparison indicates that the peaks are roughly in the same position, and that the initial declines are similar. However, small sections of the rise phase do

²⁵http://www.lmsal.com/solarsoft/index_old.html

²⁶See http://www.stereo.rl.ac.uk/Documents/HI_user_guidejuly.pdf

differ as well as the decline below one magnitude from maximum (see Figures 5.27 and 5.28). These discrepancies could be caused by differences in the response function of the instruments (STEREO peaks around 550 nm and is skewed towards the red/IR, SMEI peaks at 700 nm) or because calibrations for the HI STEREO camera are incomplete. Further complications could also be caused by the unusual PSF's of both the SMEI and the HI instruments and differences in pixel size.

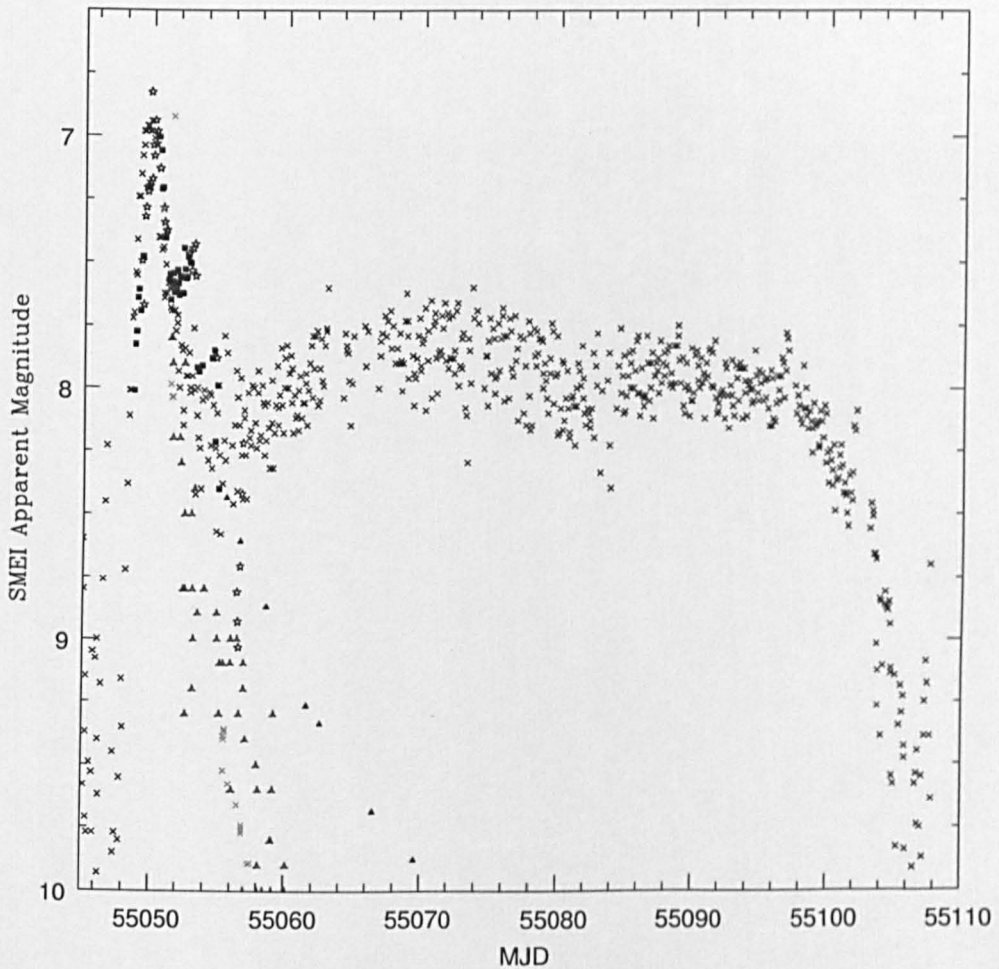


Figure 5.27: SMEI and STEREO light curve of V5583 Sgr. SMEI data with a correlation coefficient ≥ 0.3 are given as stars, data with a correlation coefficient < 0.3 are represented by squares. STEREO data is represented with crosses. The open blue triangles represent Visual data, the green crosses V-band data, and the filled red triangles R-band data, these data are from AAVSO.

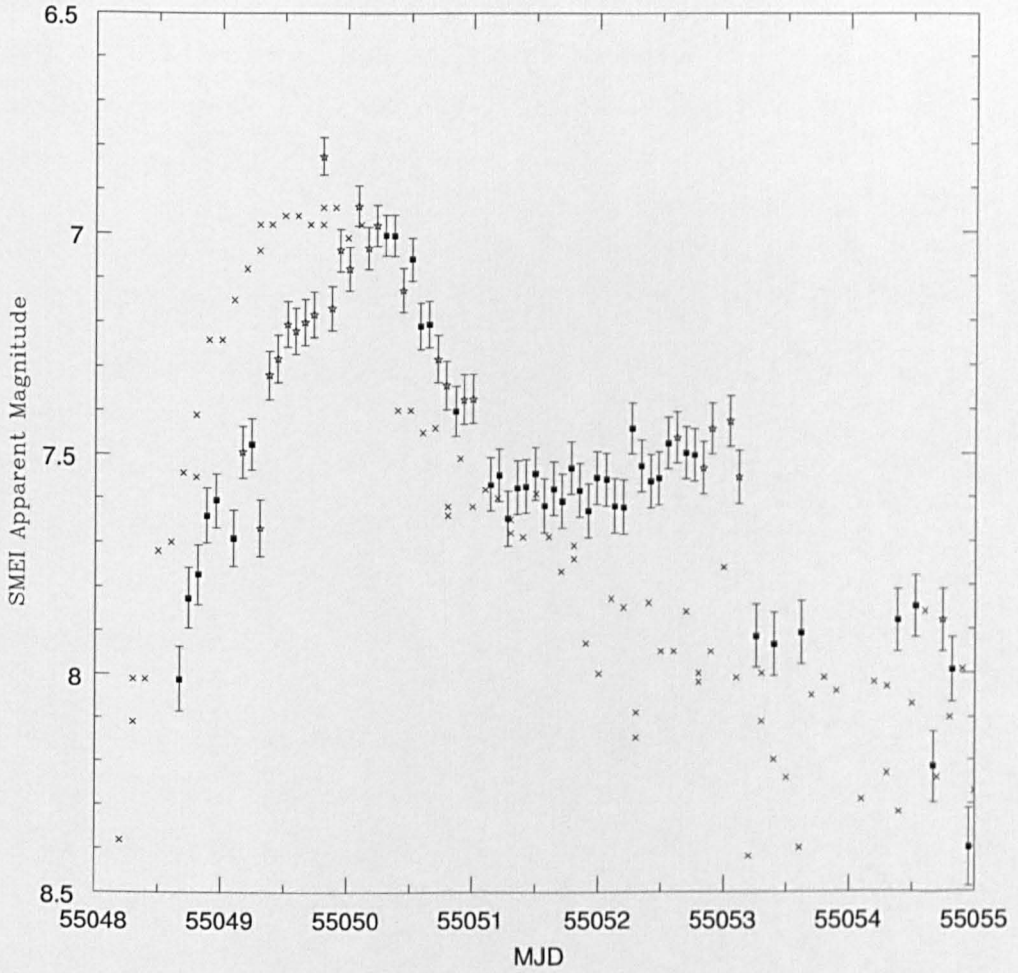


Figure 5.28: SMEI and STEREO light curves of V5583 Sag covering the epoch of the detection within the SMEI data only. Data are represented by the same symbols as in Figure 5.27. Errors are given for the SMEI data.

5.7 Detection of Transients and Variable objects

With 8.5 years of all-sky white light photometry the SMEI data archive undoubtedly hosts a plethora of transient events and variable objects which are within the instrument's detection limit. These sources may either be those which are already known of and catalogued, or they could be previously undetected objects. Discussed below are searches which have been conducted by other research groups for some transient and variable events, along with investigations which have been conducted as part of the work within this thesis.

5.7.1 Previous Detection of Transients and Variables in SMEI by Other Groups

As well as members of the SMEI team at UCSD, there are other groups that have also realised the potential of the SMEI data.

Gamma Ray Bursts

Previous work has been conducted by the UCSD group in the detection of gamma ray bursts (GRBs). In Buffington et al. (2006) a list of 91 classical (soft gamma-ray repeaters were excluded) GRB bursts between 2003 February 6th and 2005 April 6th were considered. From this list SMEI was able to provide upper limits for the optical afterglow of 58 bursts. These afterglows occur tens of minutes after the burst when different shocked regions emit optically and so remain long enough for SMEI detection. The paper indicated that whilst SMEI cannot compete with the sensitivity of instruments such as UVOT on *Swift* or ground based telescopes like ROTSE-II, SMEI observations may still be relevant, especially if these telescopes are unable to observe particular events.

Variable Objects

In work conducted by Spreckley & Stevens (2007) three years of all-sky photometry from the SMEI data archive were obtained and 13,000 light curves of stars brighter than 6th magnitude (here it is assumed that the author means roughly 4000 stars per SMEI camera as there are only ~ 5600 stars known to be brighter than 6th magnitude) were produced. Of these, 1600 were achieved with $\approx 1\%$ precision. The main research focus of this group was to search for and obtain exoplanet transiting signals within the SMEI data. In order to create a light curve for each object over the three year base line, aperture photometry was performed using a modified version of the DAOPHOT (Stetson, 1987) routines in IRAF. Outputted light curves were then corrected for the degradation of the CCD over this time period and the PSF corrected for its dependence on position across the CCD. A box fitting least squares fit (BLS) method (Kovács et al., 2002) was then implemented on each light curve to search for transiting exoplanet signals with better than 1% precision. A custom written algorithm was then implemented. This work however found no transit-like signals.

Other specific objects or type of object have also been investigated using the SMEI data. For example within Spreckley & Stevens (2008) the period and amplitude changes of Polaris (α UMi) were examined between 2003 and 2007; Tarrant et al. (2007) investigated the red giant Arcturus, and Clover et al. (2011) analysed the light curve of Epsilon Aurigae.

5.7.2 Current Search for Transients and Variables

As part of the work conducted within this thesis a search for transient objects and variable stars is being implemented using SMEI data from UCSD.

The equatorial and polar maps produced by SMEI can be processed to generate what will now be referred to as variable maps (see Figure 5.29). These are maps from which zodiacal light, sidereal background, and the list of 5600 bright stars above 6th magnitude have been subtracted. The subtraction of these stars was conducted using

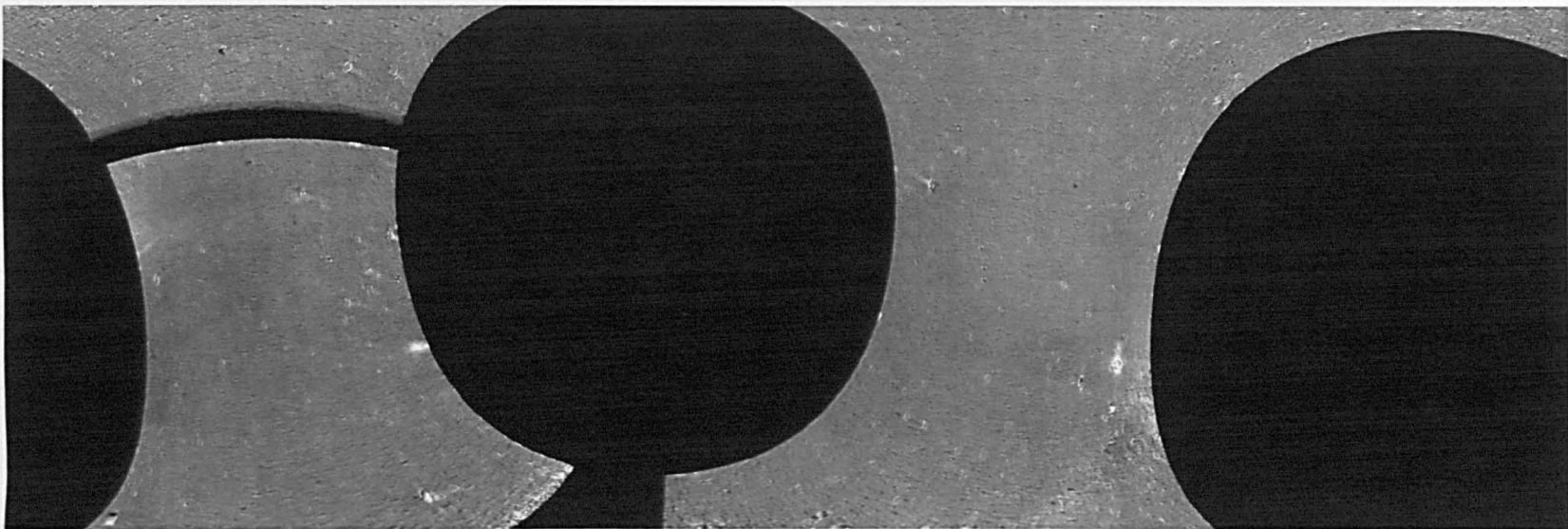


Figure 5.29: A SMEI equatorial map from which zodiacal light, sidereal background, and the 5600 stars brighter than 6th magnitude have been subtracted. With in this map the effects of poor stellar subtraction may be observed along with tails created by bright stars when near a cameras edge.

the non-iterative centroiding routine mentioned in Section 5.3.1. Anything which is left over within the variable maps should therefore be an object which has increased or decreased from its quiescent magnitude, i.e. a transient event or variable star. There are however a few issues within these maps which can prove that statement to be false; these are listed below.

- The non-iterative least squares fitting of stars brighter than 6th magnitude means that their subtraction/sky replacement is poor. For very bright stars a residual of the object may be left behind which will then appear in the variable maps and act as a false positive. This issue is addressed in step 5 of the code used to search for variable objects as described below.
- Bright stars which are located near the edge of a camera may “leak” and create tails in the image. On subtraction of this bright star the tail will still remain, again potentially leading to false positives.

The code used to detect and fit candidate objects within the variable maps is known as *smei_findpnt*. The code was written by Paul Hick (Supercomputer Center, UCSD) in IDL, with testing and adjustment/refining of the code conducted as part of the work within this thesis. The various procedures implemented on the variable maps along with important parameters are described below (a full copy of the code can be found in Appendix C).

1. **Large scale smoothing of variable maps:** The map is smoothed by subtracting a running mean for an 8° wide box. This takes out variations over spatial scales much larger than the PSF. This step mainly serves to create local maxima that are more easily sorted, i.e. it makes it easier to process maxima, descending in brightness.
2. **Small scale smoothing of variable maps:** The map now smoothed with a running mean of 1° which is the full width of the PSF. This step reduces the noise of the maps, and avoided picking up every noise spike as a separate local maxima. An example of a smoothed map may be seen in Figure 5.30.

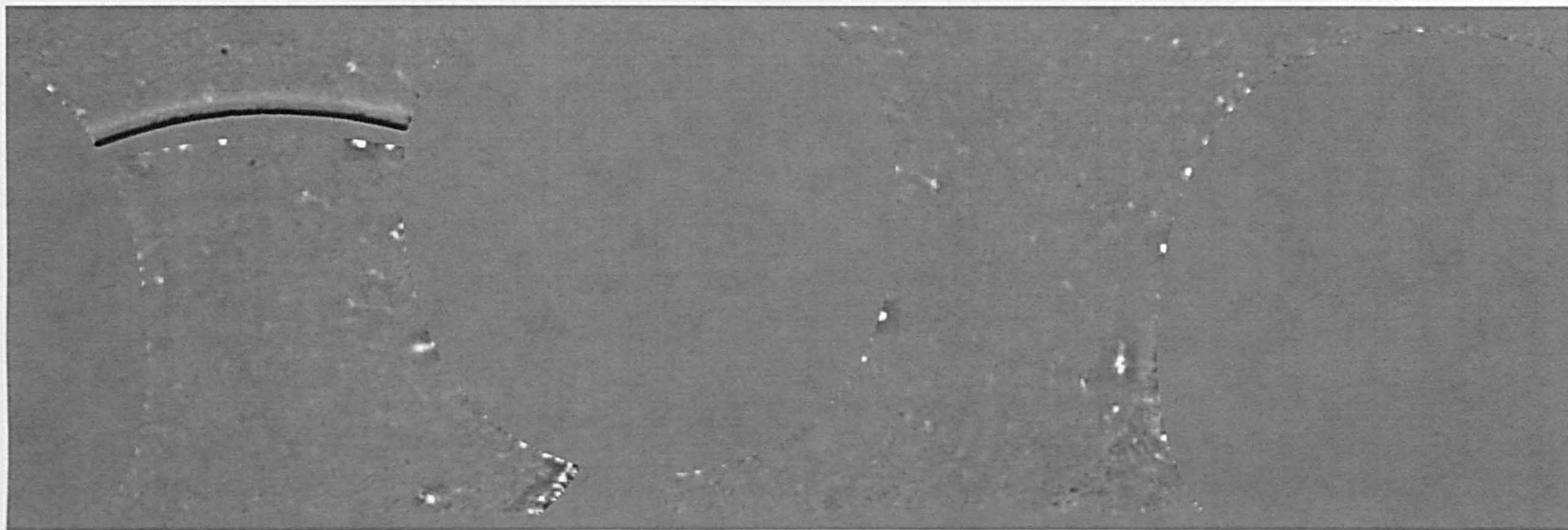


Figure 5.30: A SMEI equatorial map from which zodiacal light, sidereal background, and the 5600 stars brighter than 6th magnitude have been subtracted, and which has undergone smoothing.

3. **Preparing a list of candidate objects:** In this step the a list of all local maxima within the variable map is constructed with the brightest given first. The number of local maxima which may be found can be controlled by the user specifying a number of key words, however on testing this proves inefficient and step one seems to be the best way in which to control the output.
4. **Fitting of candidate maxima:** It is within this step that objects which look like point sources (i.e. the SMEI PSF) are fit using the default fitting procedure (*smei_star_fit*) described in Section 5.3.1. The main key word to control with this step is *fix_centroid*, with the default case being when *fix_centroid* is off. In this case the PSF is fit only once at the location of each candidate maximum. With *fix_centroid* on an iterative procedure is used to find the location in the map near the candidate maximum that provides the best fit (the highest correlation between the object in the sky-map and the standard SMEI PSF). The advantage of NOT setting *fix_centroid* is that there is a significant reduction in processing time (close to a factor of 10). The disadvantage is that the quality of the PSF fitting is much worse, which might lead to good objects going unnoticed due to a lower correlation coefficient. As a consequence of this step all candidate objects from step 3 may be sorted according to their correlation coefficient value, with those possessing the highest correlation coefficient listed first. The difference between using (or not using) *fix_centroid* is that the candidates will be sorted differently.
5. **Retention of the best fitting objects only:** The number of candidates for a certain variable map can easily be over 1400. Here the correlation coefficient keyword *cvmin* is used to retain only those objects which have a *cvmin* above a certain threshold. The default value for *cvmin* is 0.7, this higher value will typically eliminate 70% – 80% of the candidate objects leaving only those which are more likely to be valid objects. It is in this step however that the effect of using or not using *fix_centroid* in step 4 becomes evident. As the correlation coefficients are different (lower when *fix_centroid* is not used), a different set of candidate objects is retained. If *cvmin*=0.7 when *fix_centroid* is not used then

under half the number of candidates will be detected and as stated above these will not necessarily be the same objects that were detected previously. When not applying *fix_centroid* *cvmin* must be lower than 0.7. Choosing a *cvmin* value is a compromise between the detection of real objects and noise. On testing a *cvmin* value of 0.6 seems to produce the best results with the number of candidates detected only marginally greater than results obtained when using *fix_centroid* and a *cvmin*=0.7. On comparison of objects detected using both methods there is a greater than 70% overlap. Also note that when looking at individual output files the order of the candidates will be different to those produced when using *fix_centroid* and candidates may also appear in later files within the time series. Note that if *cvmin*=-1 is used, all objects are retained.

6. **Match against catalogue stars:** This step is optional. It is not done by default, but can be switched on using the keyword *use_catalogue*. Within this step the locations of the candidate maxima from step 5 are compared against the locations of the 5600 stars brighter than 6th magnitude (i.e. the SMEI star catalogue). If a candidate object is found within 0.5° of a catalogue star, then the object found is most likely the result of a bad-subtraction. In this case the candidate object will be listed in the output file under the name of the catalogued star. Note that this is not a positive or negative identification; it just indicates the proximity of a catalogue star. A low value of *cvmin* should not be used in combination with the *use_catalogue* keyword as checking a long list of candidate objects against the SMEI star catalogue will drastically increase processing time.
7. **Write output file:** The output files contains the results of the fits for all candidate objects, sorted in descending order of correlation coefficient. For candidate objects which lie in the overlapping area between the polar maps (north pole - NP, and south - SP) and the equatorial map (EQ; between 50° and 60° declination north and south) there will be two records in the output file: one for the object seen in the EQ map, the other in one of the polar maps. This needs to be taken into account when analysing the content of the file. The names assigned to each candidate object indicate in which map the object was detected, EQ, NP or

SP; followed by an integer that counts the number of objects. Note that the same object will have a different name in output files for different sky-maps. In order to obtain individual object files entries must be matched by RA and Dec.

Initial Analysis

A simpler version of this code, using now dated zodiacal models and fitting routines, was implemented by Paul Hick on four years' worth of data from Camera 2 several years ago. As an initial test the results of this run were passed through a code written by Daniel Harman (LJMU), with input based on work conducted within this thesis. The code is designed to sift through files output from the *smei_findpnt* procedure and sort each candidate object into a separate object file based on RA and Dec. This code was written in Qt create and named *smei_sort*. A description of *smei_sort* is given below.

- A sphere of N pixels is created using HEALPix (see Section 4.7 for description) with each pixel representing an area of 0.5° and having an assigned RA and Dec.
- The output files of *smei_findpnt* are read into the program and candidate objects placed within their corresponding positions on the virtual sphere.
- The number of “hits” within a pixel are counted, and an object file generated for that position if the number of hits is greater than a certain threshold value.
- The flux within a given object file is determined not only from the pixel with the highest number of hits but also from the surrounding 8 neighbouring pixels. This is to accommodate for any scatter on position that may be encountered due to centroiding issues (i.e. if *fix_centroid* is off). The object file generated indicates if the flux at a certain time is from the central pixel or from a neighbour.
- Once individual object files have been generated each position is passed through the General Catalogue of Variable Stars²⁷ (GCVS) to see if there is a correspond-

²⁷<http://www.sai.msu.su/gcvs/gcvs/index.htm>

ing object at that location of the sky and thus indicate if the object is already catalogued.

Implementation of *smei_sort* on the resultant *smei_findpnt* data led to the creation of over 1500 object files. Examination of these data revealed that the majority of objects were within the GCVS and/or were the result of poor subtraction of the bright SMEI catalogued stars. Some objects however, remained unidentified. A sample of such interesting objects can be found within Figures 5.31, 5.32 and 5.33. These data have not been “cleaned” with regards to correlation coefficient, *n_psf*, or position but are raw data taken from the above described process. A more through investigation of each object and its surrounding environment is required to validate the object as a variable and ensure that it is not caused by some of the false positive issues mentioned earlier. It should be noted that on further investigation the object shown in Figure 5.32(b) does repeat with a five year period but these peaks are of a lower brightness than the one shown here.

For comparison of the old and new versions of the *smei_findpnt* code light curves of Nova V1280 Sco were generated using both. These can be found in Figure 5.34. The light curve generated using the newer version of the *smei_findpnt* code (black squares) described in Section 5.7.2 is fractionally brighter than that generated using the old *smei_findpnt* code (red triangles). Both of these light curves were generated with *fix_centroid* on. The increase in brightness is not unexpected and probably due to the use of improved zodiacal light models. In the third light curve the newer version of the *smei_findpnt* code is used but with *fix_centroid* switched off to indicate the scatter increase (blue squares).

5.8 Discussion and Conclusion

This work has enabled unprecedentedly detailed observation of the rise to maximum for all five novae within the first class data of Section 5.5.1, and the precise date of maximum for each nova within this and Section 5.5.2. In turn, it has provided signifi-

cant, detailed, and undeniable evidence for the existence of the previously controversial pre-maximum halt, with accurate times of occurrence, duration and magnitude below peak given. The reality of this halt in all three of the fast novae observed in detail (and possibly in a slightly different form in the slow nova V1280 Sco as described in Section 5.5.1) is a challenge to detailed models of the nova outburst. From Table 5.1 it may also be noted that there does not seem to be a correlation between the properties of the pre-maximum halt (Δm_{SMEI} , Δt , number of magnitudes below maximum, and time before peak) and the properties of the nova or its eruption (speed class), although the sample size is admittedly small at present.

The time of each nova's peak optical brightness has been derived with previously unobtainable accuracy, marking as it does the time of greatest extent of the pseudophotospheric radius in each object. Perhaps the most intriguing features around maximum light are displayed by V1280 Sco where two re-brightenings may be associated with

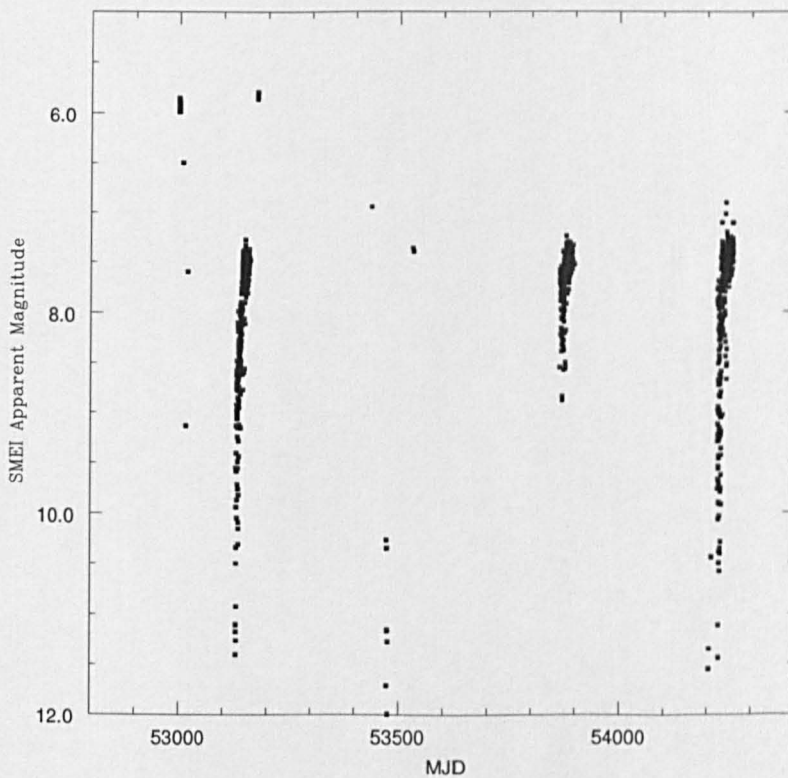
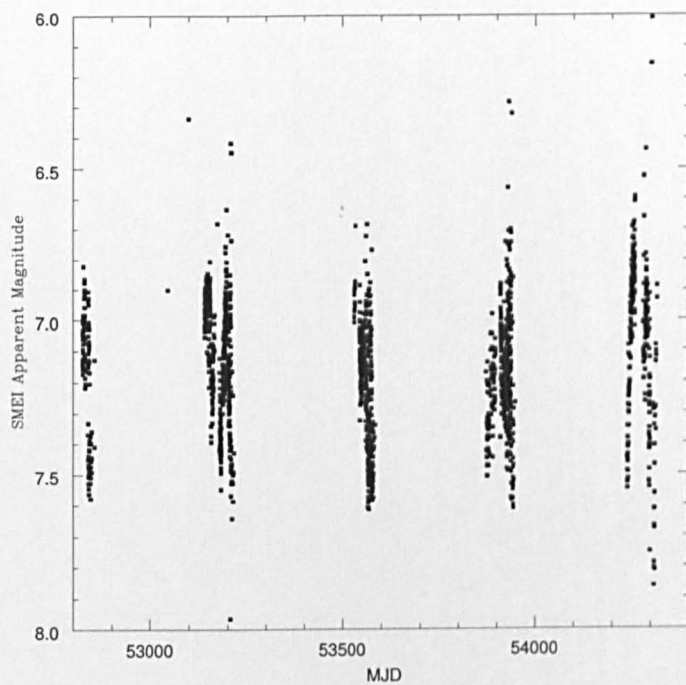
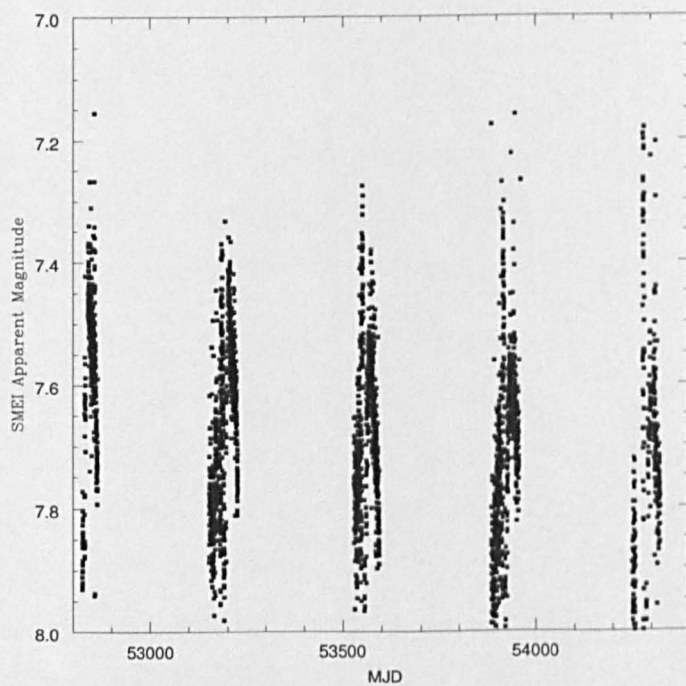


Figure 5.31: (a) Object detected at $\alpha = 02^h 33^m 52^s$ $\delta = +55^\circ 29' 27''$; J2000.



(a)



(b)

Figure 5.32: (a) Object detected at $\alpha = 06^h15^m0^s$ $\delta = +56^\circ36'13''$; J2000. (b) Object detected at $\alpha = 08^h02^m03^s$ $\delta = +63^\circ04'21''$; J2000

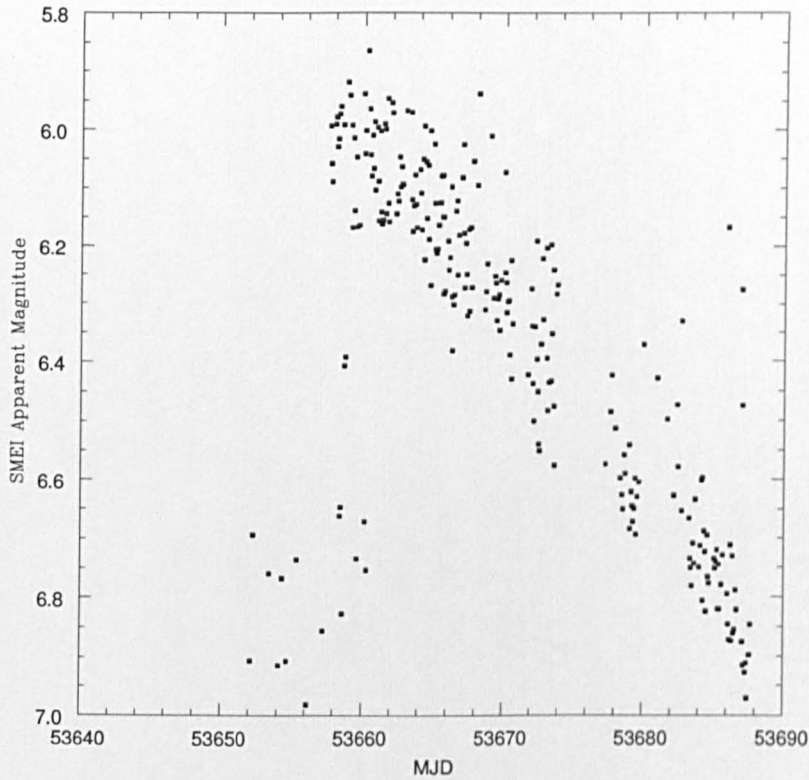


Figure 5.33: (a) Object detected at $\alpha = 19^h 12^m 40^s$ $\delta = -60^\circ 14' 43''$; J2000.

epochs of enhanced mass loss from the WD surface. What the mechanism is that would lead to such enhancements during the TNR is a matter of conjecture. Within the initial decline of each nova light curve small oscillations can also be seen.

Overall, this initial investigation of the SMEI data archive has proven how important it is to examine all-sky data with regards to transient events. As with the case of both novae V598 Pup and KT Eri, even the brightest (naked eye) novae may be missed by conventional ground-based observing techniques, Warner (1989, 2008, and references therein) reached the same conclusion. Shafter (2002) estimates that as many as six novae with maxima brighter than 8th magnitude may occur each year, instead of the one or two typically observed. This estimate suggests that over 50 novae may be found within the SMEI data archive, 60-80% of which will be unknown. Therefore the SMEI archival data will continue to be investigated, searching for previously known and unknown transient events from 2003 to 2011 (see Section 5.7.2 for details on the

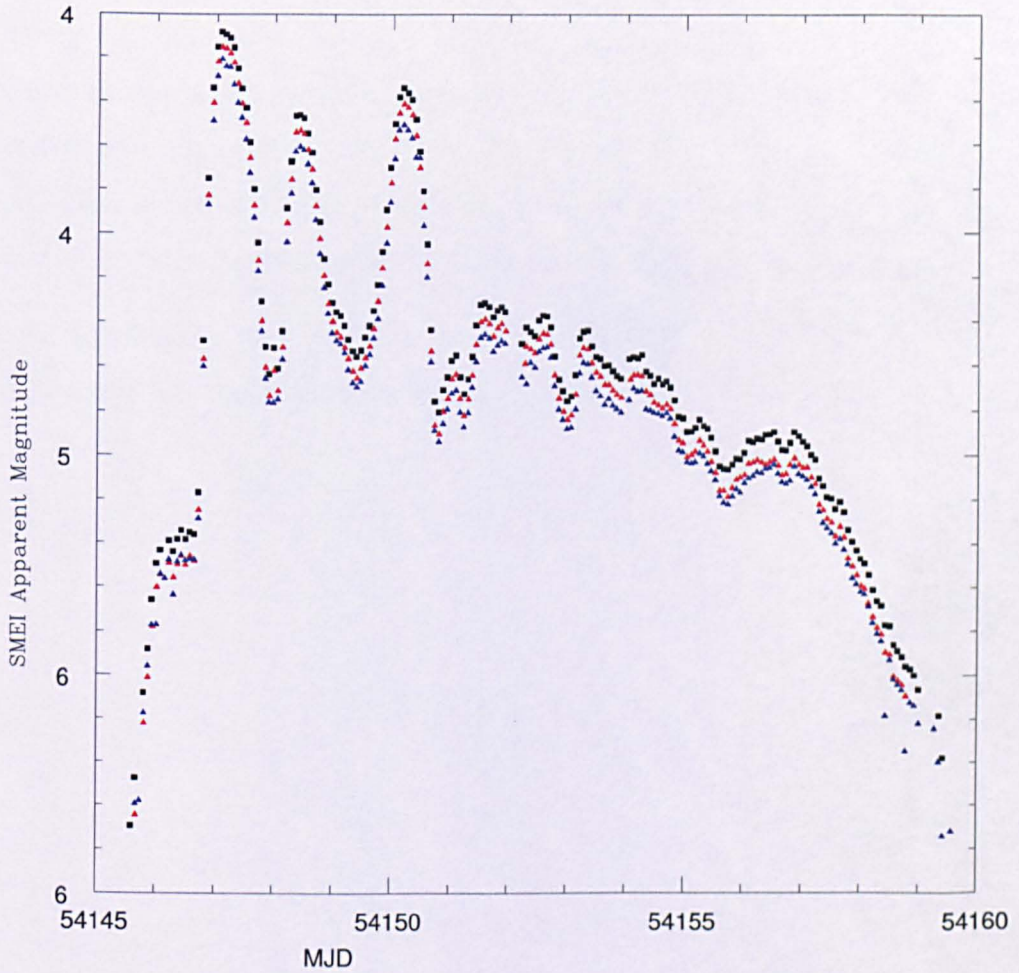


Figure 5.34: SMEI light curve of nova V1280 Sco. The black squares indicate data generated using then new *smei_findpnt* code; the red triangles are data using the old *smei_findpnt* code - both of these were conducted with *fix_centroid* switched on. The blue triangles indicate data using the new *smei_findpnt* code, but with *fix_centroid* switched off.

method of detection and Section 7.2.2 for future work planned).

In collaboration with UCSD a code to search for all transient and variable events within the SMEI data archive has been tested and updated. An initial search was conducted on four years of SMEI data from Camera 2 using an older version of the code leading to the creation of over 1500 object files some of which are unidentified and may be potentially very interesting. Initialisation of the improved code over all 8.5 year's worth of data and all cameras will be conducted imminently (see Section 7.2.2). Overall, the data provided by SMEI may well have opened a new chapter in the observation and understanding of novae, and further investigation into the transient and variable population within the SMEI data may well prove significant.

In the next Chapter, work conducted upon Nova V1721 Aquilae is presented. This is an unusually fast, luminous, and highly extinguished nova.

Chapter 6

A very luminous, highly extinguished, very fast nova - V1721 Aquilae (2008)

The content of this chapter is published within Hounsell et al. (2011a) in collaboration with Dr Matthew Darnley (LJMU), Prof. Michael Bode (LJMU), Dr Daniel Harman (LJMU), Dr Lorren Helton (SOFIA Science Center/The University of Minnesota), and Dr Greg Schwarz (West-Chester University/American Astronomical Society). The paper was written by myself with the input of Dr Matthew Darnley and Prof. Michael Bode. Post-outburst spectra were provided by Dr Lorren Helton and Dr Greg Schwarz. These spectra and all other data were analysed by myself to obtain results presented.

6.1 Introduction

Nova V1721 Aquilae ($\alpha = 19^h06^m28^s58$, $\delta = +7^\circ06'44''.3$; J2000) was discovered on 2008 September 22.5 UT by K. Itagkai. The outburst was confirmed on 2008 September 22.586 UT and reached a peak unfiltered magnitude of 14.0. Discovery of the nova was given in Yamaoka et al. (2008) along with an initial spectral investigation. Post-outburst spectra were obtained on 2008 September 25.19 and 25.25 UT using the Steward Observatory Bok 2.29 m telescope on Kitt Peak via the Boller & Chivens optical spectrograph (details of the instrumental set-up can be found in Section 6.3). Initial analysis of the spectra revealed a broad triple-peaked $H\alpha$ emission profile with a FWHM of 6450 km s^{-1} , along with OI 7773 Å and OI 8446 Å structures (Helton et al., 2008a). The ejecta velocities derived from the initial analysis of the spectra were very high indeed for a typical CN and there was initial suspicion that it may be a supernova (Prof. S. J. Smartt, Queen's University Belfast - private communication). Spectra also indicated that extinction towards the object was high and by comparison to other novae during similar evolutionary phases was estimated to be $A_V \approx 9.3$. Hence, the distance to the nova was initially derived as 5 kpc, by assuming at maximum $M_V \approx -9$ (Helton et al., 2008a). Due to the faintness of the source at maximum and its rapid decline, further follow-up spectroscopy of the object was not possible.

6.2 Distance Determination

After outburst, V1721 Aql continued to be monitored photometrically until 2008 October 6 UT (results are reproduced in Figure 6.1). These data indicate that $t_2 \approx 6$ days for the nova, classifying it as very fast (Payne-Gaposchkin, 1964). Using these data and the MMRD relation with parameters from Downes & Duerbeck (2000), an absolute magnitude at peak of $M_V = -9.4 \pm 0.5$ is calculated.

The extinction towards V1721 Aql is thought to be extremely high, with an estimate of $A_V \approx 9.3$ given in Helton et al. (2008a). This however, is based purely upon comparisons with other novae at a similar early evolutionary state. In order to obtain

an independent extinction estimate Rowles & Froebrich (2009) extinction maps were used which have a high spatial resolution and are able to detect a greater number of small-scale high extinction cores compared to other maps. These extinction maps are generated using 100 nearest-neighbour stars and give an $A_V = 11.6 \pm 0.2$, much higher than the original estimate. Using the more accurate extinction from Rowles & Froebrich (2009), a distance to V1721 Aql of 2.2 ± 0.6 kpc is derived.

The Galactic coordinates of V1721 Aql are $l^{II} \approx 41^\circ$, $b^{II} \approx -0.1^\circ$. Using Equation 4.1 a value of $z = -2.5$ pc is obtained. This indicates that V1721 Aql is located very close to the Galactic plane, and in a region of the sky in which it is typically very difficult to observe novae because of high extinction along the line of sight.

6.3 Post-Outburst Spectra

Post-outburst spectra were obtained on 2008 September 25.19 and 25.25 UT using the Steward Observatory Bok 2.29m telescope on Kitt Peak with the Boller & Chivens optical spectrograph, and are presented in Figures 6.2 and 6.3. The “Blue” set-up utilised a 400 l mm^{-1} 1st order grating with a UV blocking filter to prevent order contamination below $\sim 3600 \text{ \AA}$. The spectral coverage was from $\sim 3600 \text{ \AA}$ to $\sim 6750 \text{ \AA}$ at a spectral resolution of roughly $2.8 \text{ \AA pixel}^{-1}$. The “Red” set-up was identical but with the grating centred near 7600 \AA providing coverage from $\sim 6000 \text{ \AA}$ to $\sim 9250 \text{ \AA}$ and with a blocking filter effective below 4800 \AA . Flat fielding was performed using a continuum arc lamp. Red observations at wavelengths beyond $\sim 7700 \text{ \AA}$ are subject to fringing effects arising at the CCD that are unable to be corrected by flat fielding. The effect of this fringing on the data depends upon the target position on the sky and the target intensity. Wavelength calibration was performed using He-Ar-Ne calibration lamps at each target position. The spectroscopic standard Wolf 1346 was used for flux calibration. Spectra have also been corrected for heliocentric velocity and reddening ($A_V = 11.6$). All data reduction was performed in IRAF following standard optical data reduction procedures. Continua were modelled and subtracted using a 3 degree

²⁸ Available from <http://ooruri.kusastro.kyoto-u.ac.jp>

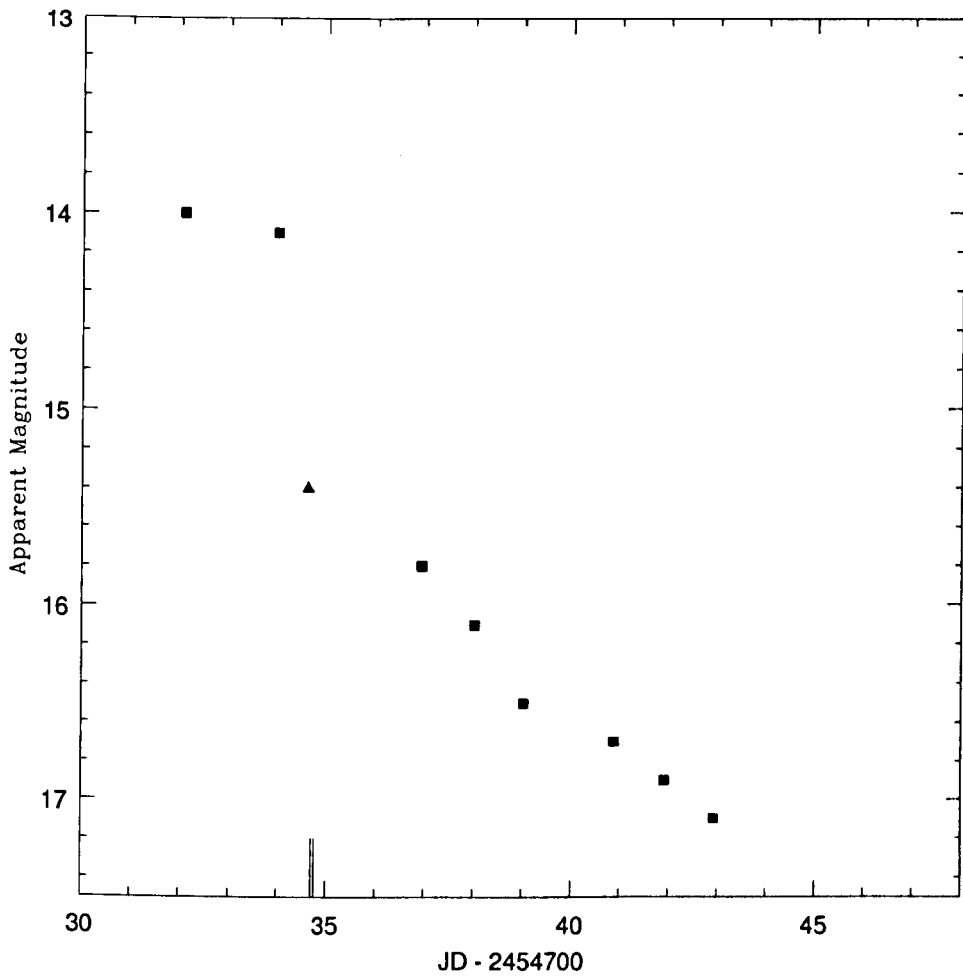


Figure 6.1: Apparent magnitudes of Nova V1721 Aql as observed by K. Itagaki (squares - unfiltered) and R. King (triangles - Visual). These results are from VSNET²⁸ and AAVSO. The two additional tick marks on the X-axis represent the dates on which the Blue (see Figure 6.2) and Red (see Figure 6.3) spectra were taken.

polynomial in Starlink's *Splat*²⁹ package.

The Blue spectrum of V1721 Aql is presented in Figure 6.2. It is important to note that this spectrum is devoid of detectable emission lines blue-wards of H α , likely owing to the very high extinction. Because of the absence of H β emission in the spectrum, a lower limit on the extinction is obtained using the Balmer decrement for Case B HI recombination and the observed intensity ratio of H α and H β (see Equations 6.1, 6.2, 6.3, and 6.4, where $I_{H\alpha o}/I_{H\beta o}$ is the emitted ratio of intensities, $I_{H\alpha}/I_{H\beta}$ is the observed ratio of intensities, $f(H\alpha)$ and $f(H\beta)$ the emitted frequency of the components, C a constant, and τ_V the interstellar extinction in the V band).

$$\frac{I_{H\alpha o}}{I_{H\beta o}} \simeq 3 \quad (6.1)$$

$$\frac{I_{H\alpha}}{I_{H\beta}} = \frac{I_{H\alpha o}}{I_{H\beta o}} e^{(-C[f(H\alpha)-f(H\beta)])} \quad (6.2)$$

$$\tau_V = Cf(V) \quad (6.3)$$

$$\tau_V \approx A_V \quad (6.4)$$

It must be noted that this spectrum is taken early in the nova outburst and although the nova is very fast, conditions may not yet be those of Case B. However, from Equations 6.1 to 6.3 a lower limit of $A_V \geq 8$ is estimated. This value is consistent with both the above determinations of A_V and helps to confirm that the extinction is indeed high.

The Red spectrum of V1721 Aql is shown in Figure 6.3 and indicates the presence of a triple-peaked H α emission line along with emission structures corresponding to OI 7773 Å and OI 8446 Å. It is necessary to determine if the “boxy” structure around H α consists of purely H α or combined lines of H α + [N II] 6482, 6548, 6584,

²⁹Information on Splat can be found at <http://star-www.dur.ac.uk/pdraper/splat/splat.html>

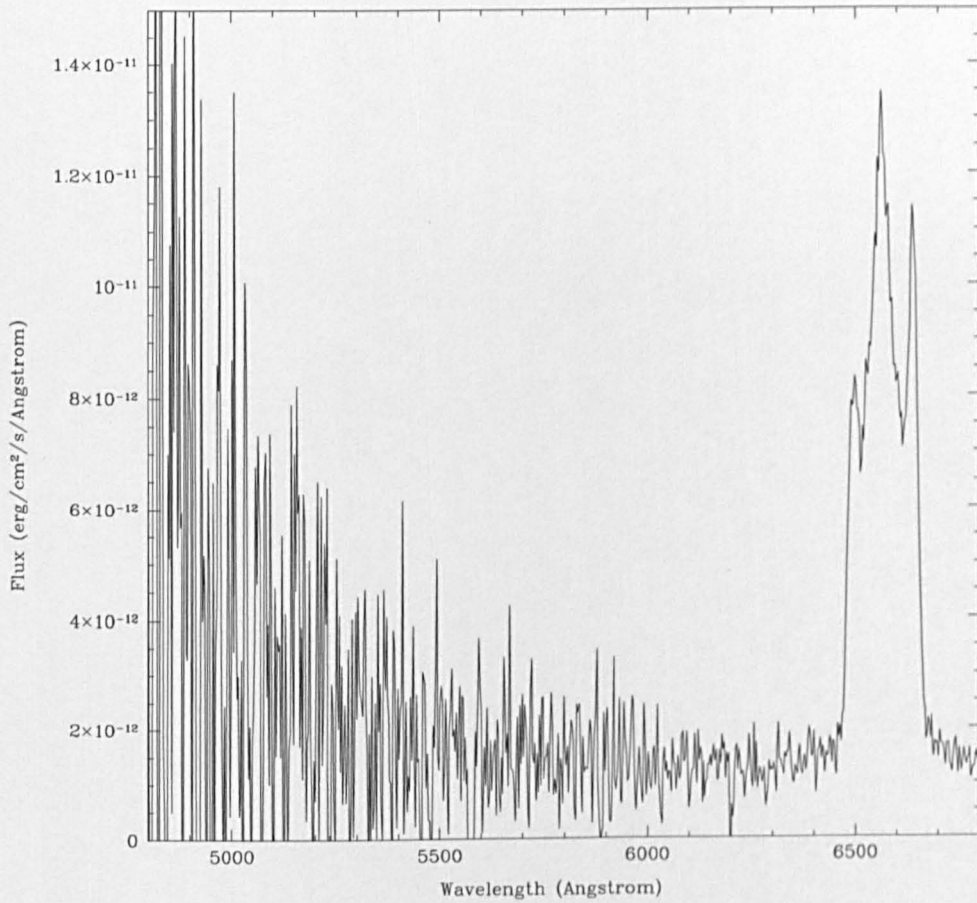


Figure 6.2: Heliocentric velocity and extinction-corrected ($A_V = 11.6$, see Section 6.2) blue wavelengths optical spectrum of V1721 Aql, taken on 2008 September 25.19 (2.69 days after discovery) with the Steward Observatory Bok 2.29 m telescope. Continua have been subtracted using a cubic polynomial. Shorter wavelengths ($3550 \leq \lambda \leq 5000$) have been excluded due to problems with noise.

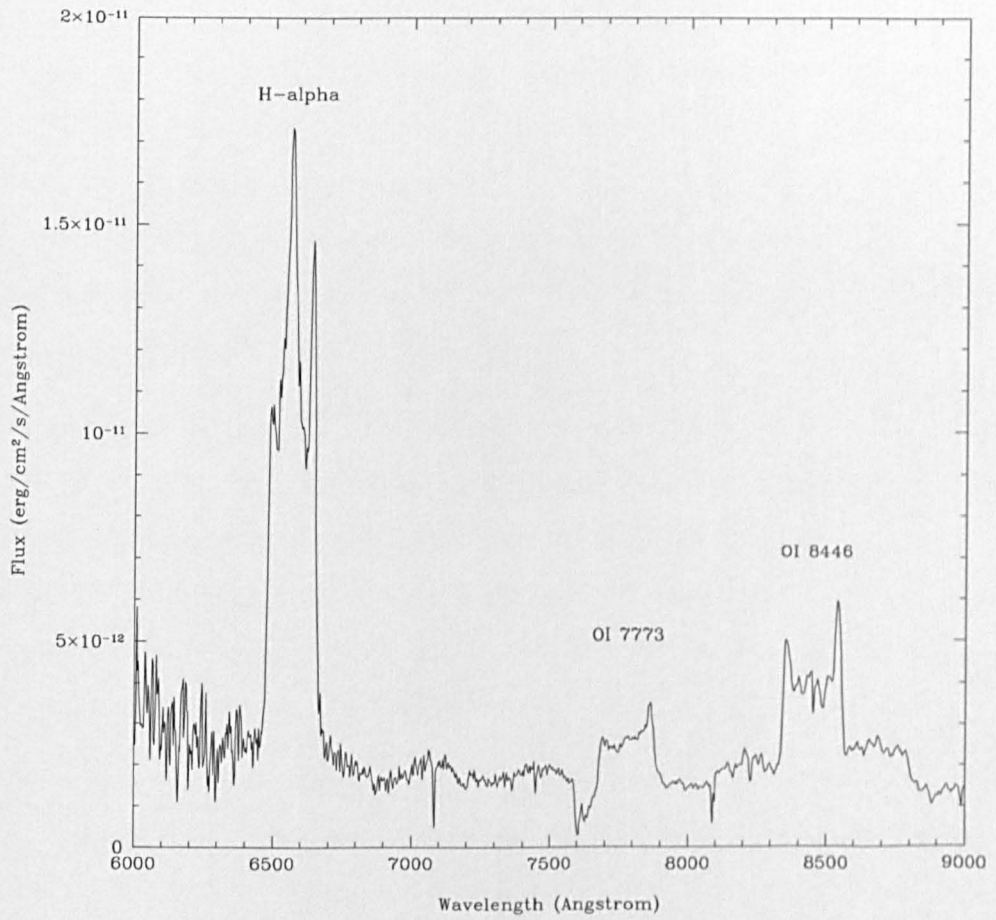


Figure 6.3: As Figure 6.2, but Red spectrum, taken on 2008 September 25.25 (2.75 days after discovery). Continua have been subtracted using a cubic polynomial.

6611 Å. However, although [N II] is expected in the spectra, this early in the outburst the [N II] line strength is unlikely to be significant in comparison to H α and so an unlikely contributor to the boxy structure. The absence of [N II] altogether may simply be owing to the fact that the nova has indeed been caught at maximum and these lines tend to develop a little later in the outburst. For example, the fast, potentially U Sco-like nova V2491 Cyg showed evidence of [N II] 4.62 days after peak magnitude, with these lines becoming more defined 32.7 to 108 days after peak (Munari et al., 2011c). The lack of [N II] 5755 Å at shorter wavelengths also contradicts the idea of a strong N II presence, although this line may have been missed due to a combination of the object's rapid evolution and high extinction. Additionally, the observed emission peaks at the blue and red edge of the H α profile in V1721 Aql are nearly symmetric and expected positions of potential [N II] contaminants are not.

A relative velocity diagram of the H α , OI 7773 Å, and OI 8446 Å structures is given in Figure 6.4. This diagram indicates that the H α and OI lines contain similar weak blue/strong red wing morphologies. However, the H α central peak is much more prominent and may arise in an emitting region distinct from the other components of the emission profile. The velocity shifts of the three components are also similar which supports the hypothesis that the H α structure consists of H α emission only.

In order to identify any potential emission lines that may be contaminating the H α structure a spectral fit of the region (using the Red spectrum, Figure 6.3) was conducted using STSDAS's³⁰ *Specfit*, the results of which are presented in Figure 6.5 and Table 6.1. It should be noted that the central H α peak was fit by two separate Gaussians with the second component added as a correction to the first in compensation for the oversimplification of the fit; a possible physical explanation for this is given in Section 6.6. The OI 8446 Å structure has also been fit, with these results presented in Figure 6.6 and Table 6.2. It is evident that fringing occurs within the spectra at wavelengths \gtrsim 8000 Å. The effect of this fringing has been to contribute to components 2 and 5 found in Figure 6.6 and to create fine structure short-ward of

³⁰STSDAS is a product of the Space Telescope Science Institute, which is operated by AURA for NASA.

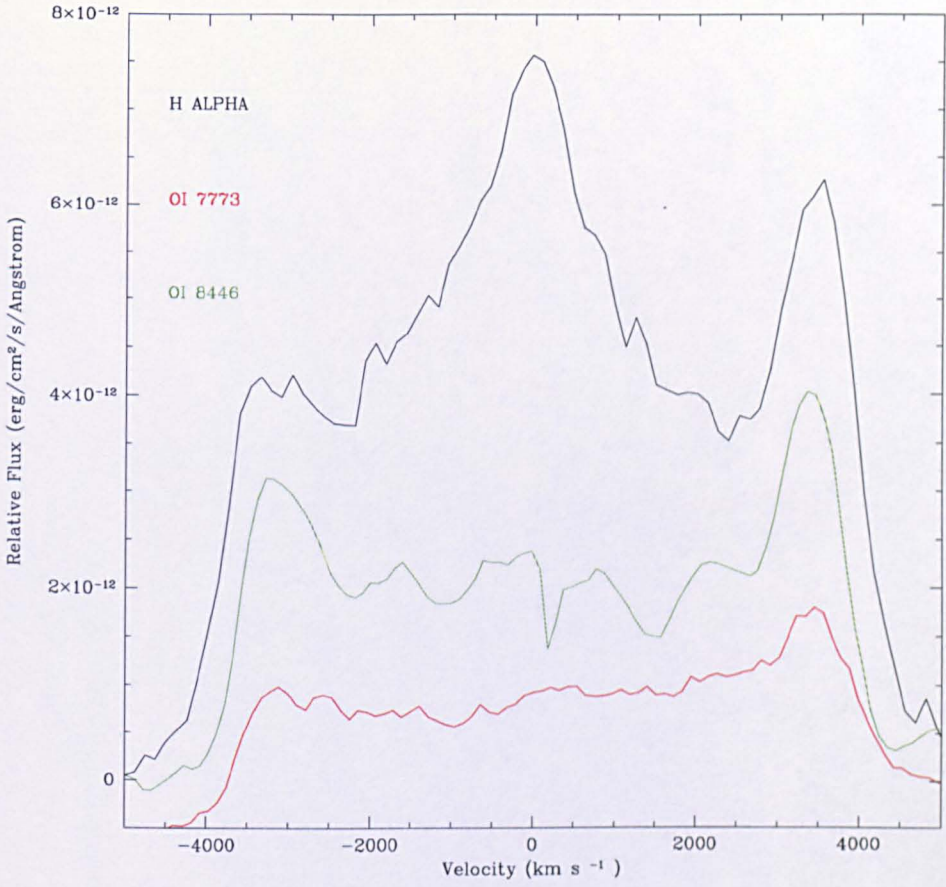


Figure 6.4: Relative velocity diagram of the $H\alpha$, OI 7773 Å and OI 8446 Å structures. Note that lines have been off-set on the y-axis for ease of comparison.

the OI 8446 Å profile. It was therefore necessary to fit these contaminating structures which would otherwise interfere with the results. Taking fringing effects into account the central structure of the OI 8446 Å line profile is most likely relatively flat.

Table 6.1: Wavelength, FWHM, and relative velocity of fitted components of the triple-peaked H α structure presented in Figure 6.5.

Gaussian	Wavelength (\AA)	FWHM (km s^{-1})	Relative velocity (km s^{-1})
1	6493 ± 3	1400 ± 100	-3200 ± 100
2	6563 ± 1	4300 ± 100	-10 ± 50
3	6563 ± 1	800 ± 100	-10 ± 50
4	6639.6 ± 0.4	1260 ± 50	3510 ± 20

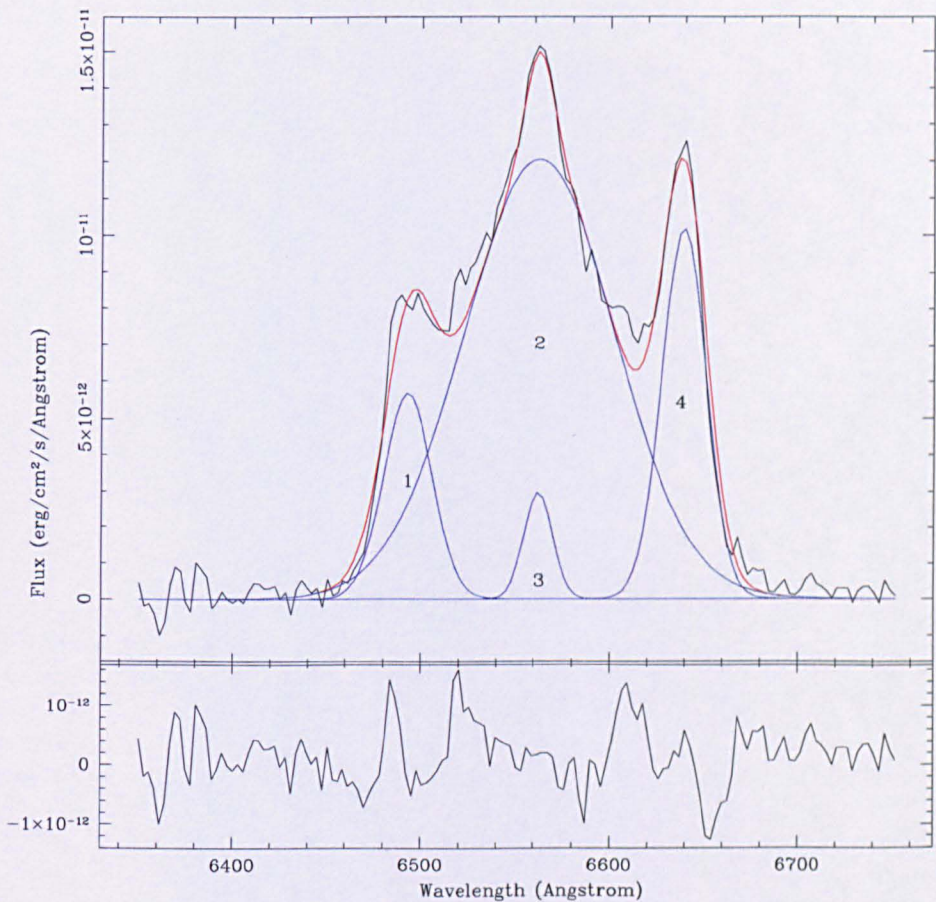


Figure 6.5: Observed H α structure (black line) with the sum of *Specfit* Gaussian components (red line). The blue lines represent separate Gaussian components. See Section 6.6 for further discussion. The lower plot shows the residual to the fit.

Table 6.2: Wavelength, FWHM, and relative velocity of primary fitted components of the triple peaked OI 8446 Å structure presented in Figure 6.6.

Gaussian	Wavelength (Å)	FWHM (km s ⁻¹)	Relative velocity (km s ⁻¹)
1	8358.7±0.5	1110±40	-3100±20
3	8447±1	3200±200	40±50
6	8541.9±0.4	930±30	3410±10

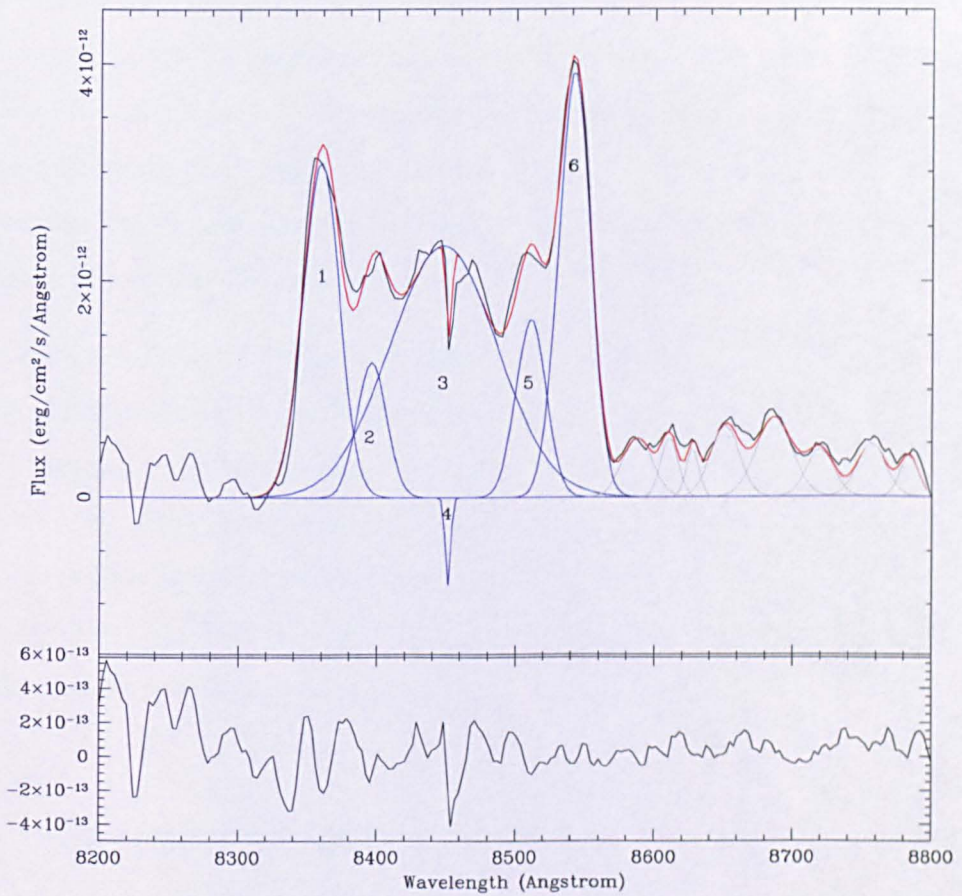


Figure 6.6: Observed OI 8446 Å structure (black line) with the sum of *Specfit* Gaussian components (red line). The blue lines represent separate Gaussian components. Gaussian 4 represents a spectral artifact. Gaussians 2 and 5 represent components within the profile that are partially caused by fringing. Grey Gaussians represent fine structure caused by fringing effects. All fringing effects required fitting in order to produce the best overall match with observations. The lower plot shows the residual to the fit.

Although there are slight inherent differences in the strengths of the red/blue peaks in the profiles of the OI 7773 and 8446 Å features, the intrinsic shape before fringing effects of the 8446 Å feature is likely very similar to the 7773 Å feature, as illustrated in Figure 6.4. The fitting of the OI 7773 Å profile has not been conducted as this structure has been severely truncated on the blue edge by an atmospheric absorption feature.

No other spectral lines expected to be found in novae match the wavelengths presented within Tables 6.1 and 6.2. Given this, and that the blue and red wings of the H α , OI 7773 Å, and OI 8446 Å profiles are similar, it can be concluded that these structures consist of H α and OI only. Combining the relative velocities of H α Gaussians 1 and 4 a mean expansion velocity of $V_{\text{exp}} = 3400 \pm 200 \text{ km s}^{-1}$ is determined. The structure of each line profile may also suggest something about the nova ejecta geometry (see Section 6.5 for further discussion).

On examination of both Blue and Red spectra, no evidence of Fe II/[Fe II] was found. This could be caused by the faintness of the spectra, noting the high extinction to the object, and hence the high noise level. There is some evidence of HeI 7001 Å and NI 8680, 8703, 8711 Å emission, however due again to noise within the spectra and fringing effects at these longer wavelengths, it is difficult to calculate their significance. Exact spectral classification of the object according to the Williams (1992) system therefore remains elusive.

6.4 Pre-Outburst Identification

Pre-outburst images of a source at the location of V1721 Aql are found within the 2MASS catalogue³¹, with NIR co-ordinates given as $\alpha = 19^{\text{h}}06^{\text{m}}28^{\text{s}}.60$, $\delta = +7^{\circ}06'44''.46$; J2000. Observed 2MASS apparent magnitudes and colours of the NIR source located at the position of the nova can be found in Table 6.3. This table also contains de-reddened colours using the extinction value $A_V = 11.6 \pm 0.2$.

³¹ Available from <http://irsa.ipac.caltech.edu/applications/Gator/>

Table 6.3: 2MASS apparent and absolute magnitudes of the V1721 Aql progenitor (candidate), colours, and de-reddened colours of the NIR source located at the position of the nova. The extinction towards the nova has been taken as $A_V = 11.6$, and its distance as 2.2 kpc.

Filter	Apparent magnitude	Absolute Magnitude	Colour	Value	De-reddened Value
<i>J</i>	16.6 ± 0.2	1.8 ± 0.6	<i>J-K_s</i>	2.0 ± 0.2	0.1 ± 0.2
<i>H</i>	15.5 ± 0.1	1.7 ± 0.6	<i>J-H</i>	1.2 ± 0.2	0.0 ± 0.2
<i>K_s</i>	14.7 ± 0.1	1.7 ± 0.6	<i>H-K_s</i>	0.8 ± 0.2	0.1 ± 0.2

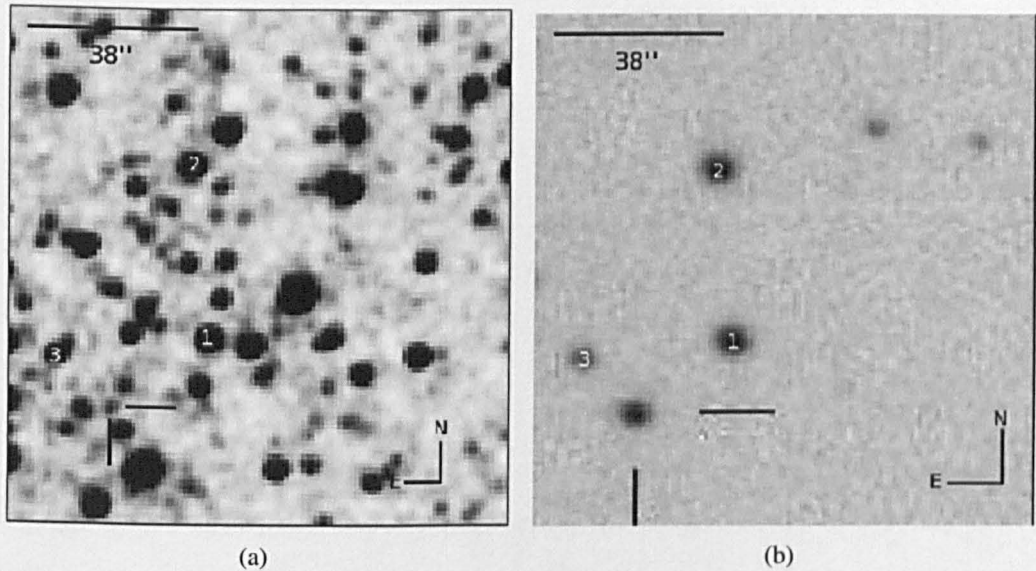


Figure 6.7: (a) 2MASS K_s band pre-outburst image. The nova is found within the centre of the black markers. (b) Unfiltered discovery image taken by K. Itagaki on 2008 September 22nd at the Itagaki Astronomical Observatory. The nova is found within the centre of the black markers.

The V1721 Aql discovery image³² and 2MASS K_s image were aligned and compared via IRAF packages. Based on the stellar density within the 2MASS K_s pre-outburst image, the probability of a chance alignment at least as close as that found between the nova and the 2MASS object is less than 1%. The archival 2MASS K_s band image is presented in Figure 6.7(a) and the discovery image presented in Figure 6.7(b).

³²Available from <http://www.astroalert.su/2008/09/24/nova-aql-2008>

6.5 The Nature of the Secondary

There are several factors that contribute to the observed NIR colours of a nova system in quiescence, (i) the spectral type of the secondary and evolutionary phase, (ii) the rate of mass transfer \dot{M} , (iii) the extinction A_V , (iv) the accretion disc and its inclination i , and (v) the mass of the primary. In CNe one would expect that the effect of the emission from the WD on the NIR colours to be negligible, and the accretion disc to only provide a significant contribution to the emission when $i \lesssim 30^\circ$, where an angle of $i = 90^\circ$ is defined as an edge-on accretion disc (Weight et al., 1994). The location of a quiescent nova on a NIR two-colour diagram ($H - K_s, J - H$) is therefore an important determinant of the nature of the secondary star in the system (see Section 1.9.2 for further discussion on this area).

The NIR apparent colours of the V1721 Aql nova system in quiescence are shown in Figure 6.8. The system's colours occupy a region which contains the RN V745 Sco, which has a giant secondary with an M5+ III spectral type, and the suspected recurrent V1172 Sgr (Weight et al., 1994), which is also thought to contain a giant secondary. The extinction of these novae however is much lower than that of V1721 Aql (for V745 Sco $A_V = 3.1 \pm 0.6$; Schaefer, 2010). Nova V1721 Aql's occupancy of this region is merely coincidental and does not indicate that it is a RN-like system. Nova Aql's de-reddening vector is indicated with a red line, the arrow head on this line represents an extinction value of $A_V = 11.6$; the surrounding red region represents the error circle of the corrected colours. The de-reddened quiescent NIR colours of the V1721 Aql nova system lie within a region occupied by many quiescent CNe. Assuming that the NIR emission of the nova system is dominated by the secondary, Figure 6.8 indicates that its spectral type is that of a late F-G (possibly K) main sequence star. However, the inclination of the accretion disc must be taken into account and if it is less than 30° (approaching face-on to the observer) then its contribution to the NIR colours would be to cause a significant blue-wards offset.

The line profiles observed in the nova spectra, and resultant high velocities, would suggest that the inclination of the disc within the binary system is low (face-on). The

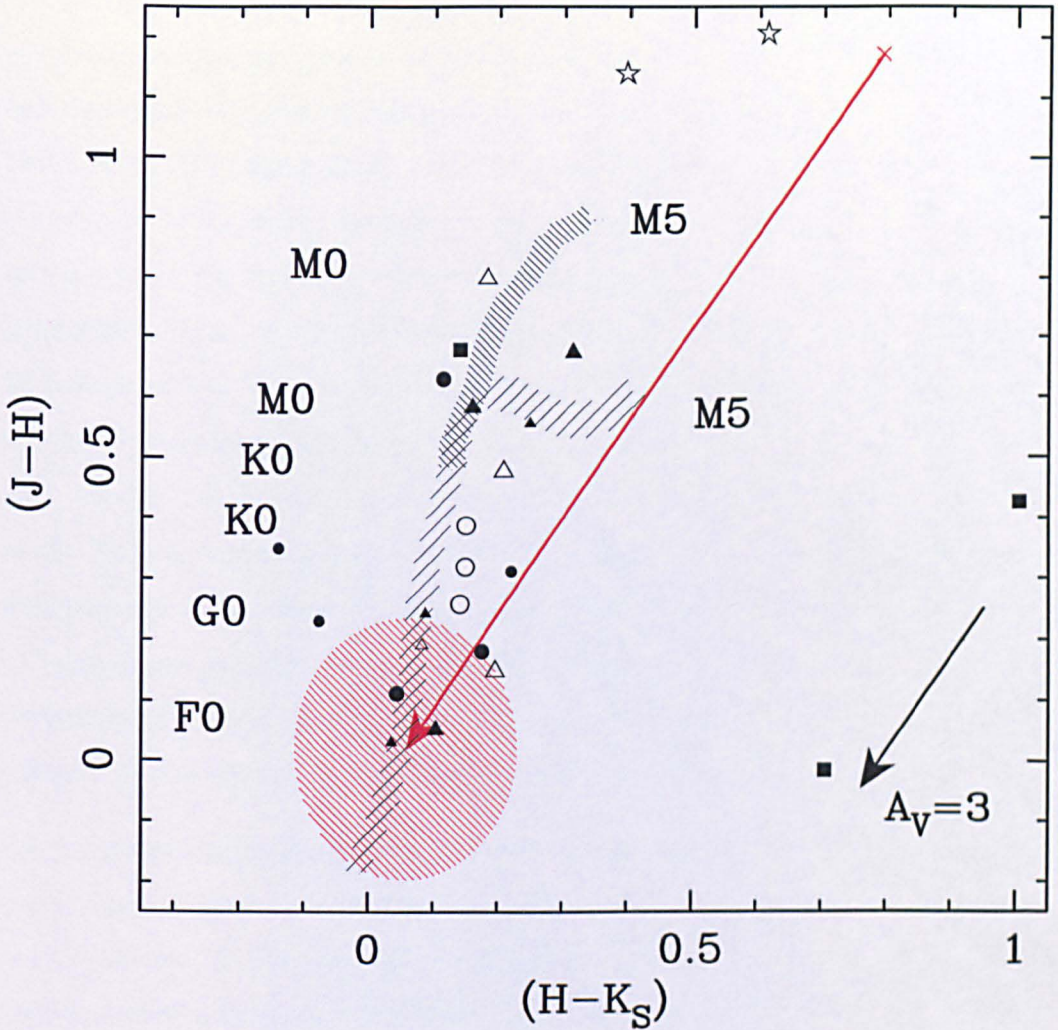


Figure 6.8: NIR colour-colour diagram of quiescent classical nova systems reproduced from Figures 4 & 7 in Hoard et al. (2002) using Table 1 of their data. The figure is adjusted to include the quiescent 2MASS colours of the nova V1721 Aql system. The light cross-hatched area represents NIR colours of main sequence stars with the denser cross-hatched area representing the giant branch (see references within Hoard et al., 2002). The black points show individual nova systems and are coded according to the time since outburst, τ , as follows; filled squares: $\tau < 25$ years; filled triangles: $\tau = 25 - 50$ years; open triangles: $\tau = 50 - 75$ years; filled circles: $\tau = 75 - 100$ years; open circles: $\tau > 100$ years. The star-shaped points are the recurrent nova systems. The nova systems presented here have not been corrected for extinction as in most cases the reddening is not accurately known, but it is assumed to be small to negligible in the NIR for most Galactic nova systems. The large points for individual nova systems have 1σ uncertainties of ≤ 0.1 magnitudes; smaller points have 1σ uncertainties of > 0.1 magnitudes. The red cross represents the observed quiescent NIR colours of the V1721 Aql nova system. The red line indicates the system's reddening vector with the arrowhead indicating its NIR colours once corrected for an extinction of $A_V = 11.6$. The region enclosed by the red cross-hatching indicates all colours the nova system could possess within the error circle of $A_V = 11.6 \pm 0.2$. A de-reddening vector corresponding to $A_V = 3$ is also shown.

blue and red peaks seen within the $H\alpha$ and OI structures would therefore be the result of material ejected along the poles towards and away from the observer (observations and shaping models predict that the minor axis of a remnant lies in the disc plane; Porter et al., 1998; Slavin et al., 1995). This inclination however would mean that the contribution by the disc to the NIR colours is significant. Taking this blue contribution into account shifts the NIR system colours along the main sequence and into the sub-giant region. Based on the speed and luminosity of the nova, the object may therefore be thought of as a U Sco-type RN system. Comparisons at quiescence between the absolute J band magnitudes and $H-K_s$ colours of V1721 Aql (see Table 6.3), U Sco ($M_J = 1.3 \pm 0.4$, $H - K_s = 0.0 \pm 0.1$ ³³), and V2491 Cyg ($M_J = 1.0 \pm 0.3$, Darnley et al., 2011, a suspected recurrent nova belonging to the U Sco class) support this argument as they all possess similar absolute J magnitudes and occupy the same region of space in an equivalent colour magnitude diagram around the sub-giant branch. The probability of a red giant as the secondary can also be ruled out as the J band absolute magnitude of the system would have to be approximately five magnitudes brighter.

Given the speed of decline of the nova, work by Slavin et al. (1995) would suggest that the axis ratio (ratio of semi-major to semi-minor axis) of Nova V1721 Aql's ejected shell is low (≈ 1). The nova ejecta may therefore be modelled by an approximately spherical shell with discreet randomly distributed knots of brighter emission. Using XS5³⁴, the morphological and kinematical modelling programme (Harman et al., 2003) for producing 3D representations of astrophysical shells, synthetic images, and spectra (see Section 4.7 for detailed discussion on this programme) Nova V1721 Aql's ejecta was modelled. The modelling was conducted by calculating the expected emission line profiles from models of the ejecta distribution and comparing them to observed profiles, specifically $H\alpha$. As stated in Section 4.7 the XS5 program allows the user to generate a geometrical shape, such as an ellipsoid or an hour-glass/bipolar structure, which can be rotated and inclined. By adjusting additional parameters, such as the major and minor axis lengths, the FWHM of line profiles from the shell, the polar axis

³³Photometry taken from (Hanes, 1985), distance and extinction taken from (Schaefer, 2010).

³⁴It should be noted that the version of XS5 used here to generate models of the nova ejecta is precursor of the one used in Chapter 4.

emission gradient, and the expansion velocity, the output emission line profile can be altered until a match with observations is achieved. Models of the nova ejecta with axis ratios between 1.0 and 2.0 (at 0.1 increments) were created. The results of this program are presented in Figures 6.9 and 6.10.

Figure 6.9(c) presents two modelled spectra compared to the observed $H\alpha$ structure. The red spectrum is that of a spherical shell, axis ratio of 1 and the blue spectrum is of an ellipsoidal-like shell with an axis ratio of 1.4. Both shells are smooth with uniform emission, and the inclination of the system is such that the central accretion disc is face-on. Figure 6.10(c) illustrates the results from the same two structures with the same inclination, but this time there is a slight emission enhancement in the equatorial region. From these modelled spectra it would seem that an ellipsoidal-like morphology may actually be more suited to the V1721 Aql ejecta, however there is far too little information to make a strong argument for this. It may be noted that this higher axis ratio is contradictory to expectations in Slavin et al. (1995). However, recent work on the 2010 outburst of U Sco by Drake & Orlando (2010) has indicated that nova ejecta can be significantly shaped by circumbinary gas and/or a high accretion disc gas density. Reproducing the stronger red peak of the $H\alpha$ emission line profile has also not been possible. This could be due to clumps in the ejecta, but more detailed data and modelling are needed to explore this further.

6.6 Discussion and Conclusion

The results presented throughout this Chapter indicate that V1721 Aql is a very fast nova ($t_2 \sim 6$ days) and very luminous ($M_V = -9.4 \pm 0.5$). The extinction of the object is high, $A_V = 11.6 \pm 0.2$ as the nova is very close to the Galactic plane. Based on the value of A_V , the distance to the nova is estimated to be 2.2 ± 0.6 kpc

Pre-outburst NIR colours of the nova have been compared to other novae in quiescence (all post-outburst) and the NIR colours of main sequence and giant stars. The results indicate that, when de-reddened, the nova occupies a region of the colour-colour phase-

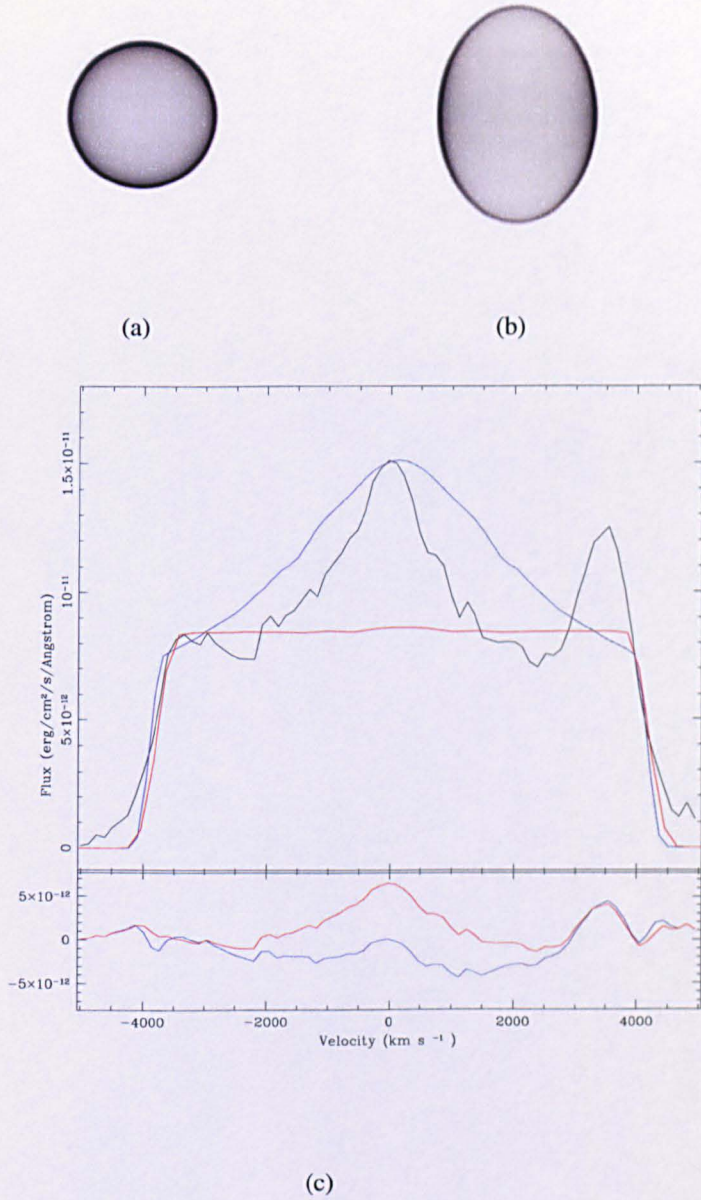


Figure 6.9: (a) Plan view of modelled nova ejecta with an axis ratio of 1. The shell is smooth with uniform emission. (b) Plan view of modelled nova ejecta with an axis ratio of 1.4. Inclination of the system is such that the accretion disc is face-on to the observer, the shell is smooth with uniform emission. (c) Relative velocity diagram of the observed H α (black) structure and the two modelled systems created in XS5. The red line represents the system with an axis ratio of 1, the blue line represents the system with an axis ratio of 1.4. The difference between the modelled and observed line profiles is given in the lower part of the diagram.

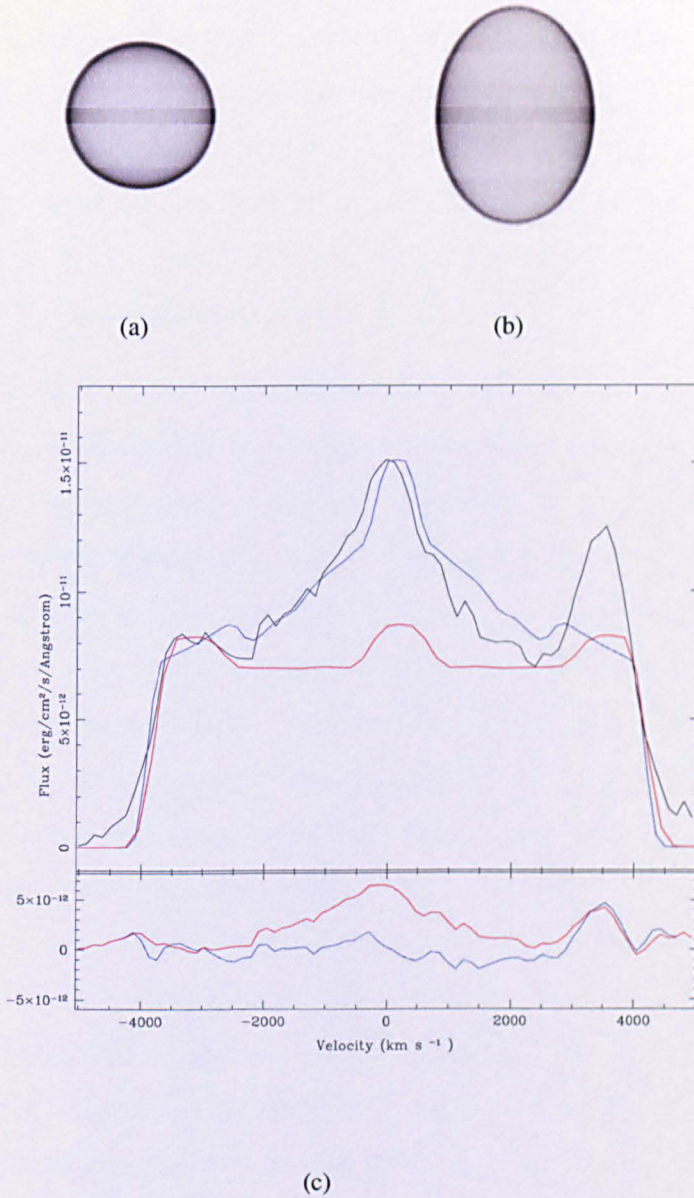


Figure 6.10: (a) Plan view of modelled nova ejecta with an axis ratio of 1. Inclination of the system is such that the accretion disc is face-on to the observer and the shell is smooth with a slight emission enhancement within the equatorial region. (b) Plan view of modelled nova ejecta with an axis ratio of 1.4. Inclination of the system is such that the accretion disc is face-on to the observer, the shell is smooth with a slight emission enhancement within the equatorial region. (c) Relative velocity diagram of the observed H α (black) structure and the two modelled systems created in XS5. The red line represents the system with an axis ratio of 1, the blue line represents the system with an axis ratio of 1.4. The difference between the modelled and observed line profiles is given in the lower part of the diagram.

space in which most CNe are found and appears to have a late (F-M) main sequence secondary or a sub-giant. However, the possibility of V1721 Aql being a RN cannot be ruled out, only that it does not appear to contain a giant secondary and can therefore not belong to the RS Oph or T CrB class of recurrent. The U Sco class of RNe however, consists of an evolved main sequence or sub-giant secondary, much like CNe, and like V1721 Aql, these novae are very fast. Similarities in absolute J band magnitudes at quiescence between V1721 Aql, U Sco, and V2491 Cyg (suspected U Sco member) also indicate that this object may be a U Sco-type RN.

Post-outburst spectra of V1721 Aql revealed boxy structures around $H\alpha$, OI 7773 Å, and OI 8446 Å. It is interesting to note that similar complex $H\alpha$ profiles have been observed in other fast novae such as the 1999 outburst of U Sco (Iijima, 2002), and nova V2672 Oph (2009, Munari et al., 2011a), a suspected U Sco-type object. Examination indicates that the features in V1721 Aql are not contaminated significantly by other emission lines. The structure of the line emission would suggest that material is being ejected from the poles of the nova shell moving towards and away from the observer, leading to the blue and red wing emission seen. This would indicate that the disc of the binary is face-on, an argument which is also supported when considering the high observed ejecta velocities of the system. If the accretion disc were edge-on, concealed velocities would be greater than those observed and this is unlikely. A face-on accretion disc is also more likely when considering the physical reasons for Gaussian 3 of Figure 6.5. This feature may represent a narrow core of $H\alpha$ emission, in which case what is observed is H recombination emission both from the expanding ejecta, which gives rise to the broad overall emission, and emission from a re-established accretion disc, or possibly even a disc that was never completely disrupted.

With a face-on accretion disc the hotter inner region of the disc is exposed possibly giving a significant blue contribution to the NIR colours of the nova and thus seriously affecting previous spectral classification of the secondary. The speed of decline of the nova also suggests that the nova shell itself has a low axis ratio so that it is almost spherical. Basic models generated by XS5 to reproduce the $H\alpha$ line profile, however, produce a best fit when using an ellipsoidal-like shell with an axis ratio 1.4.

The departure from a spherical shell is most likely due to the nature of the explosion environment (circumbinary material and/or high density disc gas; Drake & Orlando, 2010). The model shell produced is smooth with a slight emission enhancement within the equatorial region, again implying a face-on central accretion disc.

Relative velocity shifts found via spectral fitting of the H α and OI emission are comparable to those presented in Helton et al. (2008a) and an ejecta expansion velocity of $V_{exp} = 3400 \pm 200 \text{ km s}^{-1}$ along the line of sight is estimated. This V_{exp} is, perhaps, more consistent with that of a fast classical nova system rather than fast recurrent novae, which tend to have slightly higher expansion velocities of $V_{exp} \gtrsim 4000 \text{ km s}^{-1}$ (Evans et al., 2008).

There is no evidence of emission blue-wards of the H α structure. This is likely due to the high extinction towards the nova. An alternative explanation is that the nova is of the Fe II class and at this stage the shell is still optically thick. However, no dominant lines of Fe II or [Fe II] are present within the spectra. These lines may not have developed yet or may have been lost within the noise of the spectra. Therefore, an Fe II classification cannot be ruled out. Although Fe II novae tend to be slower than V1721 Aql.

The spectra show no conclusive evidence of He and N emission. This may also be due to the low signal-to-noise level within the spectra and the high extinction. No absorption features are seen in the spectra. This is unusual as absorption lines within the optically thick expansion stage are expected.

In conclusion the precise nova sub-class of this object remains elusive, and the results of this work suggest two possibilities. The first is that this is a highly energetic luminous and fast classical nova with a main sequence secondary of spectral type F-M, and that any Fe II lines that may have been observable (i.e it may have been too early for them to have developed) within the nova spectra have simply been extinguished. The second possibility is that this is a U Sco-type RN and that evidence of He/N within the spectra is lost due to the high extinction. The latter scenario may prove itself within the next few decades and therefore this object is one that merits continued monitoring

for future outbursts.

Within the next Chapter a summary of this thesis is presented along with planned future work.

Chapter 7

Summary and Future Work

7.1 Summary of Thesis Research

The results of the research conducted within this thesis are discussed below.

7.1.1 Examination of Extragalactic Novae

Using the Liverpool Telescope and Faulkes Telescope North, photometry of extragalactic novae was obtained over a three year period. Each observation was quality checked with many of the M31 novae observed used within Shafter et al. (2011). This paper examined the distribution of various speed and spectroscopic classes of novae within M31 in an attempt to fully understand nova populations within the galaxy.

7.1.2 The Planetary Nebula Surrounding Nova V458 Vulpeculae

The shapes observed in many planetary nebulae (PNe) are thought to be caused by binary systems and their evolution, with various system components and parameters leading to certain morphologies. The observation and modelling of PNe which have had novae occur within them provide a vital insight into pre-outburst nova evolution. The outbursts of both GK Per (Bode et al., 1987) and V458 Vul (Wesson et al., 2008)

occurred in PNe and were accompanied by light echoes (Couderc, 1939; Kapteyn, 1901; Wesson et al., 2008). Light from the eruptive variable is scattered by dust or re-emitted by gas in its vicinity, reaching the Earth at progressively later times as the wave of illumination is seen to propagate outwards. For astronomical purposes each echo surface is well approximated by a paraboloid.

Using the LT, 14 epochs of $H\alpha$ imaging of Nova V458 Vul were obtained after outburst. Data were also obtained from the INT, NOT, and WHT (observations made by groups outside of the ARI), giving a total of 19 epochs between July 2008 and October 2011. As described in this thesis all data have been reduced and field stars subtracted via PSF modelling in IRAF to isolate the PN. A C-language code was then used to combine the resultant images into a 3D FITS data cube with each image projected on to its appropriate paraboloid echo surface. Using XS5 a series of PN structures were generated over a range of geometric parameters and distances, and the passage of the light echo through these structures modelled. Through the comparison of the observed PN light echo data to the modelled PN light echo data a brute force χ^2 test was conducted and a PN structure with the following parameters obtained: PA1 = 28°, IN1 = 90°, A1A = 20", B1A = 6", A2A = 16", B2A = 4", FLUX ratio = 0.20, FALL = 80 days, DIST = 13 kpc³⁵. Here the external shell is modelled as a bipolar structure and the internal as an ellipsoid. It should be noted that the distance derived is consistent with results presented in Wesson et al. (2008). On application of a Gaussian to the distances obtained for the top 1% of PN configurations a value of 13.6 ± 0.9 kpc was derived. This however assumes a normalised distribution which may not be the case and can not be taken as a true value. The PN model was generated using a very coarse set of parameters and based on these initial results an additional brute force test is currently being conducted using much a much finer parameter space (see Section 7.2.1 for future work on this object).

³⁵Again it should be noted that these results are preliminary and will suffer from the same error as mentioned in footnote 16 (page 80). However, for the reasons mentioned within footnote 16 the conclusions are believed to be valid within the uncertainties of the analysis.

7.1.3 Nova Aquilae (2008)

In collaboration with Dr G. Schwarz (West-Chester University/American Astronomical Society) and Dr L. A. Helton (SOFIA Science Center/University of Minnesota), Nova V1721 Aql was studied. Within this investigation available pre- and post-outburst photometry and post-outburst spectroscopy (obtained by the Steward Observatory Bok 2.29m telescope on Kitt peak via the Boller & Chivens optical spectrograph) were used to conclude that the object is a very fast, luminous, and highly extinguished ($A_V = 11.6 \pm 0.2$) nova system with an average ejection velocity of 3350 km s^{-1} . Pre-outburst NIR colours from the 2MASS point source catalogue indicated that at quiescence the object is similar to many quiescent classical novae and appears to have a main sequence/sub-giant secondary rather than a giant counterpart. Based on the speed of decline of the nova and its emission line profiles it was hypothesised that the axis ratio of the nova ejecta is ~ 1.4 and that its inclination is such that the central binary accretion disc is face-on to the observer. As such, the accretion disc's blue contribution to the system's NIR quiescent colours may be significant. Simple models of the nova ejecta were constructed using the morphological modelling code XS5, and the results supported the above hypothesis. Precise spectral classification of this object proved to be exceptionally difficult owing to low signal-to-noise levels and high extinction, which has eliminated all evidence of any He/N or Fe II emission within the spectra. Two possibilities are suggested for the nature of V1721 Aql: that it is a U Sco type RN with a sub-giant secondary or, less likely, that it is a highly energetic bright and fast classical nova with a main sequence secondary. Future monitoring of the object for possible RN episodes may be worthwhile, as would archival searches for previous outbursts.

The results of this work have been published in Hounsell et al. (2011a) and it has been extended in Darnley et al. (2012) where NIR colours and absolute magnitudes are used to indicate the separations between the various subclasses of RNe (T Pyx, U Sco, RS Oph) and between CNe. Further NIR observations of novae pre- and post-outburst would refine accretion disc inclination and colour change relations and thus aid in the fundamental classification of system secondary and nova type.

An important topic within the nova field today is the relation between ejecta shape and speed class. Slavin et al. (1995) find that fast novae should be modelled by randomly distributed clumps of ejecta superimposed on a spherical shell, whilst slow novae should have a more structured ellipsoid remnant with rings of enhanced emission. Recent work by Drake & Orlando (2010) on the ejecta of U Sco however suggests that the ejecta shape is much more influenced by environmental factors such as circumstellar material and the gas density and mass of the accretion disc, rather than the speed class. A similar conclusion has been reached through the modelling V1721 Aql's ejecta as described within Hounsell et al. (2011a). It is evident that more detailed investigations of additional ejecta novae where possible are required to further test this hypothesis.

7.1.4 Examination of Novae using data from the Solar Mass Ejection Imager (SMEI)

In collaboration with Dr B. V. Jackson, Dr A. Buffington, Dr P. Hick, and J. M. Clover of the University of California San Diego (UCSD) and Prof. A. W. Shafter of San Diego State University (SDSU, USA) exceptionally detailed light curves of three CNe (KT Eri, V1280 Sco, V598 Pup) and two RNe (RS Oph and T Pyx) were obtained and analysed (Hounsell et al., 2011b). These light curves have been derived using data from SMEI, a space-borne instrument based on-board the Coriolis satellite (in operation since 2003, Buffington et al., 2007; Eyles et al., 2003; Jackson et al., 2004). SMEI provides near complete sky-map coverage with precision visible-light photometry at 102-minute cadence, and was originally designed to map coronal mass ejections from the Sun (Buffington et al., 2007; Jackson et al., 2004). As a by-product of its original purpose the instrument is able to detect brightness changes in point sources down to $\sim 8^{\text{th}}$ magnitude. Light curves were obtained by fitting each nova to a standard PSF using a least-squares fitting procedure implemented in IDL (Hick et al., 2005, 2007).

The light curves derived from the SMEI sky-maps offer unprecedented temporal resolution around, and especially before, maximum light, a phase of the nova eruption

normally not covered by ground-based observations. They have allowed the exploration of fundamental parameters for individual objects including the epoch of the initial explosion, the reality and duration of any pre-maximum halt (found in all fast novae examined), the presence of secondary maxima, speed of decline of the initial light curve, plus precise timing of the onset of dust formation (in V1280 Sco) leading to estimation of the bolometric luminosity, WD mass and object distance.

The undeniable evidence provided by these light curves for the existence of the previously controversial pre-maximum halt, with accurate times of occurrence, duration, and magnitude below peak given is a challenge to detailed models of the nova outburst. This work has also indicated that there does not seem to be a correlation between the properties of the pre-maximum halt (Δm_{SMEI} , Δt , number of magnitudes below maximum, and time before peak) and the properties of the nova or its eruption (speed class), although the sample size is admittedly small at present.

For KT Eri, Liverpool Telescope SkyCamT data confirm important features of the SMEI light curve. The overall results for KT Eri add weight to the proposed similarities between it and RNe rather than to CNe. In RS Oph, comparison with hard X-ray data from the 2006 outburst implies that the onset of the outburst coincides with extensive high-velocity mass loss. It is also noted that two of the four novae detected (V598 Pup and KT Eri) were only discovered by ground-based observers weeks or months after maximum light, yet these novae reached peak magnitudes of 3.46 and 5.42, respectively. This emphasizes the fact that many bright novae per year are still overlooked, particularly those of the very fast speed class. The results of this work were published as a collaborative paper in Hounsell et al. (2010a).

A number of fainter novae were also examined the using SMEI data and where possible accurate dates and magnitudes for peak, along with decline time obtained. The light curves of these novae not only illustrate any small variations they may experience, but also highlight the limitations of the SMEI detector.

In collaboration with UCSD a code to search for transient and variable events within the SMEI sky-maps has been updated and will soon be implemented. An initial search

conducted on four years of SMEI data from Camera 2 generated over 1500 object files. Examination of these data revealed that the majority of objects were within the GCVS and/or were the result of poor subtraction of the bright SMEI catalogued stars. Some objects however remained unidentified and are potentially very interesting (see Section 5.7.2).

Overall, the data provided by SMEI may well have opened a new chapter in our observation and understanding of novae. The work conducted on SMEI has also highlighted how important it is to examine all-sky data from a variety of sources with regards to transient events and variable objects in general.

7.2 Future Work to be Conducted

Future work to be conducted on areas of research presented within this thesis are discussed below.

7.2.1 Modelling of the PN Surrounding V458 Vulpeculae

Although a PN structure with an ellipsoidal internal shell and bipolar external shell have been derived, refinement of this structure's geometric parameters is required. This is currently being conducted using values derived from the results of the brute force test presented in Section 4.7.2³⁶ (see Table 4.4). The results of this secondary test should produce a more accurate PN model.

Within the brute force test, several assumptions were made, the most prominent of which being the assumption that the internal shell is an ellipsoid. This shape was chosen for simplicity. However, for completion additional tests should be implemented using both spherical and bipolar structures. The position angle of the internal shell should also be allowed to alter from that of the external. A "uniform" illumination of each shell was also assumed again for simplicity, but this may not be the case and

³⁶Results of the first initial brute force test are also being recomputed using the correct seeing of 1.9" to confirm previously obtained results.

Table 7.1: Refined parameters used within χ^2 test.

Test Refine: RISE=1 day	
FALL (days)	75 80 85 90 95 100 105
DIST (pc)	12500, 12750, 13000, 13250, 13500 13750, 14000, 14250, 14500, 14750
PA1°	27, 28, 29, 30, 31
IN1°	85, 86, 87, 88, 89, 90
A1A''	18, 19, 20, 21, 22, 23
B1A''	4, 5, 6, 7, 8
FLUX factor	0.1, 0.15, 0.2, 0.25
A2A''	11, 12, 13, 14, 15
B2A''	3, 4, 5, 6

further testing may be required. On completion of all additional tests a similar model will be constructed in *Shape* (Steffen & Lopez, 2006)³⁷ for comparison. It may also be appropriate to reproduce the stellar environment of the modelled PN, i.e with the central nova system and surrounding bright stars added. This will aid in the validation of the PN model.

Within this work a halo to the PN has not been observed. This could be as a consequence of the image processing used, or that it is simply too faint. However, over time the halo may become illuminated by the light echo (if it has not yet already been) allowing further analysis of the system. Additional observations of the object are therefore required.

Results of this work are being written up for publication in MNRAS.

7.2.2 The SMEI Data Archive

The future work to be conducted on the SMEI data set in the collaboration between LJMU and UCSD can be divided into three sections.

1. **Search for undetected bright Galactic novae:** As mentioned in Section 5.8 Shafter (2002) estimates that as many as six novae with maxima brighter than 8th magnitude may occur each year. However, of these only one or two tend to

³⁷<http://www.astrosen.unam.mx/shape/>

be observed, and these are discovered mainly by the amateur community. The estimate provided by Shafter (2002) suggest that over 50 novae may be found within the SMEI data archive, 60-80% of which will be unknown. Examination of the SMEI archive for such bright novae will potentially enable a more accurate determination of the nova rate within our Galaxy and their distribution.

2. **Search for exotic transients:** Work by various authors (e.g. Kasliwal & Kulkarni, 2009) has indicated that there is a clear luminosity gap between novae and SNe (see Figure 7.1). Surveys such as the Catalina Real-Time Transient Survey (CRTS), the Palomar Transient Factory (PTF), and Pan-STARRS are exploring this gap looking at Galactic and Extragalactic objects. On a Galactic scale however SMEI with its high cadence may provide invaluable data. Work by Yaron et al. (2005) and Shara et al. (2010) has indicated that the ranges of WD masses, temperatures, and accretion rates that can be numerically applied to produce novae are broader than previously thought. This means that there may be “extreme novae” within galaxies with eruption luminosities, metallicities, ejecta masses and velocities significantly greater or smaller than currently observed. A search of the SMEI archive may reveal several of these “extreme novae as well as previously undetected exotic luminous transients found within the luminosity gap.
3. **Examination and detection of variables:** Obtaining light curves of variable objects over long time-scales typical of the photometric behaviour of the variable star gives us information on the physical processes which are responsible for the observed brightness and colour variations. SMEI is able to produce an 8.5 year base-line for such variables with very high cadence and high photometric accuracy and thus potentially producing very valuable data. Initial analysis (see Section 5.7.2) has indicated that several of the variables that may be detected by SMEI may not be found within the GCVS and will be previously unidentified.

In order to find bright novae, exotic transients, and variable stars (catalogued and uncatalogued) *smei_findpnt* described in Section 5.7.2 will be implemented on all 8.5 years of SMEI data for all three cameras. This will be conducted with *fix_centroid* on

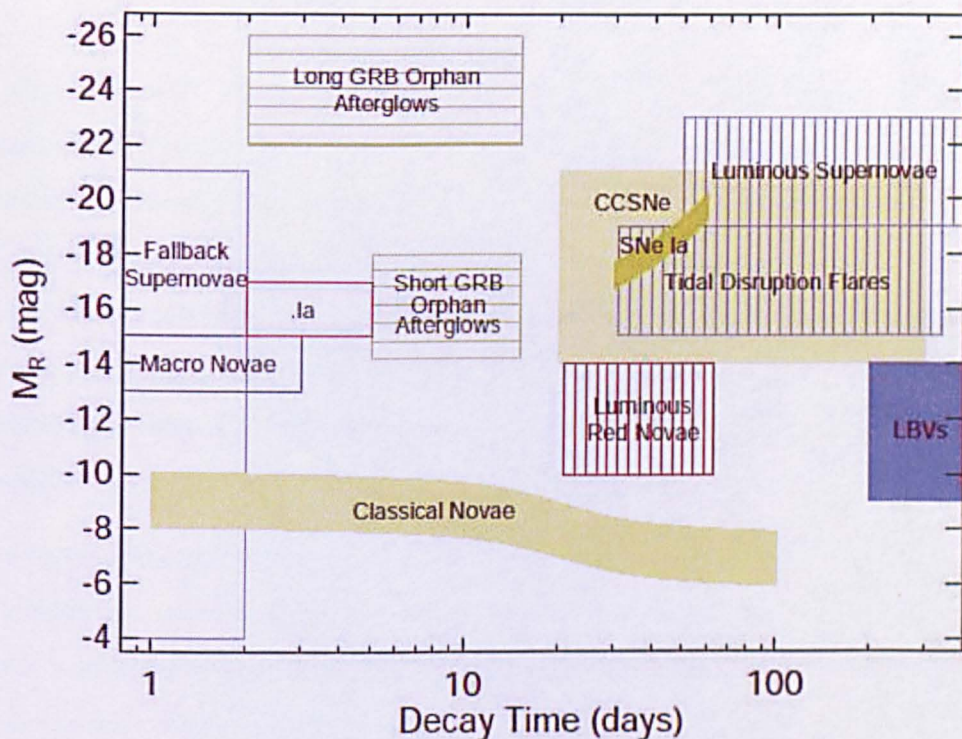


Figure 7.1: R-band peak magnitude as a function of characteristic decay time-scale (typically the time to fade from peak by 2 magnitudes) for luminous optical transients and variables. Filled boxes mark well-studied classes with a large number of known members (classical novae, Type Ia supernovae [SNe Ia], core-collapse supernovae [CCSNe], luminous blue variables [LBVs]). Vertically hatched boxes show classes for which only few (≤ 4) candidate members have been suggested so far (luminous red novae, tidal disruption flares, luminous supernovae). Horizontally hatched boxes are classes which are believed to exist, but have not yet been detected (orphan afterglows of short- and long GRBs). The positions of theoretically predicted events (fall-back supernovae, macronovae, .Ia supernovae [.Ia]) are indicated by empty boxes. The brightest transients (on-axis afterglows of GRBs) and events detectable predominantly in the Milky Way (e.g., dwarf novae) are omitted for clarity. Regions indicate the general location of each class and are not exclusive. The color of each box corresponds to the mean $g - r$ color at peak (blue, $g - r < 0$ mag; green, $0 < g - r < 1$ mag; red, $g - r > 1$ mag). Image and adapted caption taken from Rau et al. (2009).

in order to obtain the greatest accuracy in position (rms 0.05°) for the candidate objects detected.

To sort candidates found by *smei_findpnt* into their individual object files a modified version of the *smei_sort* program (see Section 5.7.2) will be written in C or IDL. This code will not only sort objects via RA and Dec but will also exclude regions around the edge of cameras within a 1° radius (and the Sunwards and anti-Sunward masks) preventing the detection of tails caused by bright objects and so false positives (see list of issues in Section 5.7.2). Multiple detections of the same object within the upper and lower regions of the EQ, SP, and NP maps must also be taken into account within this code and will be done via a search of matching RA and Dec ($\pm 0.1^\circ$). When such an event occurs the NP or SP detection will be deleted leaving only the EQ detection, unless the EQ detection lies within Camera 3 (the camera suffering from the worst degeneration, see Section 5.2) in which case the NP or SP detection will be kept.

Whilst conducting the initial analysis discussed in Section 5.7.2 it was noted that transients such as novae were not originally detected. This was because the threshold for the number of hits per HEALPix pixel was set too high (~ 100). By lowering this threshold, novae were detected. When constructing the modified version of the *smei_sort* code pixels which are found to have limited number of sequential hits (say 20-200) will create object files which are flagged as possible transients. This flagging will enable quick identification of possibly interesting objects.

On creation of individual object files and initial flagging, files will then be passed through a peak finding code which is currently in construction using C. Within this code a peak is defined based on the number of sequential hits above or below a certain number of sigma from the weighted mean of the data. Objects may then be flagged based on the number of peaks detected and the number of sigma that the maximum peak value lies above the mean. This will then enable a simple classification of objects.

Single-peaked objects detected with this method will be examined in greater detail within the SMEI archive. Using the raw data (maps in which the bright stars, zodiacal model, and sidereal background have not been subtracted) a visual inspection of

the maps will be conducted over the time line of the event, along with examination of surrounding region for bright stars. A new light curve of the object will then be generated from the raw maps using the method described in Section 5.3. This will create the best light curve for the object under examination. Based on the morphology of the light curve generated, nova classification may be applied. However, follow-up observations of the object in quiescence may be required and can be obtained via the LT and additional facilities.

For variable objects with multiple peaks over the SMEI time-line such visual inspection and fitting from the raw SMEI maps will prove impossible. For such situations the scatter of each light curve must be measured and spurious points removed via a comparison to this value. For long base-line light curves the degradation of each camera over the years and any offsets between cameras must also be taken into account. To obtain a measure of this degradation and of the offset light curves of bright non-varying stars will be created for the entire 8.5 year span and calibration calculations constructed for application to each variable object. It has been noted within Buffington et al. (2007) that the response of each camera is seen to diminish at about 1.6% per year. This however is expected to be much larger for Camera 3.

Only when all light curves have been created and corrected, the position of each object will then be run through the GCVS and other catalogues as before and possible identification obtained. Objects which are not found within the GCVS etc. will warrant further more detailed investigation with other facilities such as the LT.

As mentioned earlier, the non-iterative fitting of the brighter than 6th magnitude stars and their position has left residuals within the variable maps. Iterative fitting of these objects is currently being conducted via the supercomputer facility at UCSD. This procedure should produce variable maps of greater quality, containing less residuals and so false positives. This procedure however may take some time, and as such the initial search for objects will be conducted on the variable maps which are currently in possession. Fitting of the bright objects from the raw data using the supercomputer will also produce detailed light curves allowing examination of variable objects at and above 6th magnitude within the SMEI catalogue list.

In Section 5.3.2 it was noted that star crowding with the SMEI data can become an issue especially within a few degrees of the Galactic plane. As such novae within this region may be missed. As well as fitting each PSF via the least squares fit an alternative method may be implemented using the raw SMEI maps. Such a method could involve the use of IRAF's *DAOPHOT* routines as mentioned in Spreckley & Stevens (2007) or via Starlink's *SExtractor*³⁸. As such time-series of all objects as well as the brighter than 6th magnitude may be obtained as well as the fainter uncatalogued SMEI objects. Such a method may also take into account the quality of the data (weighting the value of the star flux obtained by the background flux sampled) and thus reduce the number of corrections to be applied to each light curve. The additional methods mentioned will also allow the examination of the 6th magnitude and brighter variables within the raw maps. These methods, however will again require more time and thought.

Complementary data of certain objects extending down to 13th magnitude may also be obtained through the used of STEREO HI as described in Section 5.6.

The SMEI archive could be harbouring many fascinating objects the physics of which may be of vital importance in the understanding many astrophysical processes. This archive therefore warrants thorough further examination.

³⁸<http://sextractor.sourceforge.net/>

Bibliography

- A. Evans, M. F. Bode, T. J. O'Brien, & M. J. Darnley, ed. 2008, *Astronomical Society of the Pacific Conference Series*, Vol. 401, RS Ophiuchi (2006) and the Recurrent Nova Phenomenon
- Abell, G. O., & Goldreich, P. 1966, *PASP*, 78, 232
- Adamakis, S., Eyres, S. P. S., Sarkar, A., & Walsh, R. W. 2011, *MNRAS*, 504
- Anupama, G. C., & Mikołajewska, J. 1999, *A&A*, 344, 177
- Balick, B., Perinotto, M., Maccioni, A., Terzian, Y., & Hajian, A. 1994, *ApJ*, 424, 800
- Bath, G. T. 1978, *MNRAS*, 182, 35
- Bath, G. T., & Shaviv, G. 1976, *MNRAS*, 175, 305
- Bode, M. F. 1979, PhD thesis, Thesis, Univ. Keele, Staffs., England
- . 2010, *Astronomische Nachrichten*, 331, 160
- Bode, M. F., & Evans, A. 2008, *Classical Novae* (Cambridge University Press)
- Bode, M. F., Roberts, J. A., Whittet, D. C. B., Seaquist, E. R., & Frail, D. A. 1987, *Nature*, 329, 519
- Bode, M. F., et al. 2006, *ApJ*, 652, 629
- . 2010, *The Astronomer's Telegram*, 2392, 1
- Bohigas, J., Echevarria, J., Diego, F., & Sarmiento, J. A. 1989, *MNRAS*, 238, 1395

- Bond, H. E. 1994, in *Astronomical Society of the Pacific Conference Series*, Vol. 56, *Interacting Binary Stars*, ed. A. W. Shafter, 179
- Brown, D. S., Bewsher, D., & Eyles, C. J. 2009, *SolarPhys*, 254, 185
- Buffington, A., Band, D. L., Jackson, B. V., Hick, P. P., & Smith, A. C. 2006, *ApJ*, 637, 880
- Buffington, A., Morrill, J. S., Hick, P. P., Howard, R. A., Jackson, B. V., & Webb, D. F. 2007, in *Presented at the Solar Physics and Space Weather Instrumentation II (SPIE) Conference*, Vol. 6689, *Solar Physics and Space Weather Instrumentation II*, ed. S. Fineschi & R. A. Viereck, 66890B1–66890B6
- Burwitz, V., et al. 2010, *Central Bureau Electronic Telegrams*, 2124, 1
- Buscombe, W., & de Vaucouleurs, G. 1955, *The Observatory*, 75, 170
- Capaccioli, M., della Valle, M., Rosino, L., & D'Onofrio, M. 1989, *AJ*, 97, 1622
- Carrier, F., Barblan, F., Burki, G., Bartholdi, P., & Nicolet, B. 2003, *A&A*, 398, 1073
- Chandrasekhar, S. 1931, *ApJ*, 74, 81
- Chesneau, O., et al. 2008, *A&A*, 487, 223
- Chomiuk, L., et al. 2011, *The Astronomer's Telegram*, 3318, 1
- Chu, Y.-H. 1989, in *IAU Symposium*, Vol. 131, *Planetary Nebulae*, ed. S. Torres-Peimbert, 105–115
- Chu, Y.-H., Jacoby, G. H., & Arendt, R. 1987, *ApJS*, 64, 529
- Ciardullo, R., Ford, H. C., Neill, J. D., Jacoby, G. H., & Shafter, A. W. 1987, *ApJ*, 318, 520
- Ciardullo, R., Shafter, A. W., Ford, H. C., Neill, J. D., Shara, M. M., & Tomaney, A. B. 1990a, *ApJ*, 356, 472
- Ciardullo, R., Tamblyn, P., Jacoby, G. H., Ford, H. C., & Williams, R. E. 1990b, *AJ*, 99, 1079

- Clover, J., Jackson, B. V., Buffington, A., Hick, P. P., Kloppenborg, B., & Stencel, R. 2011, in *Bulletin of the American Astronomical Society*, Vol. 43, American Astronomical Society Meeting Abstracts 217, 257.02
- Cohen, J. G. 1985, *ApJ*, 292, 90
- Collazzi, A. C., Schaefer, B. E., Xiao, L., Pagnotta, A., Kroll, P., Löchel, K., & Henden, A. A. 2009, *AJ*, 138, 1846
- Corradi, R. L. M., & Schwarz, H. E. 1995, *A&A*, 293, 871
- Couderc, P. 1939, *Annales d'Astrophysique*, 2, 271
- Cox, A. N., ed. 2000, *Allen's astrophysical quantities* (New York: AIP Press)
- Crause, L. A., Lawson, W. A., Menzies, J. W., & Marang, F. 2005, *MNRAS*, 358, 1352
- Cropper, M. 1990, *Space Science Reviews*, 54, 195
- Curtis, H. D. 1918, *Publications of Lick Observatory*, 13, 55
- Darnley, M. J., Ribeiro, V. A. R. M., Bode, M. F., Hounsell, R. A., & Williams, R. P. 2012, *ApJ*, 746, 61
- Darnley, M. J., Ribeiro, V. A. R. M., Bode, M. F., & Munari, U. 2011, *A&A*, 530, A70
- Darnley, M. J., et al. 2004, *MNRAS*, 353, 571
- . 2006, *MNRAS*, 369, 257
- Das, R. K., Banerjee, D. P. K., Ashok, N. M., & Chesneau, O. 2008, *MNRAS*, 391, 1874
- de Kool, M. 1992, *A&A*, 261, 188
- de Marco, O. 2009, *PASP*, 121, 316
- de Vaucouleurs, G. 1978, *ApJ*, 223, 351
- Delfosse, X., Kahane, C., & Forveille, T. 1997, *A&A*, 320, 249

- della Valle, M., Bianchini, A., Livio, M., & Orio, M. 1992, *A&A*, 266, 232
- della Valle, M., & Livio, M. 1995, *ApJ*, 452, 704
- Dominguez, I., Tornambe, A., & Isern, J. 1993, *ApJ*, 419, 268
- Dougherty, S. M., Waters, L. B. F. M., Bode, M. F., Lloyd, H. M., Kester, D. J. M., & Bontekoe, T. R. 1996, *A&A*, 306, 547
- Downes, R. A., & Duerbeck, H. W. 2000, *AJ*, 120, 2007
- Downes, R. A., Webbink, R. F., Shara, M. M., Ritter, H., Kolb, U., & Duerbeck, H. W. 2005, *Journal of Astronomical Data*, 11, 2
- Drake, A. J., et al. 2009, *The Astronomer's Telegram*, 2331, 1
- Drake, J. J., & Orlando, S. 2010, *ApJ Let.*, 720, L195
- Drew, J. E., et al. 2005, *MNRAS*, 362, 753
- Duerbeck, H. W. 1990, in *Lecture Notes in Physics*, Berlin Springer Verlag, Vol. 369, IAU Colloq. 122: Physics of Classical Novae, ed. A. Cassatella & R. Viotti, 34
- Duerbeck, H. W. 2008, *Nove: an historical perspective* (Cambridge University Press)
- Duncan, J. C. 1937, *ApJ*, 86, 496
- Evans, A., Bode, M. F., O'Brien, T. J., & Darnley, M. J., eds. 2008, *Astronomical Society of the Pacific Conference Series*, Vol. 401, RS Ophiuchi (2006) and the Recurrent Nova Phenomenon
- Evans, A., & Rawlings, J. A. C. 2008, *Dust and molecules in nova environments* (Cambridge University Press), 308
- Eyles, C. J., et al. 2003, *SolarPhys*, 217, 319
- . 2009, *SolarPhys*, 254, 387
- Fabrika, S., Sholukhova, O., Valeev, A., Hornoch, K., Kusnirak, P., & Pietsch, W. 2009a, *Central Bureau Electronic Telegrams*, 1971, 3

- Fabrika, S., Sholukhova, O., Valeev, A., Hornoch, K., & Pietsch, W. 2009b, *The Astronomer's Telegram*, 2239, 1
- Filippenko, A. V. 1997, *ARA&A*, 35, 309
- Frank, A. 1994, *AJ*, 107, 261
- . 1999, *New Astronomy Reviews*, 43, 31
- Gänsicke, B. T., Beuermann, K., & Reinsch, K., eds. 2002, *Astronomical Society of the Pacific Conference Series*, Vol. 261, *The physics of cataclysmic variables and related objects : proceedings of a conference on the occasion of Klaus Beuermann's impending 65th birthday held in Göttingen, Germany, 5-10 August 2001*, ed. B. T. Gänsicke, K. Beuermann, & K. Reinsch
- Gaposchkin, C. H. P. 1957, *The galactic novae*. (Amsterdam, North-Holland Pub. Co.; New York, Interscience Publishers, 1957.)
- Gehrz, R. D. 2008, *Infrared studies of classical novae* (Cambridge University Press)
- Gehrz, R. D., Truran, J. W., Williams, R. E., & Starrfield, S. 1998, *PASP*, 110, 3
- Gonçalves, D. R., Corradi, R. L. M., & Mampaso, A. 2001, *ApJ*, 547, 302
- Hachisu, I., & Kato, M. 2004, *ApJ Let.*, 612, L57
- . 2010, *ApJ*, 709, 680
- Hachisu, I., et al. 2006, *ApJ Let.*, 651, L141
- Hanes, D. A. 1985, *MNRAS*, 213, 443
- Harman, D. J., Bryce, M., O'Brien, T. J., & Meaburn, J. 2003, in *IAU Symposium*, Vol. 209, *Planetary Nebulae: Their Evolution and Role in the Universe*, ed. S. Kwok, M. Dopita, & R. Sutherland, 531
- Harrison, T. E. 1992, *MNRAS*, 259, 17P
- Helton, L. A., Woodward, C. E., Vanlandingham, K., & Schwarz, G. J. 2008a, *IAU Circ.*, 8989, 2

- . 2008b, *Central Bureau Electronic Telegrams*, 1379, 1
- Henden, A., & Munari, U. 2008, *Information Bulletin on Variable Stars*, 5822, 1
- Henze, M., Kaduk, F., Burwitz, V., Pietsch, W., Papamastorakis, G., Reig, P., & Strigachev, A. 2009, *The Astronomer's Telegram*, 2165, 1
- Henze, M., Pietsch, W., Burwitz, V., Hatzidimitriou, D., Reig, P., Primak, N., & Papamastorakis, G. 2008, *The Astronomer's Telegram*, 1790, 1
- Hernanz, M. 2005, in *Astronomical Society of the Pacific Conference Series*, Vol. 330, *The Astrophysics of Cataclysmic Variables and Related Objects*, ed. J.M. Hameury & J.-P. Lasota, 265
- Hernanz, M., & José, J. 2008, *New Astronomy Review*, 52, 386
- Herschel, W. 1784, *Royal Society of London Philosophical Transactions Series I*, 74, 233
- . 1785, *Royal Society of London Philosophical Transactions Series I*, 75, 213
- . 1791, *Royal Society of London Philosophical Transactions Series I*, 81, 71
- Hick, P., Buffington, A., & Jackson, B. V. 2005, in *Society of Photo-Optical Instrumentation Engineers (SPIE) Conference Series*, ed. S. Fineschi & R. A. Viereck, Vol. 5901, 340–346
- Hick, P., Buffington, A., & Jackson, B. V. 2007, in *Presented at the Solar Physics and Space Weather Instrumentation II (SPIE) Conference*, ed. S. Fineschi & R. A. Viereck, Vol. 6689, C1
- Hoard, D. W., Wachter, S., Clark, L. L., & Bowers, T. P. 2002, *ApJ*, 565, 511
- Hounsell, R., Darnley, M. J., Bode, M. F., Harman, D. J., Helton, L. A., & Schwarz, G. J. 2011a, *A&A*, 530, A81+
- Hounsell, R., et al. 2010a, *ApJ*, 724, 480
- . 2010b, *The Astronomer's Telegram*, 2558, 1

- . 2011b, *The Astronomer's Telegram*, 3373, 1
- Howell, S. B., Nelson, L. A., & Rappaport, S. 2001, *ApJ*, 550, 897
- Hubble, E. P. 1922, *ApJ*, 56, 400
- . 1929, *ApJ*, 69, 103
- Hyland, A. R., & Neugebauer, G. 1970, *ApJ Let.*, 160, L177
- Iben, Jr., I., & Tutukov, A. V. 1984, *ApJS*, 54, 335
- Iijima, T. 2002, *A&A*, 387, 1013
- Irwin, M., & Lewis, J. 2001, *New Astronomy Reviews*, 45, 105
- Itagaki, K. 2009, *Central Bureau Electronic Telegrams*, 2050, 1
- Jackson, B. V., et al. 2004, *SolarPhys*, 225, 177
- Kapteyn, J. C. 1901, *Astronomische Nachrichten*, 157, 201
- Kasliwal, M. M., Cenko, S. B., Ofek, E. O., Quimby, R., Rau, A., & Kulkarni, S. R. 2009, *The Astronomer's Telegram*, 1934, 1
- Kasliwal, M. M., Cenko, S. B., Rau, A., Ofek, E. O., Quimby, R., & Kulkarni, S. R. 2008, *The Astronomer's Telegram*, 1826, 1
- Kasliwal, M. M., & Kulkarni, S. 2009, in *Bulletin of the American Astronomical Society*, Vol. 41, American Astronomical Society Meeting Abstracts #213, #469.08
- Kato, M. 1991, *ApJ*, 369, 471
- Kato, T., Uemura, M., Haseda, K., Yamaoka, H., Takamizawa, K., Fujii, M., & Kiyota, S. 2002, *PASJ*, 54, 1009
- Kovács, G., Zucker, S., & Mazeh, T. 2002, *A&A*, 391, 369
- Kovetz, A., Prialnik, D., & Shara, M. M. 1988, *ApJ*, 325, 828
- Kraft, R. P. 1964, *Leaflet of the Astronomical Society of the Pacific*, 9, 137

- Kunszt, P. Z., Szalay, A. S., & Thakar, A. R. 2001, in *Mining the Sky*, ed. A. J. Banday, S. Zaroubi, & M. Bartelmann (Springer-Verlag), 631
- Kuulkers, E., et al. 2011, *The Astronomer's Telegram*, 3285, 1
- Kwok, S. 2000, *The Origin and Evolution of Planetary Nebulae* (Cambridge University Press)
- Kwok, S., Dopita, M., & Sutherland, R., eds. 2003, *IAU Symposium, Vol. 209, Planetary Nebulae: Their Evolution and Role in the Universe*
- Kwok, S., Purton, C. R., & Fitzgerald, P. M. 1978, *ApJL*, 219, L125
- Landolt, A. U. 1970, *PASP*, 82, 86
- Lee, T. A. 1970, *ApJ*, 162, 217
- Li, W., et al. 2011, *ArXiv e-prints*
- Liller, W. 2008, *IAU Circ.*, 9004, 1
- Liller, W., Tabur, V., Williams, P., Templeton, M., Nelson, P., Skiff, B. A., & Kazarovets, E. 2008, *IAU Circ.*, 8990, 2
- Livio, M. 1992, *ApJ*, 393, 516
- Livio, M. 1993, in *IAU Symposium, Vol. 155, Planetary Nebulae*, ed. R. Weinberger & A. Acker, 279
- Lloyd, H. M., O'Brien, T. J., & Bode, M. F. 1997, *MNRAS*, 284, 137
- Lynch, D. K., et al. 2006, *ApJ*, 638, 987
- MacDonald, J. 1980, *MNRAS*, 191, 933
- Manchado, A., Guerrero, M. A., Stanghellini, L., & Serra-Ricart, M. 1996, *The IAC morphological catalog of northern Galactic planetary nebulae (La Laguna, Spain: Instituto de Astrofísica de Canarias (IAC))*
- McLaughlin, D. B. 1945, *PASP*, 57, 69

- McLaughlin, D. B. 1960, in *Stellar Atmospheres*, ed. J. L. Greenstein, 585
- Munari, U., Dalla Via, G., Valisa, P., Dallaporta, S., & Castellani, F. 2007a, *Central Bureau Electronic Telegrams*, 897, 1
- Munari, U., Ribeiro, V. A. R. M., Bode, M. F., & Saguner, T. 2011a, *MNRAS*, 410, 525
- Munari, U., Siviero, A., Dallaporta, S., Cherini, G., Valisa, P., & Tomasella, L. 2011b, *New Astronomy*, 16, 209
- . 2011c, *New Astronomy*, 16, 209
- Munari, U., Valisa, P., Dalla Via, G., & Dallaporta, S. 2007b, *Central Bureau Electronic Telegrams*, 852, 1
- Naik, S., Banerjee, D. P. K., & Ashok, N. M. 2009, *MNRAS*, 394, 1551
- Nakano, S. 2009, *Central Bureau Electronic Telegrams*, 1659, 1
- Nakano, S., Kadota, K., Waagen, E., Swierczynski, S., Komorous, M., King, R., & Bortle, J. 2007a, *IAU Circ.*, 8861, 2
- Nakano, S., Tago, A., Itagaki, K., & Kadota, K. 2007b, *Central Bureau Electronic Telegrams*, 1181, 1
- Nakano, S., Tago, A., Itagaki, K., Kadota, K., Yamaoka, H., Munari, U., & Pereira, A. 2008a, *IAU Circ.*, 8907, 1
- Nakano, S., Tago, A., Nishiyama, K., & Sakamoto, T. 2007c, *IAU Circ.*, 8821, 1
- Nakano, S., & Yusa, T. 2009, *Central Bureau Electronic Telegrams*, 1967, 1
- Nakano, S., et al. 2008b, *IAU Circ.*, 8934, 1
- Napiwotzki, R., et al. 2004, in *Astronomical Society of the Pacific Conference Series*, Vol. 318, *Spectroscopically and Spatially Resolving the Components of the Close Binary Stars*, ed. R. W. Hilditch, H. Hensberge, & K. Pavlovski, 402

- Narumi, H., Hirose, K., Kanai, K., Renz, W., Pereira, A., Nakano, S., Nakamura, Y., & Pojmanski, G. 2006, *IAU Circ.*, 8671, 2
- Neckel, H., & Labs, D. 1984, *SolarPhys*, 90, 205
- Neill, J. D., Shara, M. M., Halbedel, E., & Malnushenko, V. 2004, in *Revista Mexicana de Astronomia y Astrofisica*, vol. 27, Vol. 20, *Revista Mexicana de Astronomia y Astrofisica Conference Series*, ed. G. Tovmassian & E. Sion, 240
- Nelson, L. A., MacCannell, K. A., & Dubeau, E. 2004, *ApJ*, 602, 938
- Nishiyama, K., & Kabashima, F. 2009, *Central Bureau Electronic Telegrams*, 2003, 1
- Nishiyama, K., Kabashima, F., & Yusa, T. 2009a, *Central Bureau Electronic Telegrams*, 2100, 1
- Nishiyama, K., et al. 2009b, *IAU Circ.*, 9061, 1
- Nordhaus, J., Blackman, E. G., & Frank, A. 2007, *MNRAS*, 376, 599
- Nordsieck, K. H., & Shara, M. 2011, *The Astronomer's Telegram*, 3289, 1
- Nugent, P. E., et al. 2011, *Nature*, 480, 344
- O'Brien, T. J., & Bode, M. F. 2008, *Resolved Nebular Remnants* (Cambridge University Press), 285–307
- O'Brien, T. J., Muxlow, T. W. B., Stevens, J., Datta, A., Roy, N., Eyres, S. P. S., & Bode, M. F. 2010, *The Astronomer's Telegram*, 2434, 1
- Orio, M., & Shaviv, G. 1993, *Ap&SS*, 202, 273
- Orio, M., Trussoni, E., & Oegelman, H. 1992, *A&A*, 257, 548
- Osaki, Y. 1974, *PASJ*, 26, 429
- . 1996, *PASP*, 108, 39
- Ovcharov, E., Valcheva, A., Georgiev, T., Kostov, A., Nikolov, Y., & Nedialkov, P. 2009a, *The Astronomer's Telegram*, 2176, 1

- Ovcharov, E., Valcheva, A., Kostov, A., Latev, G., Nikolov, Y., Georgiev, T., & Nedialkov, P. 2009b, *The Astronomer's Telegram*, 1927, 1
- Paczynski, B., & Schwarzenberg-Czerny, A. 1980, *Acta Astronomica*, 30, 127
- Payne-Gaposchkin, C. 1964, *The Galactic Novae* (New York: Dover Publication)
- Pejcha, O. 2009, *ApJ Let.*, 701, L119
- Pereira, A. J. S., McGaha, J. E., Young, J., & Rhoades, H. 2007, *IAU Circ.*, 8895, 1
- Perinotto, M. 1989, in *Proceedings IAU Symposium*, Vol. 131, *Planetary Nebulae*, ed. S. Torres-Peimbert, 293
- Pfau, W. 1976, *A&A*, 50, 113
- Pickles, A. J. 1998, *PASP*, 110, 863
- Pietsch, W., Henze, M., Burwitz, V., Updike, A., Milne, P., Williams, G., & Hartmann, D. H. 2009a, *The Astronomer's Telegram*, 1935, 1
- Pietsch, W., Kaduk, F., Henze, M., Burwitz, V., Papamastorakis, G., Reig, P., & Strigachev, A. 2009b, *The Astronomer's Telegram*, 2147, 1
- Pigott, E., & Englefield, H. C. 1786, *Royal Society of London Philosophical Transactions Series I*, 76, 189
- Poggiani, R. 2010, *New Astronomy*, 15, 170
- Pojmanski, G., Szczygiel, D., & Pilecki, B. 2007, *IAU Circ.*, 8899, 2
- Pollacco, D. L., Lawson, W. A., Clegg, R. E. S., & Hill, P. W. 1992, *MNRAS*, 257, 33P
- Porter, J. M., O'Brien, T. J., & Bode, M. F. 1998, *MNRAS*, 296, 943
- Pringle, J. E., & Wade, R. A. 1985, *Interacting binary stars* (Cambridge University Press)
- Pritchett, C. J., Howell, D. A., & Sullivan, M. 2008, *ApJ Let.*, 683, L25

- Rau, A., et al. 2009, *PASP*, 121, 1334
- Read, A. M., Saxton, R. D., & Esquej, P. 2007, *The Astronomer's Telegram*, 1282, 1
- Ritchey, G. W. 1917, *PASP*, 29, 210
- Robinson, E. L. 1975, *AJ*, 80, 515
- Rodríguez-Gil, P., Ferrando, R., Rodríguez, D., Bode, M. F., Huxor, A., Giles, P., & Mackey, D. 2009, *The Astronomer's Telegram*, 2166, 1
- Rowles, J., & Froebrich, D. 2009, *MNRAS*, 395, 1640
- Rudy, R. J., et al. 2007, in *Bulletin of the American Astronomical Society*, Vol. 38, American Astronomical Society Meeting Abstracts, 817
- Schaefer, B. E. 2010, *ApJS*, 187, 275
- Schatzman, E. 1951, *Annales d'Astrophysique*, 14, 294
- Schatzman, E. L. 1958, *White Dwarfs* (Amsterdam, North-Holland Pub. Co.; New York, Interscience Publishers.)
- Schmidt, T. 1957, *Zeitschrift für Astrophysik*, 41, 182
- Sekiguchi, K., Feast, M. W., Whitelock, P. A., Overbeek, M. D., Wargau, W., & Jones, J. S. 1988, *MNRAS*, 234, 281
- Senziani, F., Skinner, G., Jean, P., & Hernanz, M. 2008, in *Astronomical Society of the Pacific Conference Series*, Vol. 401, *RS Ophiuchi (2006) and the Recurrent Nova Phenomenon*, ed. A. Evans, M. F. Bode, T. J. O'Brien, & M. J. Darnley, 323
- Shafter, A. W. 1997, *ApJ*, 487, 226
- Shafter, A. W. 2002, in *American Institute of Physics Conference Series*, Vol. 637, *Classical Nova Explosions*, ed. M. Hernanz & J. José, 462–471
- Shafter, A. W., Ciardullo, R., Bode, M. F., Darnley, M. J., & Misselt, K. A. 2008, *The Astronomer's Telegram*, 1832, 1

- Shafter, A. W., & Quimby, R. M. 2007, *ApJ Let.*, 671, L121
- Shafter, A. W., Rau, A., Quimby, R. M., Kasliwal, M. M., Bode, M. F., Darnley, M. J., & Misselt, K. A. 2009, *ApJ*, 690, 1148
- Shafter, A. W., et al. 2011, *ApJ*, 734, 12
- Shara, M. M. 1989, *PASP*, 101, 5
- Shara, M. M., Yaron, O., Prialnik, D., Kovetz, A., & Zurek, D. 2010, *ApJ*, 725, 831
- Shara, M. M., & Zurek, D. R. 2002, in *American Institute of Physics Conference Series*, Vol. 637, *Classical Nova Explosions*, ed. M. Hernanz & J. José, 457–461
- Shklovskii, I. S. 1956, *Kosmicheskoe radiolzluchenie*. (Moskva, Gos. izd-vo tekhniko-teoret. lit-ry)
- Shore, S. N., Augusteijn, T., Ederoclite, A., & Uthas, H. 2011, *The Astronomer's Telegram*, 3306, 1
- Slavin, A. J., O'Brien, T. J., & Dunlop, J. S. 1995, *MNRAS*, 276, 353
- Smith, R. C. 2007, *AstroPh*, 1, 1
- Soker, N. 1997, *ApJS*, 112, 487
- . 2002, *MNRAS*, 330, 481
- Soker, N., & Rappaport, S. 2000, *ApJ*, 538, 241
- Somers, M. W., Mukai, K., & Naylor, T. 1996, *MNRAS*, 278, 845
- Spreckley, S., & Stevens, I. R. 2007, in *Astronomical Society of the Pacific Conference Series*, Vol. 366, *Transiting Extrapolar Planets Workshop*, ed. C. Afonso, D. Wel-drake, & T. Henning, 39
- Spreckley, S. A., & Stevens, I. R. 2008, *MNRAS*, 388, 1239
- Stanghellini, L., & Pasquali, A. 1995, *ApJ*, 452, 286

- Starrfield, S., Iliadis, C., & Hix, W. R. 2008, *Thermonuclear processes* (Cambridge University Press), 77
- Starrfield, S., Sparks, W. M., & Truran, J. W. 1985, *ApJ*, 291, 136
- Steeghs, D., Drew, J., Greimel, R., Barlow, M., Gaensicke, B., Drake, J., & Witham, A. 2007, *The Astronomer's Telegram*, 1031, 1
- Steele, I. A., et al. 2004, in *Presented at the Society of Photo-Optical Instrumentation Engineers (SPIE) Conference*, ed. J. M. Oschmann Jr., Vol. 5489, 679–692
- Steffen, W., & Lopez, J. A. 2006, *Revista Mexicana de Astronomia y Astrofisica*, 42, 99
- Stephenson, F. R., & Green, D. A. 2002, *Historical supernovae and their remnants*, by F. Richard Stephenson and David A. Green. *International series in astronomy and astrophysics*, vol. 5. Oxford: Clarendon Press, 2002, ISBN 0198507666, 5
- Sterken, C., & Jaschek, C. 1996, *Light Curves of Variable Stars, A Pictorial Atlas* (Cambridge University Press)
- Stetson, P. B. 1987, *PASP*, 99, 191
- Swierczynski, E., et al. 2010, in *Astronomical Society of the Pacific Conference Series*, ed. A. Prša & M. Zejda, Vol. 435, 297
- Tarrant, N. J., Chaplin, W. J., Elsworth, Y., Sreckley, S. A., & Stevens, I. R. 2007, *MNRAS*, 382, L48
- Tomov, T., Mikolajewski, M., Brozek, T., Ragan, E., Swierczynski, E., Wychudzki, P., & Galan, C. 2008, *The Astronomer's Telegram*, 1485, 1
- Torres, M. A. P., Jonker, P. G., Challis, P., Modjaz, M., Kirshner, R., Read, A. M., Kuulkers, E., & Saxton, R. D. 2007, *The Astronomer's Telegram*, 1285, 1
- Townsley, D. M., & Bildsten, L. 2004, *ApJ*, 600, 390
- van den Bergh, S., & Younger, P. F. 1987, *A&AS*, 70, 125

- Verbunt, F. 1982, *Space Science Reviews*, 32, 379
- Waagan, E., et al. 2011, *Central Bureau Electronic Telegrams*, 2700, 1
- Walker, M. F. 1954, *PASP*, 66, 230
- Warner, B. 1986, *MNRAS*, 222, 11
- . 1989, *Properties of novae: an overview* (John Wiley and Sons Ltd)
- . 1995, *Cataclysmic variable stars* (Cambridge Astrophysics Series, Cambridge University Press, —c1995)
- Warner, B. 2002, in *American Institute of Physics Conference Series*, Vol. 637, *Classical Nova Explosions*, ed. M. Hernanz & J. José, 3
- . 2008, *Properties of novae: an overview* (Cambridge University Press), 16
- Warner, B., & Woudt, P. A. 2003, in *Astronomical Society of the Pacific Conference Series*, ed. R. L. M. Corradi, J. Mikolajewska, & T. J. Mahoney, Vol. 303, 317
- Warner, B., & Woudt, P. A. 2009, *MNRAS*, 397, 979
- Webbink, R. F. 1984, *ApJ*, 277, 355
- Weight, A., Evans, A., Naylor, T., Wood, J. H., & Bode, M. F. 1994, *MNRAS*, 266, 761
- Wesson, R., et al. 2008, *ApJ Let.*, 688, L21
- Whelan, J., & Iben, I. J. 1973, *ApJ*, 186, 1007
- Wickramasinghe, D. T., & Ferrario, L. 2000, *PASP*, 112, 873
- Williams, R. E. 1992, *AJ*, 104, 725
- Yamaoka, H. 2004, *IAU Circ.*, 8380, 1
- Yamaoka, H., Ayani, K., Murakami, N., Kinugasa, K., Fujii, M., & Naito, H. 2007a, *Central Bureau Electronic Telegrams*, 1181, 2

-
- Yamaoka, H., Nakamura, Y., Nakano, S., Sakurai, Y., & Kadota, K. 2007b, *Central Bureau Electronic Telegrams*, 834, 1
- Yamaoka, H., et al. 2008, *IAU Circ.*, 8989, 1
- . 2009, *IAU Circ.*, 9098, 1
- Yaron, O., Prialnik, D., Shara, M. M., & Kovetz, A. 2005, *ApJ*, 623, 398

Appendix A

Nova V458 Vul Images

Within this appendix images on the left-hand side are the median combined images produced from each epoch which have then been aligned to the reference. These images have not been normalised to each other nor undergone star subtraction. The images on the right-hand side are the star subtracted, median combined images from each epoch which have been aligned to the reference and normalised. Masks mentioned in Section 4.4.4 are evident within each right-hand side image.

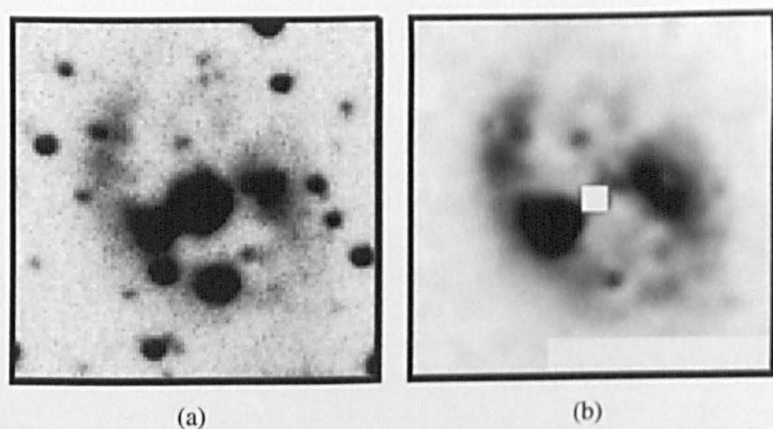


Figure A.1: 2008-05-21 data taken by the INT (a) Non-processed 99×99 pixel region centred on Nova V458 Vul. (b) Star subtracted normalised image of the same region.

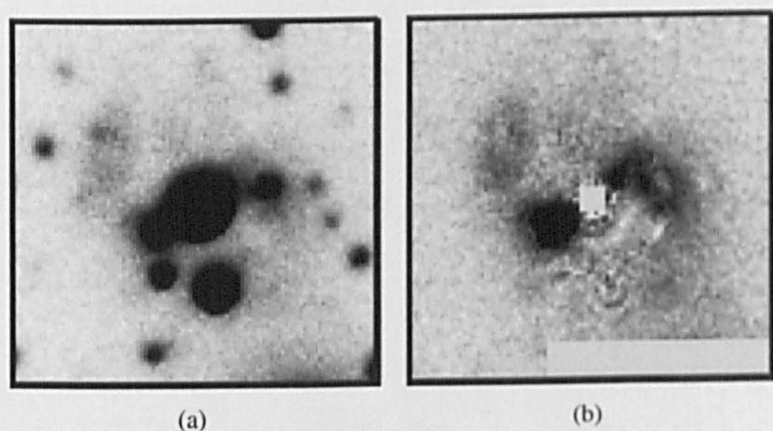


Figure A.2: Same as Figure A.1 except 2008-07-28 data taken by the LT.

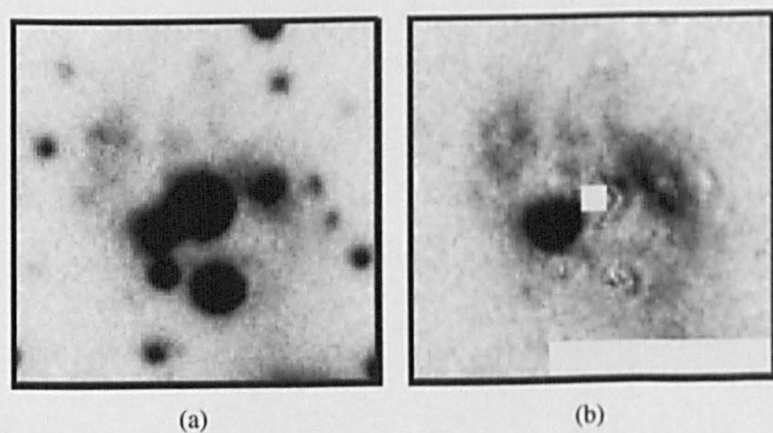


Figure A.3: Same as Figure A.1 except 2008-08-26 data taken by the LT.

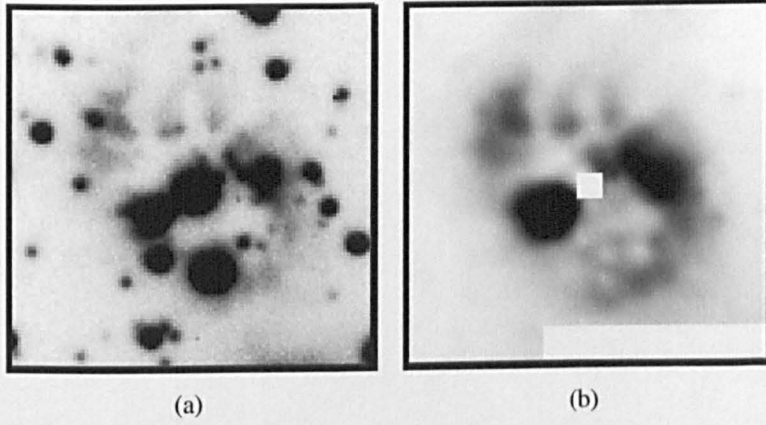


Figure A.4: Same as Figure A.1 except 2008-09-19 data taken by the NOT.

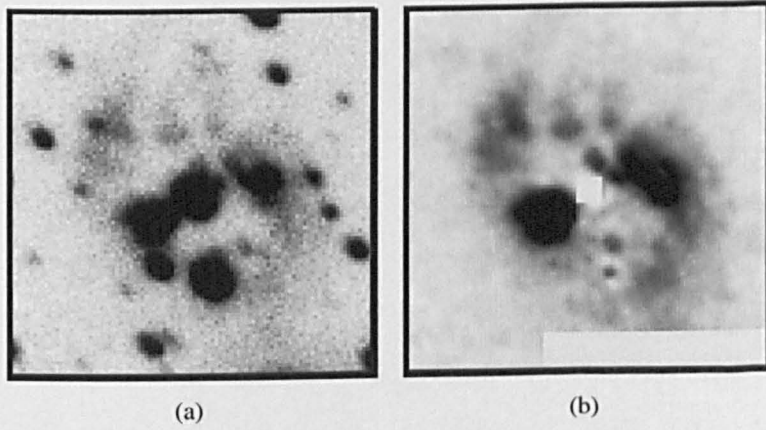


Figure A.5: Same as Figure A.1 except 2008-09-21 data taken by the LT.

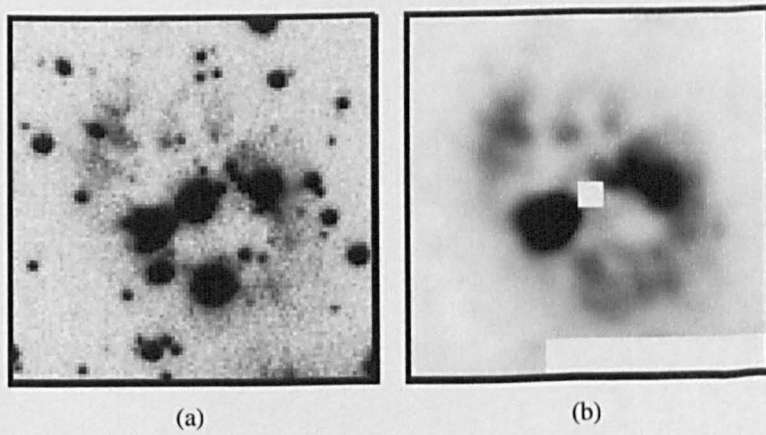


Figure A.6: Same as Figure A.1 except 2008-09-30 data taken by the NOT.

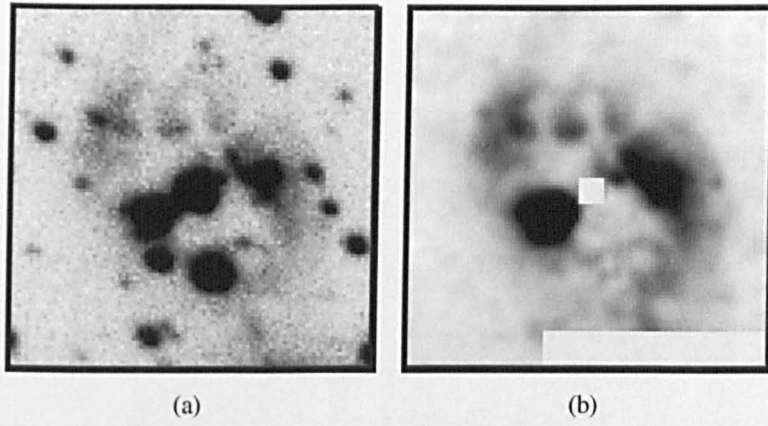


Figure A.7: Same as Figure A.1 except 2008-10-06 data taken by the LT.

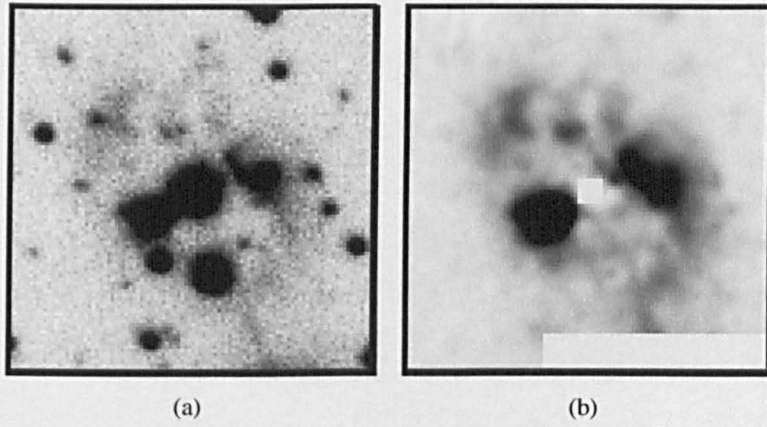


Figure A.8: Same as Figure A.1 except 2008-11-24 data taken by the LT.

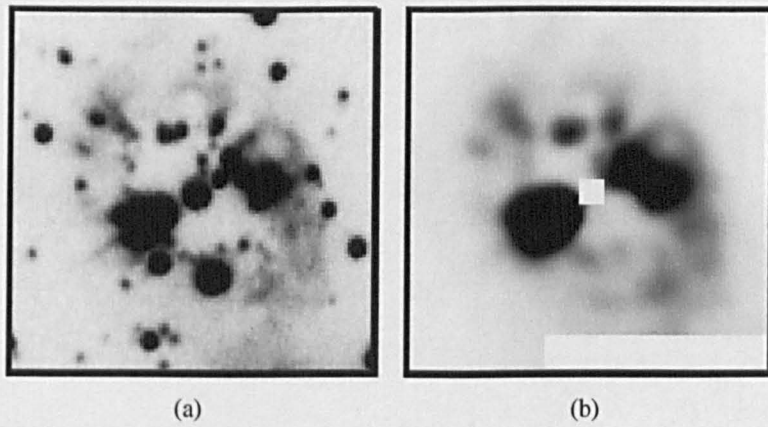


Figure A.9: Same as Figure A.1 except 2009-06-15 data taken by the WHT.

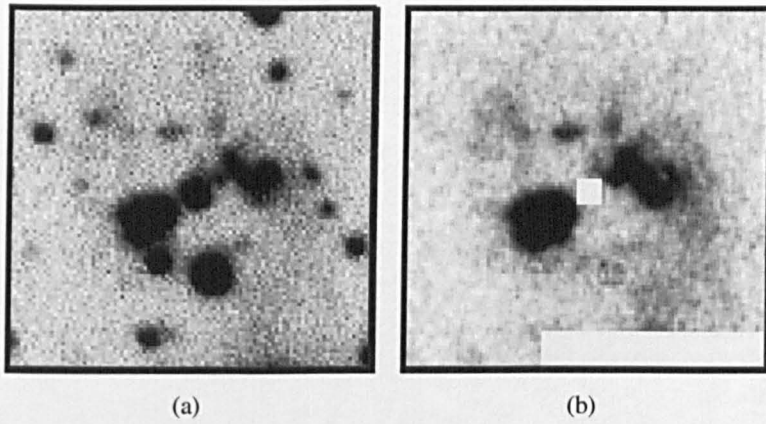


Figure A.10: Same as Figure A.1 except 2009-06-30 data taken by the LT.

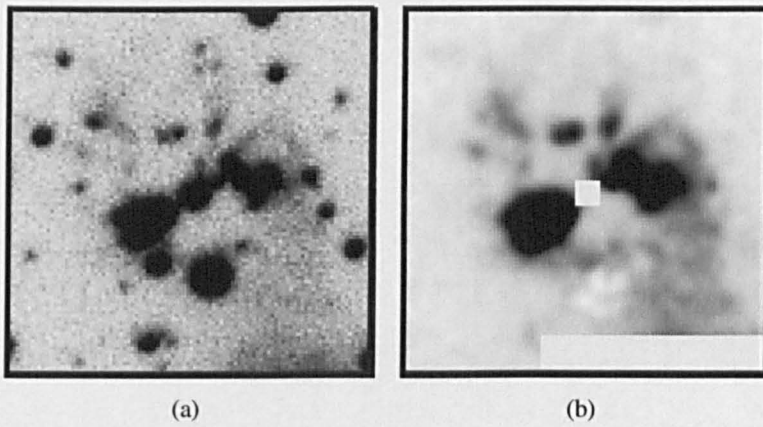


Figure A.11: Same as Figure A.1 except 2009-08-18 data taken by the LT.

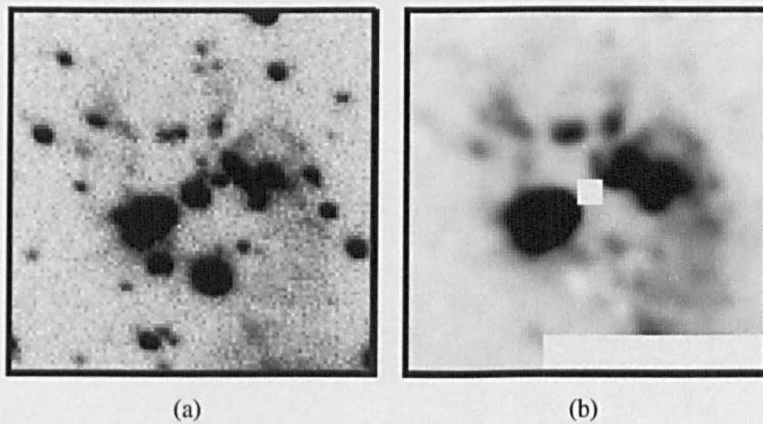


Figure A.12: Same as Figure A.1 except 2009-09-23 data taken by the LT.

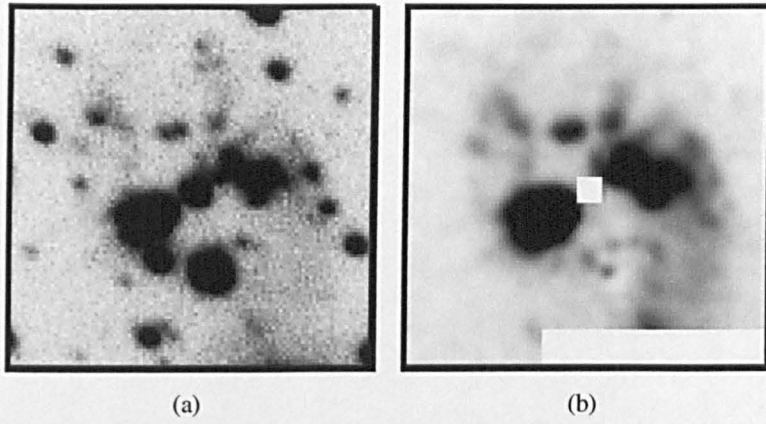


Figure A.13: Same as Figure A.1 except 2009-10-20 data taken by the LT.

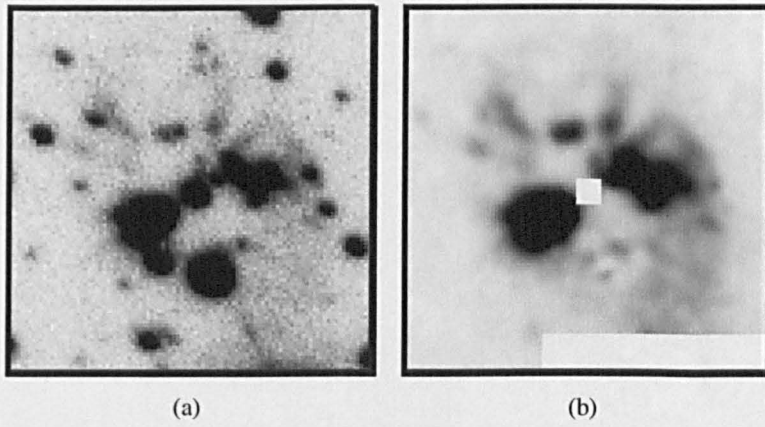


Figure A.14: Same as Figure A.1 except 2009-11-14 data taken by the LT.

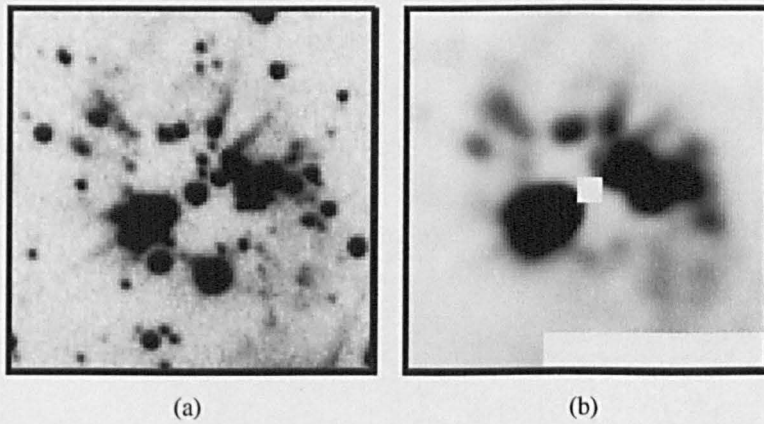


Figure A.15: Same as Figure A.1 except 2010-07-23 data taken by the WHT.

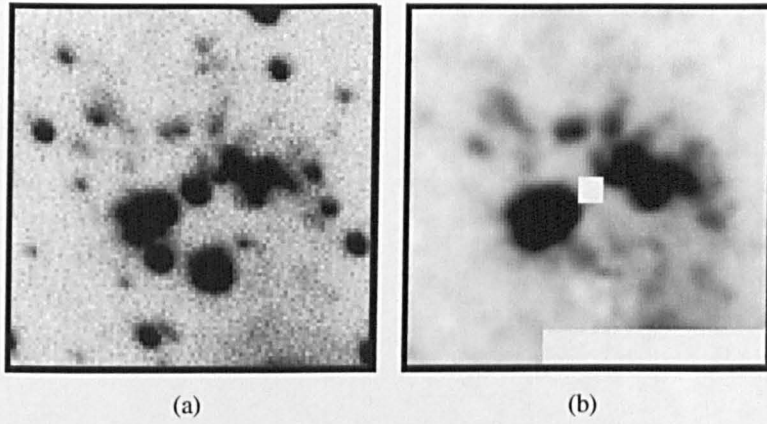


Figure A.16: Same as Figure A.1 except 2010-08-18 data taken by the LT.

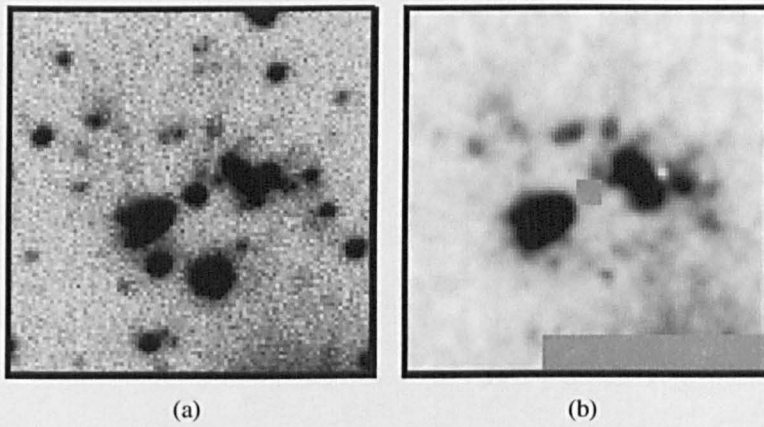


Figure A.17: Same as Figure A.1 except 2011-06-11 data taken by the LT.

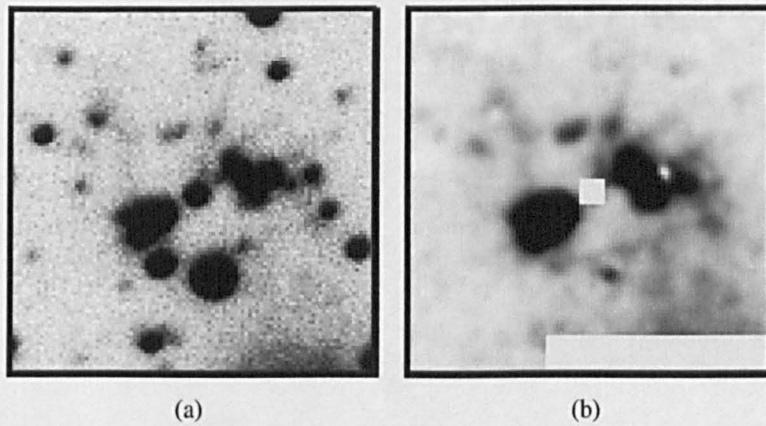


Figure A.18: Same as Figure A.1 except 2011-07-01 data taken by the LT.

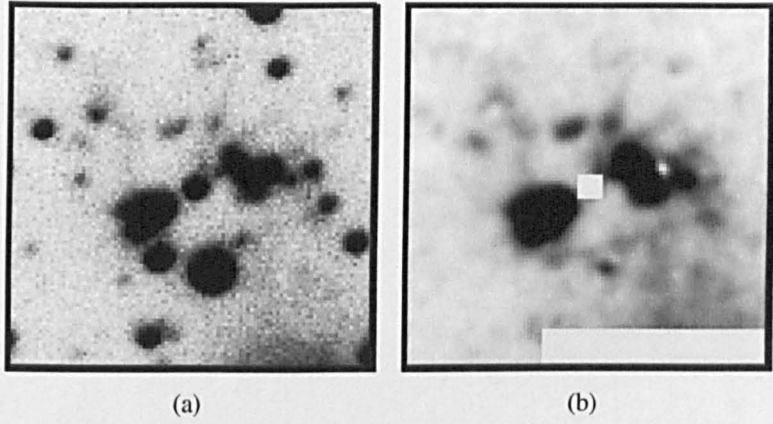


Figure A.19: Same as Figure A.1 except 2011-07-01 data taken by the LT.

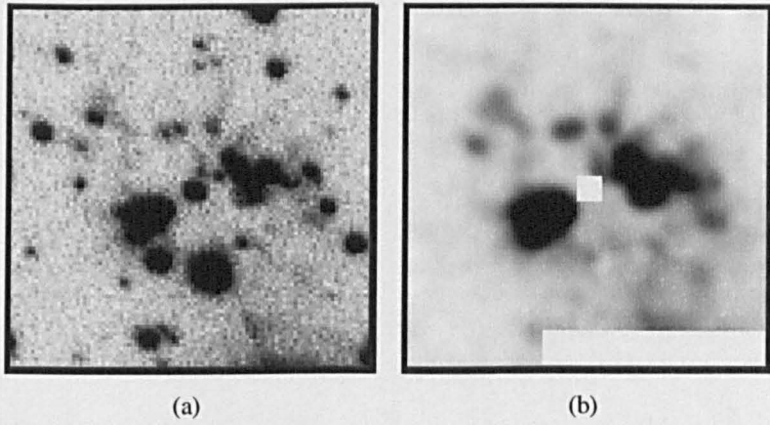


Figure A.20: Same as Figure A.1 except 2011-10-27 data taken by the LT.

Appendix B

Known novae within the SMEI database

The following tables present a list of all known novae within the UCSD SMEI database. Novae marked with a \star have provided detailed light curves under investigation (see Section 5.5.1). Novae marked with a \dagger are fainter and have produced the less detailed light curves presented in Section 5.5.2.

Table B.1: Classical and Recurrent Novae listed within the UCSD SMEI data base - continued in the next three tables.

Name	Year	Month	Discovery Date (UT)	R.A (J2000)	Dec (J2000)	Discovery Magnitude	Reference to Discovery	Visible
V4745 Sgr	2003	4	25.73	18:40:2.54	-33:26:55.1	8.9	N. Brown; M. Yamamoto	No
V2573 Oph	2003	7	10.60	17:19:14.9	-27:22:35.2	11.4	A. Takao; V. Tabur	No
V0475 Sct	2003	8	28.58	18:49:37.62	-09:33:50.3	8.4	H. Nishimura	No data
V5113 Sgr	2003	9	17.52	18:10:10.42	-27:45:35.2	9.2	N. Brown	No
DE Cir	2003	10	9.00	15:17:52.48	-61:57:16.4	7.7	W. Liller	No
V5114 Sgr	2004	3	15.82	18:19:32.29	-28:35:35.7	9.4	H. Nishimura; W. Liller; Y. Nakamura	No
V2574 Oph	2004	4	14.80	17:38:45.49	-23:28:18.5	11.1	A. Takao; Y. Nakamura	No
V1186 Sco	2004	7	3.15	17:12:51.28	-30:56:37.6	12	G. Pojmanski	No
V1187 Sco [†]	2004	8	3.58	17:29:18.81	-31:46:01.5	7.4	A. Takao	Yes
V0574 Pup	2004	11	20.67	07:41:53.56	-27:06:38.3	7.6	A. Tago; Y. Sakurai	No
V2361 Cyg	2005	2	10.85	20:09:19.05	39:48:52	9.7	H. Nishimura	No
V0382 Nor	2005	3	13.31	16:19:44.74	-51:34:53.1	9.4	W. Liller	No
V5115 Sgr	2005	3	28.78	18:16:58.96	-25:56:38.9	8.7	H. Nishimura; Y. Sakurai	No
V0378 Ser	2005	3	21.37	17:49:24.57	-12:59:59.2	11.8	G. Pojmanski	No
V1663 Aql	2005	6	9.24	19:05:12.5	05:14:12	11	G. Pojmanski	No
V5116 Sgr	2005	7	4.05	18:17:50.77	-30:26:31.2	8	W. Liller	No
V1188 Sco	2005	7	25.28	17:44:21.59	-34:16:35.7	9.1	G. Pojmanski; H. Nishimura	No

Name	Year	Month	Discovery Date (UT)	R.A (J2000)	Dec (J2000)	Discovery Magnitude	Discover(s)	Visible
V1047 Cen	2005	8	1.03	13:20:49.74	-62:37:50.5	8.5	W. Liller	No
V476 Sct	2005	9	30.52	18:32:4.75	-06:43:34.3	10.3	A. Takao; K. Haseda	No
V477 Sct	2005	10	11.03	18:38:42.93	-12:16:15.6	12	G. Pojmanski	No
V2575 Oph	2006	2	9.39	17:33:13.06	-24:21:07.1	12.1	G. Pojmanski	No
RS Oph*	2006	2	12.83	17:50:13.20	-06:42:28.48	4.5	H. Narumi	Yes
V5117 Sgr	2006	2	17.37	17:58:52.61	-36:47:36.2	9	W. Liller	No
V2362 Cyg	2006	4	2.81	21:11:32.34	44:48:03.9	10.5	H. Nishimura	No
V2576 Oph	2006	4	6.57	17:15:33	-29:09:09.9	10.5	P. Williams	No
V1065 Cen	2007	1	23.35	11:43:10.33	-58:04:04.3	8.2	W. Liller	No
V1280 Sco*	2007	2	4.90	16:57:41.2	-32:20:35.8	9.4	Y. Sakurai; Y. Nakamura	Yes
V1281 Sco	2007	2	19.86	16:56:59.35	-35:21:50.2	9.3	Y. Nakamura; H. Nishimura	Yes but faint
V2467 Cyg†	2007	3	15.79	20:28:12.52	41:48:36.5	7.4	A. Tago	Yes but faint
V2615 Oph	2007	3	19.81	17:42:44	-23:49:35.1	10.2	H. Nishimura	No
V5558 Sgr	2007	4	14.78	18:10:18.27	-18:46:52.1	10.3	Y. Sakurai	Yes but faint
V390 Nor	2007	6	15.09	16:32:11.51	-45:09:13.4	9.4	W. Liller	No
V458 Vul†	2007	8	4.54	19:54:24.64	20:52:51.7	9.5	H. Abe	Yes

Name	Year	Month	Discovery Date (UT)	R.A (J2000)	Dec (J2000)	Discovery Magnitude	Discover(s)	Visable
V597 Pup †	2007	8	14.21	08:16:18.01	-34:15:24.1	7	A. Pereira	Yes
V598 Pup*	2007	8	8.00	07:05:42.51	-38:14:39.3	10.3	Read et al. (x-ray)	Yes
V459 Vul†	2007	12	25.35	19:48:8.84	21:15:26.8	8.7	Kaneda	Yes but faint
V2468 Cyg	2008	1	7.80	19:58:33.39	29:52:6.5	8.2	Kaneda	No
NR TrA	2008	4	1.73	16:18:48.21	-60:27:48.9	9.2	Brown	No
V2491 Cyg†	2008	4	10.73	19:43:1.96	32:19:13.8	7.7	Nishiyama, Kabashima	Yes
V5579 Sgr	2008	4	18.78	18:05:58.88	-27:13:56	8.4	Nishiyama, Kabashima	No data
V2670 Oph	2008	5	25.69	17:39:50.93	-23:50:0.9	10.3	Haseda et al.	No
V2671 Oph	2008	5	31.61	17:33:29.67	-27:01:16.4	11.3	Nishiyama, Kabashima	No
V1309 Sco	2008	9	2.46	17:57:32.93	-30:43:10.1	9.5	Nishiyama, Kabashima	No
V1721 Aql	2008	9	22.5	19:06:28.58	07:06:44.3	14	Itagaki	No
QY Mus†	2008	9	29	13:16:36.44	-67:36:47.8	8.6	Liller	Yes but faint
V679 Car	2008	11	26.26	11:13:53.79	-61:13:48.2	7.6	Malek	No
V5580 Sgr†	2008	11	29.04	18:22:01.5	-28:02:39.6	8	Liller	Yes but faint
V5581 Sgr	2009	4	21.68	17:44:08.48	-26:05:47.4	12.5	Nishiyama, Kabashima	No
V5582 Sgr	2009	2	23.95	17:45:05.4	-20:03:21.5	11.5	Sun, Gao	No

Name	Year	Month	Discovery Date (UT)	R.A (J2000)	Dec (J2000)	Discovery Magnitude	Discover(s)	Visable
V1213 Cen	2009	5	8.24	13:31:15.77	-63:57:38.6	8.5	Pojmanski, Szczygiel, Pilecki	No
V5583 Sgr [†]	2009	8	6.49	18:07:07.67	-33:46:33.9	7.7	Nishiyama, Kabashima et al.	Yes but faint
V2672 Oph	2009	8	16.52	17:38:19.68	-26:44:14	10	Itagaki	No
V5584 Sgr	2009	10	26.44	18:31:32.79	-16:19:7.5	9.3	Nishiyama, Kabashima	Yes
V496 Sct	2009	10	8.37	18:43:45.65	-07:36:41.5	8.8	Nishimura	Yes but faint
KT Eri [*]	2009	11	25.55	04:47:54.21	-10:10:43.1	8.1	Itagaki	Yes
V1722 Aql	2009	12	14.40	19:14:09.73	15:16:34.7	10.9	Nishiyama, Kabashima	No
V2673 Oph	2010	1	15.86	17:39:40.94	-21:39:47.9	8.8	Nishimura	No data
V5585 Sgr	2010	1	20.72	18:07:26.95	-29:00:43.6	8.5	Seach	No data
U Sco	2010	1	28.43	16:22:30.80	-17:52:43.2	7.85	B.G. Harris, S. Dvorak	No data
V2674 Oph	2010	2	18.85	17:26:32.19	-28:49:36.3	9.4	Nishimura	No
V1310 Sco	2010	2	20.86	17:06:07.53	-37 14:27.4	10.5	Nishiyama, Kabashima	No
V5586 Sgr	2010	4	23.78	17:53:02.99	-28:12:19.4	11.2	Nishiyama, Kabashima	No
V1311 Sco	2010	4	25.79	16:55:13.16	-38:03:46.9	8.6	Nishiyama, Kabashima	No
V1723 Aql	2010	9	11.49	18:47:38.38	-03:47:14.1	12.4	Nishiyama, Kabashima	No data
T Pyx [*]	2011	4	14.29	09:04:41.50	-32:22:47.5	13.0	M. Linnolt	Yes

Appendix C

Point Source Code: *smei_findpnt*

This appendix contains the documented IDL code for the *smei_findpnt* program. This program was written by Dr Paul Hick (UCSD) with testing and modification conducted as part of the work of this thesis.

;+ ;NAME:

; smei_findpnt

;PURPOSE:

; Originally created to look for point sources in the star-subtracted
; equ files to find unknown objects (i.e. objects not included in the
; SMEI star catalogues).

;

; To run this program access is needed to the 'equ' files, If keyword
; /use_catalogue is set then also access to the 'sky' files is required.

;CATEGORY:

; smei/ucsd/camera/idl/star

;CALLING SEQUENCE:

PRO smei_findpnt, wanted_map , \$

camera = camera , \$

from_mode = from_mode , \$

to_mode = to_mode , \$

destination = destination , \$

fix_centroid = fix_centroid , \$

cvmin = cvmin , \$

use_catalogue= use_catalogue , \$

npeak = npeak , \$

silent = silent , \$

_extra = _extra

;INPUTS:

; wanted_map array[n]; type: string, time structure or integer

; passed to href=smei_getfile=.

; Selects skymap files to be processed.

; Usually this is a pair of times (start time and
; stop time) to process all maps inside a period

; of time.

;OPTIONAL INPUT PARAMETERS:

```

; camera=camera
;
;           scalar; type: integer; default: 2
;
;           camera id (1,2,3). The default camera 2 has the
;           most sky real estate.
; from_mode=from_mode
;
;           scalar; type: string; default: 'equ'
;
;           selects the type of skymap to be used.
;
;           Can also be used to 'sky' to work from the
;           unsubtracted maps, but that doesn't make much
;           sense since these maps still contain all the
;           catalogue stars.
; to_mode=to_mode
;
;           scalar; type: string; default: 'bol'
;
;           This is only used in the naming convention for
;           the output 'pnt' files: the names will look like:
;           c2bol_YYYY_DOY_hhmmss.pnt
;           where YYYY_DOY_hhmmss is the start time of
;           a SMEI orbit, taken from the associated
;           'equ' file
; destination=destination
;
;           scalar; type: string; default: $TUB
;
;           destination directory of output file
; fix_centroid=fix_centroid
;
;           if set, this turns on the 'fix_centroid' option in the
;           smei_star_fit, i.e. the centroid position of the new
;           object is iteratively improved. This gives better
;           results at the expense of a substantial increase in
;           processing time.
;
;
; cvmin=cvmin
;
;           scalar; type: float; default: 0.7

```

```

;           Only new objects with a PSF correlation
;           coefficient greater than cvmin will be written to
;           the output files
;
; /use_catalogue
;           If set, an attempt is made to match unknown
;           objects against objects in the SMEI catalogue.
;           This will pick up 'unknown' objects at the
;           location of a SMEI catalogue object, usually
;           indicating that the catalogue star was
;           imperfectly subtracted. This keyword can
;           increase processing time significantly
;           especially if combined with a low cvmin value.
; npeak=npeak
;           scalar; type: integer; default: none, i.e. no limit
;           passed to href=smei_findpeaks=.
;           Can be used to limit the number of objects on the
;           initial list of local maxima in the skymap, that
;           are further investigated by smei_star_fit.
;           Probably best avoided (see PROCEDURE)
;
; silent=silent
;           scalar; type: integer; default: 0
;           higher values suppress more informational
;           messages
;OUTPUTS:
;   Files in destination directory
;INCLUDE:
@compile_opt.pro ; On error, return to caller
;CALLS:
;   InitVar, smei_filename, smei_filepath, smei_getfile, hide_env

```

; BadValue, smei_sky, TimeSet, sphere_distance, smei_star_fit

;PROCEDURE:

; The equ files have all SMEI catalogue stars (presumably all stars
; brighter than 6th magnitude), the sidereal background and the
; zodiacal dust cloud subtracted.

;

; The search procedure consists of the following steps:

;

; 1. Smoothing of skymaps.

;

; First the map is smoothed by subtracting a running mean for an 8 degree wide box.

; This takes out variations over spatial scales much larger than the PSF. This step
; mainly serves to create local maxima that are more easily sorted, i.e. it makes
; it easier to process maxima starting with the highest and working down from there.

;

; The second step is to apply a smoothing using a running mean of 1 degree, the full
; width of the SMEI PSF. This reduces the noise in the maps, and avoids picking
; up every noise spike as a separate local maxima.

;

; 2. Prepare a list of candidate objects.

;

; In this step the procedure FindPeaks is used to make a list of all the local
; maxima in the skymap, listing the highest ones first.

; The number of local maxima can be controlled with a number of keywords
; (see [FindPeaks](#) for details). This should not really be necessary:
; step 1 has proven to be the simplest way to control the output from
; FindPeaks.

;

; 3. Fit all the candidate maxima to the PSF using [smei_star_fit](#).

;

; This step uses the default star fitting procedure for SMEI to identify

; those objects on the candidate list that look like point sources (i.e.
; look like the SMEI PSF).
;
; The main keyword to control this step is `/fix_centroid`.
; The default mode is NOT to use this keyword. In that case the PSF is fit
; once at the location of each candidate maximum. If `/fix_centroid` is ON,
; then an iterative procedure is used to find the location in the skymap
; near the candidate maximum that provides the best fit (the highest
; correlation between the object in the skymap and the standard SMEI PSF).
;
; The advantage of NOT setting `/fix_centroid` is a significant reduction
; in processing time (close to a factor of 10). The disadvantage is that
; the quality of the PSF fitting is worse, which might lead to good objects
; going unnoticed because the correlation is much worse.
;
; The result of step 3 is that all the candidate objects from step 2
; can be classified by sorting on the correlation coefficient of
; of the PSF fit. The difference between using (or not using) `/fix_centroid`
; is that the candidates will be sorted differently.
;
; 4. Retain the best fitting objects only
;
; At this stage the keyword `cvmin` is used to only retain objects that
; resulted in a correlation coefficient higher than `cvmin` (0.7 by default).
; The total list of candidates for one skymap can easily be on the order
; of 1400 or so. A significant fraction of the correlation coefficient
; (often 70-80%) of the candidates will be quite low, so it makes sense
; to reduce the search space by focusing on the higher correlations.
;
; Note that at this stage the effect of using (or not using) `fix_centroid`
; in step 3 becomes evident: since the correlation coefficients are different

; (lower when `fix_centroid` is not used), a different set of candidate objects
; is retained. If `cvmin=0.7` when `fix_centroid` is not used then
; under half the number of candidates will be detected and as
; stated above these will not necessarily be the same objects
; that were detected previously.
;
; When not applying `fix_centroid` `cvmin` must be lower than 0.7.
; Choosing a `cvmin` value is a compromise between the detection
; of real objects and noise.
; On testing a `cvmin` value of 0.6 seems to produce the best results
; with the number of candidates detected only marginally greater
; than results obtained when using `fix_centroid` and a
; `cvmin=0.7`. On comparison of objects detected using both
; methods there is a greater than 70% overlap. Also note that
; when looking at individual output files the order of the
; candidates will be different to those produced when using
; `fix_centroid` and candidates may also appear in later files
; within the time series.
;
; Note that if `cvmin=-1` is used, all objects are retained.
; This results in significantly larger output files though of
; on average 1400 objects. This may be an issue later on when
; trying to identify real object candidates.
;
; 5. Match against catalogue stars
;
; This step is optional. By default it is not done, but it can be switched
; on with keyword `/use_catalogue`.
;
; The locations of the candidate maxima from step 4 (after trimming the list
; using `cvmin`), is compared against the locations in the SMEI star

; catalogues. If a catalogue star is found within 0.5 degrees of a
; candidate object, most likely the object found is the result of
; a badly-subtracted catalogue star. In this case the candidate
; object will be listed in the output file under the name of the candidate
; object. Note that this is not a positive identification; it just indicates
; the proximity of a catalogue star.
;
; Using a low value of `cvmin` in combination with `/use_catalogue` keyword is
; not advisable: checking a long list of candidate objects against the SMEI
; star catalogue will drastically increase processing time.
;
; 6. Write output file
;
; The output file contains the results of the fits for all candidate
; objects, sorted by correlation (the best one first).
;
; Note that for objects located in the overlapping area between the polar
; maps and the equatorial map (approximately between 50 and 60 degrees
; declination north and south there will be two records in the output file:
; one for the object seen in the equatorial map, the other in one of the
; polar maps. This needs to be taken into account when analyzing the
; content of the input file (e.g. when counting the number of hits for
; a given object in a sequence of skymaps).
;
; The names of the objects indicate in which map the object was detected,
; EQ (for the equatorial map), NP and SP for north and south polar map,
; respectively; followed by an integer that counts the number of objects.
; Note that the same object will have a different name in output files
; for different skymaps. Entries will need to be matched by RA and dec.
;

;MODIFICATION HISTORY:

```
; FEB-2008, Paul Hick (UCSD/CASS)
; NOV-2011, Paul Hick (UCSD/CASS; pphick@ucsd.edu)
; Thorough review of code; added documentation.
; Most significant change to the code was the removal of the zodiacal
; dust cloud subtraction. The equ file now contain maps with the zld
; already subtracted, so this is not needed anymore.
; Reduced dependence on 'sky' files. These are needed now only if
; keyword /use_catalogue is used.
```

```
;
InitVar, camera , 2
InitVar, from_mode , 'equ'
InitVar, to_mode , 'bol'
InitVar, destination, getenv('TUB')
InitVar, fix_centroid, /key
InitVar, cvmin , 0.7
InitVar, use_catalogue, /key
InitVar, silent , 0
```

```
; Pick up list of SMEI skymaps.
```

```
given_map = smei_getfile(wanted_map, $
camera = camera , $
mode = from_mode , $
count = count , $
_extra = _extra )
```

```
; No maps found? Then stop.
```

```
IF count EQ 0 THEN $
```

RETURN

```
IF silent LE 3 THEN message, /info, strcompress(count,/rem)+ \  
' '+from_mode+' map(s)'
```

```
badval = BadValue(0.0)
```

```
missing = badval
```

```
dpr = 180.0/!pi
```

```
large_smooth= 81
```

```
small_smooth= 11
```

```
mindist = 10
```

```
relative = 1
```

```
fraction = 0.20
```

```
flat = ([1.0,0.02])[relative]
```

```
FOR imap=0,count-1 DO BEGIN ; Loop over all skymaps
```

```
T0 = TimeSystem(/silent)
```

```
equfile = given_map[imap]
```

```
equhide = hide_env(equfile)
```

```
equitime = smei_filename(equfile,camera=camera,postfix=postfix)
```

; 'skyfile' is used only to fit catalogue stars to be matched against the unknown

; objects found in 'equfile'

skyfile = smei_filepath(equitime,camera=camera,postfix=postfix,mode='sky',/full)

eclfile = smei_filepath(equitime,camera=camera,postfix=postfix,mode='ecl',/full)

bolfile = filepath(root=destination,smei_filename(equitime,camera=camera,
mode=to_mode,type='.txt'))

IF silent LE 2 THEN message, /info, equhide

; The psfn_sky, fovx_sky and time_sky array are low-res (720 x 360) arrays

smei_sky, equfile, /psfn , sky=psfn_sky, /noplot, camera=camera, /usetime, /exists, /de-
grees, hdr=hdr

smei_sky, equfile, /fovx , sky=fovx_sky, /noplot, camera=camera, /usetime, /exists, /de-
grees

destroyvar, tmp

smei_sky, equfile, /orbsecs, sky=time_sky, /noplot, camera=camera, /usetime, /exists,
exten_no=tmp

torigin = TimeSet(fxpar(headfits(equfile,exten=tmp),'TORIGIN'))

destroyvar, new_star

; =====

FOR jmap=0,2 DO BEGIN ; Equatorial, north pole, south pole

```
ikeys = [0,0,0]
```

```
ikeys[jmap] = 1
```

```
ckeys = ['eq','np','sp']
```

```
smei_sky, equfile, $ ; Get star-subtracted skymap
```

```
equatraw = ikeys[0] , $
```

```
northraw = ikeys[1] , $
```

```
southraw = ikeys[2] , $
```

```
sky = sky , $
```

```
nbin = 1 , $
```

```
/noplot , $
```

```
hdr = hdr , $
```

```
camera = camera , $
```

```
/usetime , $
```

```
/exact
```

```
hdr = hdr[0]
```

```
IF jmap EQ 0 THEN tt = TimeSet(smei=hdr.orbit)
```

```
rr = cvsmei(from_map='MAP',from_mode=ckey[jmap],/to_map,to_mode \
```

```
= 'lores' ,/silent)
```

```
rr = round(rr) ; Nearest lowres grid point
```

```
; Direction cosine angle for all bins in hires sky map
```

```
fov_x = fov_x_sky[reform(rr[0,*]),reform(rr[1,*])]
```

; This removes a small section of sky near the edge of the fov in the long dimension.
; This area tends to be filled with residuals from bad subtractions resulting from
; stars so close to edge that the PSFs are only partially present, or heavily deformed.

```
i = where(finite(sky) AND abs(fov_x) GT 29)
IF i[0] NE -1 THEN sky[i] = BadValue(sky)
```

; Skip empty maps

```
i = where(finite(sky))
IF i[0] EQ -1 THEN continue
```

; 1. Smooth the sky maps.

```
sky -= smooth(sky, large_smooth, /nan) ; Subtract large scale smoothed map
sky = smooth(sky, small_smooth, /nan) ; Smooth over 1-deg
```

; Find local maxima (as array indices into skymap)

```
rr = FindPeaks(sky, mindist=mindist, flat=flat, relative=relative, $
fraction=fraction, count=nfit, npeak=npeak)
```

```
rr = ArrayLocation(rr, dim=size(sky, /dim))
rr = cvsmei(from_map=rr, mode=ckeys[jmap], /to_equatorial, /degrees, /silent)
```

```
rr = AngleUnits(from_degrees=rr, /to_almanac, /singesign)
```

```
rr = float(rr)
```

```
rr[2,*,*] += rr[3,*,*]/1000.0
```

```
rr = rr[0:2,*,*]
```

```
star_list = replicate(smei_star_list,nfit)
```

```
star_list.name = strupcase(ckeys[jmap])+string(format='(I4.4)', lindgen(nfit)+1)+' '
```

```
star_list.ra = reform(rr[*,0,*])
```

```
star_list.dec = reform(rr[*,1,*])
```

```
; Try to fit local maxima with PSF
```

```
; with /fix_centroid set
```

```
smei_star_fit, equfile , $
```

```
northpole = ikeys[1] , $
```

```
southpole = ikeys[2] , $
```

```
star_list = star_list , $
```

```
/degrees , $
```

```
psf_map = psfn_sky , $
```

```
fov_x_map = fov_x_sky , $
```

```
time_map = time_sky , $
```

```
torigin = toorigin , $
```

```
/use_weights , $
```

```
/auto_wing , $
```

```
fix_centroid=fix_centroid , $
```

```
star_fit = star_fit , $
```

```
star_info = i , $
/silent

; Save info for equatorial map

IF jmap EQ 0 THEN star_info = i

; Add centroid offset to centroid position
; Map RA back to range [0,360]

star_fit.radec += star_fit.dradec
star_fit.radec[0] = AngleRange(star_fit.radec[0],/degrees)
star_fit.dradec = 0

; Retain only stars with correlation better than cvmin

i = where(star_fit.cvfit GT cvmin,nfit)
IF nfit EQ 0 THEN continue

; If use_catalogue is NOT set then no more work needs to be done.

IF NOT use_catalogue THEN BEGIN
boost, new_star, star_fit
continue
ENDIF

; use_catalogue IS set.
; Continue by trying to match each of the objects against the
```

```
; list of catalogues star. If a catalogue star is found within  
; 0.5 a degree or so, we are probably picking up a catalogue  
; object that was subtracted imperfectly.  
; Give the object the name of the catalogue star  
; This step is very time consuming if cvmin is set very low,  
; which is why the use_catalogue keyword was introduced.
```

```
star_fit = star_fit[i]
```

```
; Check for stars already on the star catalogue. Quite a few  
; of the stars just detected are probably stars that were not  
; fitted very well (due to bad quaternions for instance).
```

```
star_cat = smei_star_info(/get_struct,count=ncat)
```

```
cat_pos = smei_star_info(star_cat,/radec,/degrees)
```

```
fit_pos = star_fit.radec
```

```
IF nfit GT 1 THEN BEGIN
```

```
cat_pos = SuperArray(cat_pos,nfit,after=2)
```

```
fit_pos = SuperArray(fit_pos,ncat,after=1)
```

```
ENDIF
```

```
; Elongations of new stars vs catalogue stars
```

```
elo = sphere_distance(cat_pos,fit_pos,/degrees) ; array[ncat,nfit]
```

```
destroyvar, cat_pos, fit_pos
```

```
; Find catalogue star closes to new stars
```

```
tmp = min(elo,p,dim=1) ; p = array[nfit]
```

```
p = ArrayLocation(p,dim=[ncat,nfit])
```

```
p = reform(p[0,*])
```

```
; Closest catalogue stars
```

```
star_cat = star_cat[p]
```

```
; Fit closest stars in original (unsubtracted) skymap
```

```
; with /fix_centroid set to get the best possible location
```

```
;names = star_cat.name
```

```
smei_star_fit, skyfile , $
```

```
northpole = ikeys[1] , $
```

```
southpole = ikeys[2] , $
```

```
star_list = star_cat , $
```

```
/degrees , $
```

```
psf_map = psfn_sky , $
```

```
fov_x_map = fov_x_sky , $
```

```
time_map = time_sky , $
```

```
torigin = toorigin , $
```

```
/use_weights , $
```

```
/auto_wing , $
```

```

fix_centroid=fix_centroid , $
count = count_cat , $
star_fit = close_cat , $
max_stars = 1 , $
star_remove = replicate(0,nfit), $
star_index = star_index , $
skip_dist = 0.0 , $
incl_dist = 0.0 , $
/silent

IF count_cat EQ 0 THEN continue

star_cat = star_cat[star_index]
star_fit = star_fit[star_index]

; Add centroid offset to centroid position

close_cat.radec += close_cat.dradec
close_cat.radec[0] = AngleRange(close_cat.radec[0],/degrees)
close_cat.dradec = 0

elo = sphere_distance(star_fit.radec,close_cat.radec,/degrees)

p = where(elo LT 0.5,n)

FOR i=0,n-1 DO BEGIN
q = p[i]
print, star_fit[q].name, '=', close_cat[q].name, ' @ ', elo[q], ' deg'
star_fit[q].name = close_cat[q].name

```

ENDFOR

boost, new_star, star_fit

ENDFOR

; Write the output file with candidate objects

; Objects are written sorted by correlation coefficient (high first).

i = n_elements(new_star)

IF i NE 0 THEN BEGIN

message, /info, 'writing '+hide_env(bolfile)+' ('+strcompress(i,/rem)+' stars)'

smei_star_writepnt, bolfile, new_star[reverse(sort(new_star.cvfit))], star_info=star_info

ENDIF

ENDFOR

RETURN & END